

STATISTICAL ELECTROMAGNETICS

Richard Holland and Richard St. John

Shield Rite, Inc.
P. O. Box 8250
Albuquerque NM 87198

14 January 1998

Final Report

APPROVED FOR PUBLIC RELEASE; DISTRIBUTION IS UNLIMITED.

20010907 115



AIR FORCE RESEARCH LABORATORY
Directed Energy Directorate
3550 Aberdeen Ave SE
AIR FORCE MATERIEL COMMAND
KIRTLAND AIR FORCE BASE, NM 87117-5776

Using Government drawings, specifications, or other data included in this document for any purpose other than Government procurement does not in any way obligate the U.S. Government. The fact that the Government formulated or supplied the drawings, specifications, or other data, does not license the holder or any other person or corporation; or convey any rights or permission to manufacture, use, or sell any patented invention that may relate to them.

This report has been reviewed by the Public Affairs Office and is releasable to the National Technical Information Service (NTIS). At NTIS, it will be available to the general public, including foreign nationals.

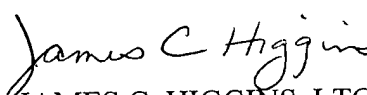
If you change your address, wish to be removed from this mailing list, or your organization no longer employs the addressee, please notify AFRL/DEBE, 3550 Aberdeen Ave SE, Kirtland AFB, NM 87117-5776.

Do not return copies of this report unless contractual obligations or notice on a specific document requires its return.

This report has been approved for publication.



PATRICK J. McDANIEL
Project Manager



JAMES C. HIGGINS, LTCOL
Chief, Advanced Systems Analysis Branch

FOR THE COMMANDER



R. EARL GOOD, SES
Director, Directed Energy

REPORT DOCUMENTATION PAGE

Form Approved
OMB No. 0704-0188

Public reporting burden for this collection of information is estimated to average 1 hour per response, including the time for reviewing instructions, searching existing data sources, gathering and maintaining the data needed, and completing and reviewing the collection of information. Send comments regarding this burden estimate or any other aspect of this collection of information, including suggestions for reducing this burden, to Washington Headquarters Services, Directorate for Information Operations and Reports, 1215 Jefferson Davis Highway, Suite 1204, Arlington, VA 22202-4302, and to the Office of Management and Budget, Paperwork Reduction Project (0704-0188), Washington, DC 20503.

1. AGENCY USE ONLY (Leave blank)			2. REPORT DATE	3. REPORT TYPE AND DATES COVERED
			14 January 1998	Final: March 95 to January 98
4. TITLE AND SUBTITLE			5. FUNDING NUMBERS	
Statistical Electromagnetics			C - F29601-95-C-0045 PE - 65502F PR - 3005 TA - C0 WU - HT	
6. AUTHOR(S)			Richard Holland & Richard St. John	
7. PERFORMING ORGANIZATION NAME(S) AND ADDRESS(ES)			8. PERFORMING ORGANIZATION REPORT NUMBER	
Shield Rite, Inc. P. O. Box 8250 Albuquerque, New Mexico 87198				
9. SPONSORING/MONITORING AGENCY NAME(S) AND ADDRESS(ES)			10. SPONSORING/MONITORING AGENCY REPORT NUMBER	
Air Force Research Laboratory 3550 Aberdeen Ave SE Kirtland Air Force Base, New Mexico 87117-5776			AFRL-DE-PS-TR-1998-1025	
11. SUPPLEMENTARY NOTES				
12a. DISTRIBUTION AVAILABILITY STATEMENT			12b. DISTRIBUTION CODE	
Approved for public release: distribution is unlimited				
13. ABSTRACT (Maximum 200 words) Deterministic treatment of High-Power Microwaves or Radio-Frequency Interference internal coupling to wiring and cabling of highly overmoded enclosures is too detailed to be practical. However, statistical models thrive on complexity. In this report, cable current distributions on the ElectroMagnetic Pulse Test AirCraft airframe, a Global Positioning Satellite bus, and the Celestron 8 satellite telescope are modeled statistically when illumination is external and penetration is through apertures or cables entering from the exterior. The observed field power fluxes and cable powers are tested against a chi-square distribution with two degrees of freedom, a beta distribution, a log-normal distribution, and a curious hybrid distribution due to Lehman, which would pertain to a variate which is the product of two chi-square distributions, one having two, and the other six, degrees of freedom. We demonstrate that, if the enclosure cables are modeled with a simulated drive having a Lehman distribution, it is possible to replicate the experimentally observed power distribution within a factor of two, although cable powers themselves look more like a chi-square distribution than a Lehman distribution. We have also constructed a hardware/software assembly incorporating a Pentium PC and an HP8753 Network Analyzer which can (1) illuminate an enclosure externally with 1 watt of power, (2) can measure the field, or cable current, response inside the enclosure, and (3) compares experiment with theory.				
14. SUBJECT TERMS			15. NUMBER OF PAGES	
HPM, RFI, statistical electromagnetics, chi-square distribution, log-normal distribution, Lehman distribution, beta distribution, EMPTAC, GPS cabling, Celestron 8 telescope, cable networks, cable drive, probability plots, Kolmogorov-Smirnov test			268	
16. PRICE CODE				
17. SECURITY CLASSIFICATION OF REPORT		18. SECURITY CLASSIFICATION OF THIS PAGE	19. SECURITY CLASSIFICATION OF ABSTRACT	20. LIMITATION OF ABSTRACT
unclassified		unclassified	unclassified	unl

TABLE OF CONTENTS

Chapter 1. THE NEED FOR STATISTICAL ELECTROMAGNETICS (SEM)	1
REFERENCES	3
Chapter 2. DISTRIBUTION AND AUTOCORRELATION OF INTERNAL FIELDS	5
PROBABILITY PLOTS	5
THE FIELD-AUTOCORRELATION ISSUE	7
MAPPING OF RANDOM NUMBERS TO GIVEN DISTRIBUTIONS	21
GENERATION AND INVERSION OF COMPOUND DISTRIBUTIONS	28
FIELD DISTRIBUTIONS AND POWER FLUX DISTRIBUTION	29
THE DETRENDING OPERATION	34
REFERENCES	35
Chapter 3. FIELD REDISTRIBUTION AND CABLE RESPONSE	37
DATA RESTORATION AFTER FORCED AUTOCORRELATION	37
THE CABLE DRIVE ALGORITHM	48
FINE TUNING THE CABLE RESPONSES	53
MORE OPTIMIZING OF CABLE DRIVER GENERATION	64
MORE THOUGHTS ON RADIATION RESISTANCE	68
SUMMARY AND CONCLUSIONS OF THIS SECTION	73
Chapter 4. THE LOG NORMAL DISTRIBUTION	74
INTRODUCTION TO THE LOG NORMAL DISTRIBUTION	74
ANALYTIC FITS FOR DECONVOLVED LOG NORMAL DISTRIBUTIONS	84
EMPIRICAL FITS FOR DECONVOLVED LOG NORMAL DISTRIBUTIONS	87
GENERATION OF LOG NORMAL FIELD DRIVERS	90
COMPARISON OF THEORY AND EMPTAC-BASED DATA	91
HYBRID NORMAL \times LOG-NORMAL FIELD DISTRIBUTIONS	94
HYBRID POWER-FLUX MODEL FOR THE CELESTRON 8 TELESCOPE	100
CONCLUSIONS FOR THIS SECTION	102
REFERENCES	102
Chapter 5. CHI SQUARE VARIANTS: THE LEHMAN DISTRIBUTION	104
PRELIMINARY OVERVIEW	104
DETAILS OF THE LEHMAN DERIVATION	107
LEHMAN FIELD DECONVOLUTION: BRIEF OVERVIEW	119
LEHMAN FIELD DECONVOLUTION: IN-DEPTH DERIVATION	123
FASTER LEHMAN FIELD DECONVOLUTION: IN-DEPTH DERIVATION	130
FIELD AND CABLE CURRENT DISTRIBUTION IN SUBENCLOSURES	138

FIELDS IN ENCLOSURES WITHIN MODE-STIRRED CHAMBERS	139
EXTRAPOLATION OF PLANE-WAVE RESPONSE FROM MODE-STIRRED MEASUREMENTS	140
REFERENCES	142
 Chapter 6. FIELD-TESTS OF LEHMAN-MODELED CABLE CURRENTS, THE BETA DISTRIBUTION, AND ACCEPTANCE LIMITS 144	
MEASUREMENTS IN THE WAVEGUIDE CHAMBER	144
A DETAILED LOOK AT A GPS RESPONSE	152
REFERENCES	167
 Chapter 7. CAVITY EIGENMODES: THEIR EVALUATION, PROPERTIES, AND PERTURBATION BY DISSIPATION AND BY APERTURES 168	
EIGENMODE DEFINITION AND EXPANSION	168
ENERGY AND POWER DISSIPATION PARTITIONING BETWEEN MODES	171
CONSIDERATION OF Q	172
START-UP TRANSIENTS	173
APERTURE DRIVE	178
LAGRANGIAN REPRESENTATION AND TECHNIQUES	179
EXPANSION OF RESPONSE OF APERTURE DRIVE	181
GREEN'S FUNCTIONS	182
EIGENMODE EXPANSION OF POWER INPUT THROUGH AN APERTURE	183
EIGENMODE EXPANSION OF POWER LOSS THROUGH AN APERTURE	184
EFFECT ON Q OF APERTURES	187
REFERENCES	187
 Chapter 8. EM PICKUP AND SCATTERING BY A WIRE 189	
HOMOGENEOUS SOLUTION FOR A WIRE	191
INHOMOGENEOUS SOLUTIONS FOR A WIRE	195
MATCHING THE HOMOGENEOUS AND INHOMOGENEOUS SOLUTIONS	199
REVIEW OF TRANSMISSION LINES	202
NUMERICAL COMPARISON WITH A SIMPLER MODEL	204
INTRODUCTION OF A GROUND PLANE	205
HOMOGENEOUS WAVENUMBER $\gamma(\omega)$ FOR A WIRE OVER A GROUND PLANE	210
SUMMARY OF DRIVER OPTIONS	211
SECTION SUMMARY	213
APPENDIX 8A. ENERGY BUILDUP AND THE MEANING OF Q	213
REFERENCES	217

Chapter 9. STATISTICAL DISTRIBUTION OF FIELDS IN COMPLEX CAVITIES: THE JAYCOR MYSTIQUE	219
SPECIFIC MODE DENSITY	219
MEASURED POWER IN AN OVERMODED CAVITY	221
PROPERTIES OF THE EIGENFUNCTION COMPONENTS	223
CAVITY RATE EQUATION AND RESONANCE FUNCTION	226
STATISTICAL PROPERTIES OF THE MEASURED POWER	231
COMPARISON OF THEORY WITH EXPERIMENT: THE K-S TEST	242
REFERENCES	243
Chapter 10. CONCLUSIONS	245

TABLE OF FIGURES

<u>FIGURE</u>		<u>PAGE</u>
2.1	Probability plots of experimentally observed, detrended EMPTAC cable powers all show good fits to the chi square distribution model with two degrees of freedom.	8
2.2	Bottom curves: unfiltered, simulated cable current $ I ^2$ inside the EMPTAC middle bay and $ I ^2$ trend. Top curve: $ I ^2$ with trend factored out: $ I ^2 / I_{trend} ^2$. This figure is based on f_{space} and f_{freq} both set to 1, and the assumption that u_{lim} has a chi square distribution.	13
2.3	Bottom curves: unfiltered, simulated cable current $ I ^2$ inside the EMPTAC middle bay and $ I ^2$ trend. Top curve: $ I ^2$ with trend factored out: $ I ^2 / I_{trend} ^2$. This figure is based on f_{space} and f_{freq} both set to 10, and the assumption that u_{lim} has a chi square distribution.	14
2.4	Bottom curves: unfiltered, simulated cable current $ I ^2$ inside the EMPTAC middle bay and $ I ^2$ trend. Top curve: $ I ^2$ with trend factored out: $ I ^2 / I_{trend} ^2$. This figure is based on f_{space} and f_{freq} both set to 100, and the assumption that u_{lim} has a chi square distribution.	14
2.5	Bottom curves: observed, unfiltered cable current $ I ^2$ inside the EMPTAC middle bay and $ I ^2$ trend. Top curve: $ I ^2$ with trend factored out: $ I ^2 / I_{trend} ^2$. This figure is based on a high-frequency experimental data sweep. Note the monopolar downward nature of the spikes on the detrended (upper) data set.	15
2.6	Probability plot of simulated cable currents squared against a chi square (two degrees of freedom) distribution assumption. When driven by field components having a chi square distribution, the simulated EMPTAC cable currents, even upon filtering for trend removal, do not fit a chi square distribution.	15
2.7	Normalized autocorrelation of the observed magnetic field along x (fuselage axis) with (dashed line) and without (solid line) the data filtered. This figure is based on the low-frequency EMPTAC middle-bay scan. Note that the autocorrelation of the filtered data is characterized by a central peak and broad plateau about .5 of the central peak.	16
2.8	Normalized autocorrelation of the observed magnetic field along x (fuselage axis) with (dashed line) and without (solid line) the data filtered. This figure is based on the high-frequency EMPTAC middle-bay scan.	17
2.9	Normalized autocorrelation of the observed cable current with (dashed line) and without (solid line) the data filtered. This figure is based on the high-frequency EMPTAC middle-bay scan.	17
2.10	Normalized autocorrelation of the simulated cable current with (dashed line) and without (solid line) the data filtered. This figure is based on f_{space} and f_{freq} both set to 1 (artificially high autocorrelation), and the assumption that u_{lim} has a chi square distribution.	19
2.11	Normalized autocorrelation of the simulated cable current with (dashed line) and without (solid line) the data filtered. This figure is based on f_{space} and f_{freq} both set to 100 (almost no correlation), and the assumption that u_{lim} has a chi square distribution.	20
2.12	Normalized autocorrelation of the simulated cable current with (dashed line) and without (solid line) the data filtered. This figure is based on f_{space} and f_{freq} both set to 100 (almost no correlation), and the assumption that u_{lim} has a chi square distribution.	20

<u>FIGURE</u>		<u>PAGE</u>
2.13	Contour of integration for evaluating the distribution density $f(x)$ when $x < 0$.	32
3.1	Plot of $z = u^2 + v^2$ for each component (u and v) of the phase-quadrature drive generated according to (2-10), (2-14) and (2-15) (normal case) with f_{space} and f_{freq} both set to 1000 (almost no autocorrelation).	40
3.2	Normalized autocorrelation of the drive variables u (real) and v (imaginary) normally generated, but before rescaling. Both phase-quadrature components essentially have no autocorrelation except for the central spike.	40
3.3	Normalized autocorrelation of the squared and summed drive based on a variable-frequency cut of the z ensemble as defined in (2-18). Note that the data bear a nice resemblance to the observed EMPTAC experimental results (Figures 2.7- 2.9), except that the central peak is too narrow, as one would expect for parameters inducing unrealistically low autocorrelation (f_{space} and f_{freq} both 1000).	41
3.4	Probability plot for the assumption that the u and v ensembles are normally distributed before rescaling. This figure is based on f_{space} and f_{freq} both set to 1000, and $\sigma_g = 0.01$, $\mu_g = 0.00$. The agreement with a 45° line is excellent.	41
3.5	Probability plot for the assumption that the z ensemble has a chi square distribution, both before and after u and v are rescaled. This figure is based on f_{space} and f_{freq} both set to 1000, on u and v being normally generated, and on $\sigma_g = 0.01$, $\mu_g = 0.00$.	42
3.6	Both u and v , even before rescaling, fall within the Kolmogorov-Smirnov 90% confidence limits for a normal distribution when they are normally generated with f_{space} and f_{freq} both 1000, and with $\sigma_g = 0.01$, $\mu_g = 0.00$.	42
3.7	Both u and v , even before rescaling, fall within the Kolmogorov-Smirnov 90% confidence limits for a normal distribution when they are normally generated with f_{space} and f_{freq} both 1000, and with $\sigma_g = 0.01$, $\mu_g = 0.00$.	44
3.8	The unscaled and the rescaled z arrays (generated under the same parameters as in Figure 3.1) fall within the Kolmogorov-Smirnov 90% confidence limits for having a chi square distribution if the defining the confidence limits are determined from the data (as opposed to being pinned at $\mu_c = 0.0002$).	44
3.9	Plot of $z = u^2 + v^2$ for each component (u and v) of the phase-quadrature drive generated according to (2-10), (2-14), and (2-15) (normal case) with f_{space} and f_{freq} both set to 10 (physically realistic autocorrelation).	45
3.10	Normalized autocorrelation of the drive variables u (real) and v (imaginary) before rescaling. Both phase-quadrature components essentially have no autocorrelation except for the central spike, which is broadened in comparison to Figure 3.2. These data are based on the same normal drive generation as Figure 3.9 (f_{space} and f_{freq} both 10, $\sigma_g = 0.01$ and $\mu_g = 0.00$).	45
3.11	Normalized autocorrelation of the squared and summed drive based on a variable-frequency cut of the z ensemble as defined in (2-18). Note that the data bear a nice resemblance to the observed EMPTAC experimental results (Figures 2.7-2.9), including a realistic breadth of the central peak.	46

FIGURE		PAGE
3.12	Probability plot for the assumption that the normally generated u and v ensembles are normally distributed before after introduction of autocorrelation, but before rescaling. This figure is based on f_{space} and f_{freq} both set to 10, with $\sigma_g = 0.01$, $\mu_g = 0.00$.	46
3.13	Probability plot for the assumption that the z ensemble has a chi square distribution, both before and after u and v are normally rescaled. This figure is based on f_{space} and f_{freq} both set to 10, with $\sigma_g = 0.01$, $\mu_g = 0.00$.	47
3.14	Neither u nor v , after forcing autocorrelation, but before rescaling, fall within the Kolmogorov-Smirnov 90% confidence limits for a normal distribution when they are generated with f_{space} and f_{freq} both 10, and with $\sigma_g = 0.01$, $\mu_g = 0.00$.	47
3.15	The summed and squared variable z , before normal rescaling of u and v , is far out of range to the left of the Kolmogorov-Smirnov 90% confidence limits for being chi square with the mean and standard deviation pinned at $\mu_c = 2\sigma_g^2 = .0002$, when f_{space} and f_{freq} are set to 10, with $\sigma_g = 0.01$, $\mu_g = 0.00$.	49
3.16	The unscaled z array, based on normal u and v with f_{space} and f_{freq} set to 10, and $\sigma_g = 0.01$, $\mu_g = 0.00$, deviates in a major way from the 90% K-S test for being chi square, even when μ_c is unpinned, and allowed to float to fit the data (left curves).	49
3.17	The phase-quadrature cable currents, resulting from autocorrelated and rescaled drive, do not fit a normal probability plot. This figure is based on normal u and v with f_{space} and f_{freq} set to 10, and $\sigma_g = 0.01$, $\mu_g = 0.00$.	55
3.18	The cable power distribution produced by rescaled cable drive does not fit a Kolmogorov-Smirnov test for being chi square, even after filtering. This figure is based on normal u and v with f_{space} and f_{freq} set to 10, and $\sigma_g = 0.01$, $\mu_g = 0.00$.	55
3.19	The unfiltered cable power distribution, based on rescaled cable drive, has an excellent match to a log normal probability plot. This figure is based on normal u and v with f_{space} and f_{freq} set to 10, and $\sigma_g = 0.01$, $\mu_g = 0.00$.	55
3.20	Addition of radiation resistance makes the phase-quadrature cable current components more nearly normally distributed. This figure is based on normal u and v with f_{space} and f_{freq} set to 10, and $\sigma_g = 0.01$, $\mu_g = 0.00$.	56
3.21	Introduction of radiation resistance brings the filtered cable power distribution closer to a chi square distribution. This figure is based on normal u and v with f_{space} and f_{freq} set to 10, and $\sigma_g = 0.01$, $\mu_g = 0.00$.	56
3.22	Introduction of radiation resistance leaves the unfiltered cable power distribution very nearly log normal. This figure is based on normal u and v with f_{space} and f_{freq} set to 10, and $\sigma_g = 0.01$, $\mu_g = 0.00$.	56
3.23	Constant Δf drive-field generation brings the phase-quadrature cable current distribution still more into agreement with a normal distribution. This figure is based on normal u and v with f_{space} and f_{freq} set to 10, and $\sigma_g = 0.01$, $\mu_g = 0.00$.	59

<u>FIGURE</u>		<u>PAGE</u>
3.24	Constant Δf drive-field generation brings cable power distribution still closer to a chi square fit. This figure is based on normal u and v with f_{space} and f_{freq} set to 10, and $\sigma_g = 0.01$, $\mu_g = 0.00$.	59
3.25	Constant Δf drive-field generation finally causes the cable power distribution to deviate from a log normal distribution. This figure is based on normal u and v with f_{space} and f_{freq} set to 10, and $\sigma_g = 0.01$, $\mu_g = 0.00$.	59
3.26	The amplitudes of the u ensemble members still have a growing trend as frequency increases, even with constant Δf . This figure is based on normal u and v with f_{space} and f_{freq} set to 10, and $\sigma_g = 0.01$, $\mu_g = 0.00$.	61
3.27	Pivoting ensemble envelopes about average values finally eliminates the cable drivers' growth trend. This figure is based on normal u with f_{space} and f_{freq} set to 10, and $\sigma_g = 0.01$, $\mu_g = 0.00$.	61
3.28	The pivoted cable current drivers yield a phase-quadrature cable current distribution which is still closer to normal, as this probability plot shows. This figure is based on normal u and v with f_{space} and f_{freq} set to 10, and $\sigma_g = 0.01$, $\mu_g = 0.00$.	62
3.29	The pivoted cable current drivers yield cable powers which come still closer to being chi square in distribution, as this Kolmogorov-Smirnov 90% confidence test shows. This figure is based on normal u with f_{space} and f_{freq} set to 10, and $\sigma_g = 0.01$, $\mu_g = 0.00$.	62
3.30	The pivoted cable current drivers yield a phase-quadrature cable current distribution which is still closer to normal, as this probability plot shows. This figure is based on normal u and v with f_{space} and f_{freq} set to 10, and $\sigma_g = 0.01$, $\mu_g = 0.00$.	63
3.31	Adding frequency dependence to the model of the radiation resistance on the cable is our final step in matching the cable power distribution to a chi square model. This figure is based on normal u and v with f_{space} and f_{freq} set to 10, and $\sigma_g = 0.01$, $\mu_g = 0.00$.	63
3.32	Summed squares of driving field phase-quadrature components computed by all four options pass the 90% K-S confidence test for being chi square with two degrees of freedom, but the recommended fs options (bottom pair) stay closer to the limit midpoint.	65
3.33	Summed squares of driving field phase-quadrature components computed by all four options have a realistic autocorrelation, but the recommended fs options (bottom pair) have smoother shoulders. It is possible the broader central spike of the sf options (top pair) is more representative of the actual physics.	66
3.34	The recommended sf summed squares of driving field phase-quadrature components have a more level baseline (bottom pair) than the fs runs (top pair).	67
3.35	The frequency-dependent radiation-resistance model (right pair) gives more chi square like summed-squares of phase-quadrature cable currents than the frequency-independent model, although only the fsd model actually produces a cable-current distribution which is 90% confident of being chi square.	69
3.36	Only the fsd cable-driver model results in a flat baseline for the output summed squares of the phase-quadrature cable currents.	70

<u>FIGURE</u>		<u>PAGE</u>
3.37	The <i>fsd</i> cable-driver model results in much flatter cable power autocorrelation shoulder than any of the other cable-drive options.	71
4.1	The log normal distribution function with $\sigma_{lg} = 1$ and $\mu_{lg} = 0$.	75
4.2	Fourier transform of the log normal distribution density function and the square root of this transform. Note how much more slowly the square-root transform goes to zero.	75
4.3	Fourier transform of the log normal distribution density function and the square root of this transform. Note how much more slowly the square-root transform goes to zero.	77
4.4	Small curve: Log normal distribution function perfectly overlaid by inverse transform of transform of this function. Larger curves: Sine and cosine inverse transforms of the square root of the transform of the log normal distribution.	77
4.5	The log normal distribution function is almost perfectly overlaid by the autoconvolution of the inverse transform of the square root of the transform of the log normal distribution function when $\sigma_{lg} = 1$.	78
4.6	Smaller curves to lower right: triple overlay of original log normal distribution $h(z)$ as calculated from (4-3), and from taking the inverse sin and cos transforms of the transform. This overlay is excellent. Larger curves to left: triple overlay of inverse sin and cos transforms of sqrt of transform, $f_1(x)$, with an analytic fit based on (4-10) and (4-11), $f_2(x)$, with f_{max} and x_{max} empirically taken from the inverse sine transform.	81
4.7	Curves at center: triple overlay of original log normal distribution as calculated from (4-3), $h(z)$, and from taking the inverse sin and cos transforms of the result. Logarithmic display indicates overlay breaks up about 40 dB below peak. Larger curves to left and top: triple overlay of inverse sin and cos transforms of sqrt of transform, $f_1(x)$, plus an analytic fit based on (4-10) and (4-11), $f_2(x)$, with f_{max} and x_{max} empirically taken from the inverse sine transform.	82
4.8	Transform and sqrt of transform of log normal distribution. This figure is based on $h(z)$ having $\mu_{lg} = 0.0$ and $\sigma_{lg} = 1.4$.	83
4.9	Phase of sqrt of transform of log normal distribution. This figure is based on $h(z)$ having $\mu_{lg} = 0.0$ and $\sigma_{lg} = 1.4$.	83
4.10	Overlay of $h(z)$ obtained from (4-3) with that obtained from autoconvolution of the inverse transform of the sqrt of the transform, $f_1(x)$, from the autoconvolution obtained from (4-10) and (4-11), $f_2(x)$, and from the autoconvolution obtained from (4-18) and (4-19), $f_3(x)$.	85
4.11	Overlay of log normal distribution for $h(z)$ with $(\sigma_{lg}, \mu_{lg}) = (1.0, 0.0)$ and autoconvolution approximation based on guess of log normal $f(x)$ with $(\sigma_{lg}', \mu_{lg}') = (1.87, -1.0)$.	88
4.12	Overlay of log normal distribution for $h(z)$ with $(\sigma_{lg}, \mu_{lg}) = (1.4, 0.0)$ and autoconvolution approximation based on guess of log normal $f(x)$ with $(\sigma_{lg}', \mu_{lg}') = (3.65, -1.2)$.	88
4.13	Overlay of log normal distribution for $h(z)$ with $(\sigma_{lg}, \mu_{lg}) = (1.8, 0.0)$ and autoconvolution approximation based on guess of log normal $f(x)$ with $(\sigma_{lg}', \mu_{lg}') = (6.0, -1.42)$.	89

<u>FIGURE</u>		<u>PAGE</u>
4.14	Overlay of log normal distribution for $h(z)$ with $(\sigma_{lg}, \mu_{lg}) = (1.9, -17.5)$ and autoconvolution approximation based on guess of log normal $f(x)$ with $(\sigma_{lg}', \mu_{lg}') = (6.6, -1.89)$.	89
4.15	Model-based cumulative distribution of the squared currents on the EMPTAC cables [with 90% Kolmogorov-Smirnov confidence limits for being log normal].	93
4.16	Measured cumulative distribution of the squared currents on the EMPTAC cables (with 90% Kolmogorov-Smirnov confidence limits for being log normal).	93
4.17	The EMPTAC model squared cable current distribution (solid line) does not stray outside the bounds provided by an overlay of three squared cable current distributions (various dashed lines) which were obtained under slightly varied measurement conditions.	94
4.18	In the real world, fields squared and currents squared usually do not fit a chi square distribution very well.	95
4.19	Generally, sums of two squared phase-quadrature components look log normal, not chi square in the real world.	95
4.20	Hybrid log-normal/chi-square distribution (solid line), with measured $ H_z ^2$ from Sweep B050MBHZ overlaid (line in long dashes). Crossover occurs at $P = 0.9$.	97
4.21	The cumulative probability distribution obtained by joining the log normal, $F(x)$ of (4-41), and the chi square, $F_2(x)$ of (4-43), at $P = 0.9$.	99
4.22	The cumulative probability distribution obtained by joining the log normal, $E(u)$ of (4-48), and the chi square, $E_2(u)$ of (4-51), at $P' = 0.95$.	101
4.23	Hybrid log-normal/chi-square distribution (solid line), with measured $ H_z ^2$ from Celestron 8 8 GHz to 18 GHz sweep overlaid (line in long dashes). Crossover occurs at $P = 0.875$.	101
5.1	Lehman distribution compared with EMPTAC magnetic-field data (100 MHz - 1 GHz sweep).	106
5.2	Lehman distribution compared with Celestron 8 magnetic-field data (8 GHz - 18 GHz sweep).	106
5.3	Comparison of the Lehman, $h_{\chi^2}(2,z)$ and the $h_{\chi^2}(6,z)$ cumulative distributions [based on $(\Lambda, \gamma_2, \gamma_6) = (1, 1, 1)$].	110
5.4	Square of magnetic field in the EMPTAC (100 MHz - 1 GHz high-frequency sweep of H_z , B050MBHZ)	112
5.5	Lehman distribution (based on $\Lambda = 3.814e+7 = 3/\mu_{data}$) and EMPTAC data from 100 MHz to 1 GHz.	112
5.6	EMPTAC data from 100 MHz to 1 GHz compared with various fits.	113
5.7	Square of magnetic field in the EMPTAC (500 MHz - 1 GHz partial low-frequency sweep of H_z , A050MBHZ).	113
5.8	Lehman distribution (based on $\Lambda = 2.591e+7 = 3/\mu_{data}$) and EMPTAC data from 500 MHz to 1 GHz.	114

<u>FIGURE</u>		<u>PAGE</u>
5.9	Square of magnetic field in the EMPTAC (300 kHz - 100 MHz low-frequency sweep of H_z , A050MBHZ).	114
5.10	Lehman distribution (based on $\Lambda = 1.63e+10 = 3/\mu_{data}$) and EMPTAC data from 300 kHz to 100 MHz.	115
5.11	Square of magnetic field in the EMPTAC (9 MHz - 100 MHz low-frequency partial sweep of H_z , A050MBHZ).	115
5.12	Lehman distribution (based on $\Lambda = 1.478e+10 = 3/\mu_{data}$) and EMPTAC data from 9 MHz to 100 MHz.	116
5.13	Power flux density distribution at focal plane in Celestron 8 satellite telescope for 1.5 GHz - 3.5 GHz sweep.	116
5.14	Lehman distribution (based on $\Lambda = 1.596e+3 = 3/\mu_{data}$) and Celestron 8 data from 1.5 to 3.5 GHz sweep.	117
5.15	Power flux density distribution at focal plane in Celestron 8 satellite telescope for 3.5 GHz - 8 GHz sweep.	117
5.16	Lehman distribution (based on $\Lambda = 4.053 = 3/\mu_{data}$) and Celestron 8 data from 3.5 to 8 GHz sweep.	118
5.17	Power flux density distribution at focal plane in Celestron 8 satellite telescope for 8 GHz - 18 GHz sweep.	118
5.18	Lehman distribution (based on $\Lambda = 1.929 = 3/\mu_{data}$) and Celestron 8 data from 8 to 18 GHz sweep.	119
5.19	Overlay of 1) random field values, plotted as summed & squared components after Lehman rescaling according to (3-3) and (5-27) and based on $\Lambda = 10$, 2) values computed directly from the Lehman cumulative distribution function (5-22) with $\Lambda = 10$, 3) values computed directly from the Lehman cumulative distribution function with $\Lambda = 3/\mu$, where $\mu = 0.34$ was obtained from the random-rescaled ensemble.	121
5.20	Two EMPTAC cable-current amplitude (unsquared) distributions based on cable model of (3-6) - (3-16) with the same parameters as those used to generate Figure 4.17, except that the Lehman electric-field distribution (5-27) was used instead of a chi square distribution. The Lehman parameter for the fields was determined from experimental data to be $\Lambda = 17600$.	122
5.21	Comparison of $K_2(z)$ and the approximate fit of (5-32).	124
5.22	Lehman distribution density and cumulative distribution for $\Lambda = 10$ (solid) and 1 (dashed).	124
5.23	Error in approximations $h_a(z, \Lambda)$ and $h_b(z, \Lambda)$ [(5-32) and (5-33)] to the Lehman pdf.	124
5.24	Integral (5-34) and high-low asymptotic (5-35) approximations to $K_5(z)$.	127
5.25	Deviation from Lehman pdf of low-z limit (5-39) of $h_n(z)$, based on low-z approximation $f_n(z, \Lambda)$ of (5-38), for $\Lambda = 1$.	127
5.26	Deviation of $h_n(z, \Lambda, \alpha, \beta, \gamma)$ of (5-41) from Lehman pdf based on $\Lambda = 1$.	127

FIGURE		PAGE
5.27	Contour plot of the misfit function $M_1(z,\Lambda)$ (5-47) for the $h_n(z,\Lambda)$ (5-46) approximation to the Lehman distribution.	129
5.28	The pdf and cdf approximations, $e_n(u,\Lambda)$ and $E_n(u,\Lambda)$, to the Lehman-associated field amplitude distribution (5-49), based on $\Lambda = 10$.	130
5.29	Comparison of the exact Lehman distribution density (5-17) and the approximate distribution density $h_n(z,1)$ obtained from autoconvolution of (5-52).	131
5.30	Comparison of the exact Lehman distribution density (5-17) and the approximate distribution density $h_n(z,1,\alpha,\beta,\gamma)$ obtained from (5-54).	132
5.31	Comparison of the exact Lehman distribution density (5-17) and the approximate distribution density $h_n(z,1,\alpha,\beta,\gamma)$ obtained from (5-55).	132
5.32	Contour plot of the second misfit function $M_2(z,\Lambda)$ for the $h_n(z,\Lambda)$ (5-56) approximation to the Lehman distribution.	133
5.33	The cdf for the phase-quadrature components squared, based on $F_n(x,\Lambda)$ for $\Lambda = 10$, from (5-57).	134
5.34	The pdf and cdf approximations, $e_n(u,\Lambda)$ and $E_n(u,\Lambda)$, to the Lehman-associated field amplitude distribution (5-26) and (5-27) or (5-59) and (5-60), based on $\Lambda = 10$.	135
5.35	Contributions of the Gaussian-like and χ^2 -like parts of the phase-quadrature cdf.	136
5.36	Inverses of $E_g(u,\sigma_g)$ and $H_{\chi^2}(6,4\Lambda^{\frac{1}{2}} u) \cdot (u/ u)$ [see (5-61)] for $\Lambda = 10$. These inverses are directly accessible from Mathcad [®] . The inverse of $F_n(x,\Lambda)$ has been found always to lie between these two inverses.	136
5.37	Evaluation of the fidelity of our algorithm for finding $F_n(x,\Lambda)$ and its inverse.	137
5.38	Two 500-point ensembles of Lehman-distribution-related phase-quadrature random variables, based on (5-60), with $\Lambda = 10$.	137
6.1	Top (front) of the J-shaped microwave chamber used for field- and current-distribution testing.	145
6.2	GPS bus (less antennas and solar panels) illuminated by a log-periodic antenna (right). Note dust mop in front of bus to give size perception.	145
6.3	Cumulative distributions of averaged, normalized waveguide-chamber electric fields (measured), compared with those predicted from Lehman (5-22) and χ^2 (2-89) models	146
6.4	Overlay of four cable current measurements (cluster of four left traces), and four cable-model predictions (cluster of three middle traces and right outlier).	147
6.5	CDF of E^2 at Loc. 1 inside the waveguide chamber. Based on measured $\Lambda = 2.986$.	148
6.6	CDF of E^2 at Loc. 2 inside the waveguide chamber. Based on measured $\Lambda = 2.954$.	148
6.7	CDF of $\text{ABS}(I)$ at Loc. 1 inside the waveguide chamber. Based on Lehman E -field distribution of Figure 6.5.	148

<u>FIGURE</u>		<u>PAGE</u>
6.8	CDF of $ABS(I)$ at Loc. 2 inside the waveguide chamber. Based on Lehman E -field distribution of Figure 6.6.	148
6.9	CDF of E^2 in lower Bay 1 of GPS. Based on measured $\Lambda = 3.486$.	149
6.10	CDF of E^2 in lower Bay 2 of GPS. Based on measured $\Lambda = 3.344$.	149
6.11	CDF of $ABS(I)$ on cable bundle in lower Bay 1 inside the GPS. Based on Lehman E -field distribution of Figure 6.9.	149
6.12	CDF of $ABS(I)$ on cable bundle in lower Bay 2 inside the GPS. Based on Lehman E -field distribution of Figure 6.10.	149
6.13	Observed E^2 at a fixed point in the 5BH bay on the lower dark-side of the GPS as frequency is stepped from 600 MHz to 2 GHz. Mean μ , standard deviation σ , and coefficient of skewness κ were found to be $(0.0170, 0.0213, 1.98)$.	153
6.14	Autocorrelation of data appearing in Figure 6.17. Displacement is in units of frequency steps.	154
6.15	The Figure 6.13 data fails a 90% K-S confidence test for fitting a chi square (two degrees of freedom) distribution, especially at midrange. This plot is based on $\mu_c = 0.0170$.	155
6.16	The Figure 6.13 data narrowly misses a 90% K-S confidence test for fitting a Lehman distribution. This plot is based on $\Lambda = 176.4$.	156
6.17	The upper 65% of the Figure 6.13 data passes 90% K-S confidence test for fitting a beta distribution. This plot is based on $(\mu, \sigma, \kappa) = (0.0170, 0.0213, 1.98)$, implying $(a, b, s) = (0.497, 5.30, 0.198)$.	157
6.18	The Figure 6.13 data does not fit a 90% K-S confidence test for being log normal; the deviation is bipolar. This plot is based on $(\mu_{lg}, \sigma_{lg}) = (-4.546, 0.972)$	158
6.19	The Figure 6.13 data lies within a $\pm 50\%$ acceptance interval for fitting a chi square (two degrees of freedom) distribution, over the upper half of its domain. This means the chi square model is probably an acceptable, even if not ideal, representation of the data.	160
6.20	The Figure 6.13 data lies well within a $\pm 50\%$ acceptance interval for fitting a Lehman distribution over its entire domain. This means the Lehman model is an excellent replication of reality	161
6.21	The Figure 6.13 data lies within a $\pm 50\%$ acceptance interval for fitting a beta distribution, over the upper 75% of its domain. This means the beta model is an acceptable representation of the data.	162
6.22	The Figure 6.13 data lies within a $\pm 50\%$ acceptance interval for fitting a chi square (two degrees of freedom) distribution, over the upper half of its domain. This means the log normal model is conditionally acceptable.	163
6.23	The Figure 6.13 field data, when modeled as chi square (with two degrees of freedom), leads to a modeled cable current which, given a $\pm 50\%$ acceptance interval, everywhere brackets the measured cable current.	164

Chapter 1. THE NEED FOR STATISTICAL ELECTROMAGNETICS (SEM)

This document reports efforts, by us and others, to understand and model statistically the electromagnetic (EM) field and cable response of an enclosed asset and its wiring during high-power microwave (HPM) attack or in the presence of other threatening radio frequency (RF) leakage and penetration. More generic and exploratory work on the statistics of such response was previously performed by us, and has been informally described elsewhere.[1]

The problem of predicting cable or pin currents in an enclosed system under high-power microwave (HPM) illumination or RF interference (RFI) at a frequency where the asset is many (> 6) wavelengths on a side (i.e., well overmoded) is all but impossible to treat deterministically. Moreover, even assuming a supercomputer and state-of-the-art finite-volume time-domain (FVTD) code were available, one could logically claim a deterministic solution would be of no value. This claim could be made because, in such a scenario, a 1° rotation of the asset or a 1 percent shift in frequency would commonly alter the excitation on any given pin or circuit device by 20 dB.

Additionally, the interior of a satellite, aircraft, or missile has wiring of almost inconceivable complexity as viewed by an FVTD practitioner who is used to zero or one (two if he is really heroic) conductors passing through each FVTD cell.[2,3]

To solve this sort of problem rigorously and deterministically, one not only needs to track the fields in 10^6 to 10^9 FVTD cells, but also to model the drive these fields impose on each conductor (or even each IC) passing through or located in each cell. The final nightmare is that each of these conductor and IC currents must then be fed back through the FVTD version of the *curl H* equation (Ampere's law) to drive the algorithm which advances the FVTD field solution. Despite 20 years' experience with FVTD and finite-difference time-domain (FDTD) codes, it is our conviction that this problem is at least two computer generations from tractability, even assuming a deterministic solution could be of any use.

Given this dark and bleak outlook on deterministic HPM and RFI analysis, the HPM/RFI community was thoroughly awakened by a statistical approach worked out by Price and Davis, which appeared in 1988.[4,5] (A statistical treatment, unlike a deterministic treatment, actually thrives on complexity. In many situations, the statistical confidence interval depends on the *inverse* square root of the amount of data provided.) This statistical approach develops a probability density distribution model for the fields inside an asset, which are not be a hair-trigger function of frequency, attack angle, wiring configuration, or any other parameter. An elegant, but very complex derivation accompanied this work. The conclusion was that the distribution of the electric or magnetic field (squared) projected along any axis would be chi square with two degrees of freedom; i.e., exponential. This distribution function is characterized by a single parameter, μ the mean value (or equivalently by μ' the median value). Because of the fundamental significance of this effort, but also because it is hard to follow and not free of errors, we reproduce it here in Section 9.

Let us assume a reasonable topography (for example, no observation points located where they are line-of-sight illuminated by the driving source through a large aperture and no small shield rooms inside a big shield room). Then there is a strong implication that this same chi square distribution (with the identical μ) would categorize the field as a function of internal position, frequency, attack angle, sensor orientation, or almost any other independent variable one would want to consider. It also appears this chi square distribution characterizes mode-stirred reverberation chambers where the paddle angle is the independent variable.[6-8] In fact, mode-stirred chambers inherently depend on statistical, not deterministic, analysis and assumptions as the basis for their application and use.

Our initial desire was to obtain access to the data Price and Davis had used to test their theory in a large steel box (2.5m on a side), a C130 transport plane, a Maverick missile, a Cessna Citation jet, and a large ground vehicle. These data were not available, and so we initially turned to data taken from the Air Force Phillips Laboratory's testing of the EMP Test AirCraft (EMPTAC) aircraft frame (basically a gutted Boeing 720 shell) when illuminated by their Ellipticus antenna. These data included internal magnetic fields, surface current density on the inner skin of the EMPTAC, and currents flowing on the EMPTAC cable bundles. It also included measurements of the externally incident fields radiated by the Ellipticus, so the internal response could be normalized by the external stimulus if desired. The EMPTAC data were given in the form of response versus frequency, where the frequency was first swept from 300 kHz to 100 MHz (the "low-frequency" sweep), and then from 100 MHz to 1 GHz (the "high-frequency" sweep). In some cases, the first sweep may have yielded data below the noise floor, but data from the second sweep were generally believed to be totally reliable.[1]

Later, we obtained a Global Positioning Satellite (G.P.S.) bus on indefinite loan from the Phillips Laboratory, and took extensive data of our own, various measurement accuracies and tolerances directly accessible to our own care and observation. In the Price and Davis work, cavity excitation was produced by an internal source.[4,5] We illuminated both our test objects externally, with EM energy leaking in through deliberate and inadvertent apertures, and by antenna feed cables. (This distinction, which we initially considered inconsequential, is now believed to be more significant than casual review would suggest.[9-11])

The Phillips Laboratory also made data available to us concerning electromagnetic fields inside the Celestron 8 space telescope when microwave illumination was directed into the main aperture, although not directly down the boresight. This excitation scenario is not a perfect match with our assumptions about the statics of resonant cavities. In particular, much of the telescope interior is in direct line-of-sight with the source. Also the aperture is so large that the high- Q requirement is questionably met. Lastly, excitation of the telescope chamber is dominated by the single large aperture, not many small apertures, thus leading to the probable existence of "hot spots". In spite of these violations of our assumptions, Celestron 8 fields interior to the telescope prove to be not badly characterized by our field statistics.

It quickly became apparent that the Price and Davis chi square distribution match between experiment and theory was less pristine than believed. In particular, their raw data had been passed through a logarithmic filter to remove a certain amount of "trend" before being compared with the experiment. The unfiltered data from the EMPTAC had a distribution much more resembling log normal than chi square.[1] The same phenomenon had been observed by Price and Davis, who were kind enough to give us an idea of the filtering process which was necessary.

The Price-Davis papers contained references to some statistical characterization procedures such as the probability plot (see following section) and the Kolmogorov-Smirnov test [12] which may be new to the EM engineer or physicist who is more used to deterministic treatment and terminology. We hope that Section 9 and Ref. [12] will be of use to a reader of this status.

REFERENCES

- [1] Holland, R. and R. St. John, "Statistical Response of Enclosed Systems to HPM Environments," PL-TR-94-1006, Air Force Phillips Laboratory, Kirtland Air Force Base, NM, 1994.
- [2] Holland, R and L. T. Simpson, "Finite-Difference Analysis of EMP Coupling to Thin Struts and Wires," *IEEE Trans. Electromagn. Compat.*, Vol. EMC-23, pp. 88-97, May 1981.
- [3] Kunz, K. S. And R. J. Luebbers, *The Finite Difference Time Domain Method for Electromagnetics*, pp. 185-190, CRC Press, Boca Raton FL, 1993.
- [4] Price, R. H., *et al*, "Determination of the Statistical Distribution of Electromagnetic Field Amplitudes in Complex Cavities," 88JAL129, JAYCOR, 1 June 1988.
- [5] Price, R. H., H. T. Davis, and E. P. Wenaas, "Determination of the Statistical Distribution of Electromagnetic-Field Amplitudes in Complex Cavities," *Phys. Rev. E*, Vol. 48, pp. 4716-4729, December 1993.
- [6] J. G. Kostas and B. Boverie, "Statistical models for a mode-stirred chamber," *IEEE Trans. Electromagn. Compat.*, vol. EMC-33, pp. 366-370, November 1991.
- [7] R. R. Lentz and H. C. Anderson, "Reverberation chambers for EMC measurements," presented at the IEEE EMC Symposium, pp. 152-159, 1985.
- [8] P. Corona, *et al.*, "Magnification factors for mode stirred chambers," *IEEE Trans. Electromagn. Compat.*, vol. EMC-18, pp. 54-59, May 1976.
- [9] Holland, R. and R. St. John, "Statistical Description of Cable Current Response Inside a Leaky Enclosure," *Conference Proceedings*, Vol. 2, pp. 1077-1085, 13th Annual Review

of Progress in Applied Computational Electromagnetics, Monterey, CA, 17-21 March 1997.

- [10] Holland, R. and R. St. John, "Statistical Coupling of EM Fields to Cables in an Overmoded Cavity," *Conference Proceedings*, Vol. 2, pp. 877-887, 12th Annual Review of Progress in Applied Computational Electromagnetics, Monterey, CA, 18-22 March 1996.
- [11] T. H. Lehman and R. M. Marshall, "Application of statistical physics to derivation of stress and strength distributions," Ball Systems Engineering Division, Albuquerque, NM, September 26, 1991.
- [12] Roe, P. R., *Probability and Statistics in Experimental Physics*, pp. 189-203, Springer-Verlag New York, Inc., New York, 1992.

Chapter 2. DISTRIBUTION AND AUTOCORRELATION OF INTERNAL FIELDS

This section is organized as follows: Initially, we introduce the probability plot, a tool often used to evaluate how well a cumulative distribution model matches observed data. Next, we consider that a statistical model of the EM fields inside an overmoded enclosure, which drives the cable currents in a realistic way, must not only obey the same probability density function (pdf) as the measured fields. It must also obey the same local autocorrelation with respect to small spatial translation or frequency shift.

We then describe how the probability density function of simulated cable-driving power flux distribution densities may be matched to an arbitrarily selected pdf through filtering random numbers. (It is of use first to consider modeling of power-flux density pdf instead of electromagnetic field pdf as the Price-Davis measurements were made with square-law detectors (i.e., power flux detectors). Also, the EMPTAC measurements were of \dot{B} (corrected to output B) absolute values, which, since phase information is lost, behave statistically more like powers than complex-valued fields. Additionally, the G.P.S. measurements were made by D -field or I absolute-value sensors, which also do not take phase information, and thus also resemble power detectors more than complex phasor sensors.)

Lastly, we examine the transformation of the power-flux density pdf to the associated cable-driving electromagnetic phase-quadrature field-distribution pdf.

PROBABILITY PLOTS

We shall begin by introducing this useful concept for distribution testing by means of an example: the Gaussian or normal distribution. To make a probability plot to test a data set for a Gaussian fit, one first orders all the measurements so they are monotonically increasing, x_1, x_2, \dots, x_N . Next, these measured values are normalized to match a normalized Gaussian distribution:

$$z_n = \frac{x_n - \mu_g}{\sigma_g} \quad (2-1)$$

where μ_g and σ_g are the mean and standard deviation. These z_n values are then marked off along the horizontal axis.

If there are a total of n values in the data set, then the experimentally obtained fraction of data points of value less than or equal to z_i is

$$p_n = (i - 1/2)/N \quad (2-2)$$

If the data obey a Gaussian distribution exactly, it would be true, as n goes to infinity, that

$$P(z_n) = (n - 1/2)/N \quad (2-3)$$

where P is the cumulative normal distribution function. Thus, if the z_n were exactly normal in distribution, $P^{-1}((n - 1/2)/N)$ would be coincident with z_n , where $P^{-1}(p)$ is the inverse of the cumulative normal distribution function. (A fitted curve approximation to $P^{-1}(p)$ appears in Eq. 26.2.23 of Zelen and Severo.[1].)

For each n obtained, now compute

$$P^{-1}((n - 1/2)/N) = y_n \quad (2-4)$$

where this computed y_n is different from the observed z_n unless the data fit to the normal model is perfect. Then mark these y_n along the vertical axis. Connecting the points (z_n, y_n) then yields the probability plot for the assumption that the data set in question obeys a normal distribution. If the normal distribution assumption is exactly correct, the resulting plot will approach a straight line at 45° as N goes to infinity.

The Price and Davis documents [2,3] also provide 90 percent confidence curves for the probability plots. These confidence limits were obtained from the Kolmogorov-Smirnov test (see Section 9) [4] and differ from the ordinary confidence limits in that the entire cumulative distribution curve must lie within for 90 percent certainty that the assumed probability distribution is correct. (More conventional tests are only valid on a point-by-point basis, and provide less readily usable information about the overall confidence of the probability plot.)

If x_i in (2-1) is replaced by $\ln(x_n)$, with μ_{lg} and σ_{lg} the mean and variance respectively of the $\{\ln(x_n)\}$, array a test is obtained for the hypothesis that the data obey a log normal distribution.

Each of the log normal probability plots appearing in this section has an indicated variance σ_{lg}^2 . This is provided because an array with a χ^2 distribution with two degrees of freedom should have an associated logarithmic array $\{\ln(x_n)\}$ with a variance of $\pi^2/6$ (see [5], Appendix B).

Chi-square probability plots, unlike Gaussian probability plots, are usually made with the data not normalized [(2-1) not applied]. For example, in the case of a χ^2 distribution with two degrees of freedom, one can show [see (2-11)] that

$$y_n = P_{\chi^2}^{-1}((n - 1/2)/N) = -\mu_c \ln(1 - (n - 1/2)/N) \quad (2-5)$$

Both x_n and y_n are then converted to decibel (dB) format before plotting,

$$z_n = 10 \log_{10}(x_n) \quad (2-6)$$

THE FIELD-AUTOCORRELATION ISSUE

It has been demonstrated by us and others that the field picked up inside an overmoded enclosure by a B -sensor, presuming the sensor responds in a square-law manner, should yield a chi-square output distribution with two degrees of freedom. This statement is true under cw conditions, and applies whether the observations are made at a fixed location while frequency is swept or whether the observations are made at a fixed frequency while the antenna is translated or rotated.[2,3,5] It does, however, depend on the cavity not having a frequency-dependent Q and on all parts of the cavity being equally shielded (i.e., no subenclosures within the enclosure). If these postulates are not obeyed, the sensor output distribution tends to appear log normal instead.[5]

The above statements presume the sensor detects only a single B -field component on a basis which is very local compared to the EM wavelength. They also apply, however, to detectors which pick up a single component of D on a very local basis, or to detectors which respond to a single component of \vec{B} or B , provided the independent variable is not frequency swept over more than about a 5% bandwidth. (We should not expect $\vec{B} = \omega B$ to produce a chi square distribution through a square-law detector if ω is not almost constant.)

In practice, the sensor output usually has to be passed through a trend-removing, high-pass filter to pull its chi-square distributional nature out of a log-normal appearance caused by the trend or slowly varying component. (We refer to this high-pass filtering as "drending"; see the final subsection of this section. Whether the simulating conductor drive in modeling applications should be based on a chi square, a log-normal, or some altogether different power distribution thus becomes an issue which may be subject to personal choice.)

Price, *et al.*,[2,3] have published a thorough derivation of the physics and statistics leading to the anticipation of a chi square attribute in the squared fields or power fluxes (refer to Section 9 of this publication). However, there is a simple approach which relies somewhat on intuition for reaching the same conclusion. Essentially, at any point in the enclosure, the field projected on any dipole consists of two components in phase quadrature, each of which should possess a nearly normal distribution when the enclosure is sufficiently overmoded to begin to have blackbody-like characteristics. (This distribution is a consequence of Bosé-Einstein statistics, which describe blackbody radiation.) The power picked up by a dipole antenna is proportional to the summed squares of these quadrature components. (Alternatively, it could be viewed that the power picked up is the summed squares of the waves going backwards and forwards.) However, this sum is exactly the definition of a function which has a chi square distribution with two degrees of freedom.

An empirical result we have observed about data pertaining to the power (current squared) carried by a cable inside an enclosure is that it *also* obeys a chi square distribution with two degrees of freedom after the power measurement sweep has its trend removed (Figure 2.1). (Test data referenced here were obtained at the Air Force Phillips Laboratory's EM effects EMPTAC facility. Before drending, EMPTAC cable powers also tend to appear log normal in

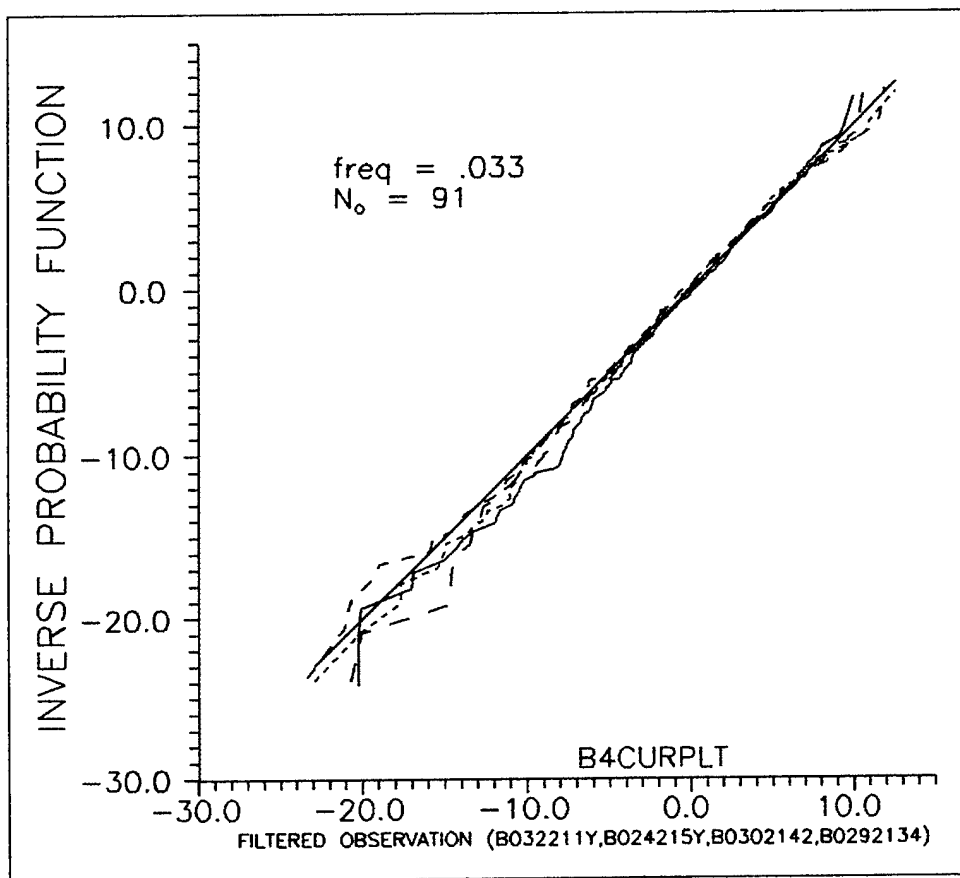


Figure 2.1. Probability plots of experimentally observed, detrended EMPTAC cable powers all show good fits to the chi square distribution model with two degrees of freedom.

distribution.) This cable power distribution result is not predicted or anticipated by the Price work.[2,3] However, if the power is viewed as the summed squares of two phase-quadrature cable current components, there is no surprise in this observation. (There is an experimentally prompted assumption here that the unsquared phase-quadrature current components also have a normal distribution; however, we do not claim our simplistic appeal to Bos  -Einstein electromagnetic field statistics should necessarily apply to cable currents for any obvious reason.)

In practice, we first modeled the cable drivers in our EMPTAC cable-current simulation code with electromagnetic fields of the form

$$E_{\parallel} = [A(n,i) \cos(\omega_n t) + B(n,i) \sin(\omega_n t)] \quad (2-7)$$

where the two terms represent the phase-quadrature components of the fields at cable segment I and frequency ω_n . These fields are projected parallel to the cables to effect drive. The amplitudes of the sine and cosine phase-quadrature amplitude terms are random numbers which can be selected to fit an arbitrary probability density function. Software for generating log normal and chi square distributions, as well as for normal distributions, is currently available to implement the statistical nature of $A(n,i)$ and $B(n,i)$ (see the next subsection). For instance, if we wish to employ a log normal model, the phase-quadrature electromagnetic fields $A(n,i)$ and $B(n,i)$ are selected according to the mapping function

$$C(n,i) = e^{\mu_g + \sigma_g u(n,i)} \quad (2-8)$$

In the more physically realistic normal case, $C(n,i)$ is obtained from (2-8) simply by omitting the exponentiation

$$C(n,i) = \mu_g + \sigma_g u(n,i) \quad (2-9)$$

The factor $u(n,i)$ is a random variable describing the cable-driving field at frequency ω_n and spatial location i . It has a probability density function tailored to the normal distribution function and must also contain frequency- and location-associated coherence. In the high-frequency limit, the spatial and frequency coherence between adjacent $u(n,i)$ may vanish, and each $u(n,i)$ may be determined solely by the chosen random distribution. Additionally, $C(n,i)$ is a shorthand notation to represent either $A(n,i)$ or $B(n,i)$, μ_g is the average, and σ_g is the standard deviation of the logarithms of the phase-quadrature field amplitudes we are trying to replicate statistically.

For a normal or log normal distribution let $R(n,i)$ be randomly selected number between 0 and 1. Then let us begin constructing $u(n,i)$ by defining $u_{lim}(n,i)$ through the inverse normal function

$$R(n,i) = \frac{1}{\sqrt{2\pi}} \int_{-\infty}^{u_{lim}(n,i)} e^{-u'^2/2} du' \quad (2-10)$$

Numerical evaluation of $u_{lim}(n,i)$ given $R(n,i)$ is described in the next subsection and [5].

(For a chi square distribution with two degrees of freedom,

$$R(n,i) = \int_0^{u_{lim}(n,i)/\mu_c} e^{-u'^2} du' \quad \text{or} \quad u_{lim}(n,i) = \mu_c \ln(1 - R(n,i)) \quad (2-11)$$

would be the corresponding equation.)

Unlike actual experimental data, this drive did not result in a cable power distribution which was chi square, even after filtering for trend removal. The problem was the $A(n,i)$ or $B(n,i)$ generated in this manner had no local autocorrelation, either between adjacent frequencies or between adjacent cable segments. Thus, the resulting simulated cable powers, unlike the experimentally observed EMPTAC cable powers (see Figure 2.9), also had no autocorrelation between adjacent frequencies. (It turns out that we don't know how to generate easily an ensemble of drivers which simultaneously and automatically has a prescribed probability density function *and* autocorrelation. Nature does this for us with the experimentally generated real-world drivers, but in our virtual reality, we here have a very difficult time replicating nature.)

It is known that the spatial autocorrelation of any component of the fields (with frequency fixed) should depend on the separation of the two observational points, $\Delta r = |\mathbf{r}_1 - \mathbf{r}_2|$, as [6-8]

$$\rho(\mathbf{r}_1, \mathbf{r}_2) = \frac{\sin(k|\mathbf{r}_1 - \mathbf{r}_2|)}{(k|\mathbf{r}_1 - \mathbf{r}_2|)} \quad (2-12)$$

and the frequency autocorrelation (with observer position fixed) should depend on the spectral separation of the two frequencies, $\Delta\omega = \omega_1 - \omega_2$, as [6]

$$\rho(\omega_1, \omega_2) = \frac{1}{1 + \beta(\omega_1 - \omega_2)^2 Q^2} \quad (2-13)$$

where β is a constant which depends in a complex way on the chamber dimensions. However, we re-emphasize that knowing what the autocorrelation and distribution of the electromagnetic fields should be does not trivialize their computerized simulation.

The first attempt to rectify this problem and to introduce autocorrelation consisted of massaging the $u(n,i)$ given by (2-10). With $R(n,i)$ still a random number uniformly distributed between 0 and 1, we associated a $u_{lim}(n,i)$ with each $R(n,i)$ through (2-10), setting $u(n,i) = u_{lim}(n,i)$.

We then defined an intermediate new $u(n,i) = u_{space}(n,i)$ through a formula empirically selected from a half dozen possible choices to force spatial autocorrelation between nearest-neighbor segments

$$u_{space}(n,i) = \frac{\frac{\lambda}{\Delta l} u(n,i-1) + f_{space} u_{lim}(n,i)}{\frac{\lambda}{\Delta l} + f_{space}} \quad (2-14)$$

where $u(n,i-1)$ is the $u(n,i)$ for the previous cable segment $i-1$, Δl is the cable segment length, and f_{space} is a number around 10. (At the left end of the cable, $u(n,1)$ was seeded as 0. Making f_{space} zero results in total correlation between adjacent segments; making it >1000 results in no noticeable correlation between adjacent segments; i.e., no change between $u_{lim}(n,i)$ and $u_{space}(n,i)$ closely approaching the EMPTAC experimental noise floor.) We then obtained a new $u(n,i) = u_{freq}(n,i)$, locally autocorrelated over both space and frequency, through a formula to force autocorrelation between adjacent frequencies

$$u_{freq}(n,i) = \frac{\frac{\lambda^2}{L\Delta\lambda} u(n-1,i) + f_{freq} u_{space}(n,i)}{\frac{\lambda^2}{L\Delta\lambda} + f_{freq}} \quad (2-15)$$

Here $u(n-1,i)$ is the $u(n,i)$ for the previous frequency $n-1$, L is the linear dimension of the cable extent, $\Delta\lambda$ is the change in wavelength between adjacent frequencies, and f_{freq} is another number around 10. [At the lowest frequency, $u(1,i)$ was again seeded as 0. Making f_{freq} zero results in total correlation between adjacent frequencies; making it >1000 results in no noticeable correlation between adjacent frequencies. The actual $u(n,i)$ used for cable drive in (2-7) - (2-9) is, in the first approximation, $u_{freq}(n,i)$ of (2-15).]

This procedure succeeds in introducing an approximate simulation of the physically occurring autocorrelation in cable power over position and frequency (compare Figure 2.8 with Figure 2.7). Unfortunately, it also succeeds in distorting the normal distribution that we desire the array of $u(n,i)$'s to possess, especially at the tails (see Figure 3.12). Additionally, the standard deviations σ_g , i.e., average amplitudes of the driver ensemble matrices $u(n,i)$ and $v(n,i)$, are reduced from .01 to about .003.

At first we made some simulation runs using the chi square distribution for the driving field on the EMPTAC cables. (These runs are simplistic, as it is actually the driving field squared which should look chi square.) Figure 2.2 shows the resulting cable power (current squared) distribution versus frequency at a point near the cable midpoint for f_{space} and f_{freq} both set to 1 (excessive autocorrelation). Figure 2.3 shows the result for f_{space} and f_{freq} both set to 10 (realistic autocorrelation), and Figure 2.4 illustrates the cable power for both f 's set to 100 (autocorrelation artificially weak). These three figures show the raw data, the trend, and the data with the trend removed. Figure 2.5 shows a typical experimental EMPTAC cable power observation versus frequency. It is easy at once to see a somewhat subjective difference between the observed and simulated results: On Figure 2.5, the detrended data only have sharp spikes downward, while the simulated data (Figures 2.2-2.4) demonstrate bipolar spikes.

The simulated cable power data shown in Figures 2.2-2.4 actually have several inappropriate properties. This is true even for Figure 2.3, which is based on realistic f_{space} and f_{freq} . For instance, besides having bipolar spikes, these simulated cable power data do not reveal an underlying chi square distribution upon passing them through the same trend-removing filter used to detrend experimental data, (see Figure 2.6, and compare with Figure 2.1). We believe that the presence of the upward-pointing spikes on the simulated cable powers has a proximate relation to the absence of an underlying chi square distribution in the simulated cable powers. In particular, these points of overexcitation cause the data autocorrelation to exhibit ragged behavior, even for large shifts, in a way the experimental data do not. (These isolated peaks are the opposite of trends, and detrending the data has no impact at all on their specious effect on the autocorrelation and distribution functions.)

Let us now consider some actual autocorrelation functions of the observed and simulated data. If $\phi(f)$ is the raw (or filtered) data as a function of frequency, the formula for the autocorrelation of $\Phi(f)$, assuming the data extend continuously from $-\infty$ to ∞ , is

$$\Phi(g) = \int_{-\infty}^{\infty} \phi(f) \phi(f + g) df \quad (2-16)$$

Our data, however, are taken only at discrete points over a finite interval. Let N be the number of points at which we have a measurement for $\phi(f)$. We can then define a local autocorrelation over $N - I$ points as

$$\begin{aligned} \Phi(j) &= \sum_{i=I/2}^{N-I/2} \phi(i) \phi(i + j) \quad j \geq 0 \\ \Phi(j) &= \sum_{i=I/2-j}^{N-I/2} \phi(i) \phi(i + j) \quad j \leq 0 \end{aligned} \quad (2-17)$$

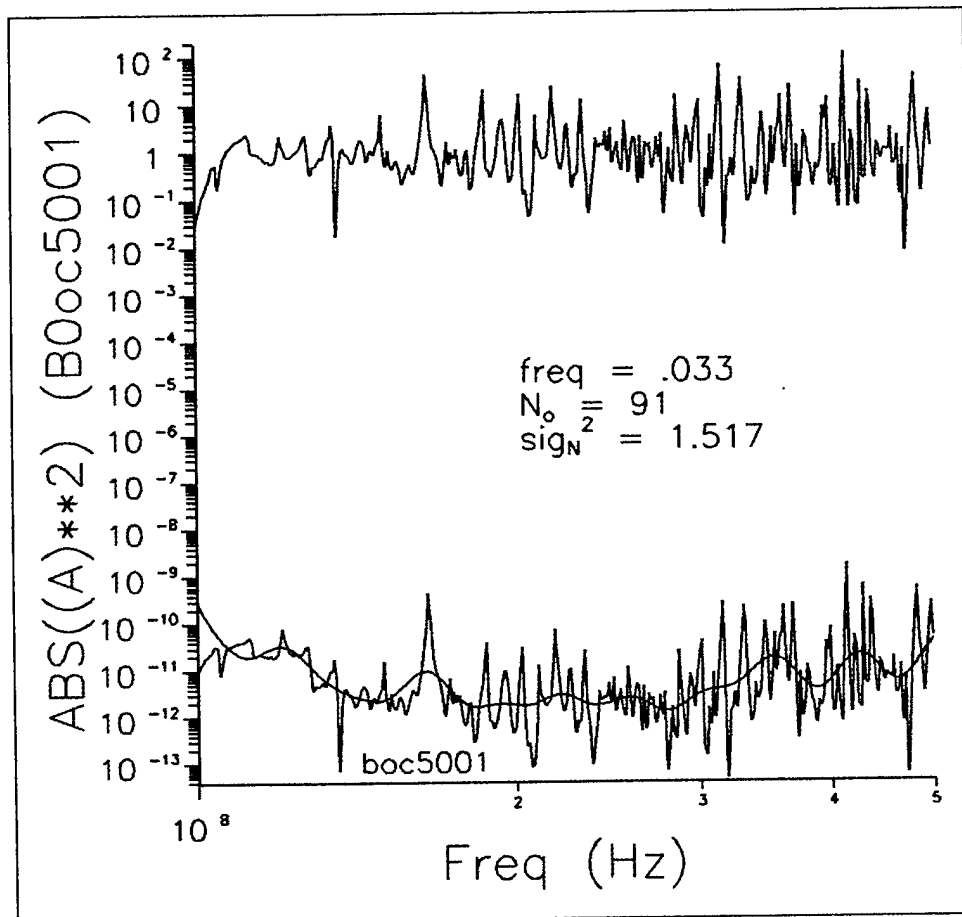


Figure 2.2. Bottom curves: unfiltered, simulated cable current $|I|^2$ inside the EMPTAC middle bay and $|I|^2$ trend. Top curve: $|I|^2$ with trend factored out: $|I|^2 / |I_{\text{trend}}|^2$. This figure is based on f_{space} and f_{freq} both set to 1, and the assumption that u_{lim} has a chi square distribution. Cable ends are terminated in 30Ω , and this observer is near the cable midpoint. Note the bipolar nature of the spikes on the detrended (upper) data set.

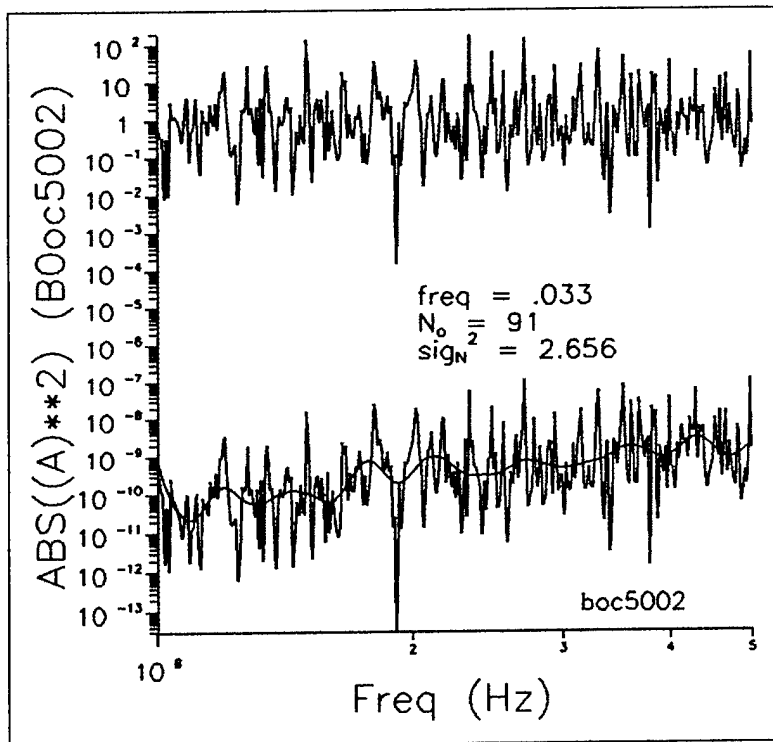


Figure 2.3. Bottom curves: unfiltered, simulated cable current $|I|^2$ inside the EMPTAC middle bay and $|I|^2$ trend. Top curve: $|I|^2$ with trend factored out: $|I|^2 / |I_{trend}|^2$. This figure is based on f_{space} and f_{freq} both set to 10, and the assumption that u_{lim} has a chi square distribution. Cable ends are terminated in 30Ω , and this observer is near the cable midpoint. Note the bipolar nature of the spikes on the detrended (upper) data set.

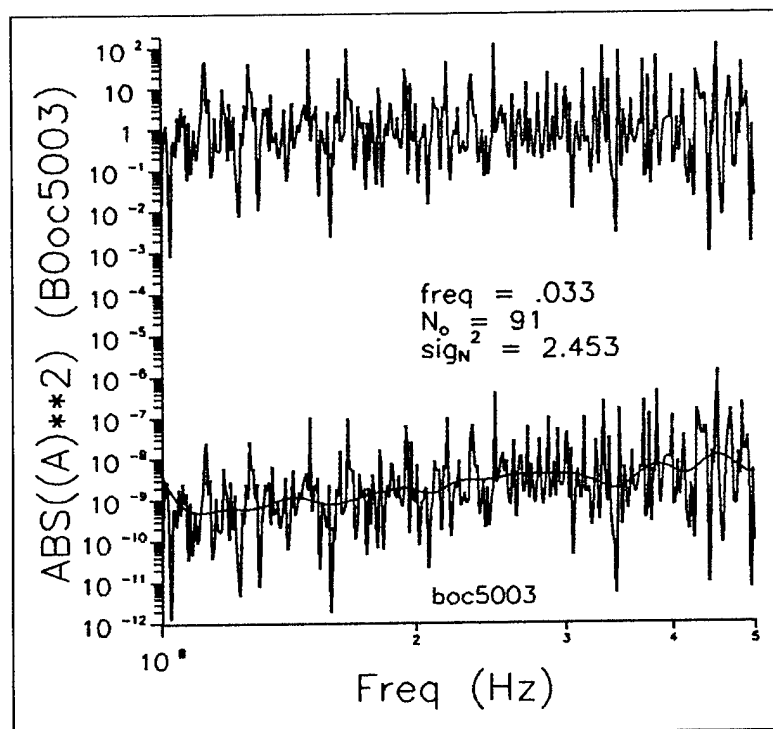


Figure 2.4. Bottom curves: unfiltered, simulated cable current $|I|^2$ inside the EMPTAC middle bay and $|I|^2$ trend. Top curve: $|I|^2$ with trend factored out: $|I|^2 / |I_{trend}|^2$. This figure is based on f_{space} and f_{freq} both set to 100, and the assumption that u_{lim} has a chi square distribution. Cable ends are terminated in 30Ω , and this observer is near the cable midpoint. Note the bipolar nature of the spikes on the detrended (upper) data set.

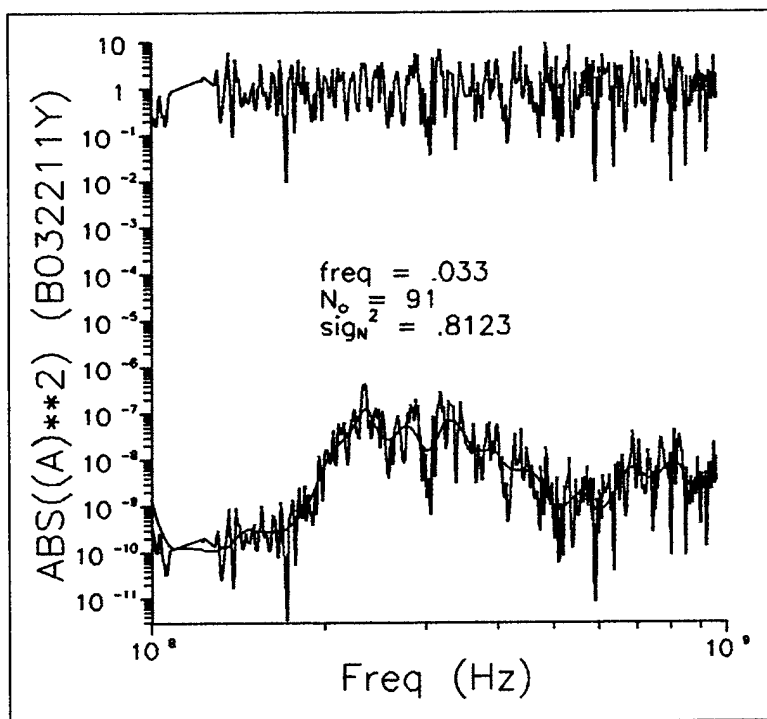


Figure 2.5. Bottom curves: observed, unfiltered cable current $|I|^2$ inside the EMPTAC middle bay and $|I|^2$ trend. Top curve: $|I|^2$ with trend factored out: $|I|^2 / |I_{trend}|^2$. This figure is based on a high-frequency experimental data sweep. Note the monopolar downward nature of the spikes on the detrended (upper) data set. This feature is characteristic of data having a chi square distribution.

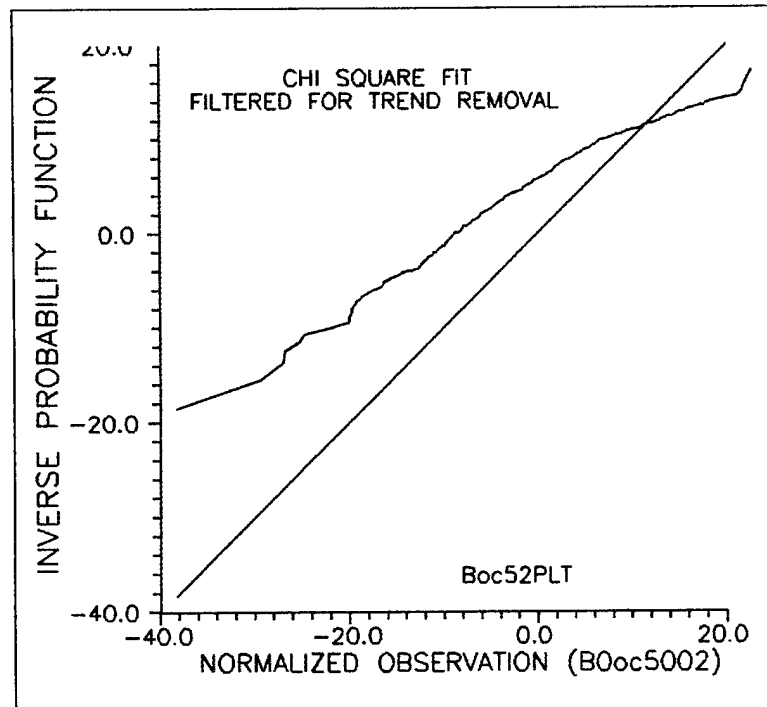


Figure 2.6. Probability plot of simulated cable currents squared against a chi square (two degrees of freedom) distribution assumption. When driven by field components having a chi square distribution, the simulated EMPTAC cable currents, even upon filtering for trend removal, do not fit a chi square distribution.

Figure 2.7 shows the discrete local autocorrelation for a low-frequency (300 kHz to 100 MHz) magnetic field (squared) EMPTAC data sweep (based on $I/2 = 80$), and Figure 2.8 shows the discrete local autocorrelation for a high-frequency (100 MHz to 1 GHz) magnetic field (squared) data sweep. The result for both the filtered and the unfiltered data sets are presented. It is readily seen that the filtered data have an autocorrelation function characterized by a central peak about 4 points wide and a relatively smooth, flat plateau of value about half the value of the central peak, extending at least from a data point offset ranging from -80 to +80. Figure 2.9 shows the corresponding autocorrelation result for a high-frequency EMPTAC cable power sweep; the filtered data plot in this figure is similar to the magnetic field results in possessing a central peak plus a broad outlying plateau.

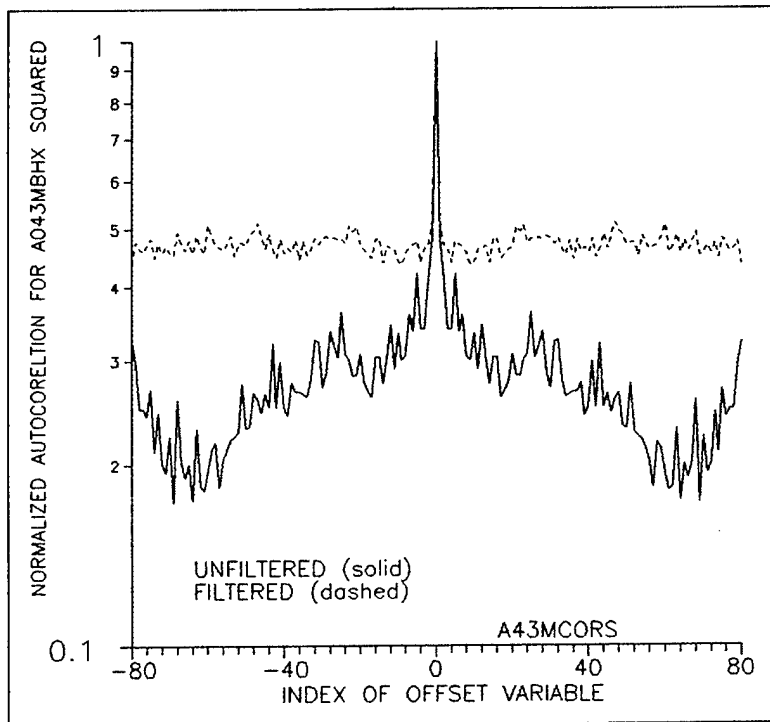


Figure 2.7. Normalized autocorrelation of the observed magnetic field along x (fuselage axis) with (dashed line) and without (solid line) the data filtered. This figure is based on the low-frequency EMPTAC middle-bay scan. Note that the autocorrelation of the filtered data is characterized by a central peak and broad plateau about .5 of the central peak.

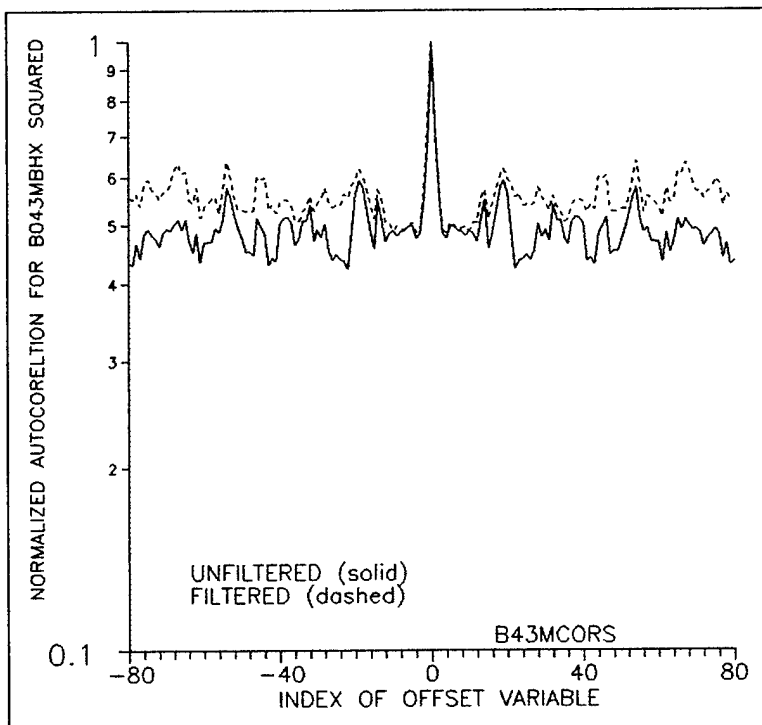


Figure 2.8. Normalized autocorrelation of the observed magnetic field along x (fuselage axis) with (dashed line) and without (solid line) the data filtered. This figure is based on the high-frequency EMPTAC middle-bay scan. Note that the autocorrelation of the filtered data is characterized by a central peak and broad plateau about .6 of the central peak.

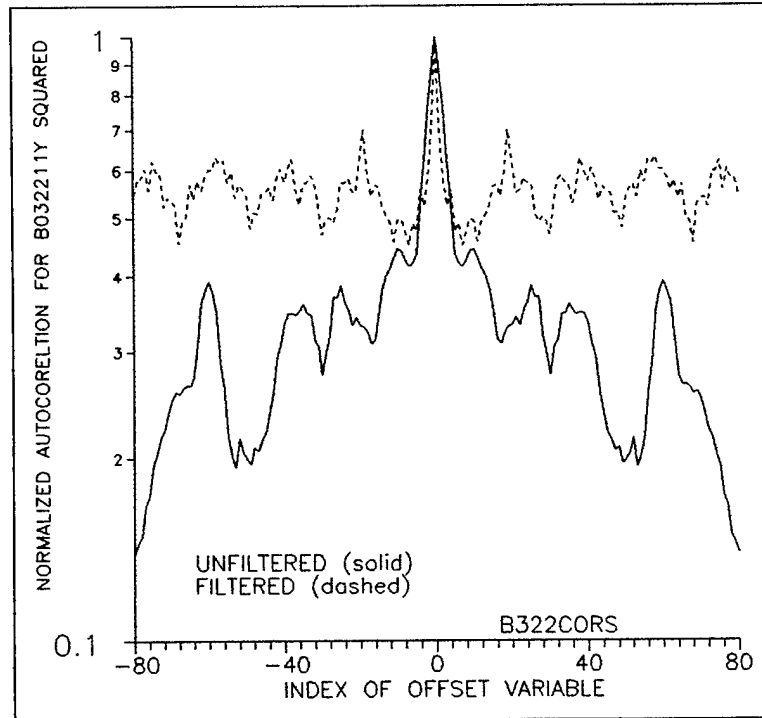


Figure 2.9. Normalized autocorrelation of the observed cable current with (dashed line) and without (solid line) the data filtered. This figure is based on the high-frequency EMPTAC middle-bay scan. Note that the autocorrelation of the filtered data is characterized by a central peak and broad plateau about .6 of the central peak.

While a true autocorrelation function can must reach its maximal value at zero offset ($g = 0$), this is not the case for a local autocorrelation. Figures 2.10-2.12 show the local autocorrelation functions corresponding to the simulated data appearing in Figures 2.2-2.4. These autocorrelations are totally different in appearance from the autocorrelations of the measured EMPTAC data. Here, there are no clearly defined side plateaus, and the central peak indeed is not necessarily the maximum value. (It is true that the offset autocorrelation values decrease as one flips from Figures 2-10 to 2-12, corresponding to an increase in the f autocorrelation parameters upon which these figures are based.) As mentioned above, we suspect the failure of the autocorrelations in Figures 2.10-2.12 to settle down to smooth side values is related to the randomly located up-going spikes seen in Figures 2.2-2.4. Where these spikes intersect, pass, and overlap each other in computing $\Phi(j)$ from (2-17), the autocorrelation function will speciously jump around as a function of j in the violent manner evident on simulated data Figures 2.10-2.12, but not on observed data Figures 2.7-2.9.

As mentioned before, there is a basic oversimplification made in driving the cables with field quadrature components obeying chi square distribution described by (2-11) (see Figures 2.2-2.4 and 2.10-2.12): Chi square distributions characterize the field components squared, not the phase-quadrature amplitudes of the fields themselves. This oversimplification is the cause of some, but not all of the difficulty evident on these plots.

It can be shown (see next subsection) that if the phase-quadrature component amplitudes squared and summed,

$$z = u^2 + v^2 \quad (2-18)$$

obey a chi square distribution with two degrees of freedom

$$h_{\chi^2_2}(z) = e^{-z/\mu_c} / \mu_c \quad (2-19)$$

then u and v , the unsquared phase-quadrature amplitudes themselves, must obey a Gaussian distribution

$$e_g(u) = e_g(v) = \frac{1}{\sqrt{2\pi}} e^{-u^2/(2\sigma_g^2)} = \frac{1}{\sqrt{2\pi}} e^{-v^2/(2\sigma_g^2)} \quad (2-20)$$

where the Gaussian variance of (2-20) and the chi square mean of (2-19) are related simply by

$$\mu_c = 2\sigma_g^2 \quad (2-21)$$

Thus, for the chi square representation, $C(n,i)$ of (2-8) should actually be obtained from (2-9)

$$C(n,i) = \mu_g + \sigma_g u(n,i) \quad (2-22)$$

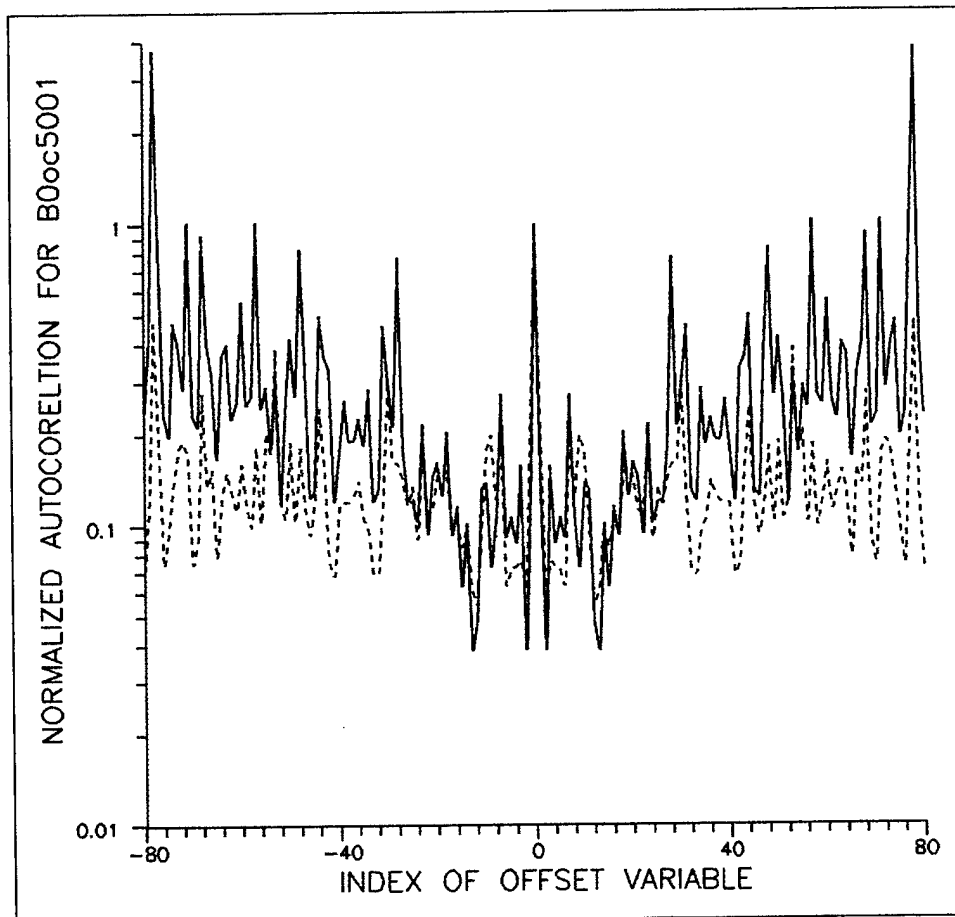


Figure 2.10. Normalized autocorrelation of the simulated cable current with (dashed line) and without (solid line) the data filtered. This figure is based on f_{space} and f_{freq} both set to 1 (artificially high autocorrelation), and the assumption that u_{lim} has a chi square distribution. Cable ends are 30Ω , and this observer is near the cable midpoint. Note that the autocorrelation of the filtered data is characterized by a central peak and very ragged sides which do not resemble a plateau at all. Cable ends are modeled as open circuit, and this observer is near the cable midpoint.

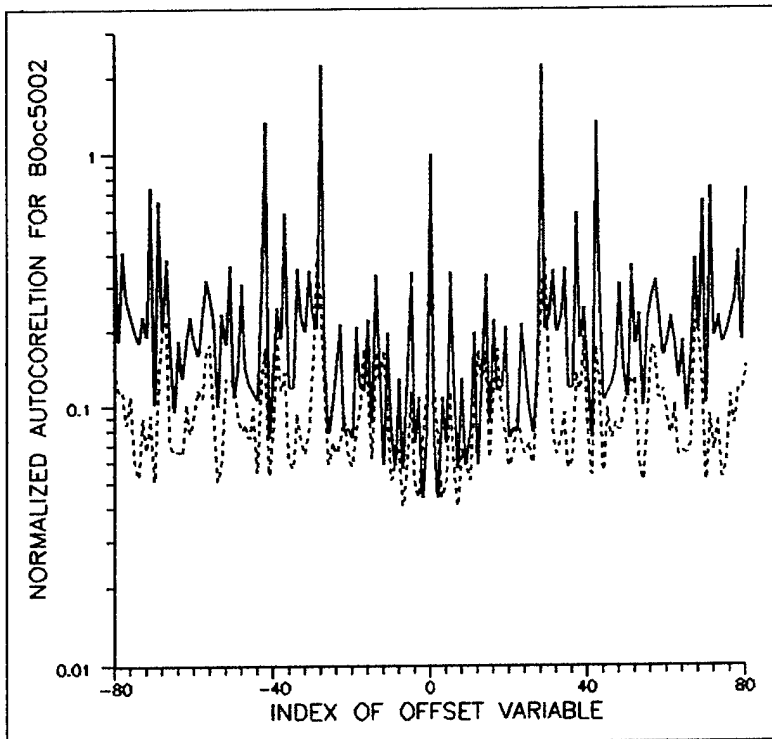


Figure 2.11. Normalized autocorrelation of the simulated cable current with (dashed line) and without (solid line) the data filtered. This figure is based on f_{space} and f_{freq} both set to 10 (realistic autocorrelation), and the assumption that u_{lim} has a chi square distribution. Cable ends are 30Ω , and this observer is near the cable midpoint. Note that the autocorrelation of the filtered data is characterized by a central peak and very ragged sides which do not resemble a plateau at all. Cable ends are modeled as open circuit, and this observer is near the cable midpoint.

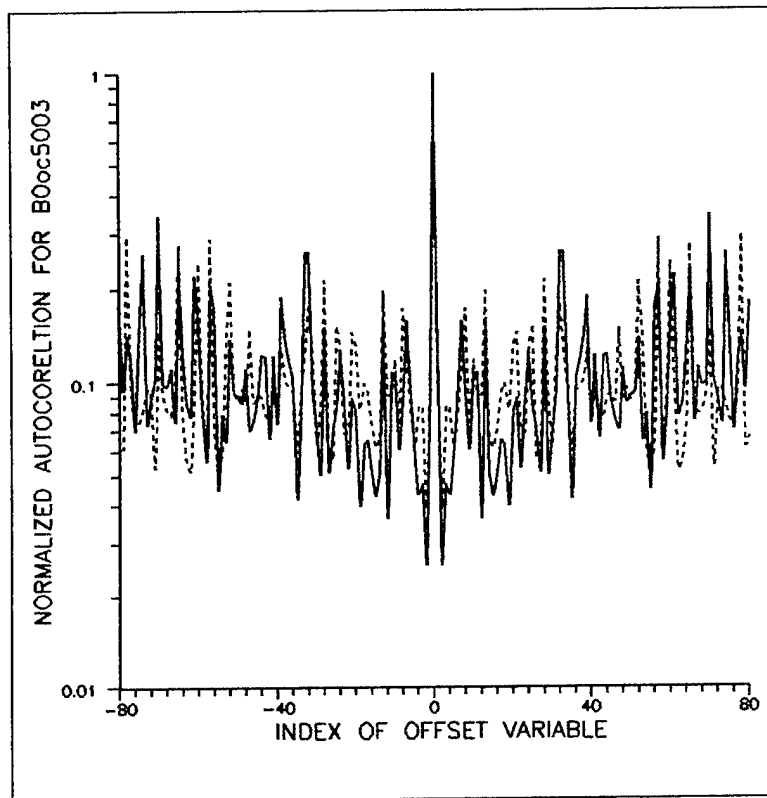


Figure 2.12. Normalized autocorrelation of the simulated cable current with (dashed line) and without (solid line) the data filtered. This figure is based on f_{space} and f_{freq} both set to 100 (almost no correlation), and the assumption that u_{lim} has a chi square distribution. Cable ends are 30Ω , and this observer is near the cable midpoint. Note that the autocorrelation of the filtered data is characterized by a central peak and very ragged sides which do not resemble a plateau at all. The correlation model used here does, at least, succeed in reducing the autocorrelation function at offsets away from the central peak, however (compare with the two previous figures). Cable ends are modeled as open circuit, and observer is near cable midpoint.

where now μ_g is the observed average and σ_g is the observed standard deviation of the quadrature components of the EMPTAC field amplitudes. As these quadrature components are unbiased, μ_g must be 0.

The actual run (for measuring the high-frequency scan of $|H_x|^2$ in the EMPTAC Middle Bay is characterized by a mean of $4.46\text{e-}8$ (A/m) 2 and a standard deviation of $6.13\text{e-}8$ (A/m) 2 (before trend removal). Thus, if the requirements for a Gaussian distribution are met, σ_g for the phase-quadrature components should be approximately $[(4.46\text{e-}8 + 6.13\text{e-}8)/4]^{1/2} = 1.62\text{e-}4$ A/m.

If the field component amplitude squared (2-18) actually obeys a log normal distribution

$$h_{lg}(z) = \frac{1}{\sqrt{2\pi}} \frac{e^{-(\ln z - \mu_{lg})^2/(2\sigma_{lg}^2)}}{\sigma_{lg} z} \quad (2-23)$$

the distribution of the individual unsquared quadrature components, u and v of (2-20), needs to be determined numerically. It is likely that there does not exist any canonical distribution for u and v which leads to a log normal distribution when two variables obeying this hypothetical distribution are squared and added, although we shall see in Section 4 that a good, simple empirical fit is possible.

MAPPING OF RANDOM NUMBERS TO GIVEN DISTRIBUTIONS

Assume p is a random number uniformly distributed between 0 and 1, which corresponds to R of (2-10) or (2-11). One may think of p as a probability, although it is not vital to make this association. Now ask the question, how does one map p onto $(-\infty, \infty)$ in such a way that x , the output variable of the map, obeys, for example, a Gaussian distribution?

$$P(u) = \int_{-\infty}^u e_g(u') du' \quad (2-24)$$

where

$$e_g(u) = \frac{1}{\sqrt{2\pi}} e^{-u^2/2} \quad (2-25)$$

This mapping, in operator notation, may be expressed as

$$u = P^{-1}(p) \quad (2-26)$$

where $P^{-1}()$ is the inverse Gaussian operator.

Zelen and Severo [1] provide formulas for $P^{-1}(p)$: Let q be $1 - p$. Then, if $q < 0.5$, they define

$$w = (\ln(1/q^2))^{1/2} \quad (2-27)$$

and $P^{-1}()$ becomes

$$P^{-1}(p) = u - \frac{c_0 + c_1 w + c_2 w^2}{1 + d_1 w + d_2 w^2 + d_3 w^3} \quad (2-28)$$

where (c_0, c_1, c_2) is $(2.515517, 0.802853, 0.010328)$ and (d_1, d_2, d_3) is $(1.432788, 0.189269, 0.001308)$. If $q > 0.5$, w of (2-27) is replaced by

$$w = (\ln(1/p^2))^{1/2} \quad (2-29)$$

and (2-26) then gives $-P^{-1}(p)$.

For a non-centered distribution,

$$e_g(u, \mu_g) = \frac{1}{\sqrt{2\pi}} e^{-(u - \mu_g)^2/2} \quad (2-30)$$

first operate on u with the operator $(-\mu_g)()$ and second with $P()$. The operator $P_{-\mu_g}^{-1}(p)$ which maps $(0, 1)$ onto $(-\infty, \infty)$ is now

$$u = P_{-\mu_g}^{-1}(p) = \mu_g + P^{-1}(p) \quad (2-31)$$

In full operator notation, this becomes

$$u = (-\mu_g)^{-1}(P^{-1}(p)) \quad (2-32)$$

where $(-\mu_g)^{-1}()$ is the inverse of the $(-\mu_g)()$ operator. In other words, the operator equation

$$P_{-\mu_g}^{-1}() = (-\mu_g)^{-1}(P^{-1}()) \quad (2-33)$$

can be used. The $(-\mu_g)^{-1}()$ operator, of course, just adds μ_g to its operand. The operator sequence described by (2-31) is the reverse inverse of the operator sequence applied to u in (2-30).

If there is a non-unity variance,

$$e_g(u, \sigma_g) = \frac{1}{\sqrt{2\pi}} \frac{e^{-(u/\sigma_g)^2/2}}{\sigma_g} \quad (2-34)$$

first operate on u with $(\div\sigma)(\cdot)$ and then with $P^{-1}(\cdot)$. Thus, the operator $P_{,\sigma}^{-1}(p)$ which maps $(0,1)$ onto $(-\infty, \infty)$ is now

$$u = P_{,\sigma}^{-1}(p) = \sigma_g P^{-1}(p) \quad (2-35)$$

In full operator notation, write

$$u = (\div\sigma_g)^{-1}(P^{-1}(p)) \quad (2-36)$$

where $(\div\sigma_g)^{-1}(\cdot)$ multiplies its operand by σ_g . Thus, one obtains the operator equation

$$P_{,\sigma}^{-1}(\cdot) = (\div\sigma_g)^{-1}(P^{-1}(\cdot)) \quad (2-37)$$

Again note that the operator sequence on p in (2-37) is the reverse inverse of the operator sequence on u in (2-34). (The σ_g in the denominator of (2-34) for the distribution function does not appear in (2-35) through (2-37) because the form of (2-35) through (2-37) is actually determined by the cumulative probability distribution,

$$P_{,\sigma}(u) = \int_0^u \frac{1}{\sqrt{2\pi}} \frac{e^{-(u'/\sigma_g)^2/2}}{\sigma_g} du' = \int_0^{t_u} \frac{1}{\sqrt{2\pi}} e^{-t'^2/2} dt' \quad (2-38)$$

where

$$t = u/\sigma_g \quad (2-39)$$

and where the differential,

$$dt = du/\sigma_g \quad (2-40)$$

does not enter in the operator equation.)

For $e(u, \mu_g, \sigma_g)$ given by

$$e(u, \mu_g, \sigma_g) = \frac{1}{\sqrt{2\pi}} \frac{e^{-(u - \mu_g)^2/(2\sigma_g^2)}}{\sigma_g} \quad (2-41)$$

one obtains

$$\begin{aligned}
u &= P_{-\mu_g, \sigma_g}^{-1}(p) = \mu_g + \sigma_g P^{-1}(p) \\
&= (-\mu_g)^{-1}((\div \sigma_g)^{-1}(P^{-1}(p)))
\end{aligned} \tag{2-42}$$

or in operator notation

$$P_{-\mu_g, \sigma_g}^{-1}() = (-\mu_g)^{-1}((\div \sigma_g)^{-1}(P^{-1}())) \tag{2-43}$$

A somewhat less trivial application of this formalism is the log normal mapping of $(0,1)$ onto $(0, \infty)$. In this case, $e_{lg}(u)$ is given by

$$e_{lg}(u) = \frac{1}{\sqrt{2\pi}} \frac{\exp(-(\ln u - \mu_{lg})^2/(2\sigma_{lg}^2))}{(\sigma_{lg} u)} \tag{2-44}$$

Define L to be the $\ln()$ operator. Then, the inverse operator $L^{-1}()$ is

$$L^{-1}() = \exp() \tag{2-45}$$

Consequently,

$$\begin{aligned}
x &= L^{-1}[(-\mu_{lg})^{-1}((\div \sigma_{lg})^{-1}(P^{-1}(p)))] \\
&= L^{-1}[(-\mu_{lg})^{-1}(\sigma_{lg} P^{-1}(p))] \\
&= L^{-1}[\mu_{lg} + \sigma_{lg} P^{-1}(p)] \\
&= \exp(\mu_{lg} + \sigma_{lg} P^{-1}(p))
\end{aligned} \tag{2-46}$$

is the formula for mapping p onto u . (The $(\sigma_{lg} u)$ in the denominator of (2-44) for the distribution function does not appear in (2-46) because the form of (2-46) is actually determined by the cumulative probability distribution,

$$P_{lg}(u) = \int_0^u \frac{1}{\sqrt{2\pi}} \frac{\exp(-(\ln u' - \mu_{lg})^2/(2\sigma_{lg}^2))}{(\sigma_{lg} u')} du' = \int_{-\infty}^{w_u} \frac{1}{\sqrt{2\pi}} e^{-w'^2/2} dw' \tag{2-47}$$

where

$$w' = (\ln u' - \mu_{lg})/\sigma_{lg} \quad (2-48)$$

and where the differential,

$$dw' = \frac{du'}{(\sigma_{lg} u')} \quad (2-49)$$

again does not enter the operator equation.)

There is empirical evidence that some HPM energy distributions look almost log log normal:

$$e_{lg^2}(u) = \frac{e^{-(\ln(-\ln u) - \mu_{lg^2})/(2\sigma_{lg^2}^2)}}{\sqrt{2\pi}(-\sigma_{lg^2} u \ln u)} \quad (2-50)$$

(If $w = \ln(-\ln u)$, (2-50) reduces to (2-41).) This function describes a fairly sophisticated distribution transformation. It does, however, have a problem: $\ln u$ can be positive if u can be greater than 1, and then $\ln(-\ln u)$ becomes complex. An *ad hoc* fix to this difficulty is to replace $\ln(-\ln u)$ with $\ln(\text{abs}(\ln u))$ in (2-50). The transformation from p to u is then

$$u = L^{-1}[(\text{abs})^{-1}\{L^{-1}[(-\mu_{lg^2})^{-1}\{(-\sigma_{lg^2})^{-1}(P^{-1}(p))\}]\}] \quad (2-51)$$

There is now a problem with (2-51). In particular, the $(\text{abs})()$ operator destroys information and increases entropy. Thus, it may be expected to have no inverse, and the operator of (2-51) seemingly is undefinable if its domain includes p values which require $(\text{abs})()$ to operate on negative quantities.

Note that the inverse operators in (2-51) are reverse chained with respect to the operators on u which appear in (2-50). While working out the permitted domain of this inverse operator as a function of μ_{lg^2} and σ_{lg^2} is complicated, it would be almost impossible conceptually had the authors not gradually built up to the reverse-chaining technique developed in this subsection. Actual expansion of the operator in (2-51), assuming the domain of the $(\text{abs})^{-1}()$ operator is never positive,

$$(\text{abs})^{-1}() = (x(-1))() \quad (2-52)$$

leads to

$$u = \exp[-\exp(\mu_{lg^2} + \sigma_{lg^2} P^{-1}(p))] \quad (2-53)$$

as the formula for mapping $p = (0, 1)$ onto $x = (0, \infty)$ for the log log normal distribution function described by (2-50).

Somewhat to our surprise, it was unexpectedly realized that the $(\text{abs})^{-1}()$ operator may be physically inferred to have an inverse in some cases, even if the range is permitted to be bipolar. This issue arose when the power distribution was assumed to be log normal:

$$h_{lg}(P) = \frac{1}{\sqrt{2\pi}} \frac{\exp(-(\ln P - \mu_{lg})^2/(2\sigma_{lg}^2))}{(\sigma_{lg} P)} \quad (2-54)$$

In this case, the probability p is mapped onto power P by the operator

$$\begin{aligned} P_P^{-1}() &= L^{-1}\left[(-\mu_{lg})^{-1}\left\{(\text{div}\sigma_{lg})^{-1}(P^{-1}(p))\right\}\right] \\ &= L^{-1}\left[(-\mu_{lg})^{-1}\left\{\sigma_{lg} P^{-1}(p)\right\}\right] \\ &= L^{-1}\left[\mu_{lg} + \sigma_{lg} P^{-1}(p)\right] \\ &= \exp(\mu_{lg} + \sigma_{gl} P^{-1}(p)) \end{aligned} \quad (2-55)$$

where the two P 's (power and the Gaussian operator) are distinguished by context. The authors next attempted to find the distribution function for the magnetic field projection on the receiving sensor dipole antenna which is associated with P :

$$P = H^2 \quad (2-56)$$

Thus, in the notation of Appendix B of [5], one could write

$$H = g(P) \quad \text{and} \quad P = g^{-1}(H) \quad (2-57)$$

where

$$g = O^{\frac{1}{2}} \quad \text{and} \quad g^{-1} = O^2 \quad (2-58)$$

and

$$f(H) = h(g^{-1}(H)) \left| \frac{dg^{-1}(H)}{dH} \right| \quad (2-59)$$

Equation (2-59) gives

$$f(H) = \frac{1}{\sqrt{2\pi}} \frac{\exp(-(\ln H^2 - \mu_{lg})^2/(2\sigma_{lg}^2))}{(\sigma_{lg} H^2)} \cdot r|H| \quad (2-60)$$

where $r = 1$ if the domain of $\varphi(H)$ is from $H = -\infty$ to $H = +\infty$, and $r = 2$ if the domain of $\varphi(H)$ is from σ to ∞ . Equation (2-60) can also be expressed as

$$f(H) = \frac{1}{\sqrt{2\pi}} \frac{\exp(-(2 \ln|H| - \mu_{lg})^2/(2\sigma_{lg}^2))}{\sigma_{lg} |H|} \quad (2-61)$$

assuming H ranges from $-\infty$ to $+\infty$. One now can express the mapping from p to H as

$$\begin{aligned} H &= (\text{abs})^{-1} \left[L^{-1} \left\{ (x2)^{-1} (-\mu_{lg})^{-1} ((\div \sigma_{lg})^{-1} (P^{-1}(p))) \right\} \right] \\ &= (\text{abs})^{-1} \left[L^{-1} \left\{ (x2)^{-1} (\mu_{lg} + \sigma_{lg} P^{-1}(p)) \right\} \right] \\ &= (\text{abs})^{-1} \left[\exp \left\{ (\mu_{lg} + \sigma_{lg} P^{-1}(p))/2 \right\} \right] \end{aligned} \quad (2-62)$$

However, in this case, it is physically apparent that H should be negative as frequently as it is positive, and thus the inverse of the $(\text{abs})()$ operator is, at least in this case, $(\text{random sign})()$

$$(\text{abs})^{-1}() = (\text{random sign})() \quad (2-63)$$

or

$$H = (\text{random sign}) \left[\exp \left\{ (\mu_{lg} + \sigma_{lg} P^{-1}(p))/2 \right\} \right] \quad (2-64)$$

The cumulative probability distribution corresponding to (2-61) is

$$F(H) = \int_{-\infty}^H f(h) dh \quad (2-65)$$

This formula leads to the probability that H is negative being given by

$$P_H(0) = \int_{-\infty}^0 \frac{-1}{\sqrt{2\pi}} \frac{\exp(-(2 \ln(-h) - \mu_{lg})^2/(2\sigma_{lg}^2))}{(\sigma_{lg} h)} dh \quad (2-66)$$

Substituting

$$2 \ln(-h) = u \quad (2-67)$$

in (2-66) will correctly yield $P_H(0) = 1/2$.

If only the distribution of the magnitude of H from 0 to ∞ , is needed, (2-61) becomes

$$f(H) = \frac{2}{\sqrt{2\pi}} \frac{\exp(-(2 \ln H - \mu_{lg})^2/(2\sigma_{lg}^2))}{(\sigma_{lg} H)} \quad (2-68)$$

Now the formula for mapping p (0 to 1) onto H (0 to ∞) is simply

$$\begin{aligned} H &= \left[L^{-1} \left\{ (x2)^{-1} (-\mu_{lg})^{-1} ((\div \sigma_{lg})^{-1} (P^{-1}(p))) \right\} \right] \\ &= \left[L^{-1} \left\{ (x2)^{-1} (\mu_{lg} + \sigma_{lg} P^{-1}(p)) \right\} \right] \\ &= \left[\exp \left\{ (\mu_{lg} + \sigma_{lg} P^{-1}(p))/2 \right\} \right] \end{aligned} \quad (2-69)$$

If a chi square distribution with two degrees of freedom is the basic distribution function, $P(x)$ of (2-24) is replaced by

$$P_{\chi_2}(z) = \int_0^z h_{\chi_2}(z') dz' = 1 - e^{-z/\mu_c} \quad (2-70)$$

where

$$h_{\chi_2}(z) = e^{-z/\mu_c}/\mu_c \quad (2-71)$$

Then $P_{\chi_2}^{-1}(p)$, the inverse chi square probability operator, is just, as (2-11) has implied,

$$z = P_{\chi_2}^{-1}(p) = -\mu_c \ln(1-p) = \mu_c \ln(1-p)^{-1} \quad (2-72)$$

which is far simpler than its Gaussian counterpart.

GENERATION AND INVERSION OF COMPOUND DISTRIBUTIONS

So far, the authors have only dealt with situations which are based on changing the variables in a Gaussian distribution. However, any function $P(x)$ with the properties

variables in a Gaussian distribution. However, any function $\mathcal{P}(x)$ with the properties

$$\begin{aligned}\mathcal{P}(\text{lower limit}) &= 0 \\ \mathcal{P}(\text{upper limit}) &= 1 \\ \frac{d\mathcal{P}(z)}{dz} &\geq 0\end{aligned}\tag{2-73}$$

can be a cumulative probability distribution. For instance,

$$\mathcal{P}(z) = (P(z))^2\tag{2-74}$$

where $P(x)$ is given by (2-24), can also be a cumulative probability distribution for mapping $(-\infty, \infty)$ onto $(0, 1)$. Now what operator maps p from 0 to 1 back onto $(-\infty, \infty)$; i.e., what is $\mathcal{P}^{-1}(p)$?

The answer to this question is again obtained by the reverse chaining of inverse operators:

$$x = \mathcal{P}^{-1}(p) = P^{-1}((p)^{1/2})\tag{2-75}$$

or

$$\mathcal{P}^{-1}(0) = P^{-1}[(0^2)^{-1}]\tag{2-76}$$

The essential differences between this operator and all that preceded is that $P^{-1}(0)$ is no longer the innermost operator of the inverse chain. In fact, one can define

$$\mathcal{P}(z) = O(P(z))\tag{2-77}$$

where $O()$ is some fully generalized operator (such as a power series where all the coefficients add up to unity). As long as $\mathcal{P}(x)$ obeys (2-70), the mapping operator for p back to z is

$$\mathcal{P}(0)^{-1} = P^{-1}(O^{-1}(0))\tag{2-78}$$

FIELD DISTRIBUTIONS AND POWER FLUX DISTRIBUTIONS

Experimental evaluation of a cavity response under HPM excitation usually yields the probabilistic power-flux density pdf as picked up by a magnetic or electric dipole feeding a square-law detector. (In some cases, experimental evaluation yields the field amplitude with loss of phase data, which conveys essentially the same information as a power measurement.) This power is usually interpreted as the sum of the squares of the two phase-quadrature components

$$z = u^2 + v^2 \quad (2-79)$$

where the power pdf of z is the observed quantity, denoted $h(z)$. In order to use this information to drive a probabilistic circuit code for the cavities electronics, it is necessary to extract the probabilistic field quadrature probability density functions $e(u) = e(v)$ from $h(z)$ given (2-79).

As a first step in this endeavor, let us find the distribution densities of the squared quadrature components

$$\begin{aligned} x &= u^2 \\ y &= v^2 \end{aligned} \quad (2-80)$$

denoted $f(x) = f(y)$, so that

$$z = x + y \quad (2-81)$$

For the moment, we shall assume that x , y , and z can all range from $-\infty$ to $+\infty$, although we shall subsequently need to employ the constraint that x , y , and z must all be positive.

The probability that x is between x and $x + dx$, and that y is between y and $y + dy$ is

$$f(x) f(y) dx dy \quad (2-82)$$

However, x , y and z are not all independent variables. If (2-81) holds, the probability that x is between x and $x + dx$ while z is between z and $z + dz$ is obtained by the variable transformation

$$\begin{aligned} x &= x' \\ y &= -x' + z' \end{aligned} \quad (2-83)$$

and the two-dimensional probability differential of (2-82) becomes

$$f(x') f(z' - x') \frac{\partial(x, y)}{\partial(x', z')} dx' dz' \quad (2-84)$$

where

$$\frac{\partial(x, y)}{\partial(x', z')} = \begin{vmatrix} 1 & -1 \\ 0 & 1 \end{vmatrix} = 1 \quad (2-85)$$

is the Jacobian of the variable transformation of (2-83). (Fortunately this Jacobian is simply unity.)

We now wish to determine the probability that z' is between z' and $z' + dz'$, regardless of x' . This 1D probability differential on z' is obtained by summing all the 2D probability differentials of (2-84) of x' and z' over dx' , i.e., by integration (2-84) over all possible x' :

$$h(z') dz' = \int_{-\infty}^{\infty} f(x') f(z' - x') dx' dz' \quad (2-86)$$

This equation leads to the surprising conclusion that $h(z)$ is just $f(x)$ convolved upon itself. In other words, if $H(\omega)$ is the Fourier transform of $h(z)$, then the desired distribution $f(x)$ is simply the inverse Fourier transform of $[H(\omega)]^{1/2}$:

$$H(\omega) = \int_{-\infty}^{\infty} h(z) e^{-j\omega z} dz \quad (2-87)$$

$$f(x) = \frac{1}{2\pi} \int_{-\infty}^{\infty} [H(\omega)]^{1/2} e^{j\omega x} d\omega \quad (2-88)$$

Canonical Treatment of Phase-Quadrature Field Extraction for the Chi-Square Special Case

Two commonly encountered cases are that $h(z)$ be log normal or chi square with two degrees of freedom. The extraction of $f(x)$ for $h(z)$ a log normal distribution must be implemented approximately (see Section 4). In fact, this is the case for most possible power pdf's $h(z)$. However, if $h(z)$ is chi square with two degrees of freedom, canonical extraction of $e(u)$ and $f(x)$ from $h(z)$ is possible, as we shall now show. The chi square probability density function is

$$h_{\chi^2_2}(z) = e^{-z/\mu_c}/\mu_c \quad z > 0 \\ = 0 \quad z < 0 \quad (2-89)$$

Thus, $H(\omega)$ is

$$H(\omega) = \frac{1}{\mu_c} \frac{1}{(j\omega + 1/\mu_c)} \quad (2-90)$$

and the probability density function $f(x)$ is

$$f(x) = \frac{1}{2\pi} \int_{-\infty}^{\infty} \frac{e^{j\omega x}}{[\mu_c (j\omega + 1/\mu_c)]^{1/2}} d\omega \quad (2-91)$$

If the branch cut appearing in the integral of (2-89) is laid out in a sensible manner (Figure 2.13) the integration contour can be closed in the totally analytic lower half of the ω plane giving

$$f(x) = 0 \quad x < 0 \quad (2-92)$$

For $x > 0$, the contour of Figure 2.13 could be closed in the upper half of the ω plane.

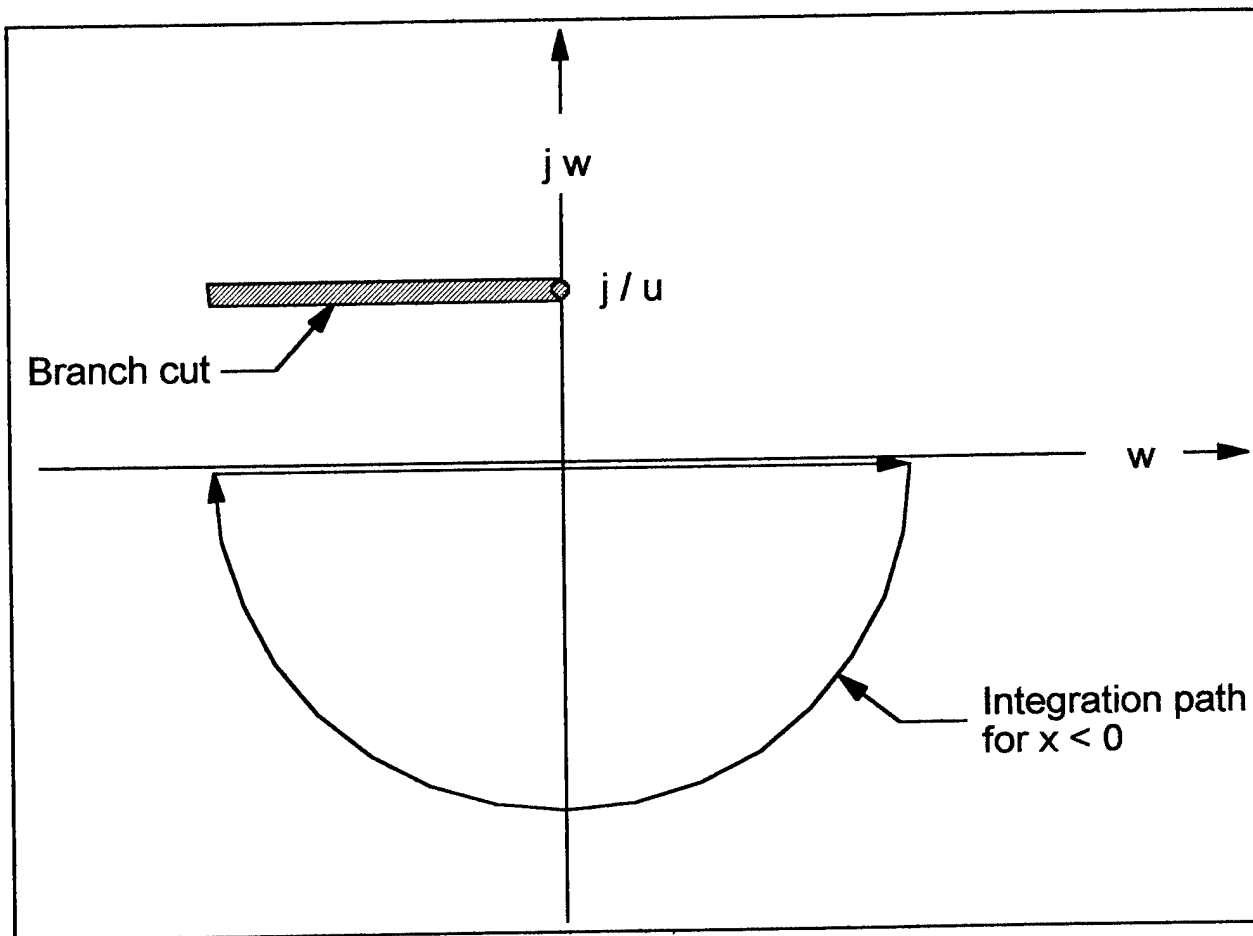


Figure 2.13. Contour of integration for evaluating the probability density function $f(x)$ when $x < 0$.

Alternatively, to evaluate (2-91), we introduce the change of variables

$$j\omega\mu_c + 1 = y^2 \quad (2-93)$$

This transforms $f(x)$ of (2-91) to

$$f(x) = \frac{1}{\pi} \frac{e^{-x/\mu_c}}{j\mu_c} \int_a^b e^{xy^2/\mu_c} dy \quad (2-94)$$

where

$$\begin{aligned} a &= e^{-j\pi/4} \infty = b^* \\ b &= e^{j\pi/4} \infty = \sqrt{j} \infty \end{aligned} \quad (2-95)$$

Note that we take $\sqrt{(-j)}$ to be $e^{-j\pi/4}$, not $e^{j\pi/4}$, so that the branch cut implied by the inverse of (2-93) is not swept across the already existing branch cut. Rearrangement of (2-94) yields

$$f(x) = \frac{1}{\pi} \frac{e^{-x/\mu_c}}{\mu_c} \cdot 2 \operatorname{Im} \left[\int_0^b e^{xy^2/\mu_c} dy \right] \quad (2-96)$$

A second transformation

$$t = e^{-j\pi/4} y \quad (2-97)$$

leads to

$$f(x) = \frac{1}{\pi} \frac{e^{-x/\mu_c}}{\mu_c} \cdot 2 \operatorname{Im} \left[e^{j\pi/4} \int_0^{\infty} e^{jxt^2/\mu_c} dt \right] \quad (2-98)$$

The bracketed factor may be integrated in closed form to give

$$[] = e^{j\pi/4} \frac{\sqrt{\pi}}{2(x/\mu_c)^{1/2}} \cdot \frac{(1+j)}{\sqrt{2}} \quad (2-99)$$

Equations (2-98) and (2-99) provide us with an expression for the probability density function $f(x)$ when $h(z)$ is chi square with two degrees of freedom:

$$f(x) = \frac{e^{-x/\mu_c}}{\sqrt{\pi x \mu_c}} \quad (2-100)$$

Let us now extract the expression for the associated phase-quadrature field pdf $e(u)$. In general, if u and x are related by the transformation function

$$u = g(x) \quad (2-101)$$

where,

$$g() = ()^{1/2} \quad (2-102)$$

then the distributions of u and x are related by

$$e(u) = f(g^{-1}(u)) \frac{dg^{-1}(u)}{du} \quad (2-103)$$

This last relationship is true if the underlying distribution of z is chi square, log normal, or anything else.

We now evaluate the desired probability density function $e(u)$ from the probability density function for $f(x)$ as given by (2-100), and the relationship between x and u of (2-80):

$$e(u) = \frac{1}{\sqrt{\pi}} \frac{e^{-u^2/\mu_c}}{\sqrt{\mu_c}} \cdot 2 \quad (2-104)$$

where the assumption is made that u , like x , only ranges from 0 to ∞ . In actuality, however, u ranges from $-\infty$ to ∞ , thus eliminating the 2 from the numerator of (2-104).

It is known that $h(z)$ for the chi square distribution with two degrees of freedom is based on $e(u)$ having a normal distribution where σ_g of $e_g(u)$ and μ_c of $h_{\chi^2}(2,z)$ are related by

$$\mu_c = 2\sigma_g^2 \quad (2-105)$$

although this relation is usually established by deriving $h_{\chi^2}(2,z)$ from $e_g(u)$, not the other way around as we have just done here. Making this substitution in (2-104) confirms the validity of (2-87) and (2-88), at least for the special case of $h(z)$ being chi square with two degrees of freedom.

THE DETRENDING OPERATION

In order to obtain a chi square (with two degrees of freedom) power flux distribution, several conditions must be met, which generally are not. For instance, if the variable on which power flux changes is frequency, the cavity must have a frequency-independent Q (which

Appendix A of Section 8 demonstrates to be an impossibility). Also, if chamber illumination is through apertures, the aperture cross-sections must also be frequency independent (another impossibility). Finally, if one is using a \vec{B} sensor, there will be a forbidden ω -dependence unavoidably attached to the measurement. It is in order to remove the effects of slowly varying factor such as these that the detrending operation was developed and is applied.

The trend on a data set in a spatial sense corresponds approximately to the slowly varying function $g(\mathbf{r})$ introduced by Price, *et al.*, [2,3] at his Equation (5). It also corresponds to the field nonuniformities observed by Hill [9] in a stirred-mode reverberation chamber, and shown in his Figures 8 and 9. It is present whether the observed EM response is measured as a function of position or frequency. We have not personally worked with data where the driver or observer position changes, although this was done in [9].

For power data taken as a function of frequency, detrending is performed as follows [5]:

Start with the data array z_n ($n = 1, \dots, N$). Let L_n be the \ln of z_n . Then convolve the L_n array with a truncation filter of the form $C_n = (\sin \alpha n) / (2\pi \alpha n)$, where the truncation of the C_n filter is symmetrically set to include the central lobe and two side lobes (the first positive-going and the first negative-going) on each side. Let us imagine that the data is actually a function of time (not frequency), with each point separated by 1 s. Let N_0 be the number of points inside or at the truncation limits of C_n . Then the convolution corresponds to passing L_n through an ideal low-pass filter of cutoff frequency $f_{co} = 3/(N_0 - 1)$. The low-pass convolution output is the trend of L_n , M_n . Thus, $(L_n - M_n)$ is the detrended data in the \ln domain, and $z_n' = \exp(L_n - M_n)$ is the actual detrended data. For EMPTAC, Celestron 8, and G.P.S. data sets, we empirically found 91 to be the best value for N_0 ; this corresponds to $f_{co} = .033$. The variable α is then adjusted so $\alpha(N_0 - 1) = 3\pi$; i.e., $\alpha = 0.1047$. One would expect the optimum value of N_0 to vary from experiment to experiment, and to depend strongly on how every data set is obtained. Thus, the concurrence of $N_0 = 91$ for three different experiments is probably serendipitous. On the other hand, a highly skilled experimentalist may (pardon us) have an intuitive feel for how densely to sample data so that nothing is lost, but also nothing extraneous is recorded, and may subconsciously set his recording equipment so $N_0 = 91$ consistently corresponds to taking data at just the right spacing.

REFERENCES

- [1] Zelen, M. and N. C. Severo, "Probability Functions," pp. 925-995 (see especially p. 933), *Handbook of Mathematical Functions*, M. Abramowitz and I. A. Stegun, editors, National Bureau of Standards, Applied Mathematics Series, No. 55, Washington, DC, June 1964.
- [2] Price, R. H., *et al.*, "Determination of the Statistical Distribution of Electromagnetic Field Amplitudes in Complex Cavities," 88JAL129, JAYCOR, 1 June 1988.

- [3] Price, R. H., H. T. Davis, and E. P. Wenaas, "Determination of the Statistical Distribution of Electromagnetic-Field Amplitudes in Complex Cavities," *Phys. Rev. E*, Vol. 48, pp. 4716-4729, December 1993.
- [4] Roe, P. R., *Probability and Statistics in Experimental Physics*, pp. 189-203, Springer-Verlag New York, Inc., New York, 1992.
- [5] Holland, R. and R. St. John, "Statistical Response of Enclosed Systems to HPM Environments," PL-TR-94-1006, Air Force Phillips Laboratory, Kirtland Air Force Base, NM, 1994.
- [6] T. H. Lehman and R. M. Marshall, "Application of statistical physics to derivation of stress and strength distributions," Ball Systems Engineering Division, Albuquerque, NM, September 26, 1991.
- [7] T. H. Lehman, "A statistical theory of electromagnetic fields in complex cavities," Air Force Phillips Laboratory, Interaction Note 494, May 1993.
- [8] D. A. Hill, "Spatial correlation function for fields in a reverberation chamber," *IEEE Trans. Electromagn. Compat.*, vol. EMC-37, p. 138, February 1995.
- [9] D. A. Hill, "Electronic mode stirring in reverberation chambers," *IEEE Trans. Electromagn. Compat.*, vol. EMC-36, pp. 294-299, November 1994.

Chapter 3. FIELD REDISTRIBUTION AND CABLE RESPONSE

Introduction of autocorrelation on the cable-driving fields, as described in the previous section, creates a problem of its own: If the fields start off with a normal distribution, as $u_{lm}(n,i)$ of (2-10), for example, our autocorrelation introduction algorithm (2-14) and (2-15) does not leave the fields, $u_{freq}(n,i)$ of (2-15), normally distributed. This problem is fixed by a rescaling operation which restores the driving fields to their original distribution while leaving the introduced autocorrelation intact. Description of this rescaling procedure is the first topic of this section.

After the distribution density and autocorrelation of the phase-quadrature field components have been worked out, there remains the details of applying these fields to drive cable currents, for example, in the EMPTAC. To do this, we picked a particular cable, divided it into 200 segments, each of 10 cm length, and probabilistically drove each segment. Actual computations were performed in the frequency domain, although input drivers and output results could be presented in the time domain. A discussion of this operation constitutes the second topic of this section.

Finally, we observed that, after all the above precautions had been taken, we still did not achieve computed cable powers simulating the observed chi square distribution. It became apparent that the radiation resistance effect (about $120 \Omega/m$ for frequencies around 300 MHz) could not be ignored as a loss term on the cables. Note that, while inclusion of this effect modifies cable powers, it does not feed back in our model and alter the phase-quadrature field distribution densities. Also, it is vital to guarantee that the cable drivers do not, themselves, yet carry some small trend into the cable response calculation. Fine-tuning these models (trendless cable drivers and radiation resistance) is the third and last subject of this section.

DATA RESTORATION AFTER FORCED AUTOCORRELATION

At this point, we set about fixing two problems with the model used in the previous section. First, we recognized that the actual phase-quadrature driving fields should be normally distributed, as dictated by (2-9) and (2-10). Second, we recognized that the use of (2-14) and (2-15) leaves the resulting fields with the desired autocorrelation, but does not preserve the desired normal distribution.

The first problem is easy to correct: Simply make the phase-quadrature field distribution normal. The second problem is much more subtle to remedy. Let us begin by generating the two-dimensional ensemble of numbers along the spatial and frequency axes according to (2-9), (2-10), (2-14), and (2-15). (Actually, we need two ensembles, one of which will eventually become $A(n,i)$ of (2-7), and the other of which eventually will become $B(n,i)$.) Then pick a particular spatial point or cable segment i and examine the one-dimensional array which characterizes the drive versus frequency at this point. To the element of this array having the lowest value, assign the index $n = 1$; to the next, assign $n = 2$; etc.; up to $n = n_{max} = N$.

In general, the elements of this array (and even the elements of the array of indices n listed versus frequency) will be in a sequence containing autocorrelation information, but the actual values of the elements of this array will have been speciously altered away from a normal distribution in the process of introducing the autocorrelation. We shall now reverse this alteration without destroying the autocorrelation by utilizing the concept that even the array of indices has some autocorrelation. (Very negative field values will tend to be next to negative field values, etc.)

Let us associate a fraction with each point in the one-dimensional array, as in (2-2):

$$f_m = (m - \frac{1}{2})/m_{\max} = (m - \frac{1}{2})/N \quad (3-1)$$

If this array actually had a normal distribution with zero mean and σ_g standard deviation, it would be true that, if $u(m,i)$ were the value of element m ,

$$P(u(m,i)/\sigma_g) = f_m \quad (3-2)$$

where $P(u(m,i)/\sigma_g)$ is the cumulative normal probability distribution function with σ_g standard deviation. Since this should be true, we shall force it to be true: Rescale each $u(m,i)$ to obey

$$u(m,i) = \sigma_g P^{-1}(f_m) \quad (3-3)$$

where $P^{-1}(f_m)$ is the inverse of the normal cumulative probability distribution function.

As noted above, this rescaling does not undo the autocorrelation because the m 's themselves contain some autocorrelation along the frequency axis. It is interesting to point out that this procedure can be used to transform the $u(m,i)$'s into an array with any desired distribution, irrespective of what the underlying initial distribution used to find $u_{lim}(m,i)$ in (2-10) was. For instance, if $P^{-1}()$ of (3-3) were replaced by the inverse chi square or log normal cumulative distribution function, the $u(m,i)$'s emerging from (3-3) would become chi square or log normal in distribution.

The following observations now seem in order:

1. This rescaling procedure must, or course, be repeated for the 1D array at each of the spatial cable drive or i points.
2. Autocorrelation also existed along the spatial axis before rescaling by virtue of (2-14) and (2-15). Since we merely rescale, not resequence, this rescaling will also preserve this autocorrelation along the spatial axis.
3. If we impose a rescaled normal distribution on the $u(n,i)$'s along the frequency axis, and if this rescaled distribution is obtained in the same manner for each spatial point, the distribution of a 1D array of $u(n,i)$ taken in the *other* direction along i (frequency constant, spatial position variable) will also approach restoration to a normal distribution as the number of spatial and frequency observation points both become large.

4. In this entire operation of rescaling the 2D ensemble, there is no reason we cannot reverse the roles of the frequency and the spatial axes across the ensemble.
5. Even in the problem is extended to three spatial (and one frequency) dimensions, rescaling needs only to be done in one direction.

Now let us back up some of the ideas we have just presented with actual results. Figure 3.1 shows a 1D cut of the 2D $z(n,i) = u(n,i)^2 + v(n,i)^2$ matrix ensemble generated from $u(n,i)$ and $v(n,i)$ with f_{space} and f_{freq} both set to 1000 (almost no autocorrelation). A normal random-number generating function with 0 mean and 0.01 standard deviation was used to initialize these underlying $u(n,i)$ and $v(n,i)$ matrix ensembles (and all others discussed hereafter in this section). This figure overlays the unscaled and rescaled values (with the unscaled plot reduced by 10^3 to separate the two plots). Note that the unscaled and rescaled fluctuations do track each other quite nicely. The drive matrices are 200 space points by 1000 frequency points. Cuts we shall examine are along the frequency direction are located near the spatial midpoint.

Figure 3.2 illustrates the autocorrelation functions obtained for variable-frequency cuts of each of the ensembles ($u(n,i)$ and $v(n,i)$) generated for (2-7). Note that both of the ensembles are uncorrelated except for a very narrow central spike (as should be the case for f values of 1000). These curves are based on $u(n,i)$ and $v(n,i)$ not yet rescaled.

Figure 3.3 illustrates the autocorrelation results from squaring and adding the normally distributed variables, both with and without rescaling. This plot bears a nice resemblance to the experimentally obtained cable current and magnetic field EMPTAC autocorrelation plots illustrated in Figures 2.7-2.9, except that the central spike is excessively narrow.

Figure 3.4 presents a probability plot for the two unsquared variables against a normal distribution assumption. Both plots are nearly perfect 45° lines, so our random number generator clearly yields a good normal distribution when f_{space} and f_{freq} are set to 1000. These curves are based on $u(n,i)$ and $v(n,i)$ not yet rescaled.

Figure 3.5 is a probability plot for the unscaled and rescaled summed and squared variable [$z(n,i)$ of (2-18)] against a chi square distribution assumption. Again, both plots are good approximations to a 45° line. This plot confirms what we already know should be: if $u(n,i)$ and $v(n,i)$ have normal distributions and the autocorrelation implementation does not modify these distributions, $z(n,i)$ will have a chi square distribution.

Figure 3.6 shows that both normally generated, unscaled ensembles remain inside the 90% Kolmogorov-Smirnov confidence limits (see Section 9), even after autocorrelation implementation. There are actually two ways to test the distribution ensembles. One can determine the mean and variance the ensembles actually exhibit, and see if the results fit a Kolmogorov-Smirnov confidence test based on these floating means and variances. Alternatively, one can pin the mean and variance to the values input to the ensemble generator (here 0 and $2 \cdot (0.01)^2$, respectively), and see if the results fit a Kolmogorov-Smirnov test based on the pinned

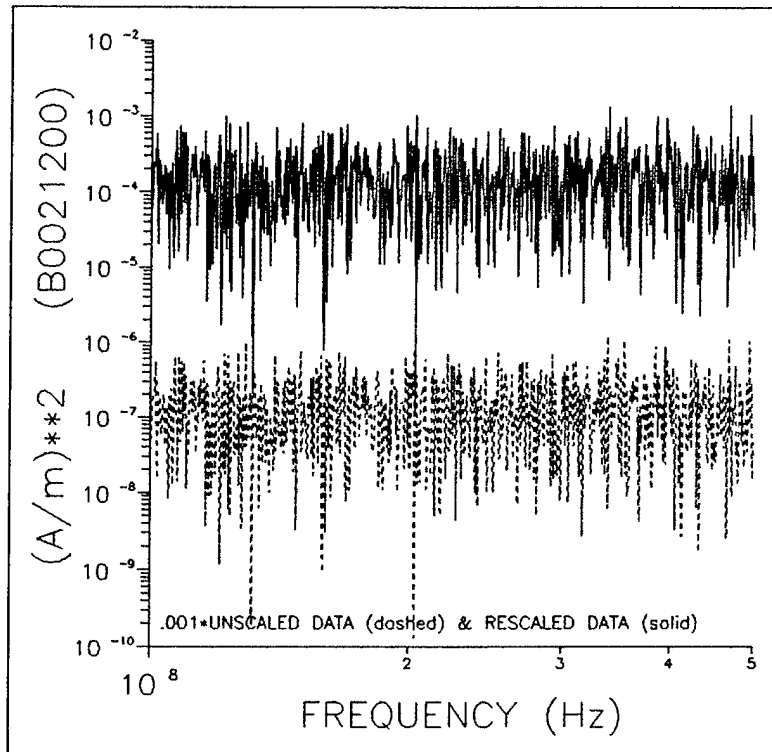


Figure 3.1. Plot of $z(n,i) = u(n,i)^2 + v(n,i)^2$ for each component (u and v) of the phase-quadrature drive generated according to (2-10), (2-14) and (2-15) (normal case) with f_{space} and f_{freq} both set to 1000 (almost no autocorrelation). The lower plot is the raw ensemble ($\times 10^{-3}$), and the upper plot is the ensemble obtained with $u(n,i)$ and $v(n,i)$ rescaled according to (3-3). The normal distribution parameters are $\sigma_g = 0.01$ and $\mu_g = 0$. Note that the rescaled data and the raw data track each other fairly closely.

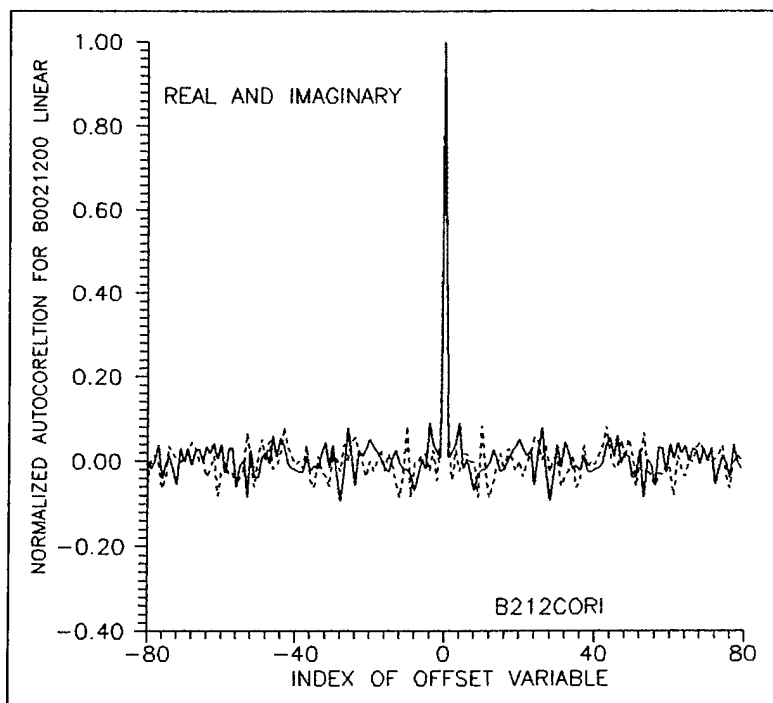


Figure 3.2. Normalized autocorrelation of the drive variables $u(n,i)$ (real) and $v(n,i)$ (imaginary) normally generated, but before rescaling. Both phase-quadrature components essentially have no autocorrelation except for the central spike. These data are based on the same drive generation as Figure 3.1 (f_{space} and f_{freq} both 1000, $\sigma_g = 0.01$, $\mu_g = 0$).

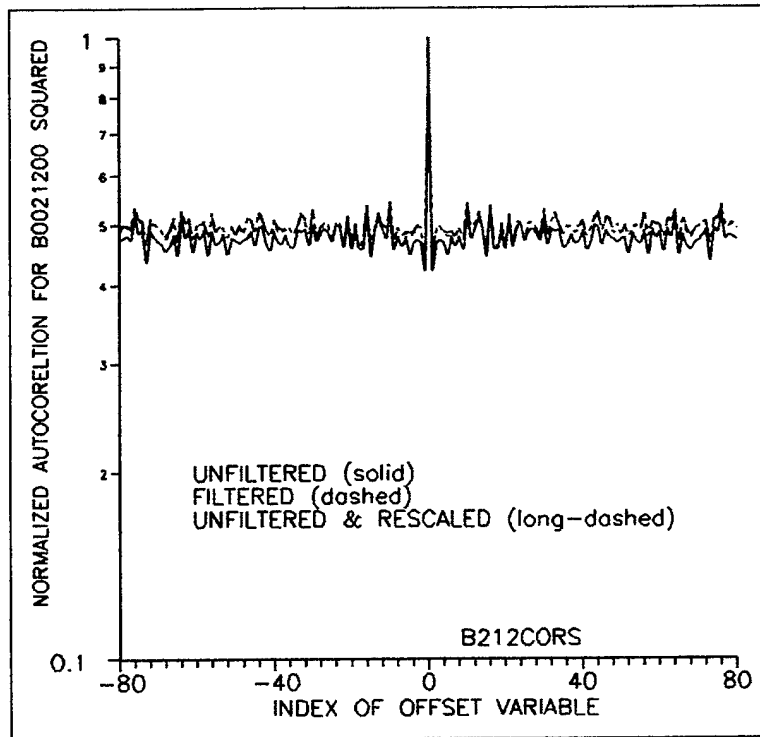


Figure 3.3. Normalized autocorrelation of the squared and summed drive based on a variable-frequency cut of the $z(n,i)$ ensemble matrix as defined in (2-18). Note that the data bear a nice resemblance to the observed EMPTAC experimental results (Figures 2.7- 2.9), except that the central peak is too narrow, as one would expect for parameters inducing unrealistically low autocorrelation (f_{space} and f_{freq} both 1000). These data are based on the same normal drive generation as Figure 3.1 ($\sigma_g = 0.01$, $\mu_g = 0.00$). Here, we see results for $z(n,i)$ based on unscaled $u(n,i)$ and $v(n,i)$ both before and after filtering, and for $z(n,i)$ based on u and rescaled but unfiltered.

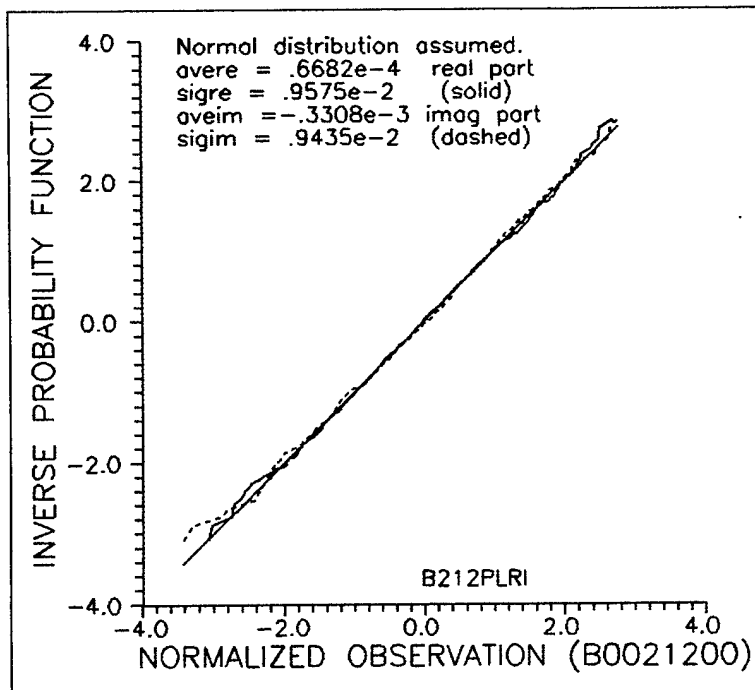


Figure 3.4. Probability plot for the assumption that the $u(n,i)$ and $v(n,i)$ ensembles are normally distributed before rescaling. This figure is based on f_{space} and f_{freq} both set to 1000, and $\sigma_g = 0.01$, $\mu_g = 0$. The agreement with a 45° line is excellent.

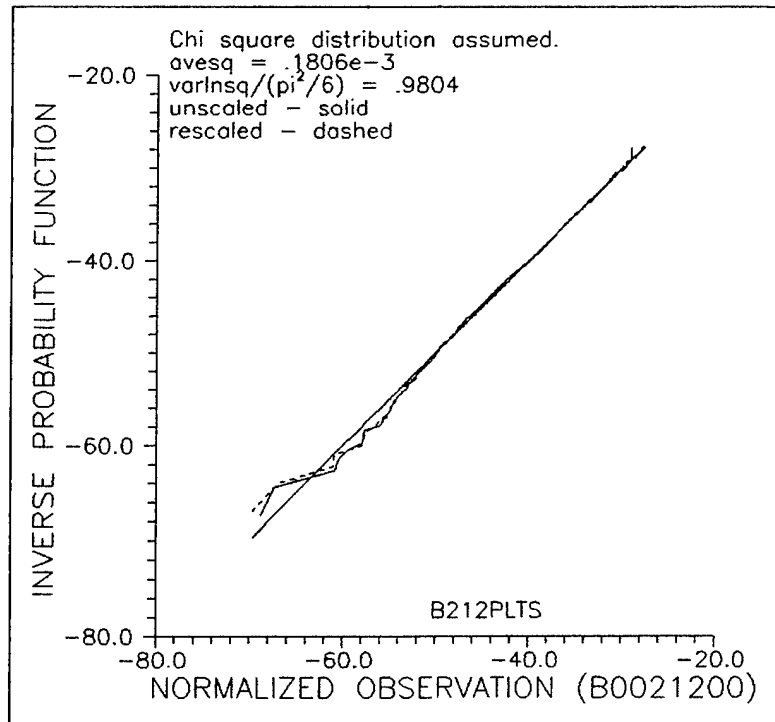


Figure 3.5. Probability plot for the assumption that the $z(n,i)$ ensemble has a chi square distribution, both before and after $u(n,i)$ and $v(n,i)$ are rescaled. This figure is based on f_{space} and f_{freq} both set to 1000, on $u(n,i)$ and $v(n,i)$ being normally generated, and on $\sigma_g = 0.01$, $\mu_g = 0$. Both plots are in nice coincidence with a 45° line.

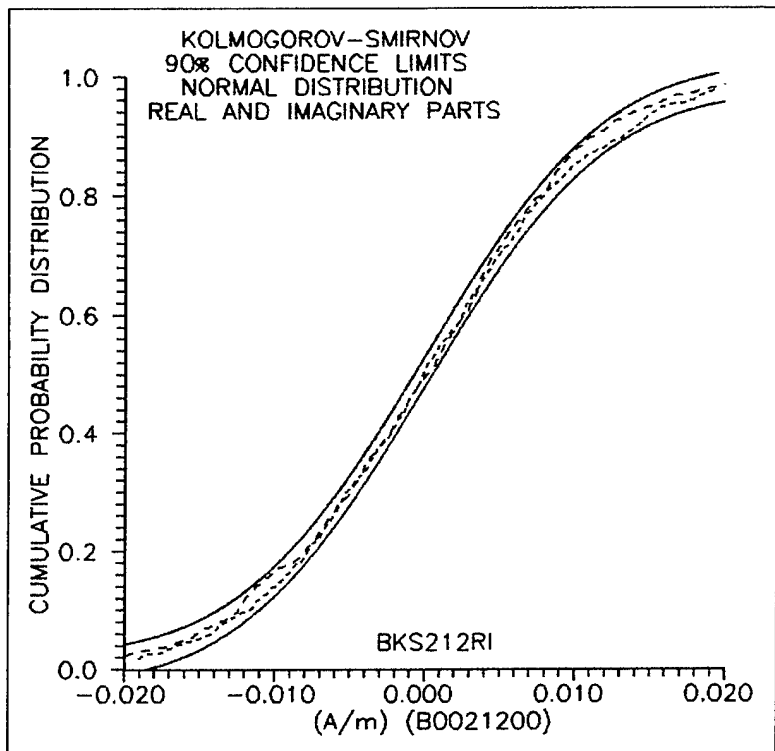


Figure 3.6. Both $u(n,i)$ and $v(n,i)$, even before rescaling, fall within the Kolmogorov-Smirnov 90% confidence limits for a normal distribution when they are normally generated with f_{space} and f_{freq} both 1000, and with $\sigma_g = 0.01$, $\mu_g = 0$.

parameters. Heretofore, we have not pinned the parameters for Kolmogorov-Smirnov testing. Figure 3.7 is an attempt to fit the squared and summed variable $z(n,i)$ to a pinned-parameter K-S test based on a chi square distribution. Even f_{space} and f_{freq} of 1000 distort the distribution enough to take the autocorrelated, unscaled array a little out of this confidence test, although the rescaled array is brought back inside the test limits. Figure 3.8 shows that the $z(n,i)$ ensemble cut with frequency n varying fits an unpinned chi square distribution test even if the results are unscaled.

Next, we shall reconsider the data and results assemblage presented in Figures 3.1-3.8, but with f_{space} and f_{freq} both set to 10 (which gives a fair approximation to the autocorrelation actually observed in the real world during EMPTAC testing). Figure 3.9 shows a 1D frequency-axis cut of the 2D $z(n,i) = u(n,i)^2 + v(n,i)^2$ ensemble generated in this manner. The normal random number generator for creating the u and v ensembles still uses a mean of 0 and a standard deviation of 0.01. Figure 3.9 shows both the unscaled and the rescaled results for $z(n,i)$ (with the unscaled plot reduced by 10^3 to separate the two plots). Note that the unscaled and the rescaled plots still track each other quite nicely. Perhaps more importantly, the subjective appearance of both curves is now reminiscent of the experimental results, Figure 3.5, with the spikes being primarily downward instead of being bipolar. This subjective impression is characteristic of functions with a chi square density distribution.

Figure 3.10 illustrates the autocorrelation functions obtained for variable-frequency cuts of the ensembles [$u(n,i)$ and $v(n,i)$] generated for (2-7) and (2-9). Note that these ensembles now have, as desired, a much broader central spike of autocorrelation than did Figure 3.2. These two curves are based on $u(n,i)$ and $v(n,i)$ not rescaled.

Figure 3.11 illustrates the autocorrelation result of squaring and adding the normally distributed variables, both with and without rescaling. This plot bears a very nice resemblance to the experimentally obtained cable current and magnetic field EMPTAC autocorrelation plots illustrated in Figures 2.7-2.9. Even the width of the central spike is reasonable.

Figure 3.12 presents a probability plot for the two unsquared variables $u(n,i)$ and $v(n,i)$ against a normal distribution function. These plots are no longer 45° lines; our correlated random number generator does not yield good normal distributions in the absence of rescaling when f_{space} and f_{freq} both set to 10.

Figure 3.13 is a probability plot for the unscaled and rescaled summed and squared variable [$z(n,i)$ of (2-18)] against a chi square distribution function. The unscaled distribution does not yield a 45° line, but the rescaled distribution satisfactorily brings the ensemble back to where it should be (without destroying the autocorrelation, as seen in Figure 3.11).

Figure 3.14 shows that the unscaled $u(n,i)$ and $v(n,i)$, based on f_{space} and f_{freq} set to 10, both have excursions outside the 90% Kolmogorov-Smirnov confidence limits. As we already know, these f values leave $u(n,i)$ and $v(n,i)$, before rescaling, with an unacceptable discrepancy from a normal distribution.

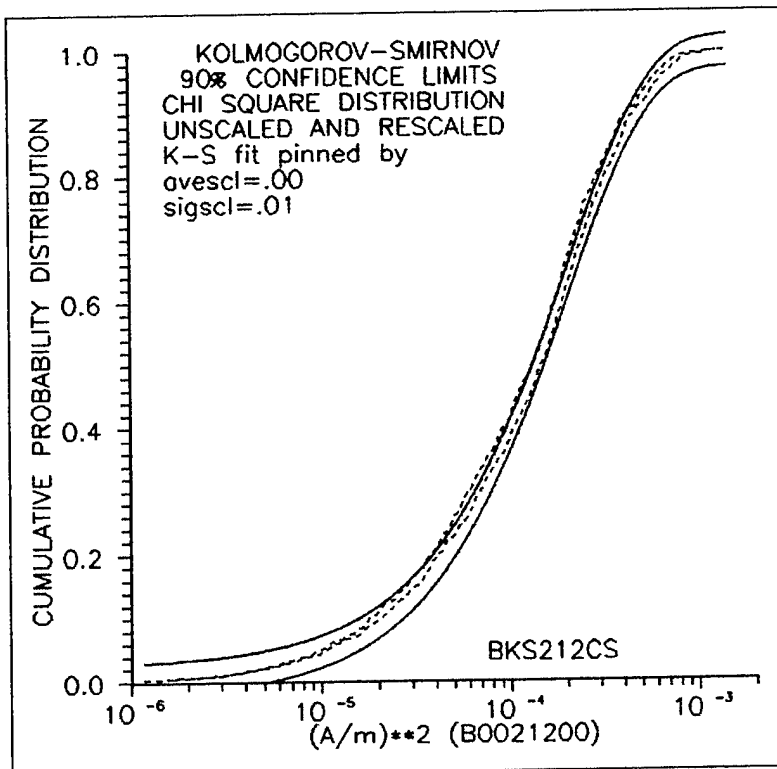


Figure 3.7. The summed and squared variable $z(n,i)$, before rescaling of normally generated $u(n,i)$ and $v(n,i)$ (with $\sigma_g = 0.01$, $\mu_g = 0.00$), does not quite fit the Kolmogorov-Smirnov 90% confidence limits for being chi square with a mean and standard deviation pinned at $\mu_c = 2\sigma_g^2 = 0.0002$, even for f_{space} and f_{freq} both 1000. Rescaling the distribution of $z(n,i)$ ($u(n,i)$ and $v(n,i)$) according to (3-3) does bring the $z(n,i)$ ensemble inside the confidence limits.

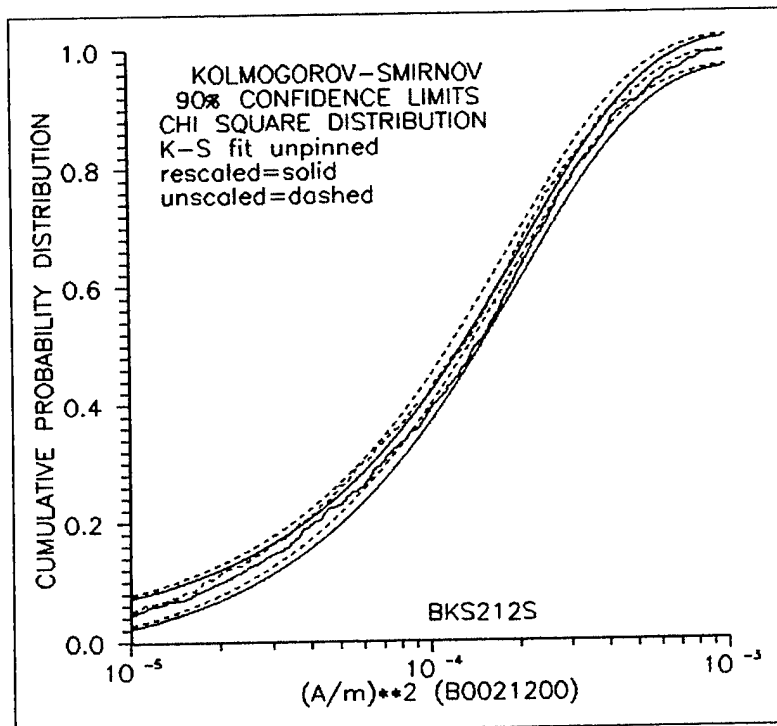


Figure 3.8. The unscaled and the rescaled $z(n,i)$ arrays (generated under the same parameters as in Figure 3.1) fall within the Kolmogorov-Smirnov 90% confidence limits for having a chi square distribution if the defining the confidence limits are determined from the data (as opposed to being pinned at $\mu_c = 0.0002$).

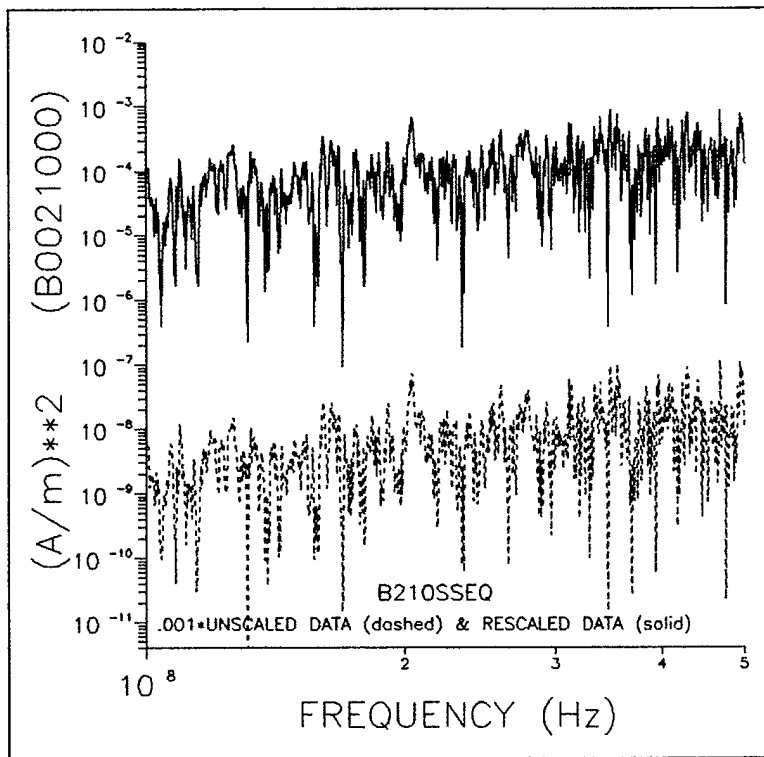


Figure 3.9. Plot of $z(n,i) = u(n,i)^2 + v(n,i)^2$ for each component (u and v) of the phase-quadrature drive generated according to (2-10), (2-14), and (2-15) (normal case) with f_{space} and f_{freq} both set to 10 (physically realistic autocorrelation). The lower plot is the raw ensemble ($\times 10^{-3}$), and the upper plot is the ensemble obtained with $u(n,i)$ and $v(n,i)$ rescaled according to (3-3). The normal distribution parameters are $\sigma_g = 0.01$ and $\mu_g = 0$. Note that the rescaled data and the raw data track each other fairly closely, and that both plots bear a subjective resemblance to the experimental data shown in Figure 3.5, with the spikes being monopolar downward.

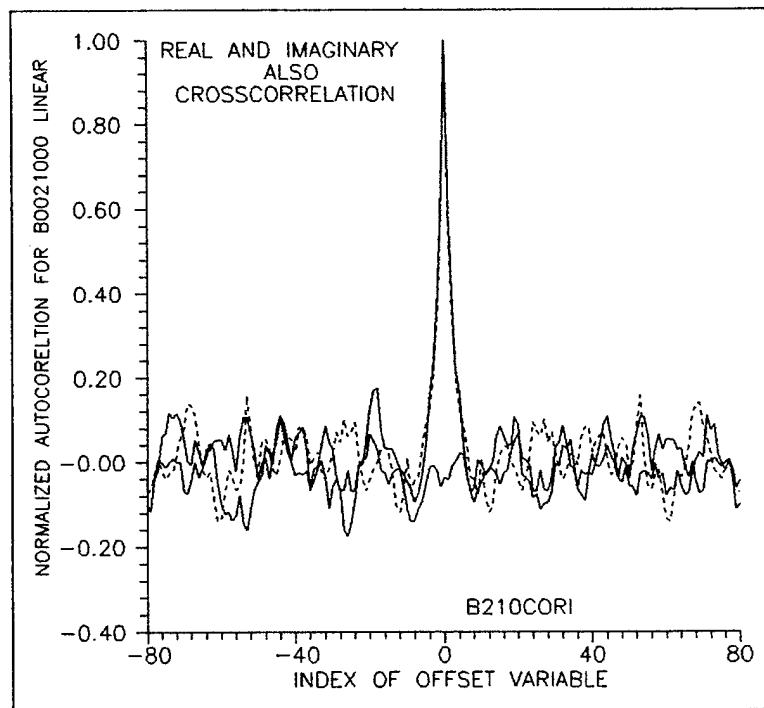


Figure 3.10. Normalized autocorrelation of the drive variables $u(n,i)$ (real) and $v(n,i)$ (imaginary) before rescaling. Both phase-quadrature components essentially have no autocorrelation except for the central spike, which is broadened in comparison to Figure 3.2. These data are based on the same normal drive generation as Figure 3.9 (f_{space} and f_{freq} both 10, $\sigma_g = 0.01$ and $\mu_g = 0$).

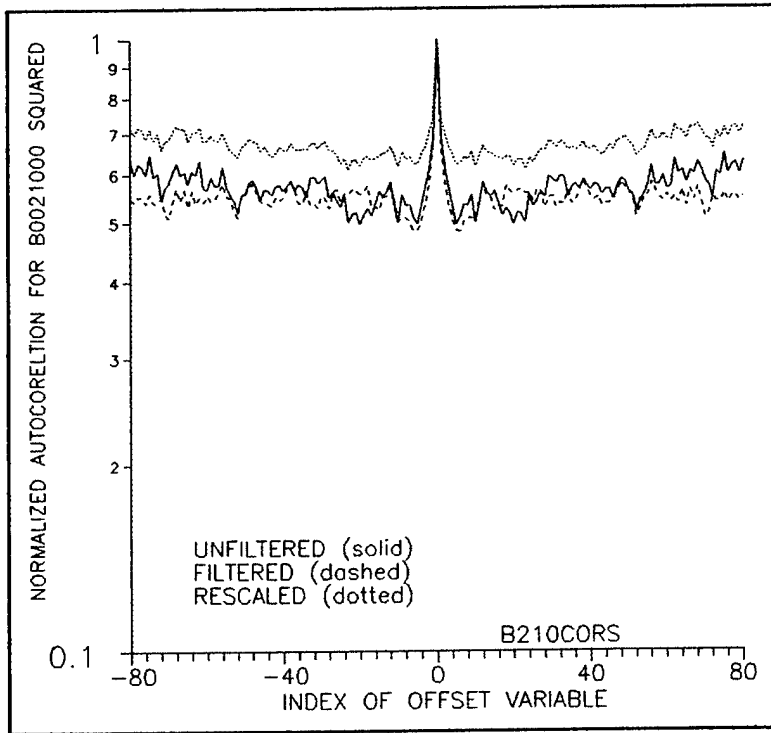


Figure 3.11. Normalized autocorrelation of the squared and summed drive based on a variable-frequency cut of the $z(n,i)$ ensemble as defined in (2-18). Note that the data bear a nice resemblance to the observed EMPTAC experimental results (Figures 2.7-2.9), including a realistic breadth of the central peak. This is what one would expect for parameters inducing a realistic autocorrelation (f_{space} and f_{freq} both 10). Here, we see results for $z(n,i)$ based on normally generated, unscaled $u(n,i)$ and $v(n,i)$ both before and after filtering, and for $z(n,i)$ based on $u(n,i)$ and $v(n,i)$ rescaled but unfiltered.

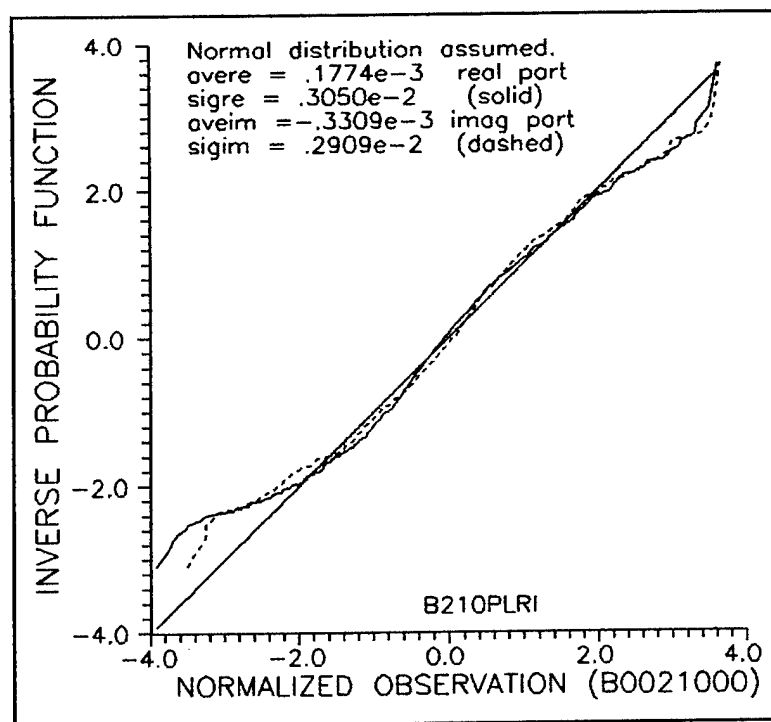


Figure 3.12. Probability plot for the assumption that the normally generated $u(n,i)$ and $v(n,i)$ ensembles are normally distributed before and after introduction of autocorrelation, but before rescaling. This figure is based on f_{space} and f_{freq} both set to 10, with $\sigma_g = 0.01$, $\mu_g = 0$. The agreement with a 45° line is not good; the algorithm for introducing autocorrelation [(2-14) and (2-15)] distorts the normal distribution of the random number generator.

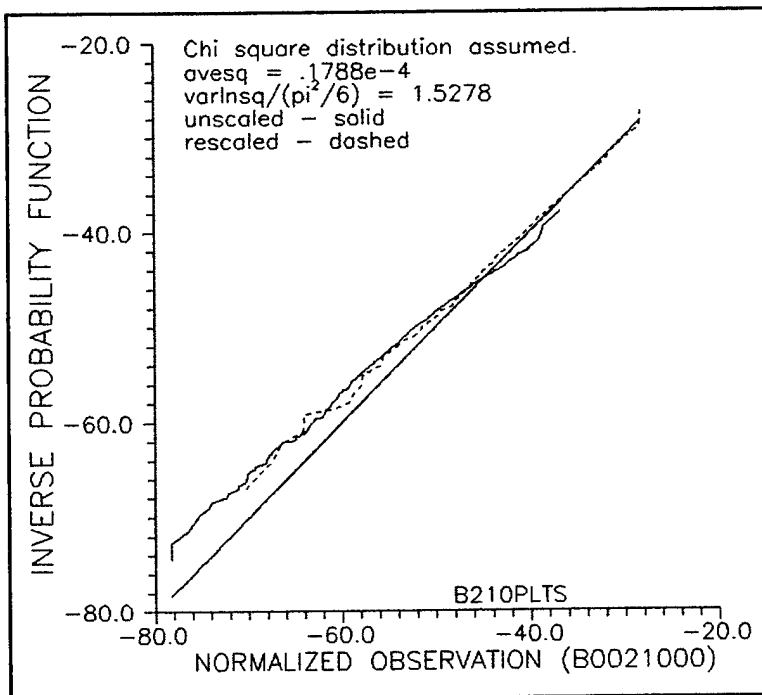


Figure 3.13. Probability plot for the assumption that the $z(n,i)$ ensemble has a chi square distribution, both before and after $u(n,i)$ and $v(n,i)$ are normally rescaled. This figure is based on f_{space} and f_{freq} both set to 10, with $\sigma_g = 0.01$, $\mu_g = 0$. Before rescaling, but after forcing of autocorrelation, agreement with a chi square distribution is not indicated. The rescaled plot is in fair coincidence with a 45° line.

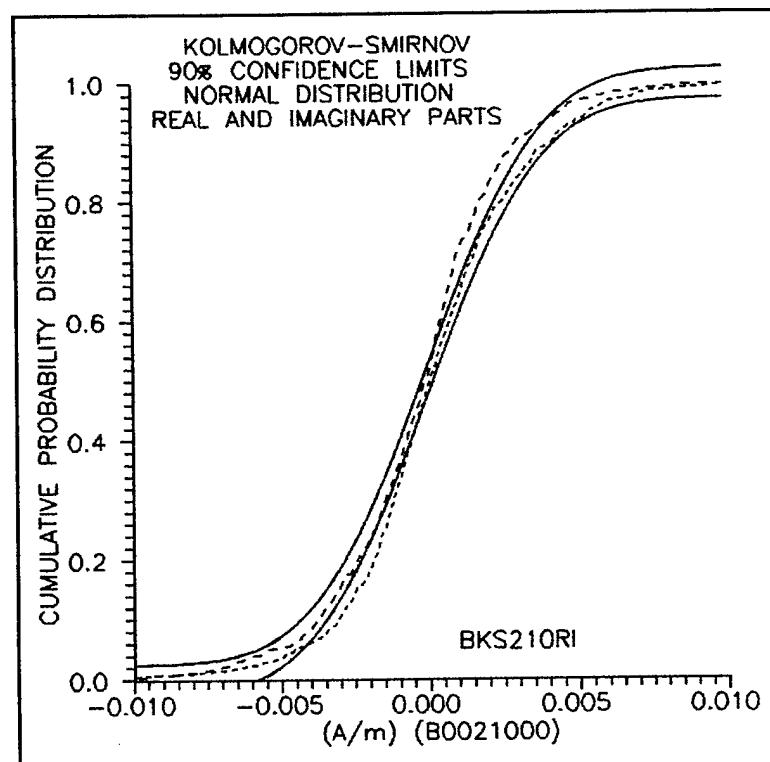


Figure 3.14. Neither $u(n,i)$ nor $v(n,i)$, after forcing autocorrelation, but before rescaling, fall within the Kolmogorov-Smirnov 90% confidence limits for a normal distribution when they are generated with f_{space} and f_{freq} both 10, and with $\sigma_g = 0.01$, $\mu_g = 0$.

Figure 3.15 illustrates that the generation of $u(n,i)$ and $v(n,i)$, without rescaling and with f_{space} and f_{freq} set to 10, yields a radically unacceptable match of $z(n,i) = u(n,i)^2 + v(n,i)^2$ to the Kolmogorov-Smirnov 90% confidence limits for a chi square distribution based on the mean of $u(n,i)$ and $v(n,i)$ pinned to 0 and the standard deviation pinned to 0.01 (i.e., μ_c pinned to 0.0002). Rescaling the ensemble according to (3-3) does not quite bring it into the 90% K-S confidence limit, although the improvement is so dramatic that we are inclined to ignore a minor excursion. Figure 3.16 indicates that the z ensemble with frequency varying, and f_{space} and f_{freq} set to 10 does not even fit an unpinned chi square 90% K-S confidence test. For the distribution not rescaled, the excursion is major; after rescaling, the excursion is very minor.

THE CABLE DRIVE ALGORITHM

An attempt was made to match the output of a model consisting of a network of segmented cables with the response experimentally observed on cables at the EMPTAC. The model allows the network to be driven by arbitrary fields at each segment. It yields current or voltage at any place on the cable which may be directly compared to the measurements made by a network analyzer. The network model is composed of up to 200 10 cm transmission-line segments. Actual computations are performed in the frequency domain. Defining equations employ continuity of the current and voltage at each junction and end conditions relating the current and voltage through a terminating impedance.

The line response and drivers are coherent over space and frequency at low frequencies. To mimic the random behavior seen in the EMPTAC data, the excitation over the segments and from one frequency to the next becomes less coherent at intermediate and higher frequencies. At the highest frequencies, the segment drives are nearly random with respect to each other. To achieve this effect, each segment is driven with a field of the form given in (2-7).

The amplitudes of the sine and cosine terms can be determined from an arbitrary distribution; however, as discussed previously, normal distributions with zero mean μ_g represent $A(n,i)$ and $B(n,i)$ of (2-7) in the most physically realistic manner. The distribution of $u(n,i)$ as applied in (2-9) is the inverse of the normal distribution and contains parameters to force a frequency- and location-dependent coherence at lower frequencies as described by (2-14) and (2-15). In the high-frequency limit, there is little spatial or frequency relation between the amplitudes, and each is determined solely by the chosen random distribution.

The f_{space} and Δl parameters in (2-14) are used to give a frequency-dependent correlation between the $u(n,i)$ values at different drive points. Whenever the wavelength is large compared to the cable segments, the $u(n,i)$ parameter is close to that used at the previous drive point. Similarly, varying f_{space} between 0 and infinity allows the $u(n,i)$ to vary from exactly that used at the previous segment to a totally random value.

The f_{freq} and $\lambda^2/(L\Delta\lambda)$ parameters appearing in (2-15) are used to give a frequency-dependent correlation between the $u(n,i)$ values at different frequencies. Whenever the

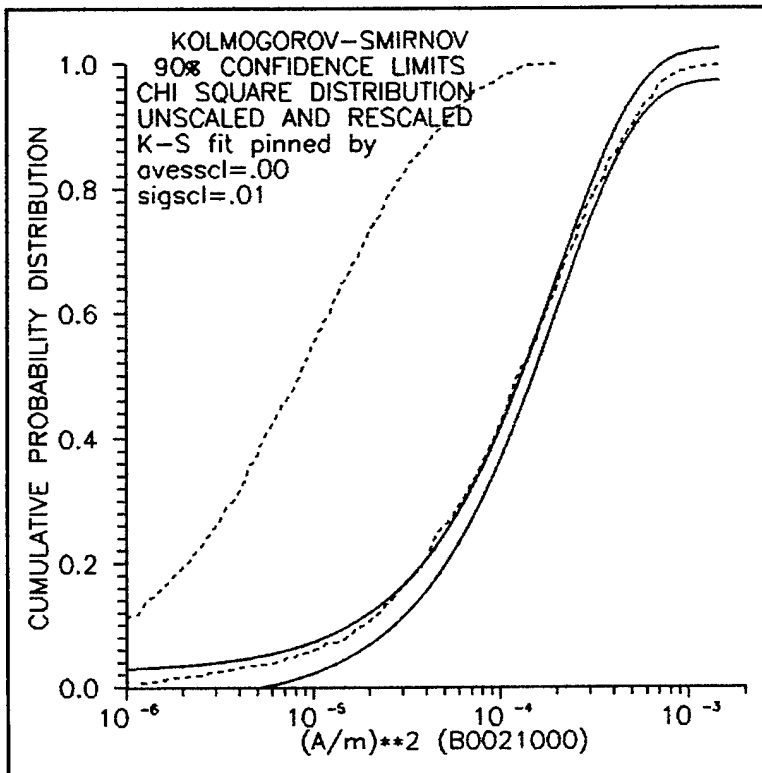


Figure 3.15. The summed and squared variable $z(n,i)$, before normal rescaling of $u(n,i)$ and $v(n,i)$, is far out of range to the left of the Kolmogorov-Smirnov 90% confidence limits for being chi square with the mean and standard deviation pinned at $\mu_c = 2\sigma_g^2 = .0002$, when f_{space} and f_{freq} are set to 10, with $\sigma_g = 0.01$, $\mu_g = 0$. Rescaling the distribution of $z(n,i)$ ($u(n,i)$ and $v(n,i)$) according to (3-3) almost brings the $z(n,i)$ ensemble inside the chi square confidence limits.

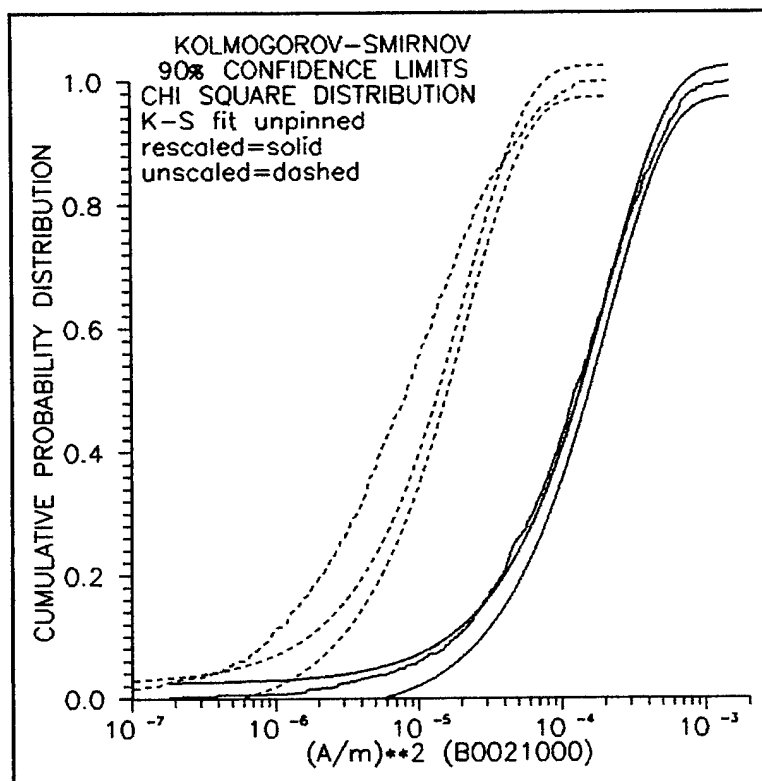


Figure 3.16. The unscaled $z(n,i)$ array, based on normal $u(n,i)$ and $v(n,i)$ with f_{space} and f_{freq} set to 10, and $\sigma_g = 0.01$, $\mu_g = 0.00$, deviates in a major way from the 90% K-S test for being chi square, even when μ_c is unpinned, and allowed to float to fit the data (left curves). The rescaled $z(n,i)$ array also deviates from the Kolmogorov-Smirnov 90% confidence limits for having a chi square distribution, although by a much smaller amount (right curves).

wavelength is large compared to the linear dimension of the network or when the wavelength is large compared to the change in the wavelength, the $u(n,i)$ parameter is close to that used at the previous frequency. Similarly, varying f_{freq} between 0 and ∞ allows the $u(n,i)$ to vary from exactly that used at the previous frequency to a totally random value resulting from frequency-incoherence.

The solution of the telegrapher's equations

$$\begin{aligned}\frac{dV}{dx} &= -ZI + Ee^{\alpha x} \\ \frac{dI}{dx} &= -YV\end{aligned}\tag{3-4}$$

where

$$\alpha = j \mathbf{k} \cdot \mathbf{r} \tag{3-5}$$

can be found on each segment to give

$$\begin{aligned}I &= ae^{\gamma x} + be^{-\gamma x} - \frac{YE}{\alpha^2 - \gamma^2} e^{\alpha(x + x_n)} \\ V &= -Z_c (ae^{\gamma x} - be^{-\gamma x}) + \frac{\alpha E}{\alpha - \gamma^2} e^{\alpha(x + x_n)}\end{aligned}\tag{3-6}$$

$$\gamma = \sqrt{ZY} \quad Z_c = \sqrt{\frac{Z}{Y}}$$

where E is the component of the random field parallel to the line, x is the position along the segment and x_n is the location of the center of the Segment n . (This result, and its implied assumptions are discussed in more detail in the Section 8.)

The form of the cable drive in (2-7) allows the transform of the response into the time domain to be done analytically. This is done using a driver for each segment which is made of a random part multiplying a sine or cosine term. Since only the random part is unique to each

segment, the sine and cosine terms may be divided out of the overall driving term. After the inversion is made to find the a and b homogeneous-solution coefficients (3-6) of the transmission-line response, the effects of the common sine and cosine terms may be restored in the analytical transform.

Employing equations for the continuity of the current and voltage at the intersections of the segments and a relationship between the voltage, current, and termination impedance at each end, the unknown a and b coefficients in (3-6) can be found as a solution of a set of simultaneous equations (one set for each frequency n),

$$[M]_n [x]_n = [d]_n \quad (3-7)$$

where $[M]_n$ is a matrix, $[x]_n$ is a vector containing the unknown terms, and $[d]_n$, with the sine and cosine terms, is a vector of the form

$$[d]_n = [d_{sin}]_n \mathcal{F}[\cos(\omega_n t)] + [d_{cos}]_n \mathcal{F}[\cos(\omega_n t)] \quad (3-8)$$

where the \mathcal{F} operator indicates a Fourier transform. The sine and cosine terms each have a pair of poles in the frequency domain,

$$\mathcal{F}[\sin(\omega_n t)] = \frac{\omega_n}{(s + j\omega_n)(s - j\omega_n)} \quad \mathcal{F}[\cos(\omega_n t)] = \frac{s}{(s + j\omega_n)(s - j\omega_n)} \quad (3-9)$$

which allow the analytic transformation into the time domain to be made. The solution of (3-8) to determine the unknown a and b coefficients of (3-6) required the development of a routine to invert a matrix with alternating, quaddiagonal entries. Using a procedure similar to the inversion of a tridiagonal matrix, the routine first solves forward in the matrix to find the last unknown and then solves backwards to find the others.

The code output to be compared to the network analyzer data from the EMPTAC test requires an analytic conversion of the results into the time domain. The test equipment measures magnitude and phase of a frequency component only; it does not find a quantity/Hz form which results from a frequency-domain analysis. The conversion to the time domain assumes that the only poles not at the origin of the complex plane were introduced by the driver at $s = \pm j\omega_n$. This form is assured by including loss terms in the transmission-line parameters. The magnitude and phase of the frequency component are now found from

$$I(t)_n = \frac{e^{at}}{2\pi j} \int_{a-j\infty}^{a+j\infty} T(s) \left(\frac{C_{sin}(s)_n \omega_n}{(s + j\omega_n)(s - j\omega_n)} + \frac{C_{cos}(s)_n s}{(s + j\omega_n)(s - j\omega_n)} \right) e^{st} ds \quad (3-10)$$

where C_{sin} and C_{cos} are the coefficients (different for each n) of the sine and cosine terms resulting from the inversion of the matrix and $T(s)$ is the impulse response of the transmission line. This

form gives a time-domain solution as a function of the symmetric and antisymmetric parts of

$$C(t)_n = S [C_{sin}(j\omega_n)T(j\omega_n)] \sin(\omega_n t) + S [C_{cos}(j\omega_n)T(j\omega_n)] \cos(\omega_n t) + \\ -jA [C_{sin}(j\omega_n)T(j\omega_n)] \cos(\omega_n t) + jA [C_{cos}(j\omega_n)T(j\omega_n)] \sin(\omega_n t) \quad (3-11)$$

Since the time-domain solution must be real, the real part is symmetric and the imaginary part is antisymmetric giving

$$C(t)_n = \text{Re} [C_{sin}(-j\omega_n)T(-j\omega_n)] \sin(\omega_n t) + \text{Re} [C_{cos}(-j\omega_n)T(-j\omega_n)] \cos(\omega_n t) \\ -\text{Im} [C_{sin}(-j\omega_n)T(-j\omega_n)] \cos(\omega_n t) + \text{Im} [C_{cos}(-j\omega_n)T(-j\omega_n)] \sin(\omega_n t) \quad (3-12)$$

The pole at the origin introduced by the transmission line is ignored since it has only a dc component and will not be detected by the network analyzer.

A test of the code using EMPTAC data was made by forming a driver from the measured magnetic field and comparing the current it induced with a measured cable current. The comparison was made with the 20 m axial cable running near the skin of the EMPTAC and supported through holes in the aircraft ribs. The statistically modeled magnetic field was described by its fitted log normal average and standard deviation and evaluated as discussed in the Probability Plots part of the preceding section. Magnitude of the associated driving electric field was given by

$$E = 2\mu_0 s_n H h \quad (3-13)$$

where H is the magnetic field, s_n is the Laplace transform variable, μ_0 is the permeability of free space, and the value of E has been doubled for the reflection of the magnetic field. As the height above the ground plane becomes large compared to a wavelength, the field is of the form

$$E = Z_0 H \quad (3-14)$$

where Z_0 is the characteristic impedance of free space. The field modified by the presence of the ground plane can be represented as a linear combination of the two limiting cases,

$$E = \left[\frac{Z_0 \xi_n + 2\mu_0 s_n h}{\xi_n + 1} \right] H \quad (3-15)$$

where

$$\xi_n = \left(\frac{4\pi h}{\lambda_n} \right)^2 \quad (3-16)$$

The f_{freq} and f_{space} variables were set to vary from 1 (high correlation in space and frequency) to 1000 (almost no correlation). The current calculated by the code was described by its average and standard deviation and compared with the EMPTAC data. For a cable loss of 1 mΩ/m, a cable height of 5 cm, and 30 Ω termination impedances, the results for the current at the cable center (bottom entry) and at the end (top entry) of the line for various f_{space} and f_{freq} autocorrelation parameters are shown in Table 1. Cable loss and height over ground in this simulation were selected to represent actual EMPTAC cable parameters. The termination impedance was selected to match what we estimated the actual characteristic impedance of the EMPTAC cable to be. For the simplest representation of the telegrapher's equations (which were used for all computations reported in this section), the inductance per unit length L was entered as 10 μH/m, and a corresponding capacitance per unit length C was selected to yield a propagation velocity c_0 . It can be seen that the best comparison in the experimental data occurs when the spatial and frequency correlations are both somewhat greater than 10.

Table 1. Comparison of code and EMPTAC cable current results.

f_s	μ of $ I ^2$	σ of $ I ^2$	μ of $\ln I ^2$	σ of $\ln I ^2$
Data	9×10^{-5}	1×10^{-4}	-9.7	1.1
1	4.3×10^{-6}	5.3×10^{-6}	-13.0	1.2
	5.7×10^{-6}	5.4×10^{-6}	-12.5	1.1
10	4.9×10^{-5}	8.4×10^{-5}	-10.8	1.3
	5.8×10^{-5}	8.1×10^{-5}	-10.5	1.3
100	1.3×10^{-4}	2.4×10^{-4}	-9.8	1.3
	1.4×10^{-4}	1.9×10^{-4}	-9.5	1.3
1000	1.6×10^{-4}	2.5×10^{-4}	-9.5	1.3
	1.8×10^{-4}	2.4×10^{-4}	-9.2	1.2

FINE TUNING THE CABLE RESPONSES

The above results give the impression that rescaling pretty well fixes the magnetic field $u(n,i)$ and $v(n,i)$ magnetic-field cable-driver matrix ensembles. Consequently, we next examined the real and imaginary distributions of the phase-quadrature components of the simulated EMPTAC cable currents. Figure 3.17 shows that the simulated cable current quadrature

components do not fit a normal probability plot. Figure 3.18 is a Kolmogorov-Smirnov 90% confidence test of the cable power distribution (after filtering to remove the trend). As anticipated from Figure 3.17, the cable power distribution does not pass the Kolmogorov-Smirnov test for being chi square, even after being passed through a trend-removing filter. Figure 3.19 shows, however, that the unfiltered cable power simulation is excellently matched by a log normal distribution.

At this point, we considered the fact that we had not introduced any mechanism to put the cable current into thermodynamic equilibrium with the electromagnetic environment. To accomplish this, we computed the radiation resistance per unit length of a cable with centerline h (of 5 cm) over a ground plane and diameter small compared to a wavelength: the magnetic vector potential in the far field for a wire carrying a current I this configuration is

$$A = \frac{\mu_0 e^{-j\pi/4}}{2} \sqrt{\frac{2}{\pi kr}} I \sin(ka \cos \phi) i_z \quad (3-17)$$

The associated Poynting vector is

$$S = \frac{1}{2} \mathbf{E} \times \mathbf{H}^* = \frac{\mu_0 \omega}{2\pi r} \cdot |I|^2 \cdot \left(\frac{1 - \cos(2ka \cos \phi)}{2} \right) i_r \quad (3-18)$$

which, upon integration over ϕ from 0 to π , yields the desired radiation resistance per unit length formula

$$R = \mu_0 \omega \frac{[1 - J_0(2kh)]}{4} \approx \frac{\mu_0 \omega}{4} (kh)^2 = \mu_0 \omega \pi^2 \left(\frac{h}{\lambda} \right)^2 \quad (3-19)$$

The EMPTAC tests we are trying to match were performed with frequency swept from 100 MHz to 1 GHz. At 317 ($= [100 \cdot 1000]^{1/2}$) MHz, the above formula leads to a radiation resistance of 120 Ω/m . Consequently, this resistance was next inserted in our cable model. [Part of the justification for doing this was the knowledge that an actual cable at some fixed observation point only responds (correlates) to the driving field over a range of a wavelength or two.] Figure 3.20 shows a considerable improvement for the resulting cable current quadrature components matching a normal distribution (compare with Figure 3.17). Also, the cable power distribution with trend removed is now closer to being chi square (compare Figure 3.21 with Figure 3.18), although it still leaves much to be desired. The unfiltered cable power distribution does still look much more log normal than chi square, however (see Figure 3.22).

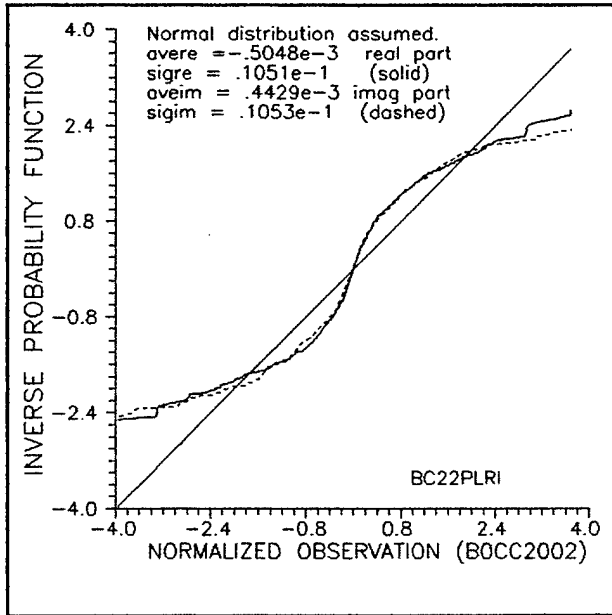


Figure 3.17. The phase-quadrature cable currents, resulting from autocorrelated and rescaled drive, do not fit a normal probability plot. This figure is based on normal $u(n,i)$ and $v(n,i)$ with f_{space} and f_{freq} set to 10, and $\sigma_g = 0.01$, $\mu_g = 0$.

Figure 3.18. The cable power distribution produced by rescaled cable drive does not fit a Kolmogorov-Smirnov test for being chi square, even after filtering. This figure is based on normal u and v with f_{space} and f_{freq} set to 10, and $\sigma_g = 0.01$, $\mu_g = 0$.

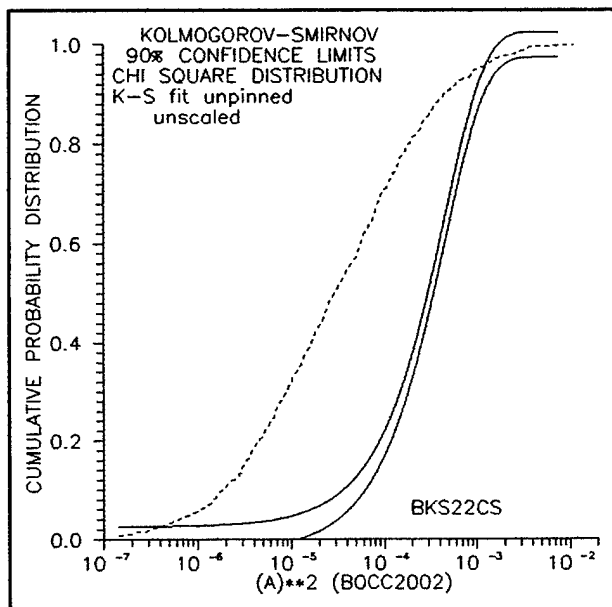
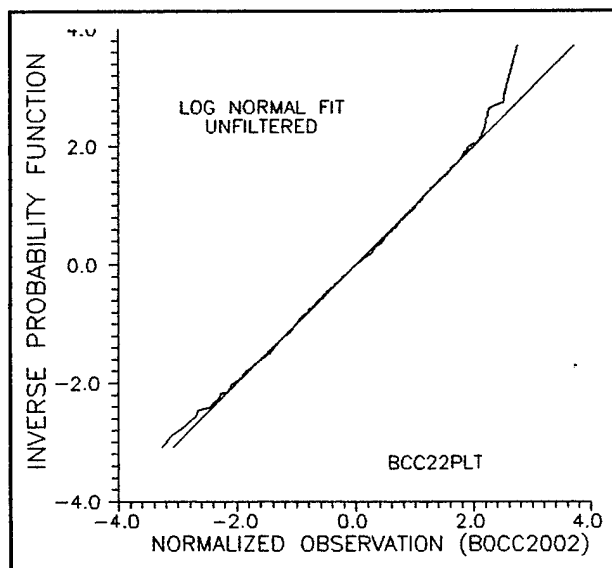


Figure 3.19. The unfiltered cable power distribution, based on rescaled cable drive, has an excellent match to a log normal probability plot. This figure is based on normal $u(n,i)$ and $v(n,i)$ with f_{space} and f_{freq} set to 10, and $\sigma_g = 0.01$, $\mu_g = 0$.

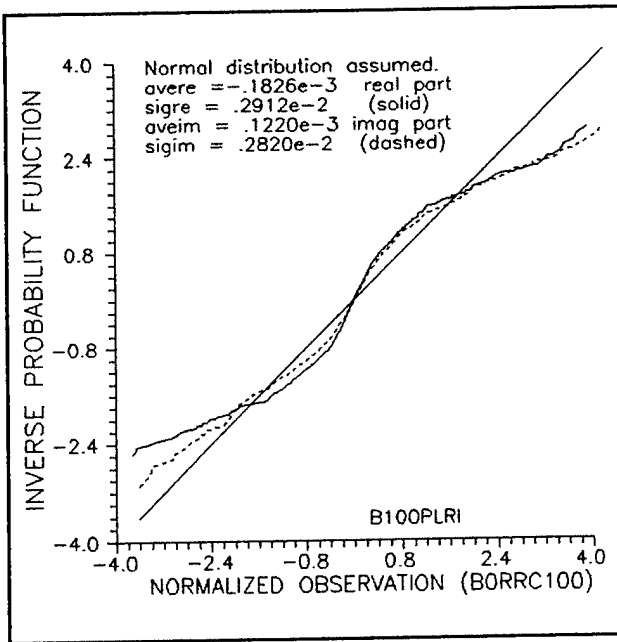


Figure 3.20. Addition of radiation resistance makes the phase-quadrature cable current components more nearly normally distributed. This figure is based on normal $u(n,i)$ and $v(n,i)$ with f_{space} and f_{freq} set to 10, and $\sigma_g = 0.01$, $\mu_g = 0$.

Figure 3.21. Introduction of radiation resistance brings the filtered cable power distribution closer to a chi square distribution. This figure is based on normal $u(n,i)$ and $v(n,i)$ with f_{space} and f_{freq} set to 10, and $\sigma_g = 0.01$, $\mu_g = 0$.

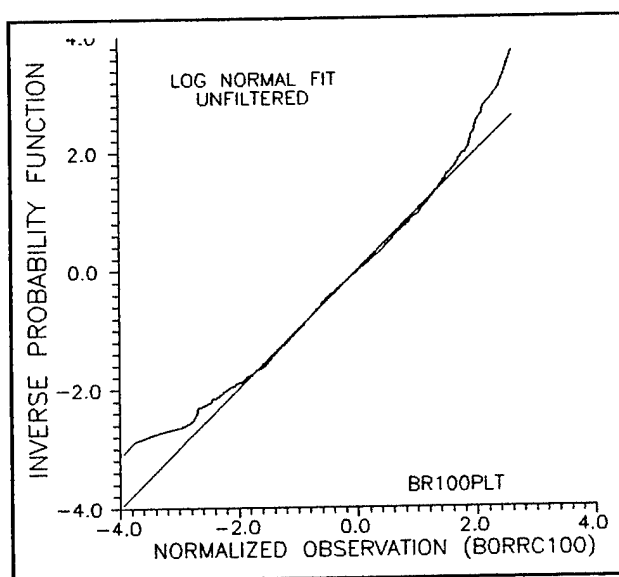
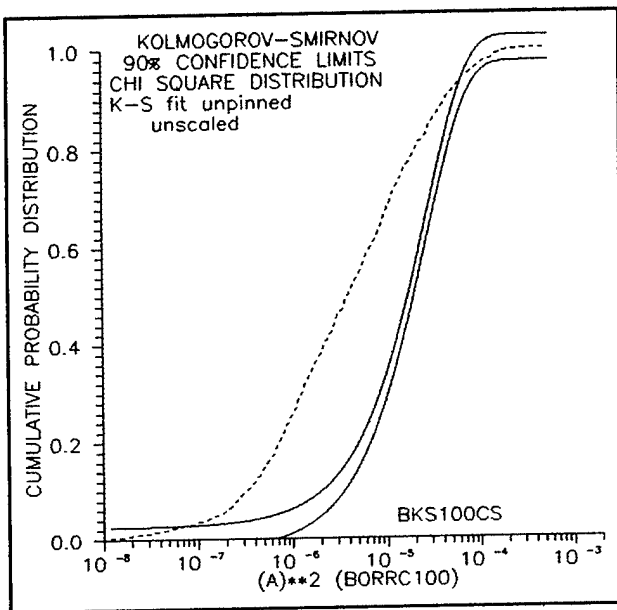


Figure 3.22. Introduction of radiation resistance leaves the unfiltered cable power distribution very nearly log normal. This figure is based on normal $u(n,i)$ and $v(n,i)$ with f_{space} and f_{freq} set to 10, and $\sigma_g = 0.01$, $\mu_g = 0$.

After all the above procedures had been carried out, a tendency (trend) for the cable drive amplitude, and resulting cable current amplitude to grow with frequency was still present. This trend was eventually traced back to the cable drive-field generation (2-9), (2-10), (2-14), and (2-15). We observed that if the drive-field advance equations were made over constant frequency increments [Δf , $\lambda^2/(L\Delta\lambda)$ constant], (2-15) could not contribute to this drive amplitude shifting: Previously, we had always used an exponentially expanding Δf . Making Δf constant implies that the relative proportions of old and new values, i.e., the effective f_{freq} , cannot change during the generation of the drive-field ensembles, although at the end of this section, we shall demonstrate that this modification is not materially significant.

A similar procedure cannot reasonably be applied to the equation which advances the drive-field along the position axis, as keeping $(\lambda/\Delta l)$ constant requires using a different cable segmenting scheme (different Δl) at every frequency.

Use of the (2-14)-(2-15) scheme where cable drive field is first advanced in the space direction results in the contamination of the subsequent frequency-directed drive advancement as well. Consequently, we reversed the order of the frequency and space cable-drive advancement so the frequency advancement, at least, could be kept pure of changing f_{space} effects. Also, we changed these equations to make drive-field advancement occur in $R(n,i)$ space [varying from 1 to I in (2-10)], not $u(n,i)$ and $v(n,i)$ space. In other words, (2-10) is now used to find the $u(n,i)$ and $v(n,i)$ ensembles after the $R(n,i)$ ensembles have been generated. Thus, the equations for creating $R(n,i)$ ensembles now become

$$R_{freq}(n,i) = \frac{\frac{c\Delta f}{L}R(n-1,i) + f_{freq}R(n,i)}{\frac{c\Delta f}{L} + f_{freq}} \quad (3-20)$$

and

$$R_{space}(n,i) = \frac{\frac{\lambda_n}{\Delta l}R(n,i-1) + f_{space}R_{freq}(n,i)}{\frac{\lambda_n}{\Delta l} + f_{space}} \quad (3-21)$$

with (2-10) subsequently applied to $R_{space}(n,i)$ to find the $u(n,i)$ and $v(n,i)$. [Wherever one needs access to an $R(n,1)$, it is seeded at $\frac{1}{2}$. Reversing the order of application of (2-10) and (2-14)-(2-15) is purely cosmetic, and does not change any actual values in the final rescaled drive.] Additionally, we now are very careful to create an entire 2D $R_{freq}(n,i)$ intermediate arrays, so there can be no possible ambiguity about where to find the definition of the look-back values $R(n,i-1)$ and $R(n-1,i)$.

These additional precautions lead to an even more improved (but still not perfect) approach of the $u(n,i)$ and $v(n,i)$ magnetic field ensembles to a normal distribution (compare the probability plots of Figure 3.23 with those of Figures 3.17 and 3.20). Also, the filtered cable power distribution now approaches chi square much more closely (compare Figure 3.24 with Figures 3.18 and 3.21). Also, the unfiltered cable power distribution finally begins to pull away from the ubiquitous log normal form (compare Figure 3.25 with Figures 3.19 and 3.22).

There is still some growth trend remaining on the $u(n,i)$ and $v(n,i)$ magnetic field ensembles as a function of frequency, even after all this correcting, however (see Figure 3.26). The last of this growth trend was removed by fitting the absolute magnitudes of the all the local extrema (all points with magnitudes of $u(n,i)$, $U_{ext}(n,i)$, which are both preceded and followed by points of lesser magnitude) to a least-squares linear fit: if $U_{ext}(n,i)$ is made to match

$$U_{ext}(n,i) = \alpha_i f_n + \beta_i \quad (3-22)$$

in a least-squares sense, one minimizes

$$S_i = \sum_{n \text{ at ext}} (U_{ext}(n,i) - \alpha_i f_n - \beta_i)^2 \quad (3-23)$$

and finds

$$\alpha_i = \frac{\sum_{n \text{ at ext}} (U_{ext}(n,i) - \bar{U}_{ext}(i))(f_n - \bar{f})}{\sum (f_n - \bar{f})^2} \quad (3-24)$$

$$\beta_i = \bar{U}_{ext}(i) - \alpha_i \bar{f}$$

In (3-22)-(3-24), note is made that $U_{ext}(n,i)$ does not exist at all n , only at n values of locally maximal $U_{ext}(n,i)$. Also, quantities with an overhead bar represent quantities averaged over n (frequency). One then pivots all the points in the ensemble about the center frequency f_c

$$(u(n,i)' - \bar{u}(i)) = (u(n,i) - \bar{u}(i)) \cdot (u_c(i)/u(n,i))$$

and obtains a new driver ensemble matrix $u(n,i)'$

$$u(n,i)' = \bar{u}(i) + \frac{(u(n,i) - \bar{u}(i))(\alpha_i f_c + \beta_i)}{\alpha_i f_n + \beta_i} \quad (3-26)$$

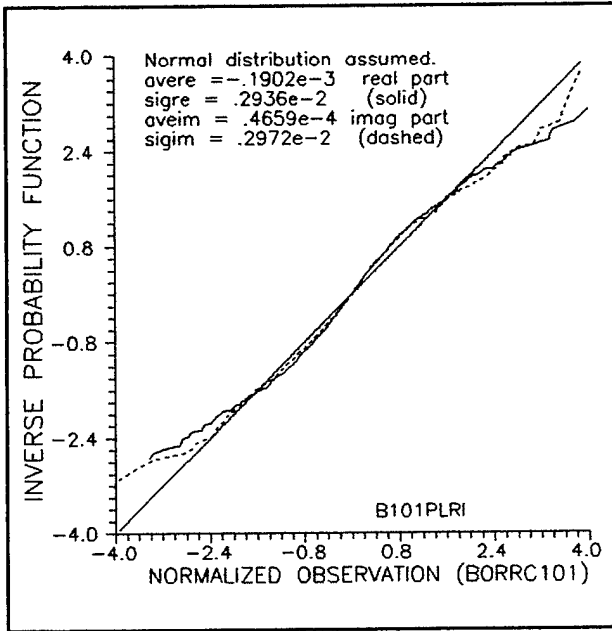


Figure 3.23. Constant Δf drive-field generation brings the phase-quadrature cable current distribution still more into agreement with a normal distribution. This figure is based on normal $u(n,i)$ and $v(n,i)$ with f_{space} and f_{freq} set to 10, and $\sigma_g = 0.01$, $\mu_g = 0$.

Figure 3.24. Constant Δf drive-field generation brings cable power distribution still closer to a chi square fit. This figure is based on normal $u(n,i)$ and $v(n,i)$ with f_{space} and f_{freq} set to 10, and $\sigma_g = 0.01$, $\mu_g = 0$.

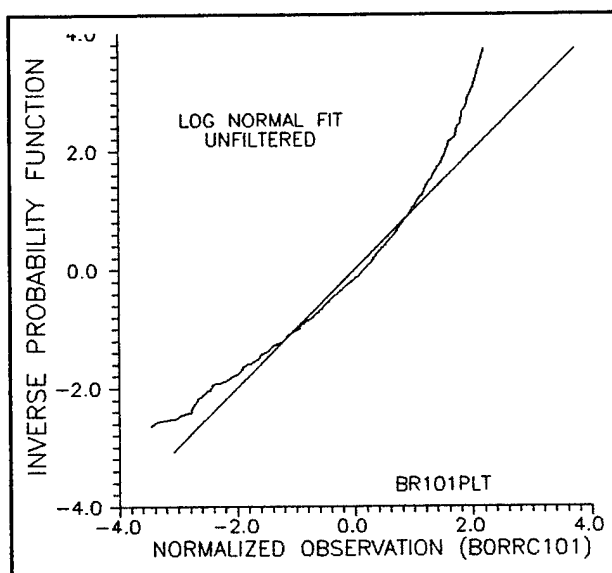
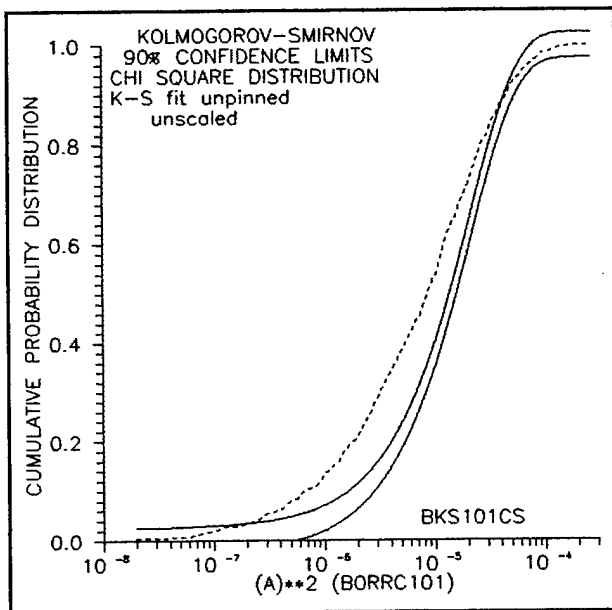


Figure 3.25. Constant Δf drive-field generation finally causes the cable power distribution to deviate from a log normal distribution. This figure is based on normal u and v with f_{space} and f_{freq} set to 10, and $\sigma_g = 0.01$, $\mu_g = 0.00$.

This forces the extremal points envelope to lie in a flat line with other points placed between them in appropriate ratios. In this way, we finally compelled $u(n,i)$ and $v(n,i)$ to come out trendless (see Figure 3.27). Upon applying the pivoted cable drivers to the cable model, we obtained cable quadrature currents with even better fits to the normal probability plots (see Figure 3.28). Also, the cable power distribution induced by the pivoted drivers comes still closer to passing a 90% Kolmogorov-Smirnov confidence test for being chi square (see Figure 3.29).

As a last exercise, we put a frequency dependence into the radiation resistance of the cable: (3-19) was modeled as

$$R_n = 120 \cdot [f_n(\text{MHz})/317]^3 \quad (3-27)$$

not just as $R = 100$ or 120 . The resulting cable current quadrature components now fit a normal probability plot still better (see Figure 3.30). The cable power distribution (see Figure 3.31) is now so close to passing the Kolmogorov-Smirnov 90% confidence test for being chi square that detecting the excursion almost strains the eyes.

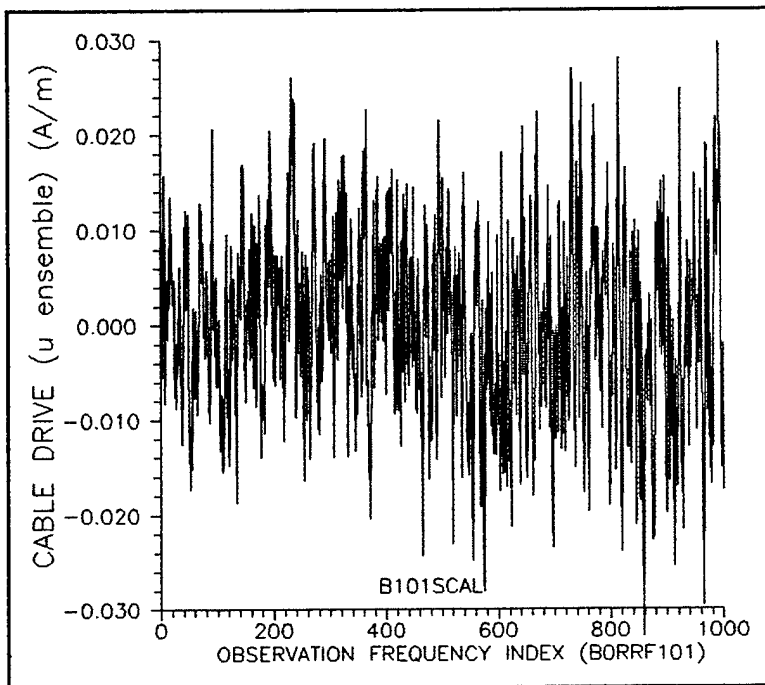


Figure 3.26. The amplitudes of the u ensemble members still have a growing trend as frequency increases, even with constant Δf . This figure is based on normal u and v with f_{space} and f_{freq} set to 10, and $\sigma_g = 0.01$, $\mu_g = 0.00$.

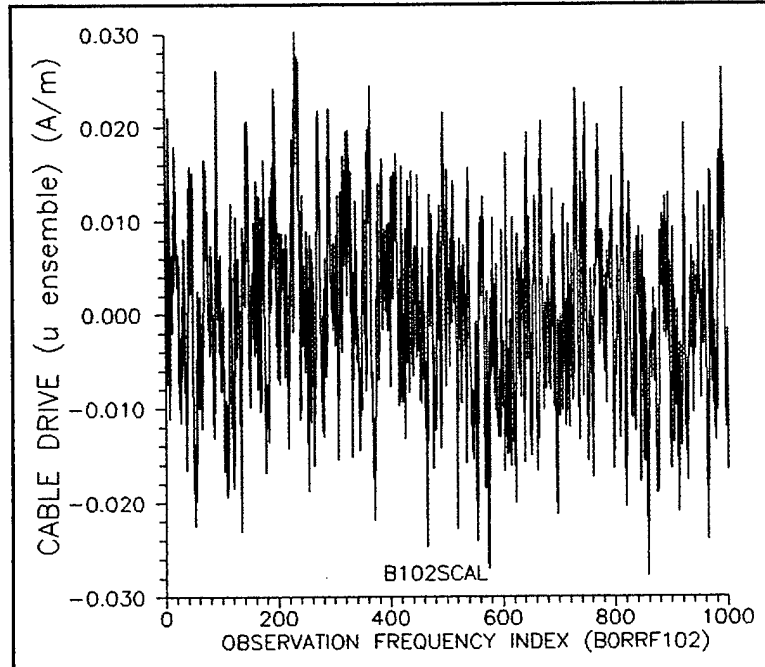


Figure 3.27. Pivoting ensemble envelopes about average values finally eliminates the cable drivers' growth trend. This figure is based on normal u with f_{space} and f_{freq} set to 10, and $\sigma_g = 0.01$, $\mu_g = 0.00$.

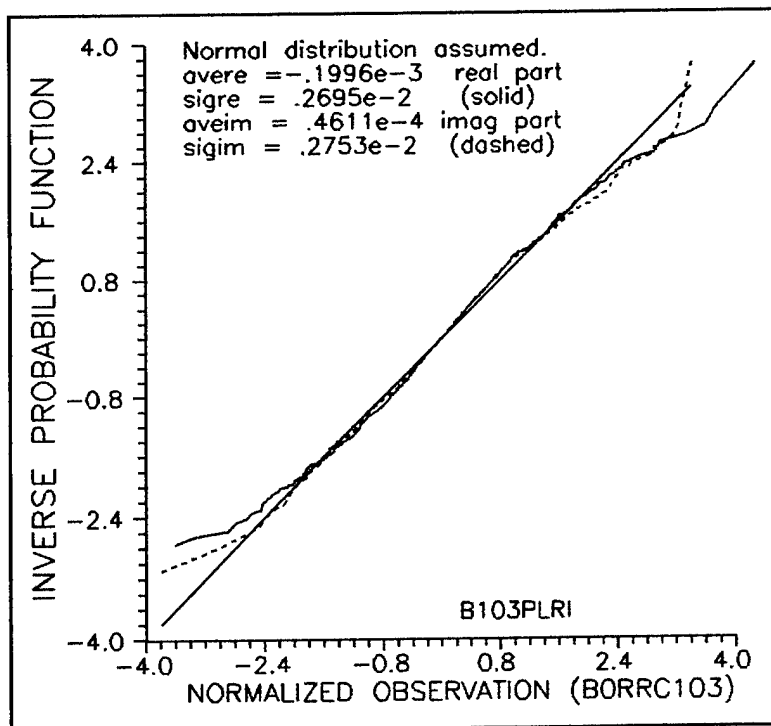


Figure 3.28. The pivoted cable current drivers yield a phase-quadrature cable current distribution which is still closer to normal, as this probability plot shows. This figure is based on normal u and v with f_{space} and f_{freq} set to 10, and $\sigma_g = 0.01$, $\mu_g = 0.00$.

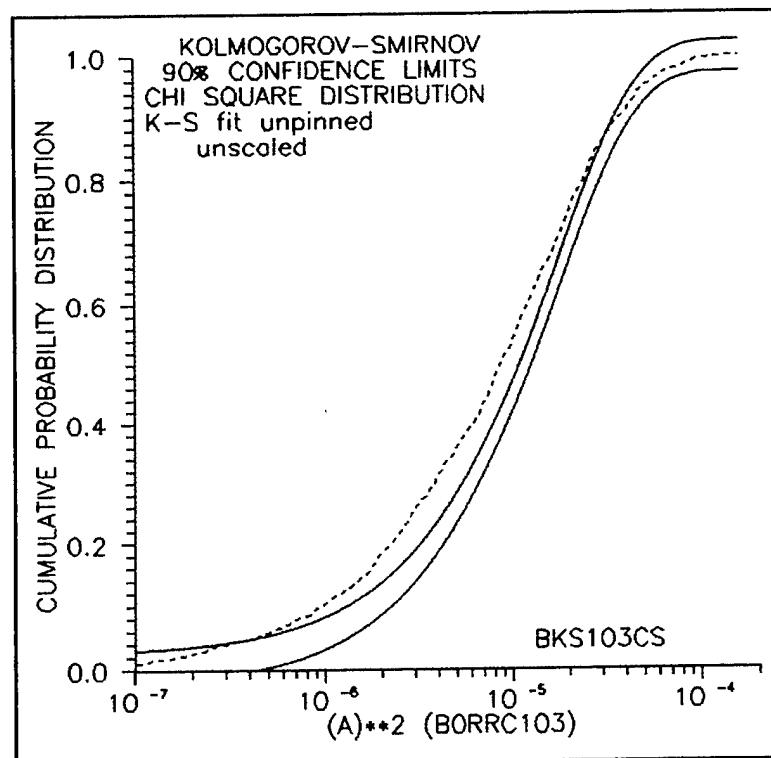


Figure 3.29. The pivoted cable current drivers yield cable powers which come still closer to being chi square in distribution, as this Kolmogorov-Smirnov 90% confidence test shows. This figure is based on normal u with f_{space} and f_{freq} set to 10, and $\sigma_g = 0.01$, $\mu_g = 0.00$.

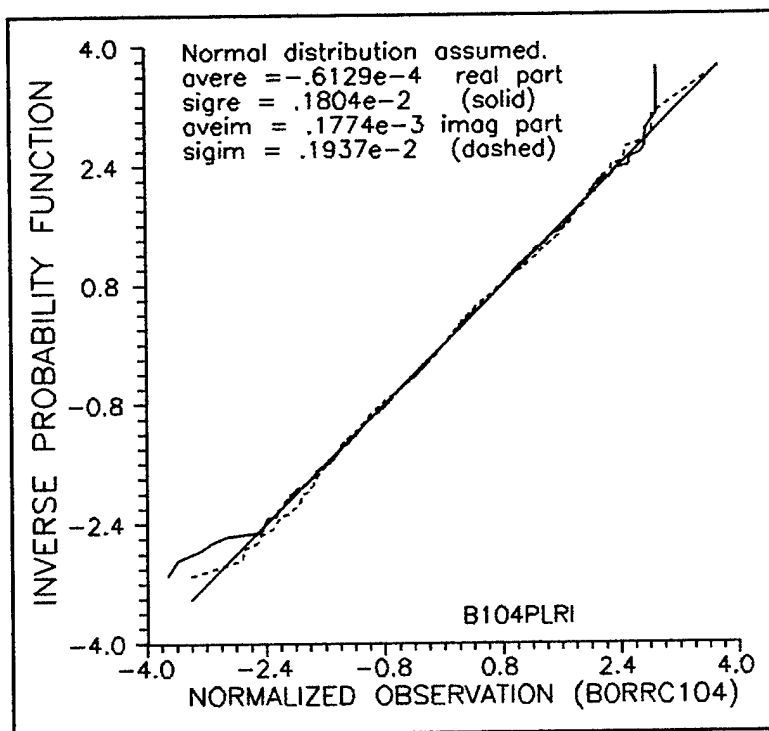


Figure 3.30. Adding frequency dependence to the radiation resistance of the cable is the last step in making the phase-quadrature cable current components match a normal distribution probability plot. This figure is based on normal u and v with f_{space} and f_{freq} set to 10, and $\sigma_g = 0.01$, $\mu_g = 0.00$.

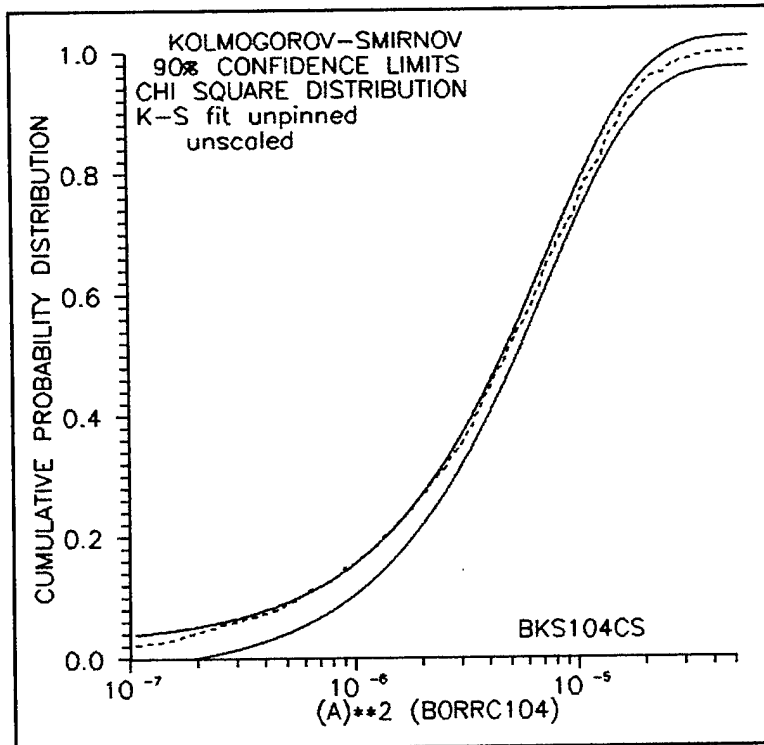


Figure 3.31. Adding frequency dependence to the model of the radiation resistance on the cable is our final step in matching the cable power distribution to a chi square model. This figure is based on normal u and v with f_{space} and f_{freq} set to 10, and $\sigma_g = 0.01$, $\mu_g = 0.00$.

MORE OPTIMIZING OF CABLE DRIVER GENERATION

At this point, we still found ourselves somewhat unsure we had determined the best possible procedure for generating cable drivers which simultaneously possessed the optimum fit to realistic distribution and autocorrelation. We believed that generation in accordance with (3-20) and (3-21), where $R(n,i)$ and $u(n,i)$ or $v(n,i)$ are related by (2-10), followed by rescaling according to (3-3) and pivoting to remove trend according to (3-26) was optimum, but an element of doubt remained.

We shall refer to (3-20) and (3-21) as the *fs* option, and its reverse,

$$R_{space}(n,i) = \frac{\frac{\lambda_n}{\Delta l} R(n,i-1) + f_{space} R(n,i)}{\frac{\lambda_n}{\Delta l} + f_{space}} \quad (3-28)$$

$$R_{freq}(n,i) = \frac{\frac{c(\Delta f)_n}{L} R(n-1,i) + f_{freq} R_{space}(n,i)}{\frac{c(\Delta f)_n}{L} + f_{freq}} \quad (3-29)$$

as the *sf* option. Additionally, we shall refer to use of a uniform Δf as the *n* option, and to a geometrically (exponentially) expanding Δf as the *g* option. We believed the uniform or *n* option was preferable to the growing or *g* option, but weren't absolutely positive. Thus, this left us with four choices to pick from, *sfg*, *sfn*, *fsg*, and *fsn*. Plots of $z(n,i) = u(n,i)^2 + v(n,i)^2$ were checked for a chi square fit. Results appear in Figure 3.32. All four curves pass a 90% K-S confidence test, but the *fs* runs (as expected) consistently stay closer to the middle of the limits. Also, as Figure 3.33 shows, the *fs* runs seem to have a smoother autocorrelation shoulder. Finally, Figure 3.34 demonstrate that the *fs* runs have a smoother baseline (no dips at the left side of the plot)

The preference between the uniform Δf and the geometrically expanding Δf is less clearly exhibited by these tests. In the absence of a clear superiority for linear Δf spacing, we are inclined to reverse our previous choice, and to use the geometrical Δf option, as it is usually aesthetic to have an equal number of sample frequencies in each octave or decade.

All results reported in this and the next subsection are based on $u(n,i)$ and $v(n,i)$ having a Gaussian distribution (2-10) with no bias and .01 standard deviation.

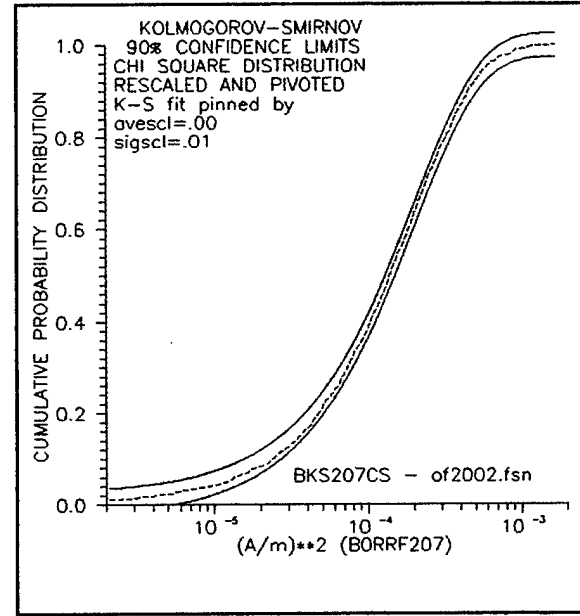
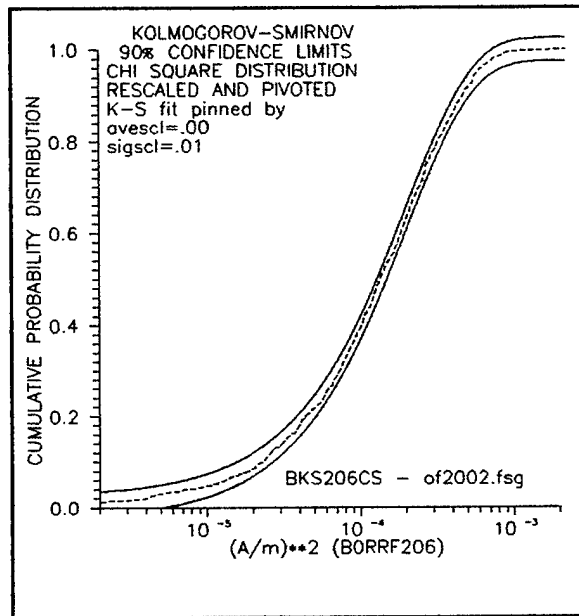
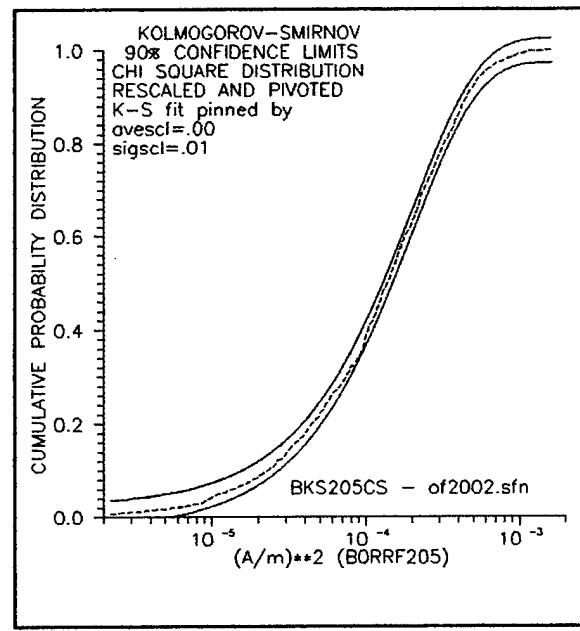
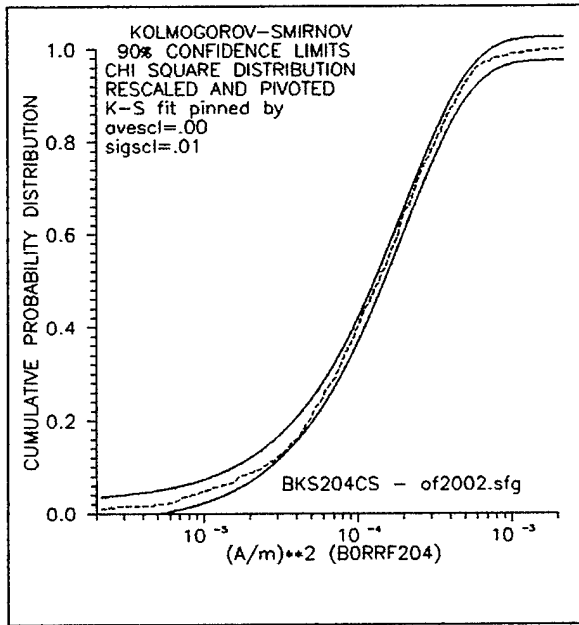


Figure 3.32. Summed squares of driving field phase-quadrature components computed by all four options pass the 90% K-S confidence test for being chi square with two degrees of freedom, but the recommended *fs* options (bottom pair) stay closer to the limit midpoint.

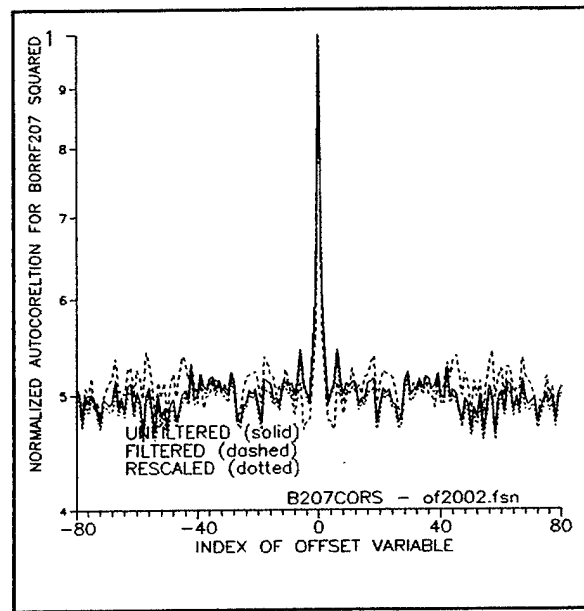
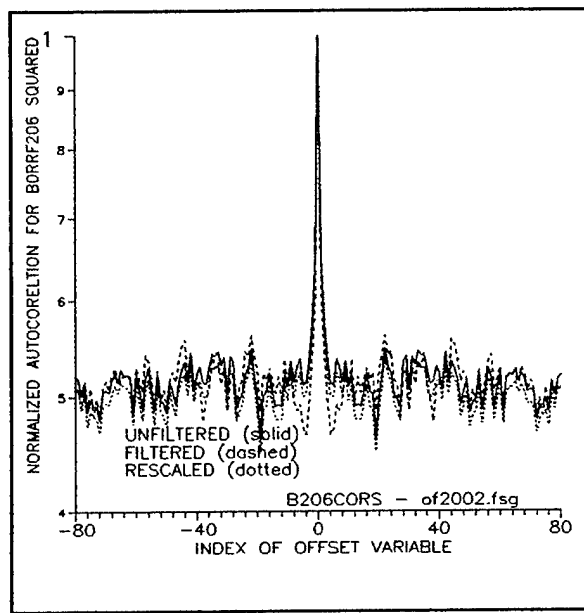
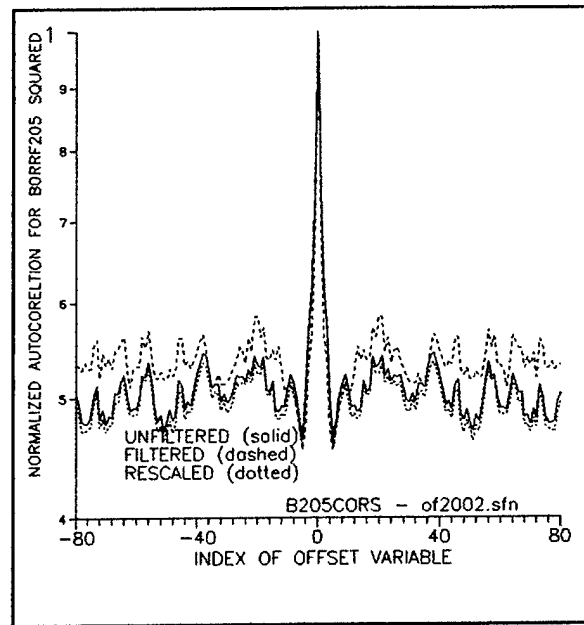
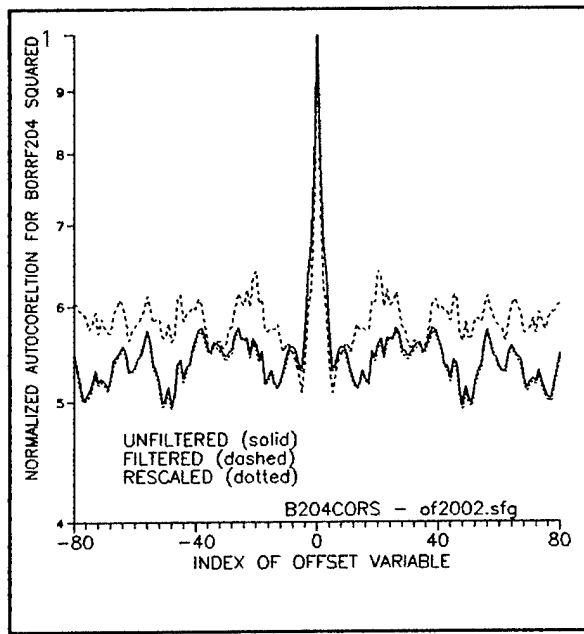


Figure 3.33. Summed squares of driving field phase-quadrature components computed by all four options have a realistic autocorrelation, but the recommended *fs* options (bottom pair) have smoother shoulders. It is possible the broader central spike of the *sf* options (top pair) is more representative of the actual physics.

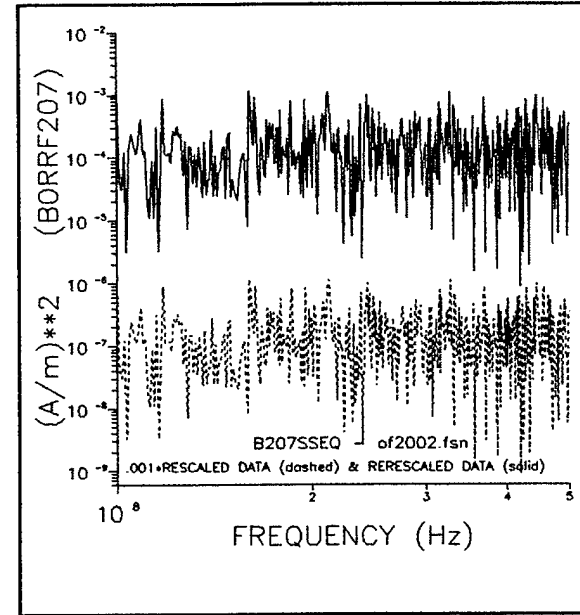
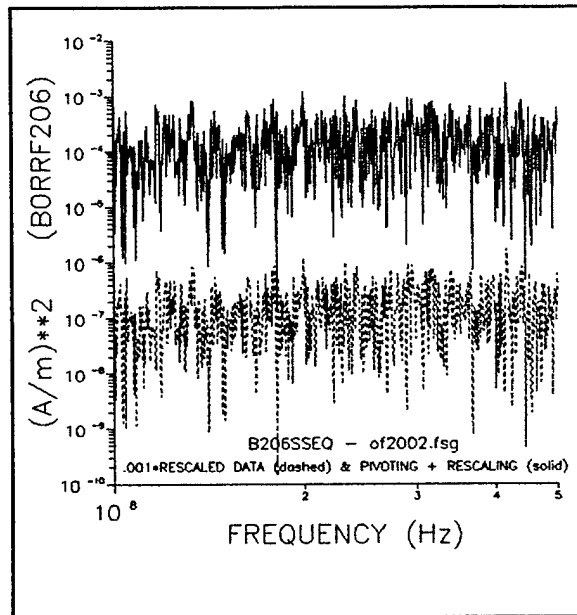
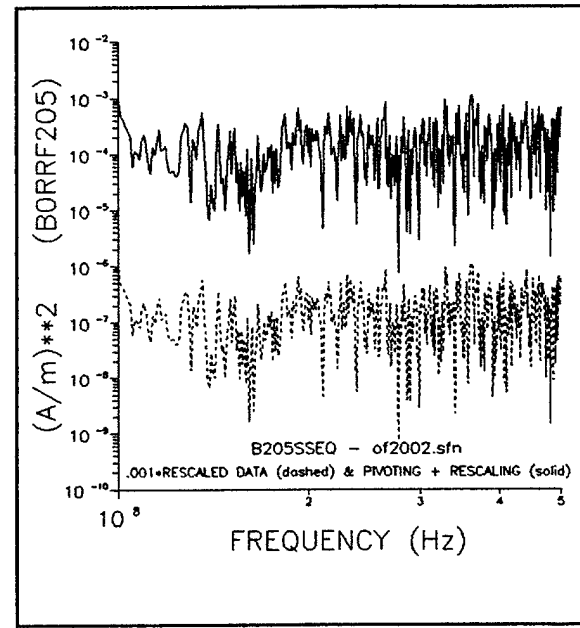
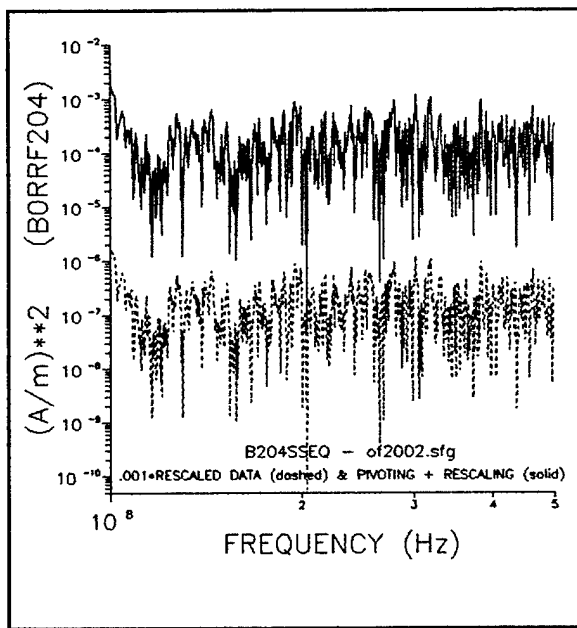


Figure 3.34. The recommended *sf* summed squares of driving field phase-quadrature components have a more level baseline (bottom pair) than the *fs* runs (top pair).

MORE THOUGHTS ON RADIATION RESISTANCE

Although we now know the homogeneous solution of an infinite wire in free space does not radiate (see Section 8), this fact was not originally clear to us. Even now, for a cable running along a ribbed wall of an aircraft, it is not clear that each rib cannot scatter some energy off the homogeneous solution. We, thus, see considerable justification for introducing (and continuing to use) a radiation resistance into real-world cables which do not run from nowhere to nowhere, passing nothing. Empirically [and with considerable physical justification as described earlier in (3-19)], we have found a good value for radiation resistance on EMPTAC cables to be

$$R = 120\Omega \quad (3-30)$$

for frequencies between 100 MHz and 1 GHz. This estimate, derived above, is based on attributes of the driven, or inhomogeneous portion of the cable currents (see Section 8). These driven currents, unlike the homogeneous portions, have been indeed shown to have a radiation resistance. Representation of this radiation resistance by (3-30) is designated to be the frequency-independent option (option *i*).

[The "discoveries" we have made about radiation resistance may, in the light of reciprocity, almost be tautologies (see Section 8). In particular, currents which can be field driven (the particular solutions) must produce radiating fields. Also, currents which cannot be field driven (the homogeneous solutions) cannot radiate.]

A frequency-dependent radiation-resistance option (option *d*) has also been offered, (3-27). Figure 2.1 illustrated that the cable currents squared should, like the fields, have a chi square distribution. Actual model currents were obtained from the field drivers in accordance with (3-6)-(3-16) Figure 3.35 shows that, of the *sfi*, *sfd*, *fsi*, and *fsd* options, only the *fsd*-based cable current drive actually leads to a cable current distribution squared which passes a 90% K-S confidence test for being chi square (although the *sfd* option is not very far outside the 90% K-S limits). Figure 3.36 shows that the *fsd* option also has the flattest baseline, and Figure 3.37 shows this option has the smoothest autocorrelation shoulder. All results appearing in Figures 3.35-3.37 are based on the frequency-independent *L* and *C* model for the wavenumber γ and characteristic impedance Z_c in (3-6)--see discussion following (3-16)

In summary, the best results for a simple transmission-line fixed-parameter model are obtained with the driving-field-matrix *fs* filling option, [(3-20) and (3-21)], and a radiation resistance empirically fit (3-27) (option *d*). More aesthetic results are obtained with a geometrically expanding Δf (option *g*), although actual accuracy does not seem compromised by a uniform, constant Δf .

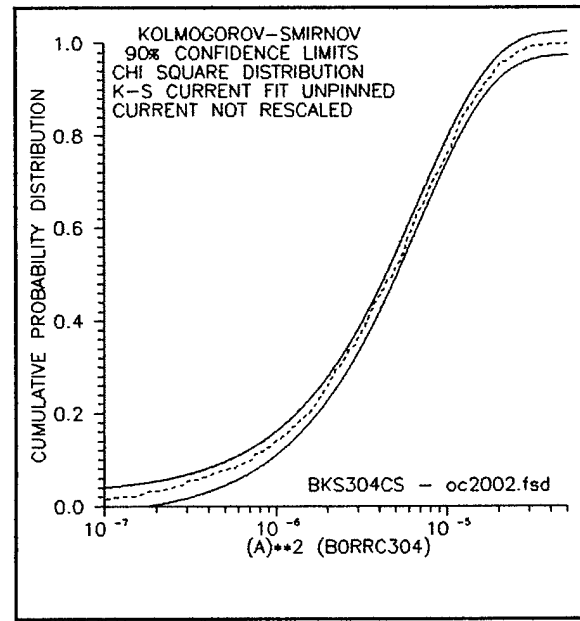
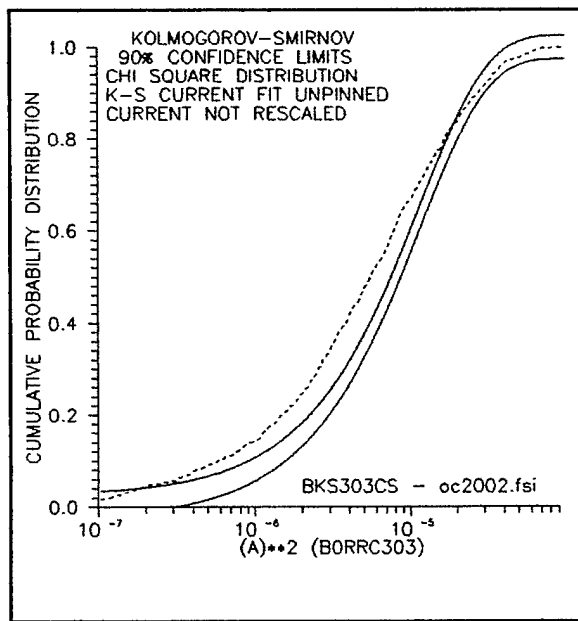
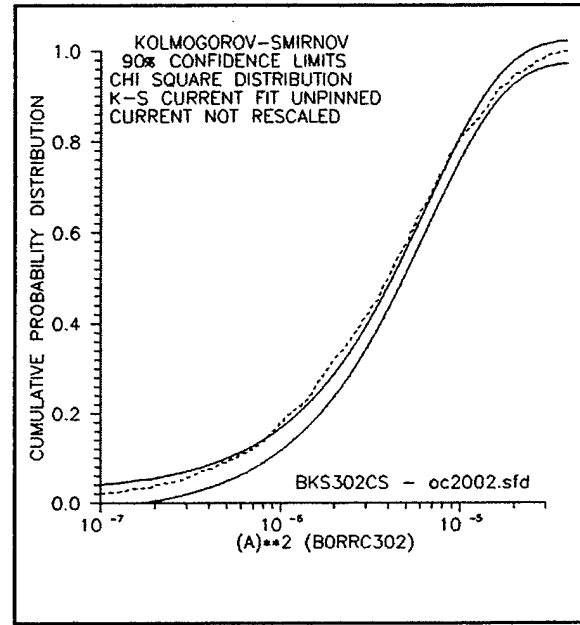
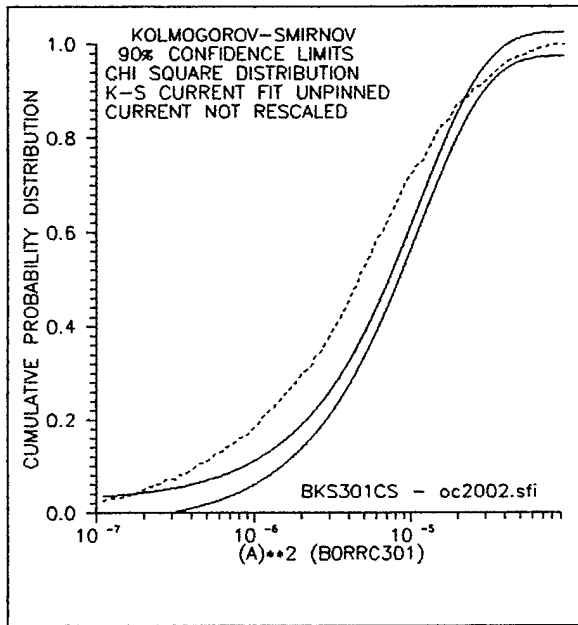


Figure 3.35. The frequency-dependent radiation-resistance model (right pair) gives more chi square like summed-squares of phase-quadrature cable currents than the frequency-independent model, although only the *fsd* model actually produces a cable-current distribution which is 90% confident of being chi square.

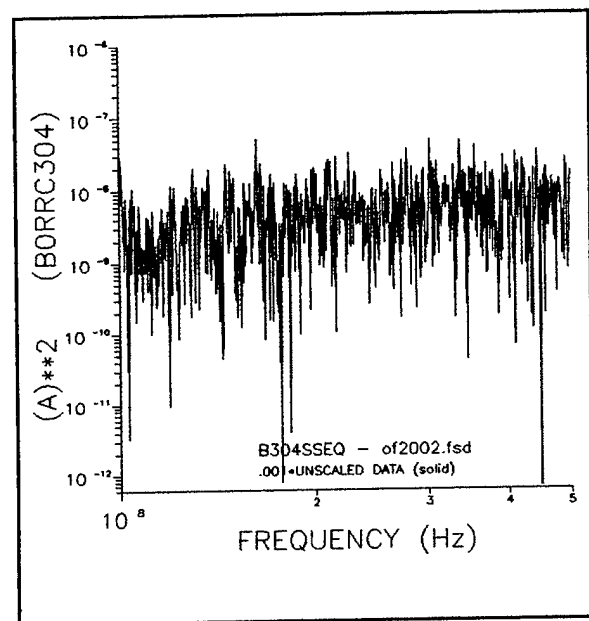
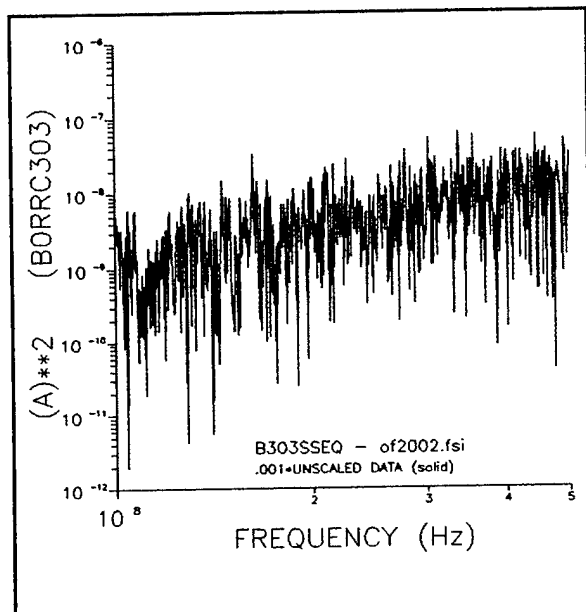
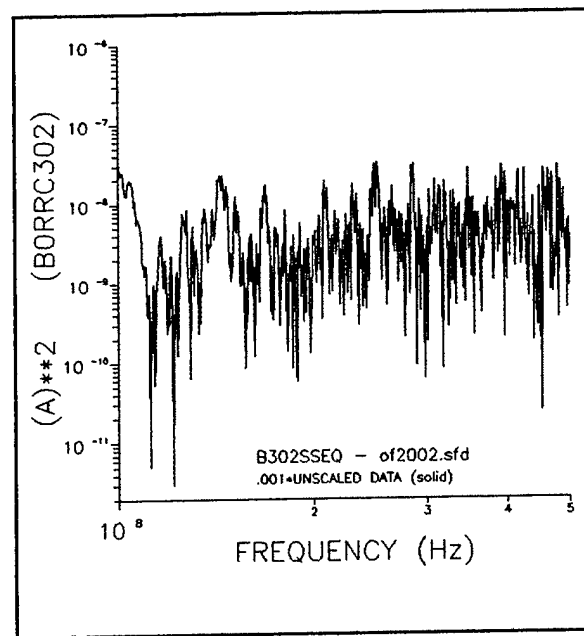
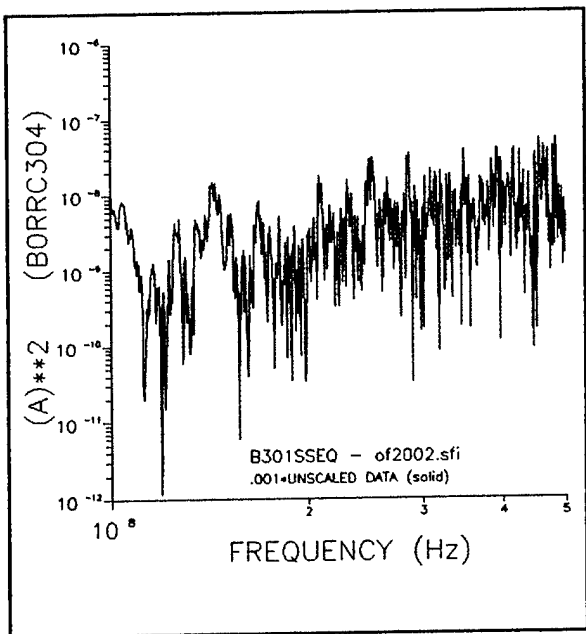


Figure 3.36. Only the *fsd* cable-driver model results in a flat baseline for the output summed squares of the phase-quadrature cable currents.

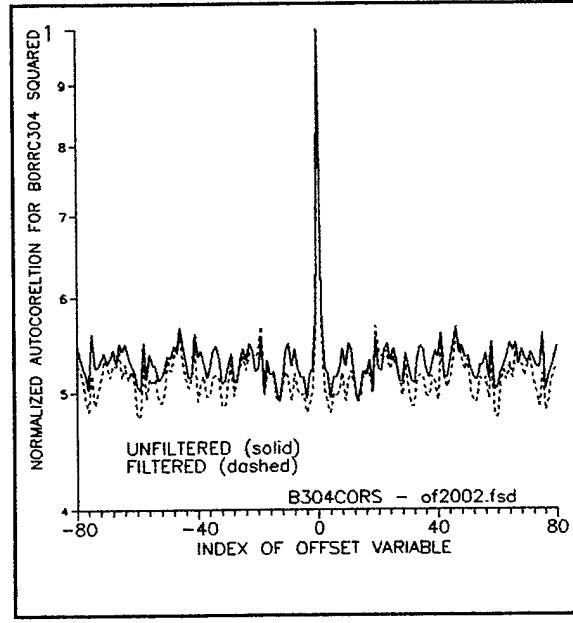
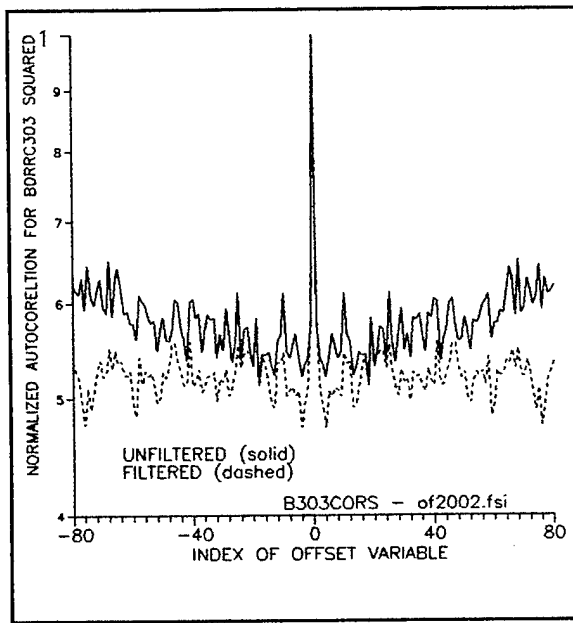
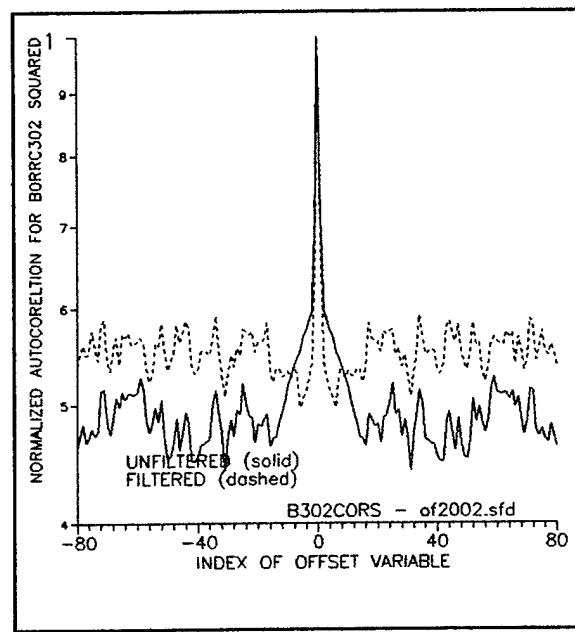
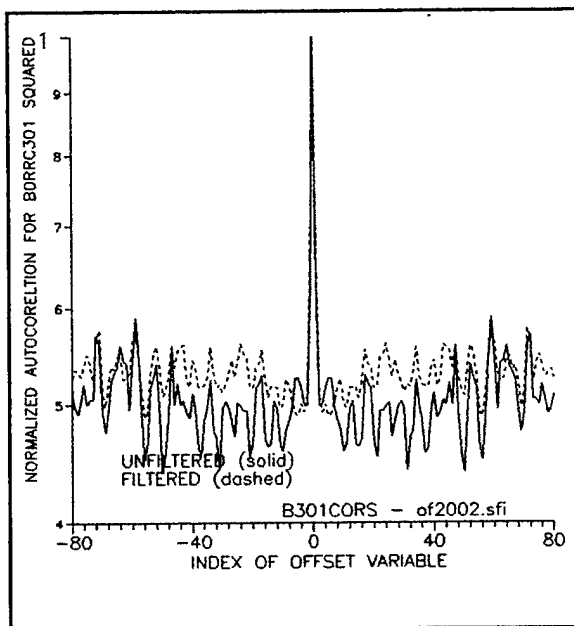


Figure 3.37. The *fsd* cable-driver model results in much flatter cable power autocorrelation shoulder than any of the other cable-drive options.

SUMMARY OF ALGORITHM TO GENERATE THE CABLE-DRIVE MATRIX

Let us now summarize now algorithm for generating the cable-drive fields in an overmoded enclosure. First of all, we need two field-drive matrix ensembles $A(n,i)$ or $B(n,i)$ to represent the two phase-quadrature components of the field at each frequency n and at each cable segment i . These two ensembles are to be completely uncorrelated with each other. The generation procedures for the two ensembles are identical, so we shall only discuss $A(n,i)$. The initial step is to generate a random number matrix having elements $R(n,i)$ uniformly distributed between 0 and 1. The matrix $R(n,i)$ is to be $N \times I$, so all frequencies and cable segments are represented.

The next step is to force local coherence on $R(n,i)$ as functions of n (frequency) and i (position). This coherence should approximately replicate (2-12) and (2-13) (see Figures 2.8 and 2.9), although we have found the results with respect to simulated cable current response to be quite forgiving if these two correlation formulas are not precisely matched. It is only important that the central lobe of the autocorrelation function be approximately the same width as that experimentally observed or suggested by (2-12) and (2-13). Equations (3-28) and (3-29) describe one transformation which can be used on $R(n,i)$ to enforce this autocorrelation. Values around 10 usually work for f_{space} and f_{freq} .

This enforced transformation will distort the original distribution placed on the original $R(n,i)$ matrix. It is thus necessary to restore this distribution, or even better, to convert it to a normal distribution. Use of (3-1) - (3-3) will accomplish this. If one decides that a distribution other than normal is desired, at this point, one needs only substitute the alternative inverse cumulative distribution for $P_g^{-1}(f_m)$ in (3-3).

One next maps $R(n,i)$ onto $A(n,i)$ in the manner described by (2-9) and (2-10) with $u(n,i) = u_{lim}(n,i)$. These particular equations result in an $A(n,i)$ ensemble with a normal distribution having zero mean and σ_g variance. If some other distribution is desired, that distribution should be substituted for the normal in (3-2) and (3-3).

Especially if f_{space} and f_{freq} are chosen smaller than 10, application of (3-3) may destroy some of the autocorrelation. In this case, one iterates the generation of $A(n,i)$ by reapplying (3-28) and (3-29), this time on the $A(n,i)$'s instead of on the $R(n,i)$'s. Then one reapplies (3-1) - (3-3). This iteration process may be cycled until further iteration no longer alters the $A(n,i)$ matrix ensemble. Up to 50 iterations are required for very small f_{space} and f_{freq} .

It may occur that, even after all this work, a small growth trend as a function of n (frequency) will remain on the matrix. If this occurs, the pivoting technique for eliminating this trend is described in (3-22)-(3-26).

SUMMARY AND CONCLUSIONS OF THIS SECTION

An electromagnetic enclosure driven well into the overmoded regime will have a power-flux distribution which (as seen by a dipole antenna) is chi square with two degrees of freedom if the observer is fixed and frequency is swept, or if the frequency is fixed and the sensor is translated or rotated. The same power distribution will also be seen on cables and conductors within the enclosure. To obtain this distribution, the enclosure must not have a frequency-dependent Q or shielding which varies throughout the enclosure volume. If either of these (or similar) situations occur, the power and power-flux distribution densities generally distort towards being log normal.

This entire set of statistical phenomena may be numerically simulated provided one is very careful. For instance, one cannot merely apply normally distributed random electric fields (which correspond to chi square power fluxes) to drive the cables and conductors. The cable-drive fields must be generated so they are additionally endowed with local autocorrelation along spatial and frequency axes as seen in actual experimental data. Also, it is necessary to put a radiation resistance per unit length on the cable to simulate factors which put the cable and the enclosure into electromagnetic thermodynamic equilibrium. Additionally, one must be cautious that the cable-drive fields are free of all trends, including those which may arise from the process of enforcing a local autocorrelation onto the cable-drive field ensemble.

Chapter 4. THE LOG NORMAL DISTRIBUTION

The log normal distribution is extremely important and very frequently encountered in our universe. There is a simple explanation why almost any data set which depends on a bunch of ill-determined factors will be approximately log normal. This approximate relationship may be inferred from the Central Limit Theorem, and if each of the ill-determined factors has an identical distribution, the approximate relationship becomes exact. To be more specific, any sum of M components $x_i, i = 1, \dots, M$ where $E\{x\}$ and $\text{var}\{x\}$ exist will itself converge to a normal distribution as M goes to infinity.^[1] (Cauchy's distribution^[2] is an example where $E\{x\}$ and $\text{var}\{x\}$ do not exist, and where a sum of components does not converge to a normal distribution. The no-house-limit on doubling a wager each time a coin toss results in a head produces another such distribution for winnings. Both these examples set up a situation where a few of the variates can be so large as to dominate the sum. Then the sum is effectively only over a few variates, not over a large number, and it is not surprising that there is a problem.) Consequently, the log ensemble of a data set with a bunch of ill-determined factors, where each factor has the same distribution, will approach a normal distribution, as the log operator converts the product of factors to a sum of components. This means the original data set itself will have a distribution which is (approximately) log normal.

In this section, we shall describe some properties of a log normal distribution, including the development of the fields associated with an environment which has a log normal power-flux distribution. Previously (Section 2), we demonstrated that these fields should have a distribution density derivable (at least numerically) from the log normal power flux. In particular, we Fourier transform the log normal power-flux distribution density, take the square root of the Fourier transform, and then inverse transform the square root function. This should, at least in principle, yield the desired field distribution density associated with a log normal power-flux distribution.

In practice, it is not numerically possible to perform the inverse transform if the standard deviation of the $\{\ln z_i\}$ array is larger than about 1.2 (which, unfortunately, typifies most of our data). This occurs because log normal distributions can possess unreasonably long distribution tails: there is a not-small-enough chance that a few points may lie very far out. Unlike the two examples mentioned above, the tail is not so long that $E\{\ln z\}$ and $\text{var}\{\ln z\}$ do not exist. It is merely long enough to cause extreme numerical complications. It also implies a concomitant physical problem: an unconstrained, log normally generated random distribution will occasionally give absurdly large values, implying possibilities of the sort that RFI from someone's microwave oven on Long Island brought down TWA Flight 800.

INTRODUCTION TO THE LOG NORMAL DISTRIBUTION

Let us begin by illustrating some behavior of this distribution with scale factors stripped away. In this context, Figure 4.1 shows the log normal distribution density function

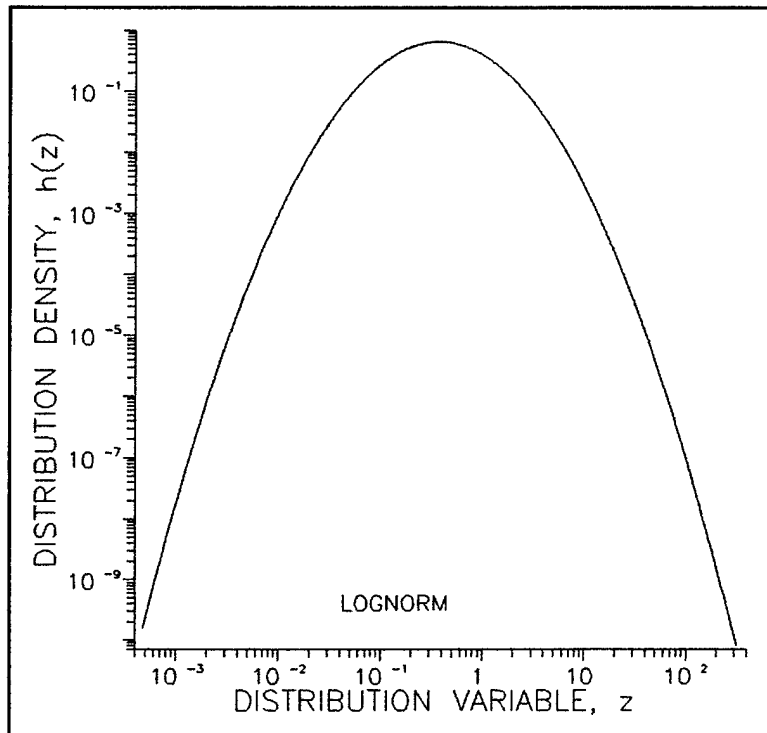


Figure 4.1. The log normal distribution function with $\sigma_{lg} = 1$ and $\mu_{lg} = 0$.

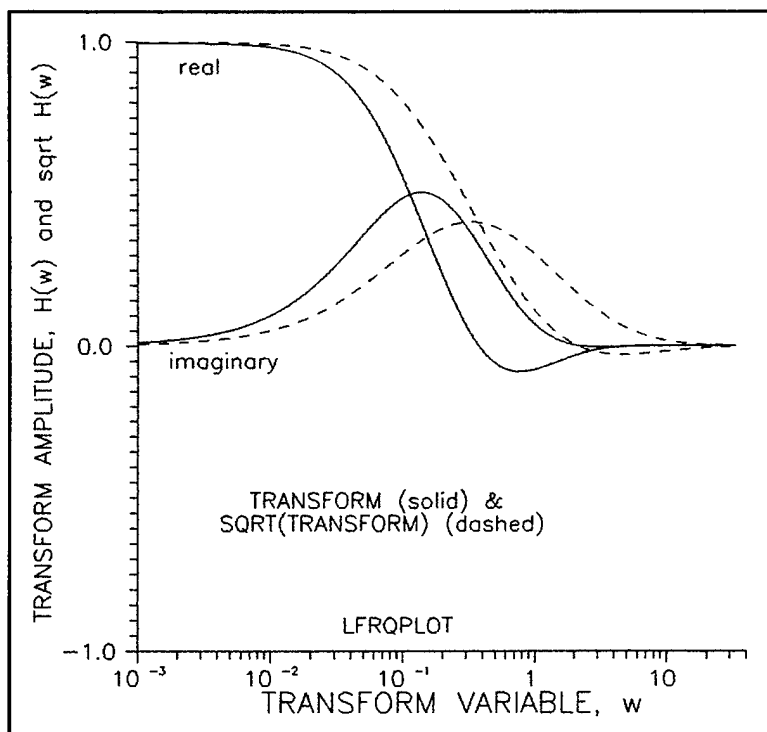


Figure 4.2. Fourier transform of the log normal distribution density function and the square root of this transform. Note how much more slowly the square-root transform goes to zero.

$$h(z) = \frac{1}{\sqrt{2\pi}} \frac{e^{-(\ln z)^2/2}}{z} \quad (4-1)$$

Note that the standard deviation of $\{\ln z\}$ of this distribution is 1, which is smaller than 1.2. Thus, attempting to transform it will not crash your computer. Figure 4.2 shows the Fourier transform of this distribution and also the square root of this transform. (We use w instead of ω to denote the transform variable because it here has no relation to periodicity, either spatial or temporal.) Part of the numerical difficulty with deconvolving power-distribution densities to obtain field-distribution densities is apparent here. By taking the square root of the transform, we greatly extend the range on the horizontal axis in Figure 4.2 over which one must integrate when finding the inverse. For instance, if the transform itself has dropped off to an acceptable 10^{-4} , the square root will only have dropped off to an unacceptable 10^{-2} . Also, the range one will have to go out bring the square root transform down to 10^{-4} may increase exponentially, not linearly--that is, merely integrating out 100 times farther out the abscissa may not do the trick. Lastly, because the square root tail drops off so slowly, the energy of the square-root tail below 10^{-4} may be much greater than that of the corresponding simple transform tail below 10^{-4} . Thus, just because ordinate reduction to 10^{-4} works for the simple transform doesn't mean it will suffice for the square-root transform.

Figure 4.3 is a plot in the complex plane of the locus of the Fourier transform and its square root. Figure 4.4 is a multiple overlay showing 1) the untransformed distribution, 2) the inverse transform of the log normal distribution (which perfectly overlies the original distribution, thus proving our transform routine is working), and 3) the sine and cosine inverse transforms of the square root of the transformed distribution. These final inverse transforms do not overlap perfectly because the square root transform is more difficult to inverse transform. We believe the inverse transform of the square root transform is zero at $x = 0$, although it is a little hard to prove this for the cosine transform because the long-tail problem applies to the lower tail, as well as the upper tail, especially when plotted with the abscissa logarithmic. Be glad the deconvolution of the field distribution doesn't involve a fourth root!

If we take the average of the sine and cosine inverse transforms of the square root function, and autocorrelate the result back upon itself, we get back the log normal distribution density function as we should (see Figure 4.5).

In Section 2, we demonstrated that, given some major assumptions, many quantities inside an overmoded enclosure will theoretically obey a chi square distribution with two degrees of freedom. These quantities include the square of the current on a cable, the squares of both surface current components on a perfect conductor, and the square of the projection of the electric or magnetic field on any dipole antenna. The basis of this conclusion was that quantities such as those enumerated above are formed as the sum of two squares of phase-quadrature components

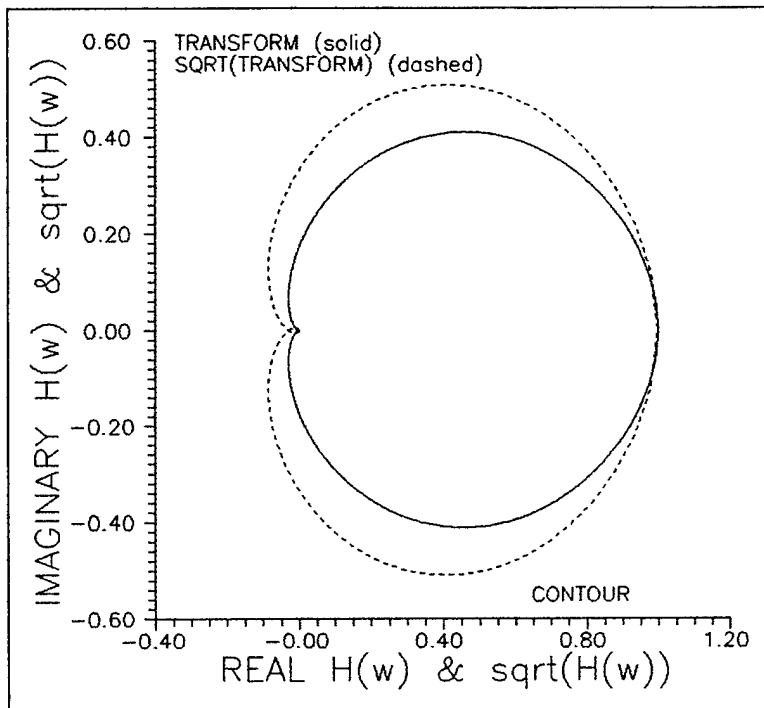


Figure 4.3. Fourier transform of the log normal distribution density function and the square root of this transform. Note how much more slowly the square-root transform goes to zero. In both cases, increasing w corresponds to counterclockwise motion. Note that both transforms assume the probabilistically required value of $(1,0)$ at zero w .

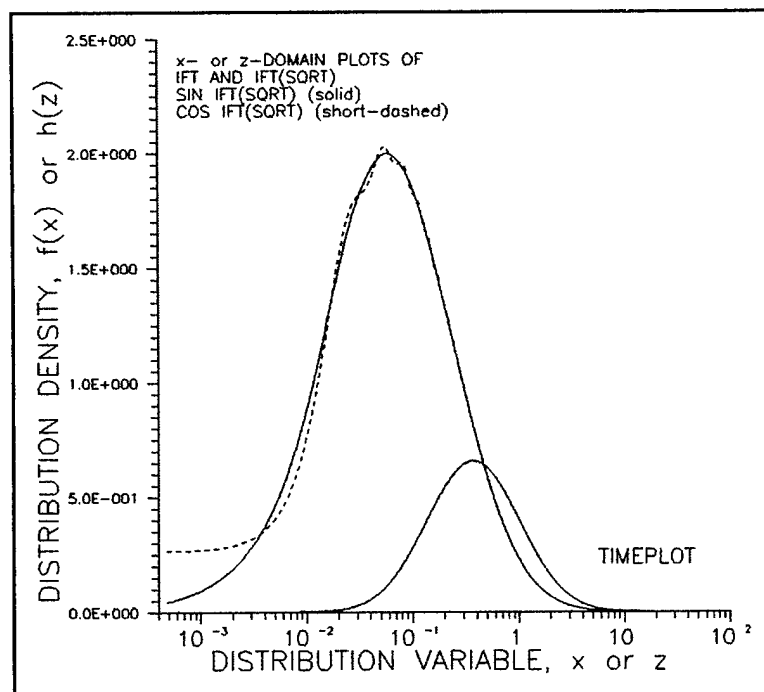


Figure 4.4. Small curve: Log normal distribution function perfectly overlaid by inverse transform of transform of this function. Larger curves: Sine and cosine inverse transforms of the square root of the transform of the log normal distribution. We believe this inverse transform should actually go to zero at $x = 0$. On a linear scale, the actual area between the sine and cosine inverse transforms is minimal.

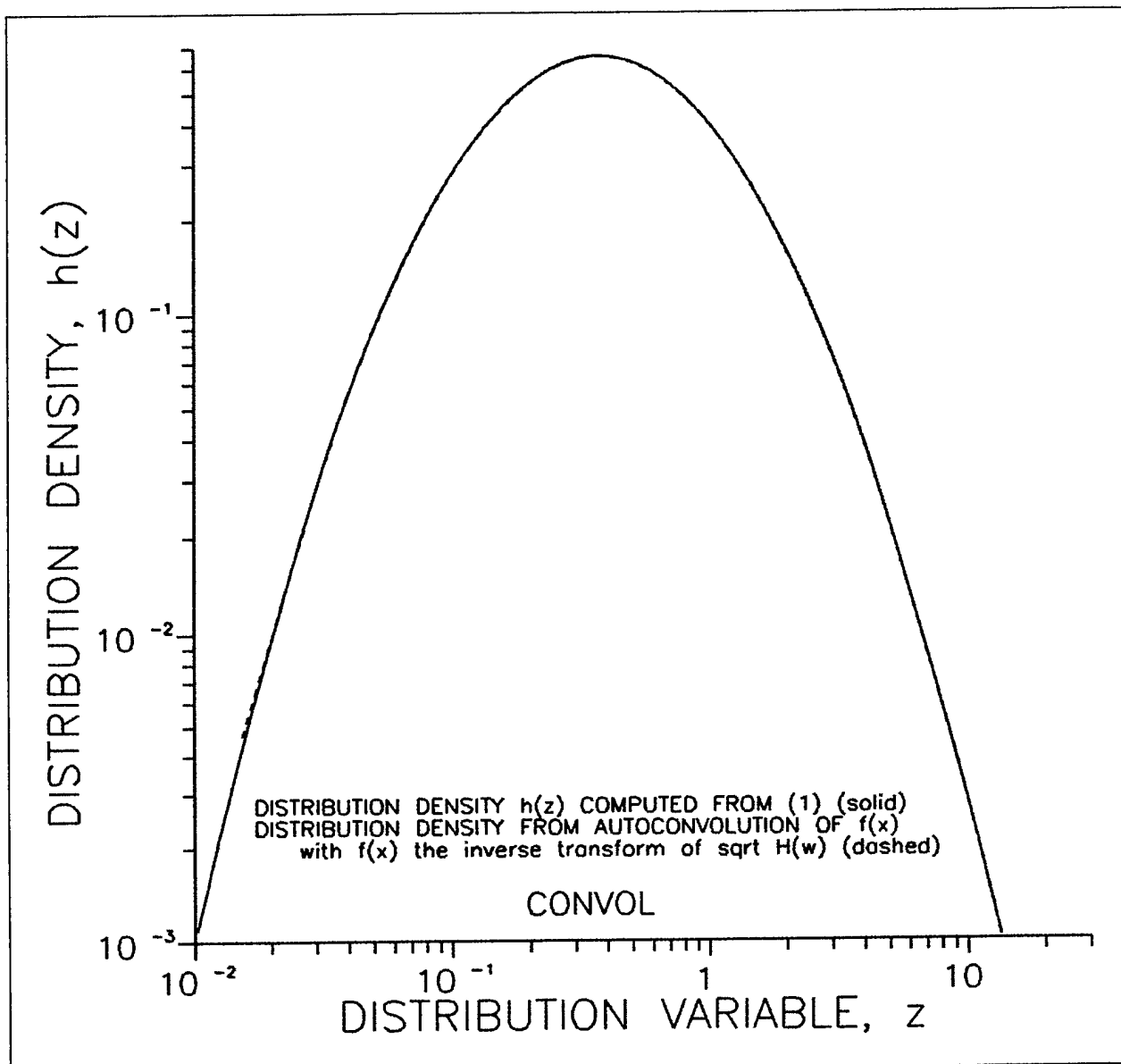


Figure 4.5. The log normal distribution function is almost perfectly overlaid by the autoconvolution of the inverse transform of the square root of the transform of the log normal distribution function when $\sigma_g = 1$.

$$z = u^2 + v^2 \quad (4-2)$$

where u and v themselves obey a normal distribution. This basis seems reasonable in overmoded scenarios by appeal to Maxwell-Boltzmann statistics for thermodynamic equilibrium between the fields and the cavity contents. Appeal to Bosé-Einstein statistics gives essentially the same answer. The above-mentioned distributions may be taken with frequency, position, or dipole orientation as the independent variable. It does assume the two-phase quadrature quantities (or right- and left-going waves) are uncorrelated, which is normally a valid caveat.

A pure chi square distribution, however, is actually observed infrequently. This is true because of inherent assumptions and requirements such as a frequency-independent Q , a relatively uniform distribution of shielding and dissipation within the enclosure, and points of entry which leak omnidirectional and frequency independently. In the real world, such demands likely won't be met. Thus, it turns out that actual squared quantities of the form of z more often have a log normal distribution. Early on in the work discussed in this document, we largely focussed on deducing the distribution of u given that z was chi square (see Section 2). Fields deduced in this manner were then used to drive, for example, EMPTAC cable models.

A problem with this approach is that a chi square distribution has only one variable parameter μ_{χ^2} , which is both the mean and the standard deviation. A typical cable current squared (or driving field) usually needs two variables to characterize it adequately in statistical terms: the average or mean (of the log) and the wiggle or variance (of the log) which is superimposed on the mean. Hence, in this section, we focus on determining the distribution of u assuming z is log normal:

$$h(z) = \frac{1}{\sqrt{2\pi}} \frac{\exp(-(\ln z - \mu_{lg})^2 / (2\sigma_{lg}^2))}{z \mu_{lg}} \quad (4-3)$$

Let us designate z as

$$z = x + y = u^2 + v^2 \quad (4-4)$$

The first (and biggest) step then is that of determining the distribution of x and y . In Section 2, it was shown that the distribution of z , $h(z)$, is the autoconvolution of the distribution of x , $f(x)$:

$$h(z) = \int_{-\infty}^{\infty} f(x) f(z - x) dx \quad (4-5)$$

or that $f(x)$ is given as the inverse Fourier transform of the square root of the Fourier transform of $h(z)$:

$$f(x) = \frac{1}{2\pi} \int_{-\infty}^{\infty} [H(w)]^{1/2} e^{jwx} dw \quad (4-6)$$

If σ_{lg} is very close to unity ($.98 < \sigma_{lg} < 1.02$), $f(x)$ can easily be evaluated numerically from (4-6), as we demonstrated in Figure 4.5. This statement is true for any reasonable μ_{lg} (μ_{lg} between -16 and +16). However, for realistic σ_{lg} 's observed in EMPTAC data (say, $\sigma_{lg} \sim 1.8$), numerical evaluation of (4-6) has thoroughly thwarted all computational attempts. Even at $\sigma_{lg} = 1.4$, use of 15,000 exponentially expanding points on each side of the Fourier evaluation fails; Figure 4.6 shows the result of such a attempt when these parameters are tried. Figure 4.7 shows similar data plotted logarithmically on the vertical axis. Figure 4.8 shows the real and imaginary parts of $H(w)$ and $[H(w)]^{1/2}$, and Figure 4.9 shows the phase associated with $[H(w)]^{1/2}$. The problem with these runs is that both $h(z)$ and $H(w)$ have such long tails for $\sigma_{lg} > 1.2$ that it is almost impossible to run the inverse Fourier transform integrals far enough or finely enough, at least using 64-bit FORTRAN. At $\sigma_{lg} \sim 1.8$, the consequences of these effects seem absolutely beyond hope of working with or around.

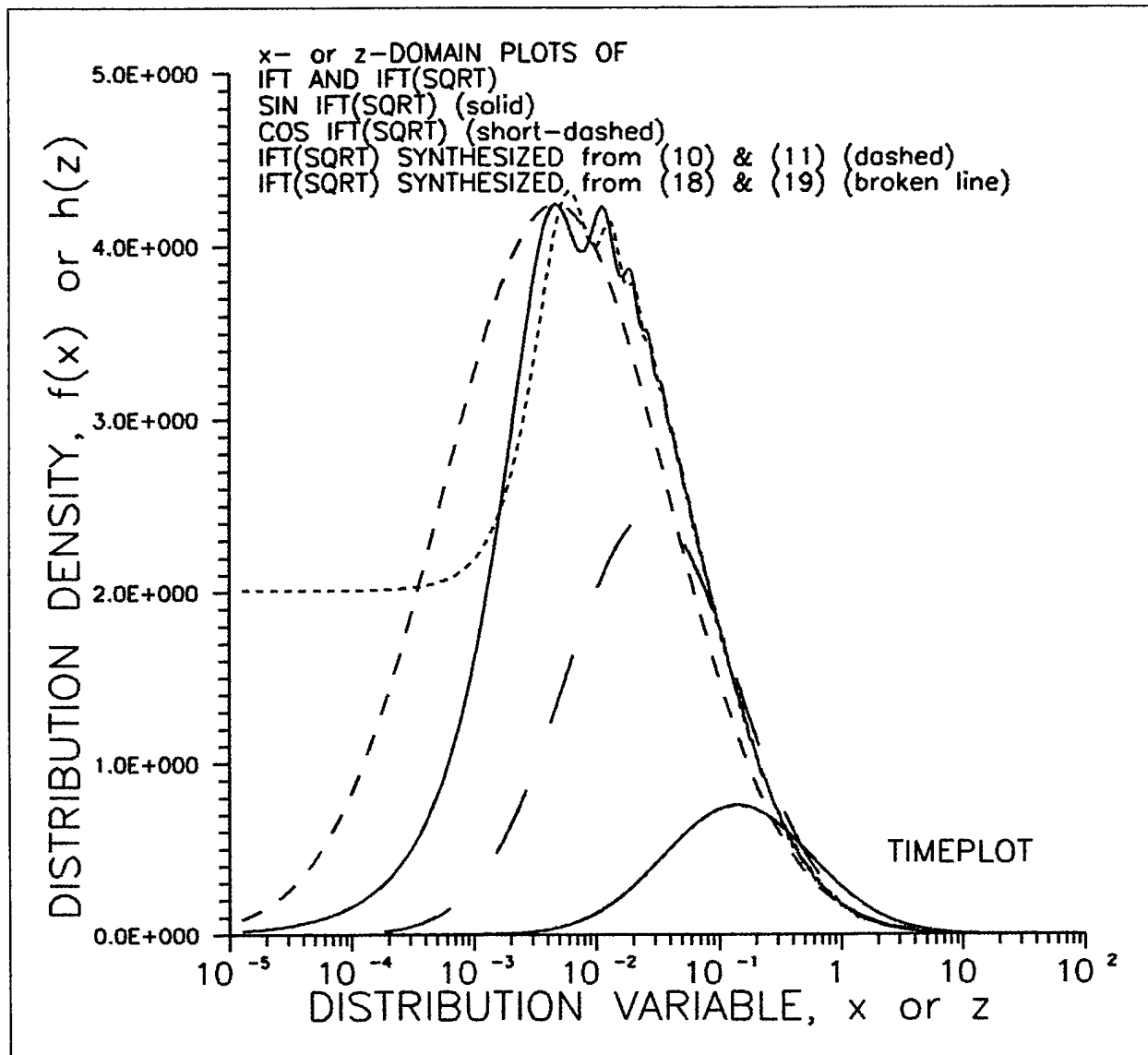


Figure 4.6. Smaller curves to lower right: triple overlay of original log normal distribution $h(z)$ as calculated from (4-3), and from taking the inverse sin and cos transforms of the transform. This overlay is excellent. Larger curves to left: triple overlay of inverse sin and cos transforms of sqrt of transform, $f_1(x)$, with an analytic fit based on (4-10) and (4-11), $f_2(x)$, with f_{max} and x_{max} empirically taken from the inverse sine transform. This overlay is not satisfactory. Middle broken line: analytic fit to inverse transform of sqrt of transform based on (4-18) and (4-19), $f_3(x)$, [which, for some reason, doesn't work]. This figure is based on z having a log normal distribution with $\mu_{lg} = 0.0$, and $\mu_{lg} = 1.4$.

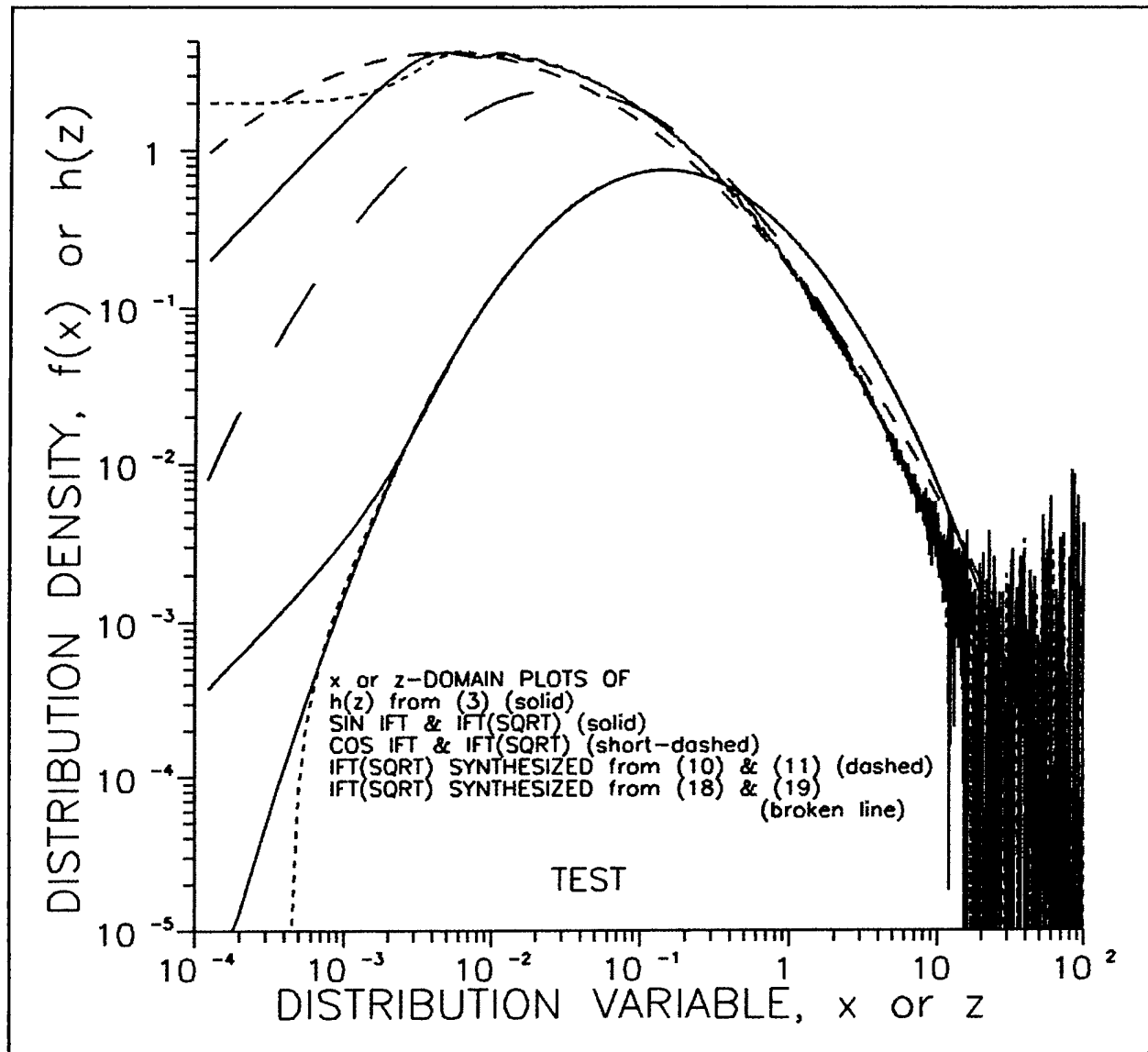


Figure 4.7. Curves at center: triple overlay of original log normal distribution as calculated from (4-3), $h(z)$, and from taking the inverse sin and cos transforms of the result. Logarithmic display indicates overlay breaks up about 40 dB below peak. Larger curves to left and top: triple overlay of inverse sin and cos transforms of sqrt of transform, $f_1(x)$, plus an analytic fit based on (4-10) and (4-11), $f_2(x)$, with f_{max} and x_{max} empirically taken from the inverse sine transform. These results are not satisfactory. Middle broken line: analytic fit to inverse transform of sqrt of transform based on (4-18) and (4-19), $f_3(x)$, [which, for some reason, doesn't work]. This figure is based on z having a log normal distribution with $\sigma_{lg} = 0.0$, and $\mu_{lg} = 1.4$.

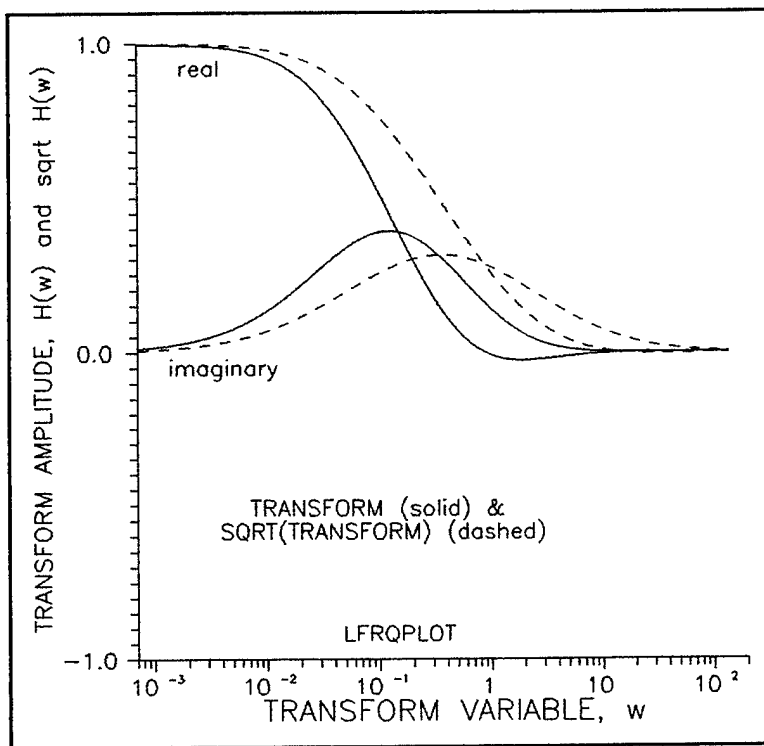


Figure 4.8. Transform and sqrt of transform of log normal distribution. This figure is based on $h(z)$ having $\mu_{lg} = 0.0$ and $\sigma_{lg} = 1.4$.

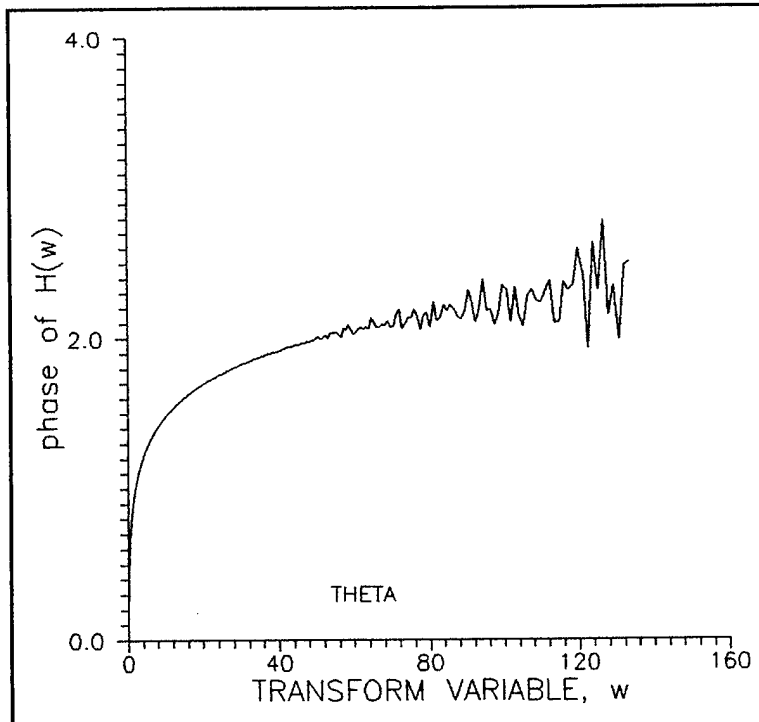


Figure 4.9. Phase of sqrt of transform of log normal distribution. This figure is based on $h(z)$ having $\mu_{lg} = 0.0$ and $\sigma_{lg} = 1.4$. Note that the phase calculation begins to break up around $w = 60$, before the sqrt of the transform, as shown above in Figure 4.8, has reached zero.

ANALYTIC FITS FOR DECONVOLVED LOG NORMAL DISTRIBUTIONS

Fits Based on Distribution Density Maxima

We have noticed that, if $h(z)$ is log normal, $f(x)$ is very nearly log normal also. While we cannot mathematically prove this statement, we can test it by attempting to find σ'_{lg} and μ'_{lg} to characterize $f(x)$ and then autoconvolving $f(x)$ back upon itself to recover $h(z)$. (Primes denote parameters of the deconvolved $f(x)$ distribution; unprimed parameters refer to the convolved $h(z)$ distribution.) For $\sigma_{lg} \sim 1$, where $f(x)$ can be numerically determined, this effort works very nicely (see Figure 4.10). In general, it is true that a log normal distribution is uniquely defined by $(\sigma'_{lg}, \mu'_{lg})$, or alternatively by the value x_{max} where $f(x)$ takes its maximum value and f_{max} where

$$f_{max} = f(x_{max}) \quad (4-7)$$

In particular, f_{max} occurs at

$$x_{max} = e^{\mu'_{lg} - \sigma'^2_{lg}} \quad (4-8)$$

and has value

$$f_{max} = \frac{1}{\sqrt{2\pi}} \frac{e^{\sigma'^2_{lg}/2 - \mu'_{lg}}}{\sigma'_{lg}} \quad (4-9)$$

Alternatively, if we know x_{max} and f_{max} , σ'_{lg} may be determined by solving

$$\sigma'^2_{lg} + \ln \sigma'^2_{lg} = -2 \left(\ln f_{max} + \ln \sqrt{2\pi} + \ln x_{max} \right) \quad (4-10)$$

with μ'_{lg} being

$$\mu'_{lg} = \ln x_{max} + \sigma'^2_{lg} \quad (4-11)$$

Around $\sigma_{lg} = 1.0$, the above relationships have been used to find μ'_{lg} and σ'_{lg} for $f(x)$, assuming $f(x)$ is log normal, and given that $h(z)$ is log normal (with $\sigma_{lg} = 1.0$). In particular, we first extracted $f(x)$ directly from (4-6) giving $f_1(x)$. We then determined x_{1max} where $f_1(x)$ had a maximal value f_{1max} . From this, we obtained $f_2(x)$ by assuming $f_2(x)$ was log normal with σ'_{lg} and μ'_{lg} given by (4-10) and (4-11). Both $f_1(x)$ and $f_2(x)$ were then autoconvolved with the result compared to the original $h(z)$. As long as σ_{lg} was very close to 1.0, both comparisons were excellent regardless of

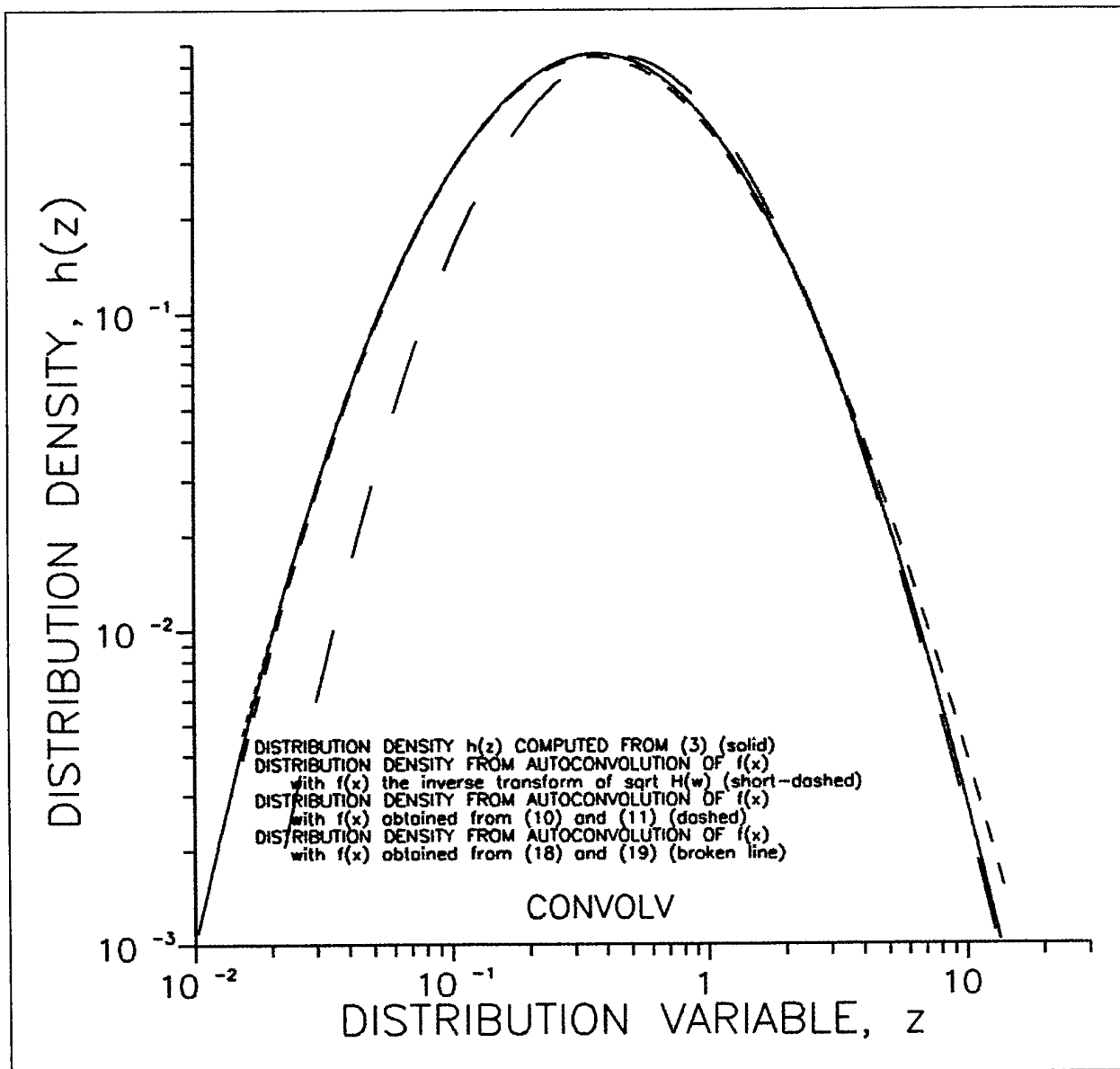


Figure 4.10. Overlay of $h(z)$ obtained from (4-3) with that obtained from autoconvolution of the inverse transform of the sqrt of the transform, $f_1(x)$, from the autoconvolution obtained from (4-10) and (4-11), $f_2(x)$, and from the autoconvolution obtained from (4-18) and (4-19), $f_3(x)$. All curves but the last agree very nicely. This figure is based on $(\sigma_{lg}, \mu_{lg}) = (1.0, 0.0)$, which leads to an inverse sine transform (see Figure 4.6) of the sqrt of the transform having $(\sigma_{lg}^{-2}, \mu_{lg}') = (1.86, -0.992)$.

the value of the original μ_{lg} (see Figure 4.10). In fact, we observed that, for $\sigma_{lg} = 1.0$, the mean μ_{lg}' of the deconvolved distribution was always closely approximated by

$$\mu_{lg}' = \mu_{lg} - 1.0 \quad (-16.0 \leq \mu_{lg} \leq 16.0) \quad (4-12)$$

irrespective of the initial value of μ_{lg} .

These approaches, however, just don't work for $\sigma_{lg} > 1.2$ due to the failure of the inverse Fourier transforms to converge given any computationally practical range of integration over w (see Figures 4.6 and 4.7).

Fits Based on Statistical Relationships

There is another approach which we thought should work, but doesn't. If $h(z)$ is given by (4-3), the expectancy of z is [3]

$$E[z] = e^{\mu_{lg} + \frac{1}{2}\sigma_{lg}^2} \quad (4-13)$$

and the variance of z by

$$\text{var}[z] = e^{2\mu_{lg} + \sigma_{lg}^2} (e^{\sigma_{lg}^2} - 1) = E[z]^2 R[z] \quad (4-14)$$

where (4-14) serves to define the statistic $R[z]$. If x and y have the same distribution and are independent (uncorrelated), then the expectations and variances of x and z are related by

$$E[x] = \frac{1}{2}E[z] \quad (4-15)$$

$$\text{var}[x] = \frac{1}{2}\text{var}[z] \quad (4-16)$$

$$R[x] = 2R[z] \quad (4-17)$$

Assuming $f(x)$ is log normal, μ_{lg}' and σ_{lg}' can then be obtained by inverting (4-13) and (4-14)

$$\sigma_{lg}' = (\ln(2R[x]) + 1)^{\frac{1}{2}} \quad (4-18)$$

$$\mu_{lg}' = \ln(2E[x]) - \frac{1}{2}\ln(2R[x] + 1) \quad (4-19)$$

Equations (4-18) and (4-19) enable us to construct a third $f(x)$, $f_3(x)$, which can be compared with $f_1(x)$ and $f_2(x)$ or autoconvolved for comparison with $h(z)$. As Figures 4.6 and 4.7 show, however, this doesn't work. In fact, Figure 4.10 shows this approach doesn't even work for $\sigma_{lg} = 1.0$.

EMPIRICAL FITS FOR DECONVOLVED LOG NORMAL DISTRIBUTIONS

After dishing out the preceding ration of bad news, we are glad to report that we do have a successful fall-back position. It turns out to be easy to estimate values for μ'_{lg} and σ'_{lg} which, when inserted in a log normal distribution and autoconvolved, will give back $h(z)$ with any desired μ_{lg} and σ_{lg} . Figure 4.11 shows an approximate log normal deconvolution for $\sigma_{lg} = 1.0$, $\mu_{lg} = 0.0$. Figure 4.12 shows an approximate log normal deconvolution for $\sigma_{lg} = 1.4$, $\mu_{lg} = 0.$, and Figure 4.13 shows an approximate log normal deconvolution for $\sigma_{lg} = 1.8$, $\mu_{lg} = 0.0$. Figure 4.14 shows an approximate log normal deconvolution for typical EMPTAC field data, $\sigma_{lg} = 1.9$, $\mu_{lg} = -17.5$. It turns out that σ'_{lg} depends almost entirely on σ_{lg} and μ'_{lg} on μ_{lg} . The following empirical formulas give an excellent starting point for evaluation of $(\sigma'_{lg}, \mu'_{lg})$ given (σ_{lg}, μ_{lg}) :

$$\mu'_{lg} = \mu_{lg} - 1. - .5(\sigma_{lg} - 1.) \quad (4-20)$$

$$\sigma'^2_{lg} = - .1 + .2\sigma_{lg} + 1.8\sigma_{lg}^2 \quad (4-21)$$

The correction to σ'_{lg} associated with μ_{lg} is not yet known, but is expected also to be negligible. Even without the benefit of (4-20) and (4-21), we were always able to find $(\sigma'_{lg}, \mu'_{lg})$ to $1\frac{1}{2}$ significant figures in six or fewer convergent tries. [It is extremely unlikely one will ever have experimental data for (σ_{lg}, μ_{lg}) reliable to $1\frac{1}{2}$ significant figures.]

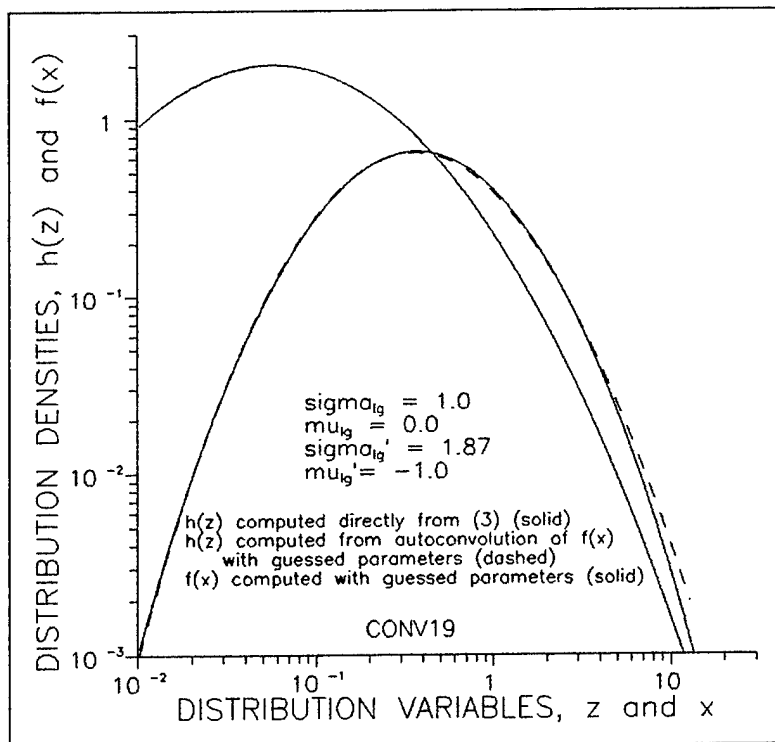


Figure 4.11. Overlay of log normal distribution for $h(z)$ with $(\sigma_{lg}, \mu_{lg}) = (1.0, 0.0)$ and autoconvolution approximation based on guess of log normal $f(x)$ with $(\sigma'_{lg}, \mu'_{lg}) = (1.87, -1.0)$.

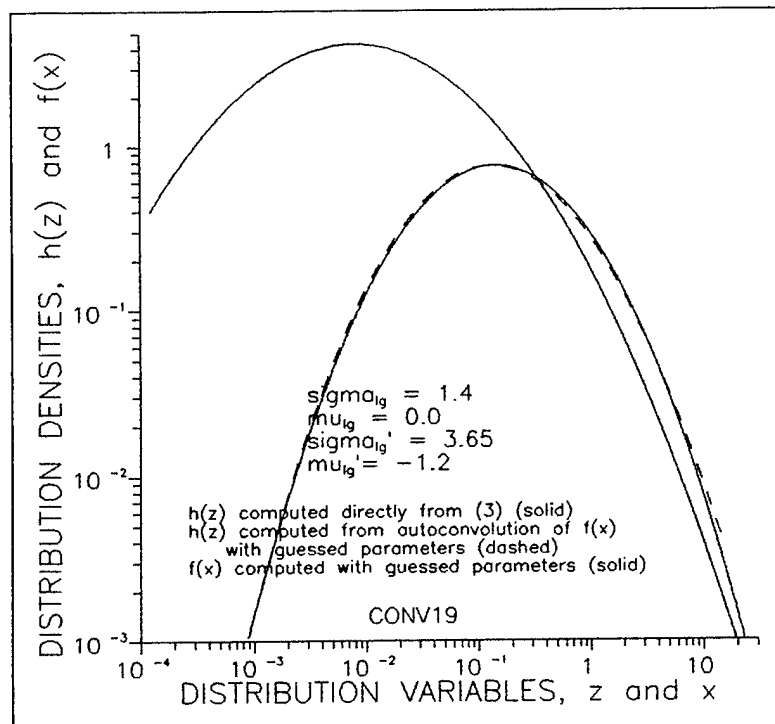


Figure 4.12. Overlay of log normal distribution for $h(z)$ with $(\sigma_{lg}, \mu_{lg}) = (1.4, 0.0)$ and autoconvolution approximation based on guess of log normal $f(x)$ with $(\sigma'_{lg}, \mu'_{lg}) = (3.65, -1.2)$.

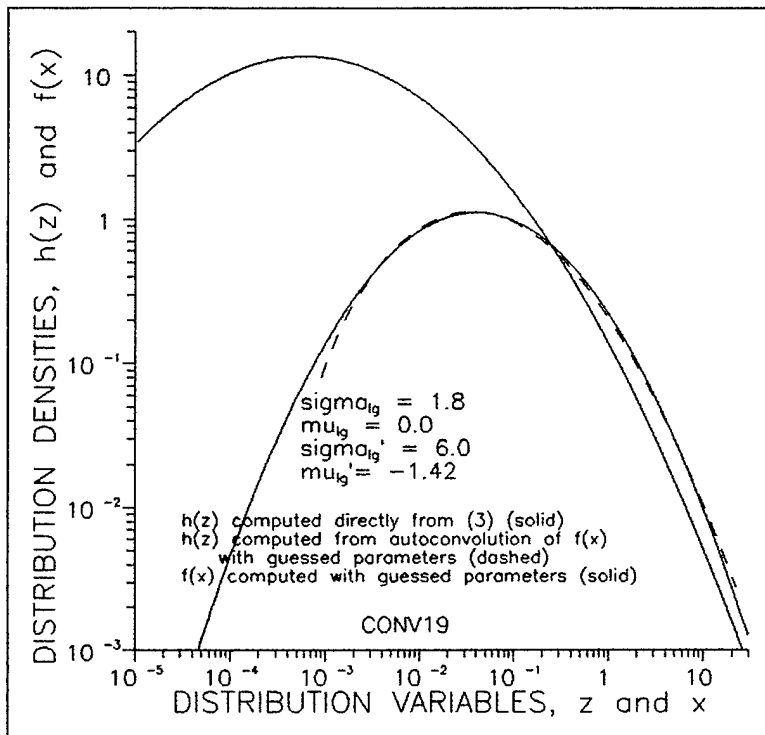


Figure 4.13. Overlay of log normal distribution for $h(z)$ with $(\sigma_{lg}, \mu_{lg}) = (1.8, 0.0)$ and autoconvolution approximation based on guess of log normal $f(x)$ with $(\sigma'_{lg}, \mu'_{lg}) = (6.0, -1.42)$.

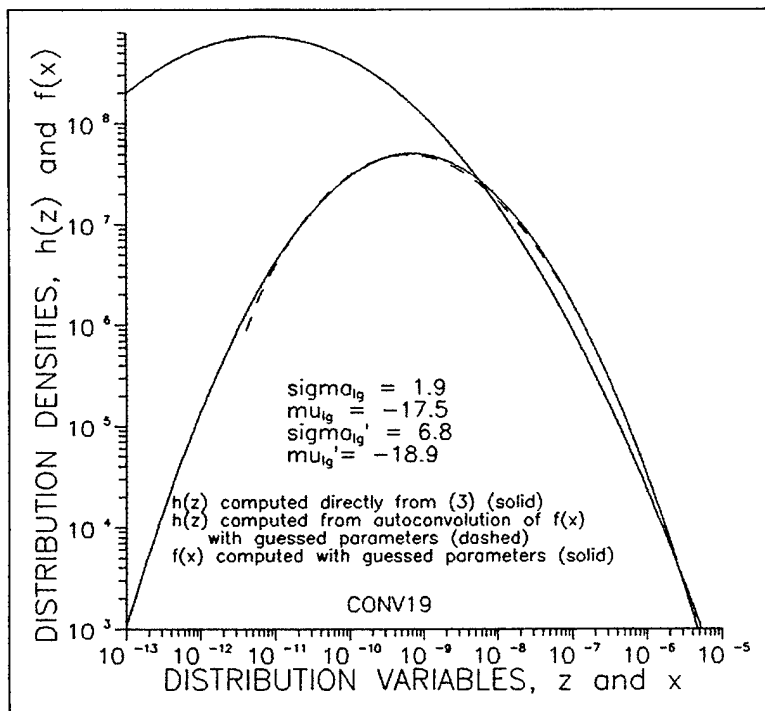


Figure 4.14. Overlay of log normal distribution for $h(z)$ with $(\sigma_{lg}, \mu_{lg}) = (1.9, -17.5)$ and autoconvolution approximation based on guess of log normal $f(x)$ with $(\sigma'_{lg}, \mu'_{lg}) = (6.6, -1.89)$. These parameters are typical of EMPTAC magnetic fields. Note the extreme dynamic range (along both axes).

GENERATION OF LOG NORMAL FIELD DRIVERS

Given the distribution of x , finding the distribution of u (or its generation by random numbers) should be easily accomplished by the use relationships in Section 2. The rescaling operation to restore this distribution after the introduction of correlation may be a little more complicated because u is bipolar, while x is not (refer to Section 3). In particular, if p is a random number between 0 and 1, the operator for generating the driving field is

$$u = (\text{random sign}) \left[\exp\left\{(\mu'_{lg} + \sigma'_{lg} P^{-1}(p))/2\right\} \right] \quad (4-22)$$

Here $P^{-1}(\)$ is the inverse Gaussian operator. Equation (4-22) corresponds to the distribution density function [see (2-60)]

$$e(u) = \frac{1}{\sqrt{2\pi}} \frac{e^{-(2 \ln |u| - \mu'_{lg})^2 / (2\sigma'^2_{lg})}}{|\sigma'_{lg}|u|} \quad -\infty < u < \infty \quad (4-23)$$

The associated log normal rescaling operator is as follows: Let f_i be

$$f_i = (i - 1/2)/n \quad (4-24)$$

where n are the number of random numbers to be rescaled. If f_i is less than $1/2$, we have $u_i < 0$ and

$$P(w_i) = \frac{1}{\sqrt{2\pi}} \int_{-\infty}^{w_i} \frac{e^{-(2 \ln (-w') - \mu'_{lg})^2 / (2\sigma'^2_{lg})}}{-\sigma'_{lg} w'} dw' \quad (w < 0) \quad (4-25)$$

where

$$w_i = \frac{2 \ln (-u_i) - \mu'_{lg}}{-\sigma'_{lg}} \quad (4-26)$$

or

$$f_i = \frac{1}{2}P\left(\frac{2 \ln|u_i| - \mu'_{lg}}{-\sigma'_{lg}}\right) \quad (4-27)$$

so that

$$u_i = -\exp\left\{\frac{1}{2}\left(\mu'_{lg} - \sigma'_{lg}P^{-1}(2f_i)\right)\right\} \quad (4-28)$$

It can readily be seen that $f_i = 0$ yields $u_i = -\infty$ and $f_i = \frac{1}{2}$ yields $u_i = 0$.

If f_i is greater than $\frac{1}{2}$, we have $u_i > 0$ and

$$P(w_i) = \frac{1}{2} + \int_0^{w_i} \frac{e^{-(2 \ln w' - \mu'_{lg})^2/(2\sigma'_{lg}^2)}}{\sigma'_{lg} w'} dw' \quad (4-29)$$

where now

$$w_i = \frac{2 \ln u_i - \mu'_{lg}}{\sigma'_{lg}} \quad (4-30)$$

or

$$f_i = \frac{1}{2} + \frac{1}{2}P\left(\frac{2 \ln u_i - \mu'_{lg}}{\sigma'_{lg}}\right) \quad (4-31)$$

so that

$$u_i = \exp\left\{\frac{1}{2}\left(\mu'_{lg} + \sigma'_{lg}P^{-1}(2f_i - 1)\right)\right\} \quad (4-32)$$

We see that $f_i = \frac{1}{2}$ again yields $u_i = 0$, while $f_i = 1$ yields $u_i = +\infty$.

COMPARISON OF THEORY AND EMPTAC-BASED DATA

As we have observed, the current response of cables in a complicated, highly overmoded chamber is not a problem which is tractable by deterministic solution of Maxwell's equations.

Our approach, which is probably the only feasible one, has been first to characterize the statistical distribution of electromagnetic fields or power flux in the chamber.[4-10] This distribution, in general, may have frequency or position as the independent variable. Depending on the nature of the enclosure (frequency-dependent Q , degree of homogeneity, etc.) the electromagnetic fields have a zero-bias normal distribution, a bipolar log-normal distribution, some mix of the two, or (as we shall demonstrate in Section 5) some, as yet unevaluated, distribution with the property that the associated power-flux distribution $h(z)$ looks like a modified Bessel function of the second kind [6,9,10]

$$h(z) = \Lambda^2 z K_2(2\sqrt{\Lambda z}) \quad \Lambda = 3 / \text{mean}[z] = 3 / \mu \quad (4-33)$$

A normal field distribution leads to a chi square (with two degrees of freedom) power-flux distribution. A bipolar log-normal field distribution leads, at least approximately, to a monopolar log-normal power-flux distribution. Formulas relating the field-distribution parameters to the power-flux distribution parameters prove to be quite simple for the normal, log-normal, and mixed distributions (see following subsection). This also proves to be true for the modified Bessel distribution, although the requisite modified Bessel function algebra is a little more complicated.

Our goal, then, is one of modeling the cavity field or power flux distribution from measured samples. These fields are then applied as drivers to a model of the chamber cables. Lastly, the resulting cable currents on the model are compared in statistical distribution to measured cable currents. When the driven cable model yields currents with a distribution in good agreement with the measured cable current distribution, we consider the simulation to be performing well.

A typical case to which we have applied this technique is the Air Force Phillips Laboratory EMPTAC 720 shell externally illuminated by the Ellipticus antenna and swept from 100 MHz to 1 GHz (the high-frequency sweep). The magnetic field squared observed axially in this configuration (Sweep B050MBHZ, Figures 4.18 - 4.20) essentially has a monopolar log-normal distribution with a mean μ_{lg} of 7.86e-8 (A/m)² and a standard deviation σ_{lg} of 1.28e-7 (A/m)². These values correspond to a field whose amplitude has a standard deviation σ_{lg}' of 1.7e-4 (A/m). This last value was used to generate a chi-square-model driving field ensemble [see discussion following (2-15)] which, after appropriate manipulations to restore bipolarity, has a square with a mean μ of 5.02e-8 (A/m)² and a standard deviation σ of 1.08e-7 (A/m)². Applying fields thusly characterized to the model of the EMPTAC cable network resulted (Run B0oc2002.3, Figure 4.15) in cable currents squared with a mean of 3.27e-8 A² and standard deviation of 10.62e-8 A². On the other hand, measured EMPTAC cable currents (Sweep B032211Y, Figure 4.16), when squared, had a mean of 2.65e-8 A², and a standard deviation of 5.91e-8 A². This result is typical of 20 or so tests we have made, and indicates model fidelity well within a factor of 2. (This factor, in turn, is probably a fair guess at the repeatability or uncertainty in the measurements-- both of cavity fields and of cavity cable currents; see Figure 4.17.)

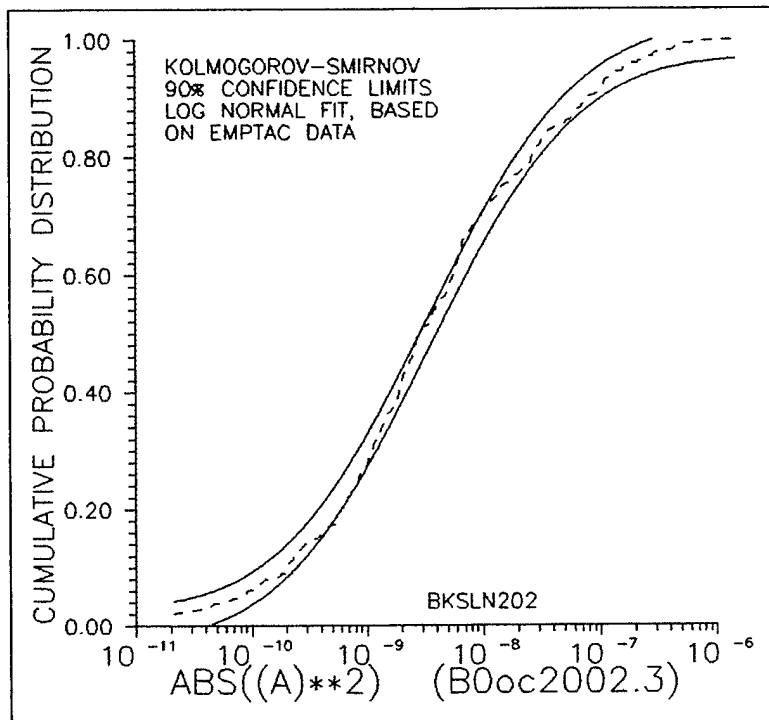


Figure 4.15. Model-based cumulative distribution of the squared currents on the EMPTAC cables [with 90% Kolmogorov-Smirnov confidence limits (see Section 9) for being log normal].

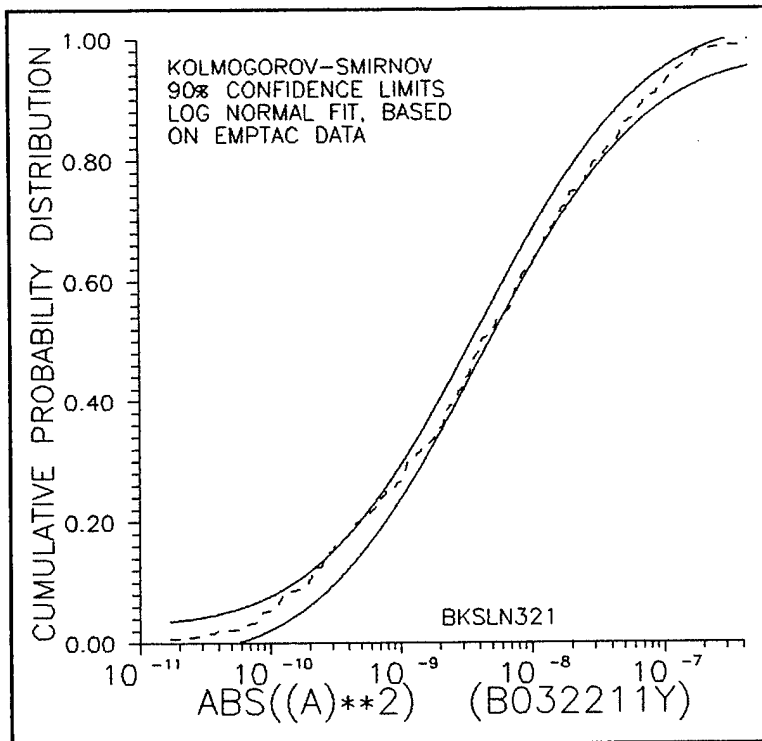


Figure 4.16. Measured cumulative distribution of the squared currents on the EMPTAC cables (with 90% Kolmogorov-Smirnov confidence limits for being log normal).

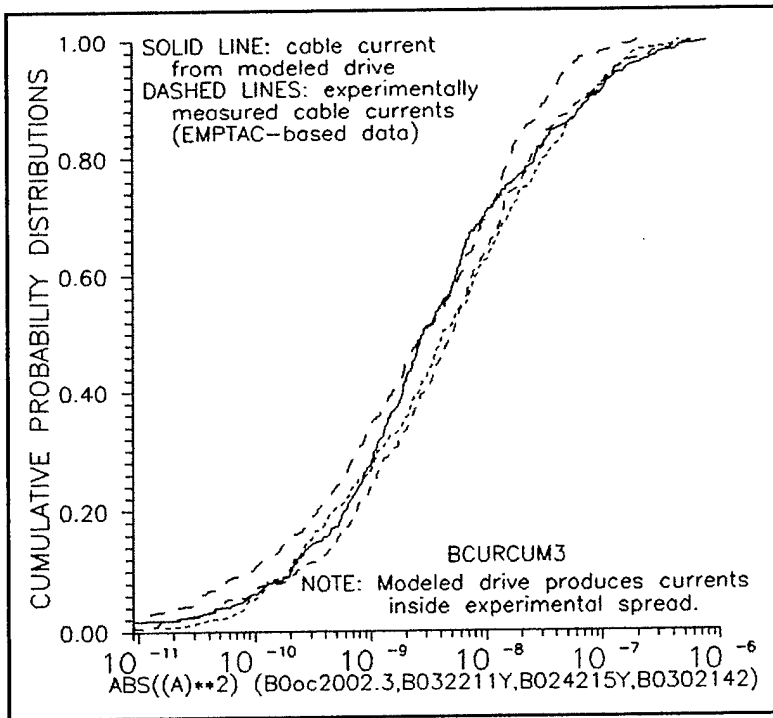


Figure 4.17. The EMPTAC model squared cable current distribution (solid line) does not stray outside the bounds provided by an overlay of three squared cable current distributions (various dashed lines) which were obtained under slightly varied measurement conditions.

HYBRID NORMAL \times LOG-NORMAL FIELD DISTRIBUTIONS

We shall discuss primarily the mixed normal/log-normal field quadrature distribution here, as this case encompasses the pure normal and pure log-normal cases by implication. Essentially there are three types of quantities for which we require distribution definitions. The first are bipolar phase quadrature field components such as $H_z \sin \phi$ or $H_z \cos \phi$, which we shall generically denote as u or v . The second are phase quadrature field components squared, which we shall generically denote as x or y . Thirdly, we have power fluxes which we shall denote as z , and which are the sum of two squares [see (4-4)].

Conventional wisdom has been that, under ideal conditions, z should have a chi square distribution with two degrees of freedom. In reality, we find it usually is more nearly log-normal in distribution (4-3) (see Figures 4.18 and 4.19), and the cumulative probability distribution resembles $H(z)$

$$H(z) = \int_{-\infty}^{\frac{\ln z - \mu_{lg}}{\sigma_{lg}}} \frac{1}{\sqrt{2\pi}} \exp(-z'^2/2) dz' = P\left(\frac{\ln z - \mu_{lg}}{\sigma_{lg}}\right) \quad (4-34)$$

where $P(\cdot)$ is the cumulative normal distribution function. Thus, if z is selected to be greater than fraction $H(z) = p$ of the values, we would have

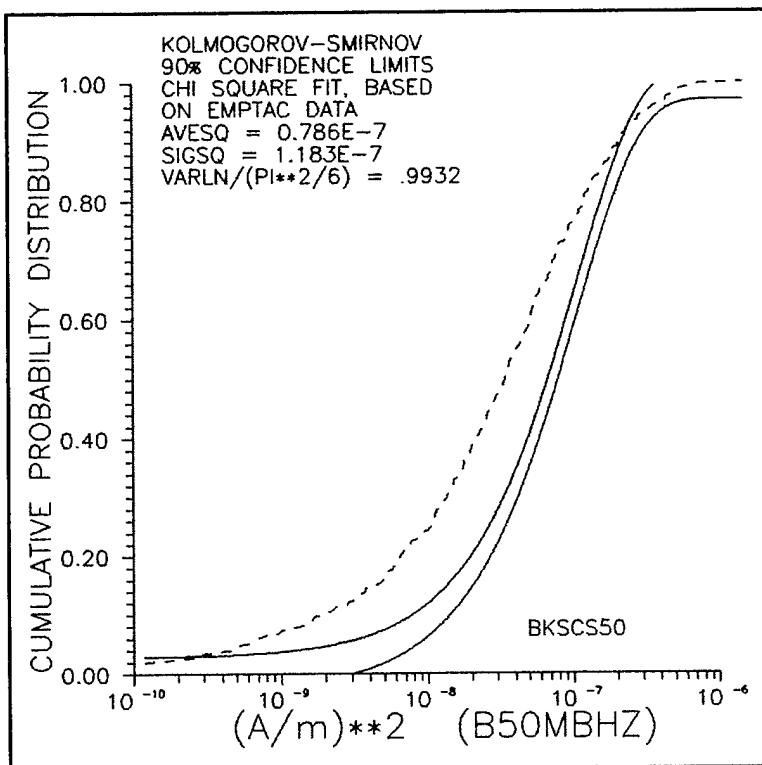


Figure 4.18. In the real world, fields squared and currents squared usually do not fit a chi square distribution very well.

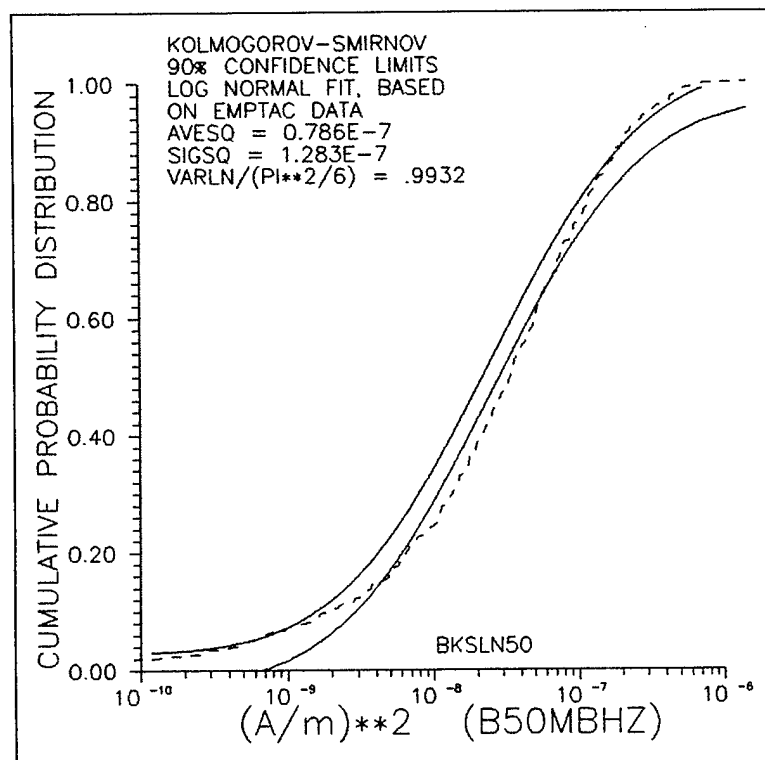


Figure 4.19. Generally, sums of two squared phase-quadrature components look log normal, not chi square in the real world.

$$z(p) = H^{-1}(p) = e^{\mu_{lg} + \sigma_{lg} P^{-1}(p)} \quad (4-35)$$

where $P^{-1}()$ is the inverse of the cumulative normal distribution function. However, as mentioned earlier in this section, this formula tends to generate a distribution with an upper tail having unrealistically large values of z .

This problem is resolved by mandating that, above some cross-over probability P , the distribution density of z shall be chi-square with two degrees of freedom,

$$h_2(z) = \frac{e^{-z/v}}{v} \quad (4-36)$$

giving a cumulative probability distribution of

$$H_2(z) = 1 - e^{-z/v} \quad (4-37)$$

For $H_2(z) = p$ above P , we thus have

$$z(p) = -v \ln(1 - p) \quad (4-38)$$

In general, μ_{lg} and σ_{lg} will be known and P can be guessed at; usually, P is around 0.9. Also, (4-35) and (4-38) must match at P . This gives us an equation uniquely determining v

$$v = \frac{e^{\mu_{lg} + \sigma_{lg} P^{-1}(P)}}{-\ln(1 - P)} \quad (4-39)$$

Figure 4.20 shows $H(z)$ and $H_2(z)$ joined at $P = .9$, with the cumulative distribution of EMPTAC data set B050MBHZ overlaid. For this data set, with $P = 0.9$ we found (4-39) to give $v = 7.62E-8$.

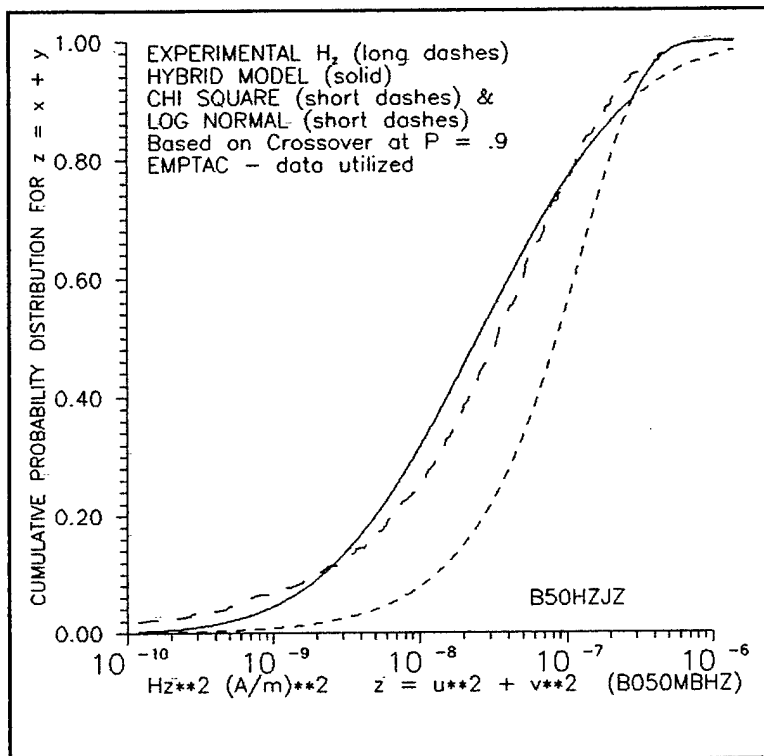


Figure 4.20. Hybrid log-normal/chi-square distribution (solid line), with measured $|H_z|^2$ from Sweep B050MBHZ overlaid (line in long dashes). Crossover occurs at $P = 0.9$.

Distribution of the Squares

In general, the distribution of $x = u^2$ is not very interesting, although we cannot go from the distribution of z to the distribution of u (which is needed) without, in the process, finding $f(x)$, the distribution of x . We have already shown that, if z has a distribution density $h(z)$, x and y have a distribution density $f(x)$, which, upon being autoconvolved, gives back $h(z)$.

We have already presented numerical evidence that the distribution of x must be log normal if z is log normal. Thus, for $p \leq P$ we have the distribution density function

$$f(x) = \frac{1}{\sqrt{2\pi}} \frac{\exp\left(-(\ln x - \mu'_{lg})^2/(2\sigma'_{lg}^2)\right)}{x\sigma'_{lg}} \quad (4-40)$$

and the cumulative probability distribution,

$$F(x) = P\left(\frac{\ln x - \mu'_{lg}}{\sigma'_{lg}}\right) \quad (4-41)$$

where, to a fairly good approximation, we have empirically found that $(\sigma_{lg}', \mu_{lg}')$ are related to (σ_{lg}, μ_{lg}) by (4-20) and (4-21).

For the region ($p > P$) where z has a chi square distribution, the transform of $f_2(z)$ and the inverse transform of the square root can be taken canonically. This manipulation yields a distribution density for x [see (2-100)]

$$f_2(x) = \frac{e^{-x/v}}{\sqrt{\pi x v}} \quad (4-42)$$

and a cumulative distribution function $F_2(x)$ of

$$F_2(x) = 2P(\sqrt{2x/v}) - 1 \quad (4-43)$$

at least for p and $F_2(x) \geq 1/2$. [In (4-43), P is still the cumulative Gaussian distribution, not the cumulative chi square distribution.] If x is selected to be greater than $F(x) = p$ of the values, we have, for $p \leq P$

$$x(p) = e^{\mu_{lg}' + \sigma_{lg}' P^{-1}(p)} \quad (4-44)$$

and for $p \geq P$

$$x(p) = \frac{v}{2} (P^{-1}((p + 1)/2))^2 \quad (4-45)$$

If (4-20) and (4-21) were exact, (4-44) and (4-45) would meet at $p = P$. In actuality, they will differ slightly

$$r e^{\mu_{lg}' + \sigma_{lg}' P^{-1}(p)} = \frac{v}{2} P^{-1}((P + 1)/2) \quad (4-46)$$

where $r \approx 1$ and $\ln r \approx 0$. This slight mismatch may be incorporated into the model by replacing μ_{lg}' with $\mu_{lg}' + \ln r$, which is alright as (4-20) for μ_{lg}' is only an approximate fit anyway. Figure 4.21 shows $F(x)$ and $F_2(x)$ joined at $P = 0.9$.

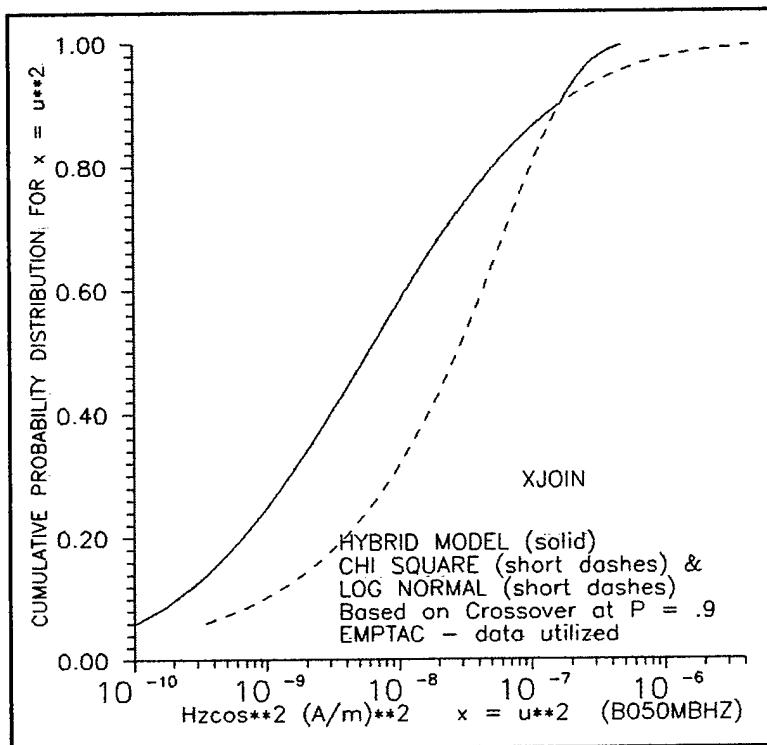


Figure 4.21. The cumulative probability distribution obtained by joining the log normal, $F(x)$ of (4-41), and the chi square, $F_2(x)$ of (4-43), at $P = 0.9$.

Distribution of the Bipolar Phase Quadrature Components

If $x = u^2$ has a monopolar log-normal distribution density $f(x)$ given by (4-40), u will have a bipolar log-normal distribution density $e(u)$ given by [see (2-61)]

$$e(u) = \frac{1}{\sqrt{2\pi}} \frac{\exp\left(- (2 \ln|u| - \mu'_{lg})^2 / (2\sigma'_{lg}^2)\right)}{\sigma'_{lg}|u|} \quad (4-47)$$

and a cumulative probability distribution

$$E(u) = \frac{1}{2} + \frac{1}{2}P\left(\frac{2 \ln u - \mu'_{lg}}{\sigma'_{lg}}\right) \quad (4-48)$$

at least for $u > 0$ or $E(u) > \frac{1}{2}$. Thus, if u is selected to be greater than the fraction $E(u) = p$ of the values, we have, for $p < P'$,

$$u(p) = e^{(\mu'_{lg} + \sigma'_{lg}P^{-1}(2p - 1))/2} \quad (4-49)$$

at least for $p = E(u) > 1/2$ or $u > 0$. We must here note that P' , the u crossover probability, introduced just above differs from P , the crossover probability of x and z . If we want x and z to crossover at $P = 0.90$, u must crossover at $P' = 0.05$ and 0.95, as u is bipolar, while x and z were monopolar.

For the region $p > 0.95 = P'$, where z has a chi square distribution density, u has a normal distribution,

$$e_2(u) = \frac{1}{\sqrt{2\pi}} \frac{e^{-u^2/(2\sigma_g^2)}}{\sigma_g} \quad (4-50)$$

or

$$E_2(u) = P(u/\sigma_g) \quad (4-51)$$

where σ_g is related to v by [see (2-105)]

$$v = 2\sigma_g^2 \quad (4-52)$$

If u is selected to be greater than $S_2(u) = p$ of the values, we have for $p \geq P'$

$$u(p) = \sigma_g P^{-1}(p) \quad (4-53)$$

At $p = P'$, (4-49) and (4-53) for $u(P')$ might not match perfectly:

$$\rho e^{(\mu_{lg}' + \sigma_{lg}' P^{-1}(2P' - 1))/2} = \sigma_g P^{-1}(P') \quad (4-54)$$

where $\rho \approx 1$. This situation permits two varieties of correction: σ_g is related to v , which [through (4-39)] is not a very precisely defined quantity, and may be replaced by σ_g/ρ . Alternatively, μ_{lg}' , which also is not very precise, may be replaced by $\mu_{lg}' + 2 \ln \rho$. We do not know if $2 \ln \rho = \ln r$, nor does this seem a very important issue, as both are *ad hoc* corrections to heuristic factors. Figure 4.22 shows $E(u)$ and $E_2(u)$ joined at $P' = 0.95$.

HYBRID POWER-FLUX MODEL FOR THE CELESTRON 8 TELESCOPE

A hybrid normal/log-normal fit to the cumulative distribution of the magnetic field squared was also attempted for the Celestron 8 satellite telescope data for frequency swept from 8 GHz to 18 GHz. In this case, it turns out that a hybrid fit is better made with crossover at $p = 0.875$. Figure 4.23 shows $F(z)$ and $F_2(z)$ joined at $P = 0.875$, with the cumulative distribution of the

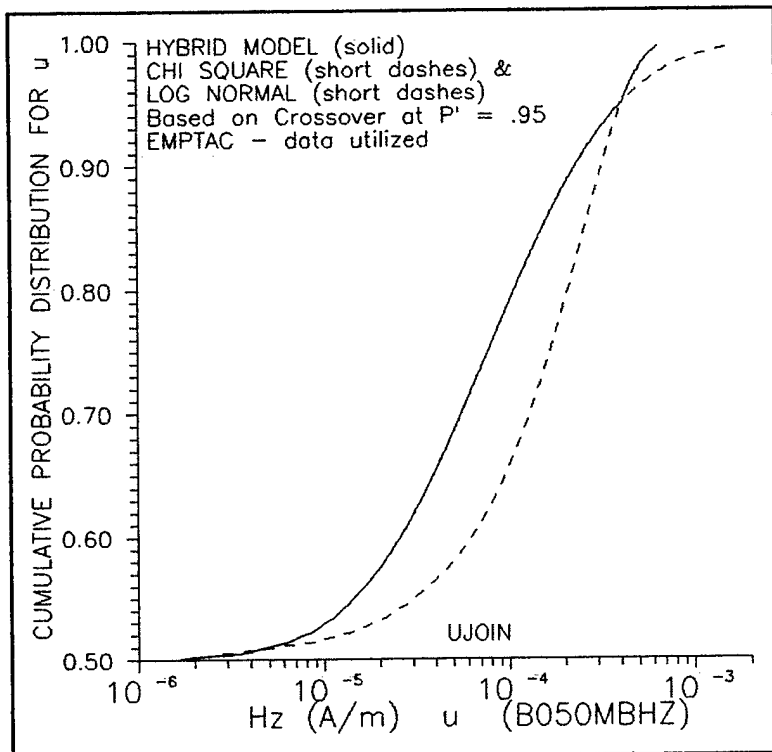


Figure 4.22. The cumulative probability distribution obtained by joining the log normal, $E(u)$ of (4-48), and the chi square, $E_2(u)$ of (4-51), at $P = 0.95$.

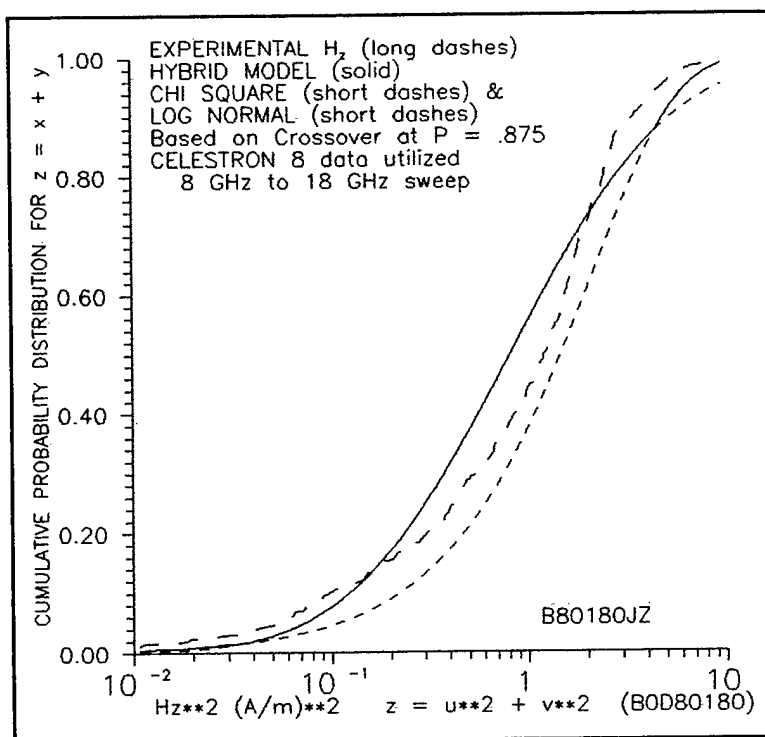


Figure 4.23. Hybrid log-normal/chi-square distribution (solid line), with measured $|H_z|^2$ from Celestron 8 8 GHz to 18 GHz sweep overlaid (line in long dashes). Crossover occurs at $P = 0.875$. This hybrid fit to the data is not so good as the EMPTAC data fit appearing in Figure 4.20.

Celestron 8 data set overlaid. For this data set, with $P = 0.875$ we found (4-39) to give $v = 2.104$.

CONCLUSIONS FOR THIS SECTION

EM power flux inside an overmoded cavity can be statistically represented by a normal/log-normal distribution or by a modified Bessel function of the second kind. Deducing the distribution of electromagnetic fields within the cavity, given the distribution of power flux is a fairly simple procedure. It is necessary to have the statistical field distribution to model the fields which actually couple to and drive the enclosure cabling. Chi square modeling of the power-flux distribution leads to a field distribution model which is normal. This procedure for deducing the cable-drive field distribution yields predicted cable currents with distributions which lie well within experimental uncertainty and repeatability (i.e., well within a factor of two).

REFERENCES

- [1] R. Lupton, *Statistics in Theory and Practice*, Princeton: Princeton University Press, 1993 (see especially pp. 36-37).
- [2] G. A. Korn and T. M. Korn, *Mathematical Handbook for Scientists and Engineers*, New York: McGraw-Hill, 1968 (see, especially pp. 632-633).
- [3] Mood, Graybill, and Boes, p. 117, Eq. (39), *Introduction to Theoretical Statistics*, 3rd Ed., McGraw-Hill, 1974.
- [4] R. Holland & R. St. John, "Statistical Responses of Enclosed Systems to HPM Environments," *Conference Proceedings, 10th Annual Review of Progress in Applied Computational Electromagnetics*, Monterey, CA, Vol. II, pp. 554-568, 21-26 March 1994.
- [5] R. Holland & R. St. John, "Enforcing Correlation of Statistically Generated EM Cable Drivers," *Conference Proceedings, 11th Annual Review of Progress in Applied Computational Electromagnetics*, Monterey, CA, Vol. I, pp. 308-320, 20-25 March 1995.
- [6] R. Holland & R. St. John, "Statistical Coupling of EM Fields to Cables in an Overmoded Cavity," *Conference Proceedings, 12th Annual Review of Progress in Applied Computational Electromagnetics*, Monterey, CA, Vol. 2, pp. 877-887, 18-22 March 1996.
- [7] Price, R. H., *et al*, "Determination of the Statistical Distribution of Electromagnetic Field Amplitudes in Complex Cavities," 88JAL129, JAYCOR, 1 June 1988.

- [8]. Price, R. H., H. T. Davis, and E. P. Wenaas, "Determination of the Statistical Distribution of Electromagnetic-Field Amplitudes in Complex Cavities," *Phys. Rev. E*, Vol. 48, pp. 4716-4729, December 1993.
- [9]. T. H. Lehman and R. M. Marshall, "Application of statistical physics to derivation of stress and strength distributions," Ball Systems Engineering Division, Albuquerque, NM, September 26, 1991.
- [10]. T. H. Lehman, "A statistical theory of electromagnetic fields in complex cavities," Air Force Phillips Laboratory, Interaction Note 494, May 1993.

Chapter 5. CHI SQUARE VARIANTS: THE LEHMAN DISTRIBUTION

PRELIMINARY OVERVIEW

Recently, obscurely disseminated work by Lehman has come to our attention which deduces a somewhat different overmoded enclosure power-flux distribution that the simple chi square result [1-4]. This new formulation shows excellent agreement between theory and observation on the upper tail of distributions, which is where harmful effects will occur if they occur at all. While we are not sure just why this novel procedure should yield power-flux distributions which agree with the upper tail (as opposed to the midpoint, where most models seem to work best, or, for that matter, as opposed to the lower tail), we are most impressed with the result.

This new work also presumes that the internal cavity response should incorporate the physics which leads to a power-flux distribution for z_1 which is chi square with two degrees of freedom. However, a hypothesis is additionally put forward that the field external to the cavity can illuminate the apertures from any of three directions, or two phase quadratures, and thus should result in inward power leakage z_2 which is chi square with six degrees of freedom. These assumptions imply the overall internal cavity response should have a power-flux probability density function which is the product of these two variates

$$z = z_1 z_2 \quad (5-1)$$

In two dimensions, the power flux probability density function thus becomes representable as

$$h_{\chi_2^2}(z_1) h_{\chi_6^2}(z_2) dz_1 dz_2 \quad (5-2)$$

where this expression gives the probability that z_1 is between z_1 and $z_1 + dz_1$, while z_2 is between z_2 and $z_2 + dz_2$. However, z , z_1 , and z_2 are not all independent variables. If (5-1) holds, the probability that z_1 is between z_1 and $z_1 + dz_1$, while z is between z and $z + dz$ is obtained from the variate transformation

$$\begin{aligned} z_1 &= z'_1 \\ z_2 &= z'/z'_1 \end{aligned} \quad (5-3)$$

The two-dimensional probability density function then becomes

$$h_{\chi_2^2}(z'_1) h_{\chi_6^2}(z'/z'_1) \frac{\partial(z_1, z_2)}{\partial(z'_1, z')} dz'_1 dz' \quad (5-4)$$

where

$$\frac{\partial(z_1, z_2)}{\partial(z'_1, z')} = \begin{vmatrix} \partial z_1 / \partial z'_1 & \partial z_2 / \partial z'_1 \\ \partial z_1 / \partial z' & \partial z_2 / \partial z' \end{vmatrix} = \begin{vmatrix} 1 & -1/z_1'^2 \\ 0 & 1/z_1' \end{vmatrix} = 1/z_1' \quad (5-5)$$

is the Jacobian of the variate transformation. We now wish to find the probability that z is between z and $z + dz$ regardless of z'_1 . This 1D probability differential is obtained by summing all the 2D probability differentials of z'_1 and z' over z'_1 ; i.e., by integrating (5-4) over all possible z'_1

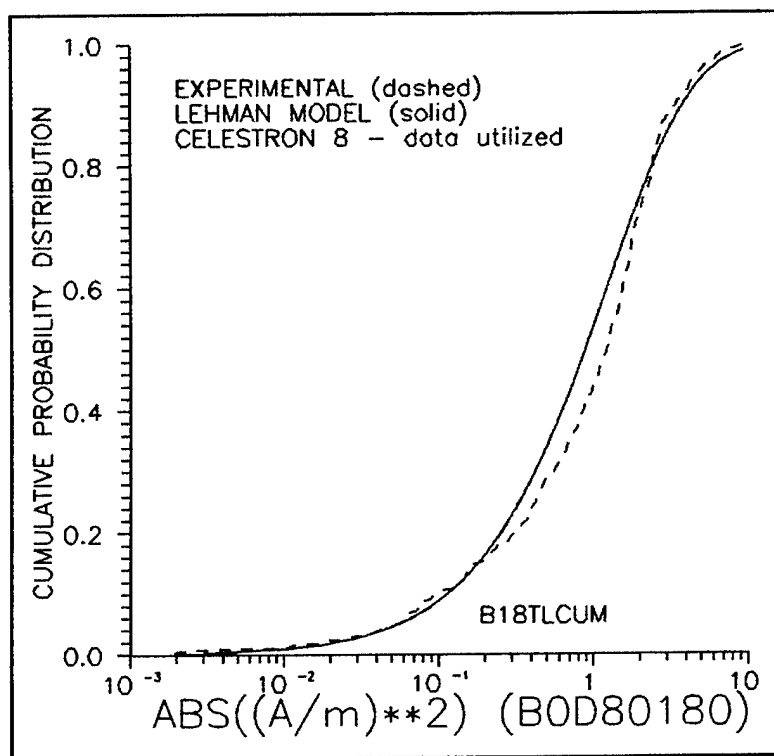
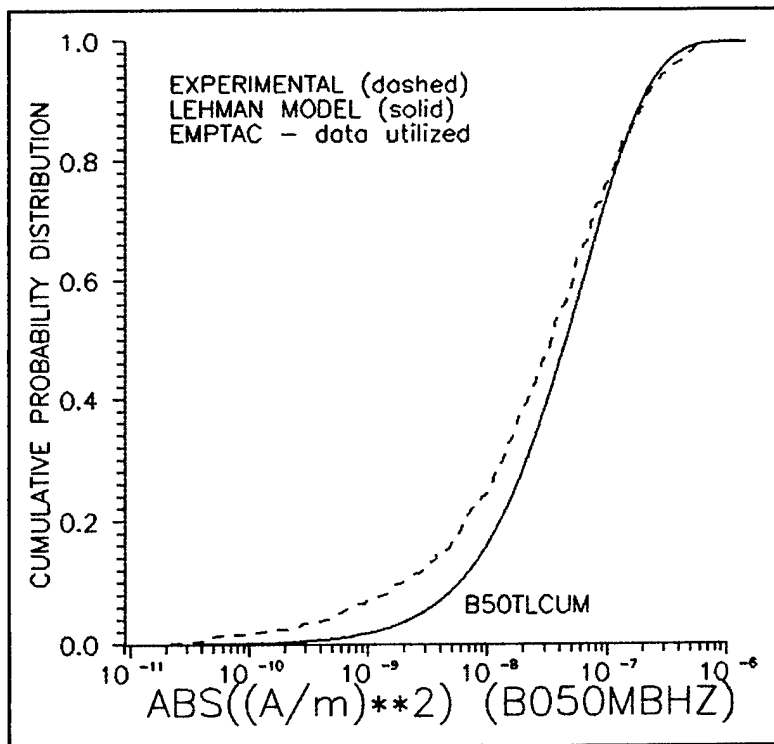
$$\begin{aligned} h_l(z') dz' &= \int_0^\infty h_{\chi_2^2}(z'_1) h_{\chi_6^2}(z'/z'_1) \frac{dz'_1 dz'}{z'_1} = \int_0^\infty [\gamma'_2 e^{-\gamma'_2 z'_1}] [\gamma_6'^3 (z'/z'_1)^2 e^{-\gamma'_6 z'/z'_1}] \frac{dz'_1 dz'}{z'_1} \\ &= \Lambda^2 z'^2 K_2(2\sqrt{\Lambda z'}) dz' \end{aligned} \quad (5-6)$$

In the future, we shall refer to $h_l(z')$ as the Lehman distribution. In (5-6), γ'_2 , γ'_6 , and Λ are constants related by

$$\Lambda = \gamma'_2 \gamma'_6 \quad (5-7)$$

with Λ related to the mean or the standard deviation of the power-flux probability density function by (4-33).

Figure 5.1 illustrates the cumulative probability distribution agreement between the Lehman distribution and EMPTAC data (100 MHz to 1 GHz sweep), while Figure 5.2 illustrates the agreement for the Celestron 8 satellite telescope (8 GHz to 18 GHz sweep). We do not know, at this time, if the Lehman distribution would apply to the situation where the microwave source is actually internal to the cavity, as in the Price-Davis study,[5,6] although we believe this configuration would have power flux simply chi square with two degrees of freedom. Also, we believe the power fluxes external to an open geometry (such as a helicopter) could be characterized simply as a chi square distribution with six degrees of freedom. It seems that this model somehow manages to ignore the "trend" on power-flux data (see Section 2), and to give a correct upper-tail representation irrespective of the gross overall shape of the response distribution. This accomplishment is a major keystone in the successful representation of cable-driving fields; previously, we had no clear idea how to restore "trend" effects into the model (other than using a log normal representation). The Lehman model, as represented in Figures 5.1 and 5.2, provides something that Figures 4.20 and 4.23 do not: a smooth, data-derived representation for the upper end of the distribution which does not require case-by-case tweaking.



Approximate deconvolution of the phase-quadrature field-component distribution out of the Lehman distribution for the power flux is a bit complicated, and will be described in a later subsection. Taking the inverse transform of the square root of the Fourier transform of $h_l(z)$ in (4-33) or (5-6), either numerically or canonically, seems formidable. It also occurs that we are unable to deduce a precise function which, when autoconvolved, gives back $h_l(z)$ of (4-33) or (5-6).

DETAILS OF THE LEHMAN DERIVATION

Lehman has suggested that the power in a cavity with apertures is best described by a combination of two different distributions: $h_{\chi_2}(2,z)$ and $h_{\chi_2}(6,z)$. The physical rationale behind this thinking is the power in a perfect cavity is described by a $h_{\chi_2}(2,z)$ distribution whereas the drivers resulting from the apertures are described by $h_{\chi_2}(6,z)$ (two polarizations over three directions); the two multiplied variates together then give the desired description.

The multiplication of the two distributions is equivalent to multiplying (point-by-point) a set of numbers with one distribution by points in the other. Relative to the pdf (probability distribution function) densities of the $h_{\chi_2}(2,z)$ and $h_{\chi_2}(6,z)$ distributions, this is accomplished by [see (5-6)]

$$h_l(z) = \int_0^\infty \frac{1}{|z'_1|} h_{\chi_2}(z/z'_1) h_{\chi_2}(z'_1) dz'_1 \quad (5-8)$$

where the h_{χ_2} distribution with v degrees of freedom and a scaling factor of γ_v is

$$h_{\chi_v}(z) = \frac{z^{\frac{v-2}{2}} e^{-\frac{z}{2\gamma_v}}}{(2\gamma_v)^{\frac{v}{2}} \Gamma(v/2)} \quad (5-9)$$

[In (5-9), the γ_v are related to the γ'_v of (5-7) by $\gamma'_v = 1/(2\gamma_v)$.] This yields a Lehman distribution of

$$h_l(z) = \frac{1}{4\gamma_2(2\gamma_6)^3} \int_0^\infty z'_1 e^{-\alpha z'_1 - \frac{z}{2\gamma_2 z'_1}} dz'_1 \quad (5-10)$$

where $\alpha = 1/(2\gamma_6)$. The integral has been written in this form to employ the trick,

$$ze^{\alpha z} = \frac{\partial e^{\alpha z}}{\partial \alpha} \quad (5-11)$$

The probability density function can now be written as

$$h_t(z) = -\frac{1}{4\gamma_2(2\gamma_6)^3} \int_0^\infty \frac{\partial}{\partial \alpha} e^{-\alpha x - \left(\frac{z}{2\gamma_2 x}\right)} dx \quad (5-12)$$

Using Gradshteyn and Ryzhik,[7] Eq. (3.324.1), this reduces to

$$h_t(z) = -\frac{1}{4\gamma_2(2\gamma_6)^3} \frac{\partial}{\partial \alpha} \left[\sqrt{\frac{2z}{\gamma_2 \alpha}} K_1 \left(\sqrt{\frac{2z\alpha}{\gamma_2}} \right) \right] \quad (5-13)$$

Where K_1 is the first order, modified Bessel function of the second kind.

Taking the partial derivative with respect to α yields,

$$h_t(z) = -\frac{1}{4\gamma_2(2\gamma_6)^3} \sqrt{\frac{2z}{\gamma_2}} \frac{1}{2\alpha} \left[\frac{-1}{\sqrt{\alpha}} K_1 \left(\sqrt{\frac{2z\alpha}{\gamma_2}} \right) + \frac{1}{\sqrt{\alpha}} \sqrt{\frac{2z\alpha}{\gamma_2}} K_1' \left(\sqrt{\frac{2z\alpha}{\gamma_2}} \right) \right] \quad (5-14)$$

Then, using the Bessel-function relationship

$$z K_1'(z) = K_1(z) - z K_2(z) \quad (5-15)$$

shows that the Lehman power-flux probability density function is

$$h_t(z) = \frac{z}{2^4(\gamma_2 \gamma_6)^2} K_2 \left(\sqrt{\frac{z}{\gamma_2 \gamma_6}} \right) \quad (5-16)$$

or, equivalently, as in [1-4]

$$h_l(z) = z \Lambda^2 K_2(2\sqrt{\Lambda z}) \quad (5-17)$$

where Λ is the single scaling factor of (5-7), and K_2 is the second order, modified Bessel function of the second kind.

The primary attributes of interest for this pdf are the cumulative distribution function (cdf), the mean μ_l , and the standard deviation σ_l . The cdf is the integral of the pdf, and is given as

$$H_l(z) = \int_0^z z_1' \Lambda^2 K_2(2\sqrt{\Lambda z_1'}) dz_1' \quad (5-18)$$

By using the Bessel-function relation,

$$\frac{d}{dz} (z^n K_n(z)) = -z^n K_{n-1}(z) \quad (5-19)$$

the Lehman cdf becomes

$$H_l(z) = -\frac{1}{8} (z_1')^3 K_3(z_1') \Big|_0^{2\sqrt{\Lambda z}} \quad (5-20)$$

Amazingly enough, we can find that

$$\lim_{z \rightarrow 0} z^3 K_3(z) = 8 \quad (5-21)$$

and the cdf is then shown to be

$$H_l(z) = 1 - (\Lambda z)^{3/2} K_3(2\sqrt{\Lambda z}) \quad (5-22)$$

The cumulative Lehman distribution is shown with the $h_{\chi^2}(2,z)$ and the $h_{\chi^2}(6,z)$ distribution functions in Figure 5.3. The Lehman distribution is the solid line meeting the $h_{\chi^2}(6,z)$ distribution at the upper end and the $h_{\chi^2}(2,z)$ distribution at the lower end. This figure is based on Λ , γ_2 , and γ_6 all set to 1.

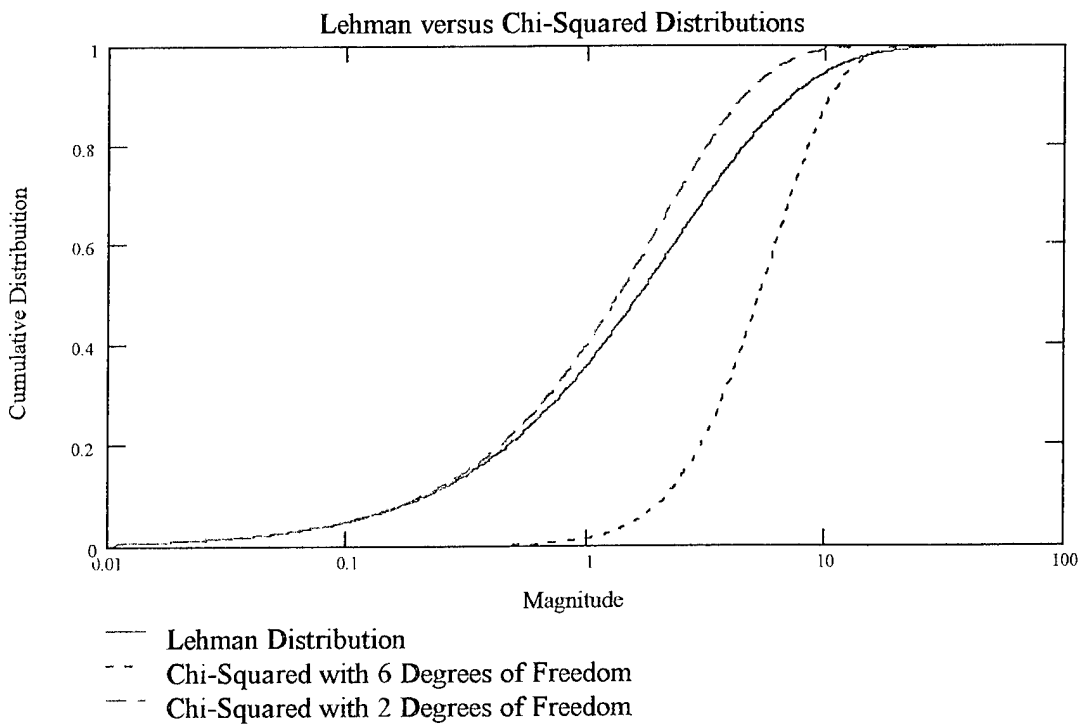


Figure 5.3. Comparison of the Lehman, $h_{\chi^2}(2,z)$ and the $h_{\chi^2}(6,z)$ cumulative distributions [based on $(\Lambda, \gamma_2, \gamma_6) = (1, 1, 1)$].

The mean and standard deviation are computed through definite integrals,

$$\mu_l = \int_0^{\infty} z h_l(z) dz \quad \sigma_l^2 = \int_0^{\infty} z^2 h_l(z) dz - \mu_l^2 \quad (5-23)$$

Use of Gradshteyn and Ryzhik, [7] Eq.(6.561.16), yields

$$\int_0^{\infty} z^{\mu} K_v(\alpha z) dz = 2^{\mu-1} \alpha^{-\mu-1} \Gamma\left(\frac{1+\mu+v}{2}\right) \Gamma\left(\frac{1+\mu-v}{2}\right) \quad (5-24)$$

Thus, the Lehman mean and standard deviation are found to be

$$\mu_l = \frac{3}{\Lambda} \quad \sigma_l = \frac{\sqrt{15}}{\Lambda} \quad (5-25)$$

The fit of the Lehman distribution to two sources of experimental data was undertaken to examine its applicability to reality. The first fit was made to the square of the magnetic field found in the EMPTAC illuminated by the Ellipticus antenna; these data are shown in Figure 5.4 for the high-frequency sweep (100 MHz to 1 GHz). It can be seen that there is a trend in the data where the magnitude increases with frequency. Using the average of this data to define the Λ parameter, the fit is given in Figure 5.5. (In Figure 5.6, additional comparisons include log normal and chi square matches.) The solid line is the EMPTAC data and the dashed line is the Lehman distribution. It can be seen that the best fit is for the largest values of the magnetic field. This is probably due to dominance of the field variations over the trend only at the largest values. To verify this assumption, the fit of the EMPTAC data from 500 MHz to 1 GHz was found. These limits were chosen to use data for which there was no obvious trend (see Figures 5.3 and 5.7.) The improved fit in Figure 5.8 indicates that, in this restricted range, the Lehman distribution describes the data well, even at and below midrange.

In Figure 5.9, we see EMPTAC data for the low-frequency sweep (300 kHz to 100 MHz). The lower values in this plot are believed to be beneath the noise floor. Even so, the Lehman fit (Figure 5.10) matches the data distribution nicely, especially (again) at the upper tail. Figure 5.11 shows a partial low-frequency sweep (9-100 MHz). This data is actually less well matched (Figure 5.11), although the upper tail ($cdf \geq .7$) is still not badly anticipated.

The second set of experimental data to be examined was that taken by Pohle of the Air Force Phillips Laboratory on the Celestron 8 telescope. Data were taken from 1.5 GHz to 18 GHz in three sweeps. Figure 5.13 shows the 1.5 - 3.5 GHz data, and Figure 5.14 shows that the Lehman distribution matches even this strange measurement result. Figure 5.15 shows the 3.5 - 8.0 GHz data. This is a case where the Lehman procedure has been pushed too far (see Figure 5.16). It is not clear at this time what is the critical difference between the Figure 5.14 data and the Figure 5.16 data. Finally, data from the 8 to 18 GHz sweep was compared with the Lehman distribution. These data are shown in Figure 5.17. Even at the highest frequencies, there is here a residual trend, but the match with the Lehman distribution is still quite good (see Figure 5.18).

Based on these comparisons, the Lehman distribution fits as well as or better than the hybrid chi-squared distribution. In addition, there is a physical basis in the approach of two-degrees-of-freedom power in the cavity driven by six-degrees-of-freedom apertures. The capability of the Lehman distribution to fit the data well at the highest values obviously advocates its use in its present or enhanced form.

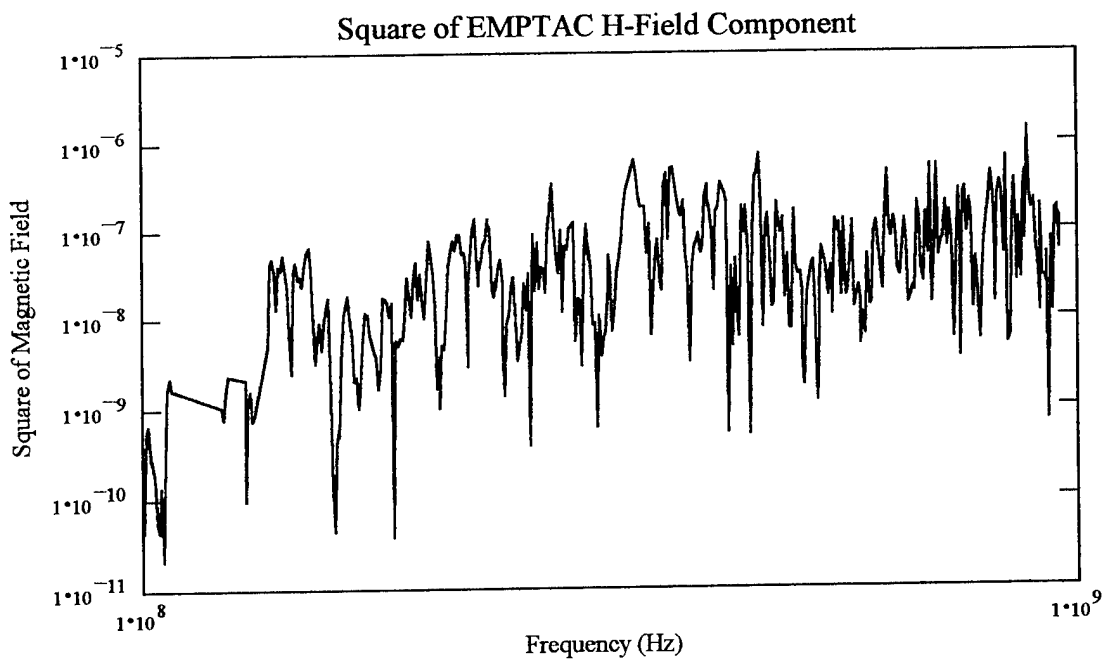


Figure 5.4. Square of magnetic field in the EMPTAC (100 MHz - 1 GHz high-frequency sweep of H_z , B050MBHZ)

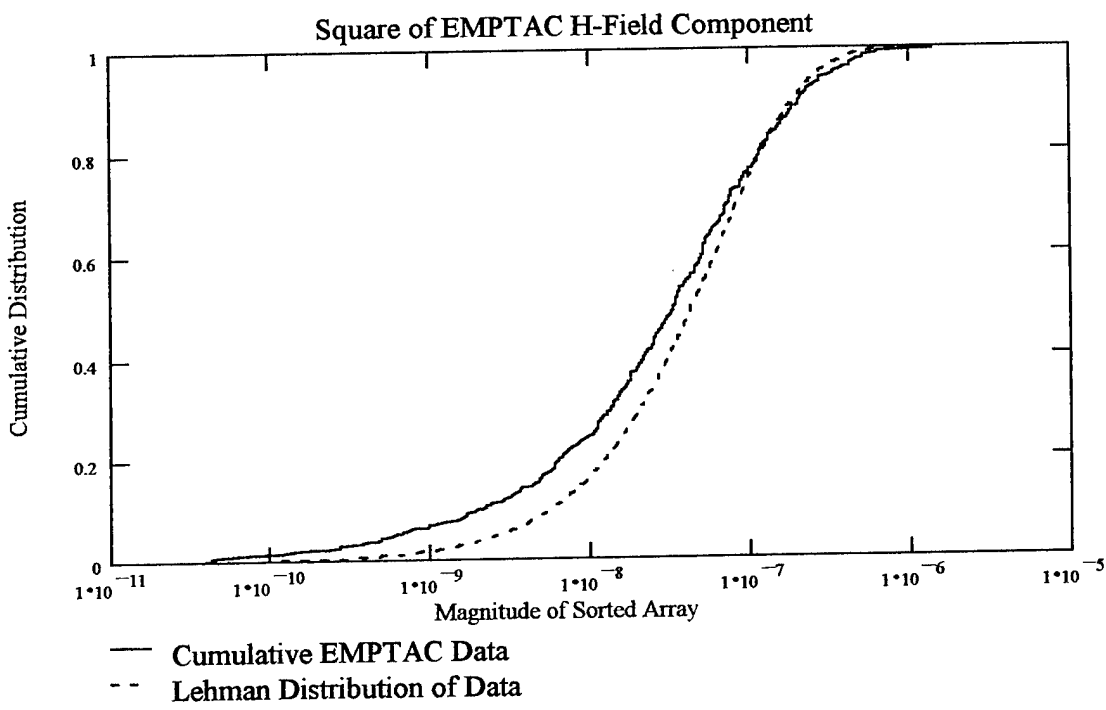


Figure 5.5. Lehman distribution (based on $\Lambda = 3.814e+7 = 3/\mu_{data}$) and EMPTAC data from 100 MHz to 1 GHz.

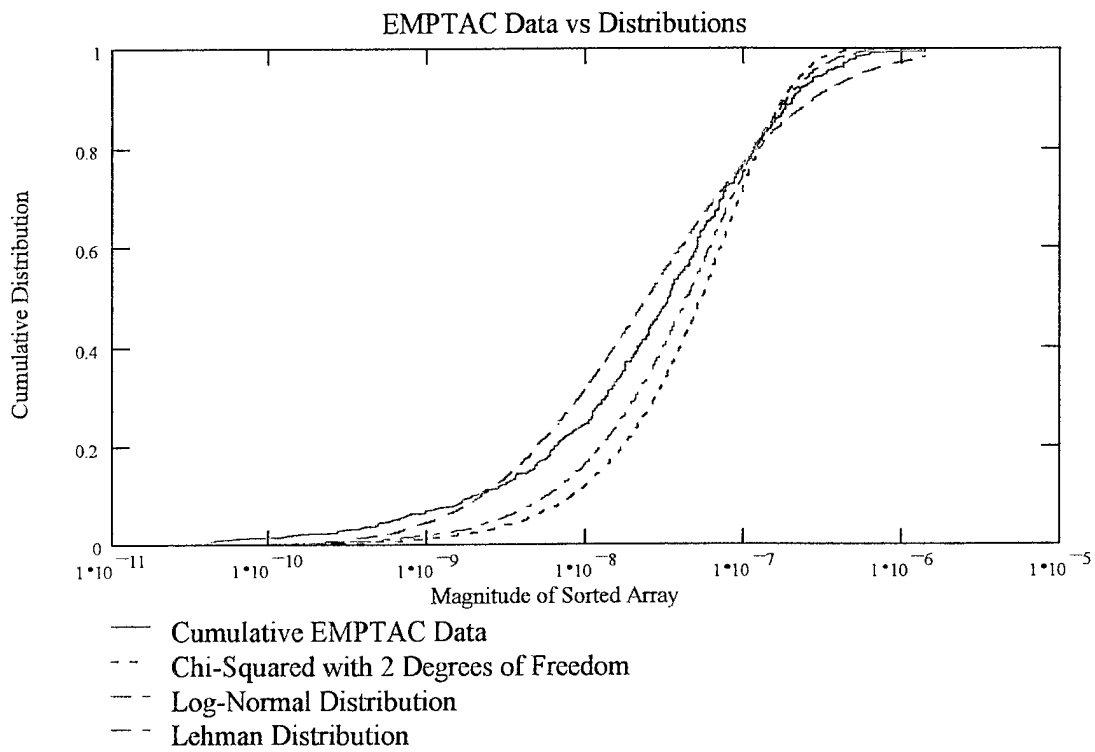


Figure 5.6 EMPTAC data from 100 MHz to 1 GHz compared with various fits.

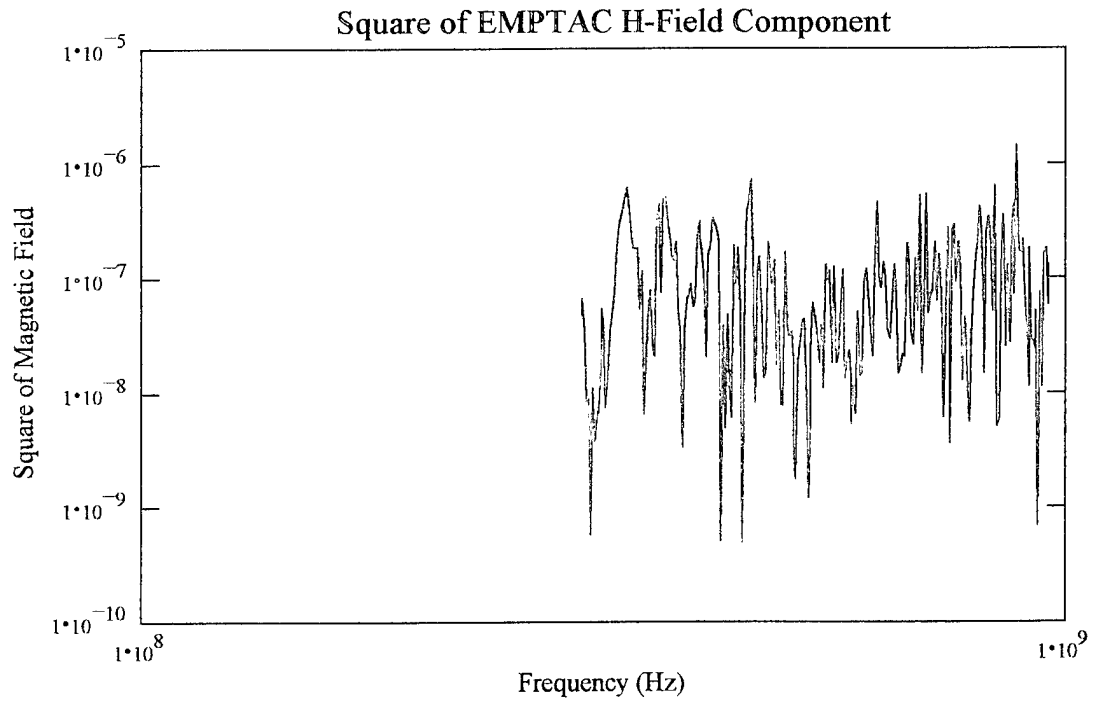


Figure 5.7. Square of magnetic field in the EMPTAC (500 MHz - 1 GHz partial low-frequency sweep of H_z , A050MBHZ).

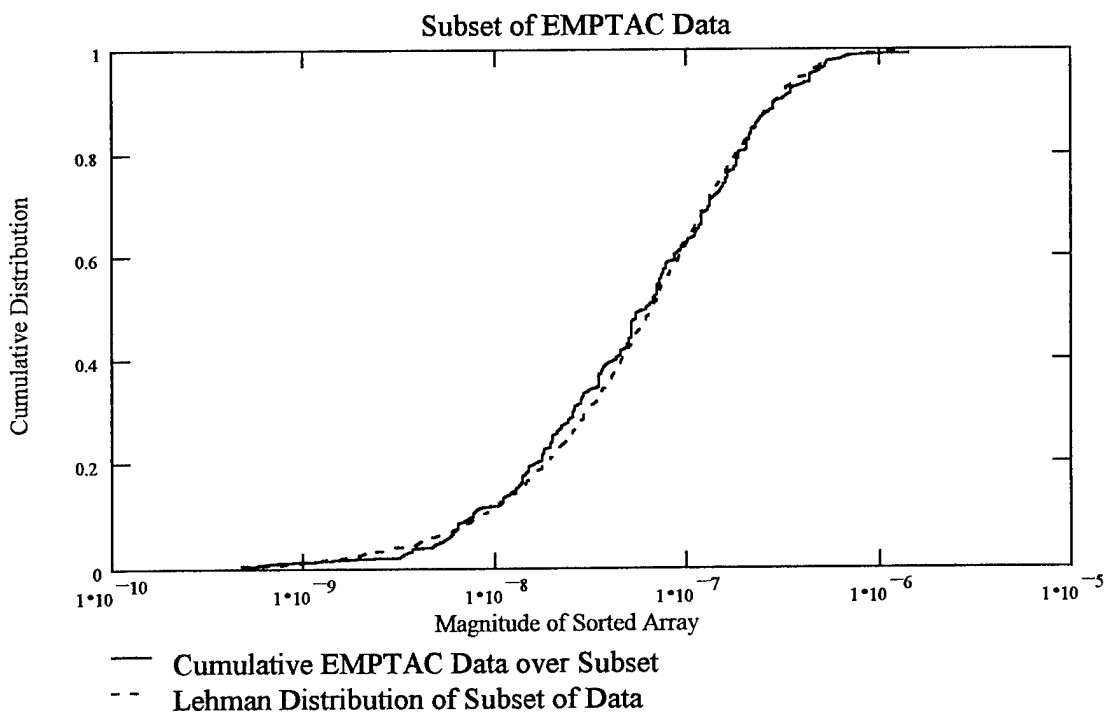


Figure 5.8. Lehman distribution (based on $\Lambda = 2.591e+7 = 3/\mu_{\text{data}}$) and EMPTAC data from 500 MHz to 1 GHz.

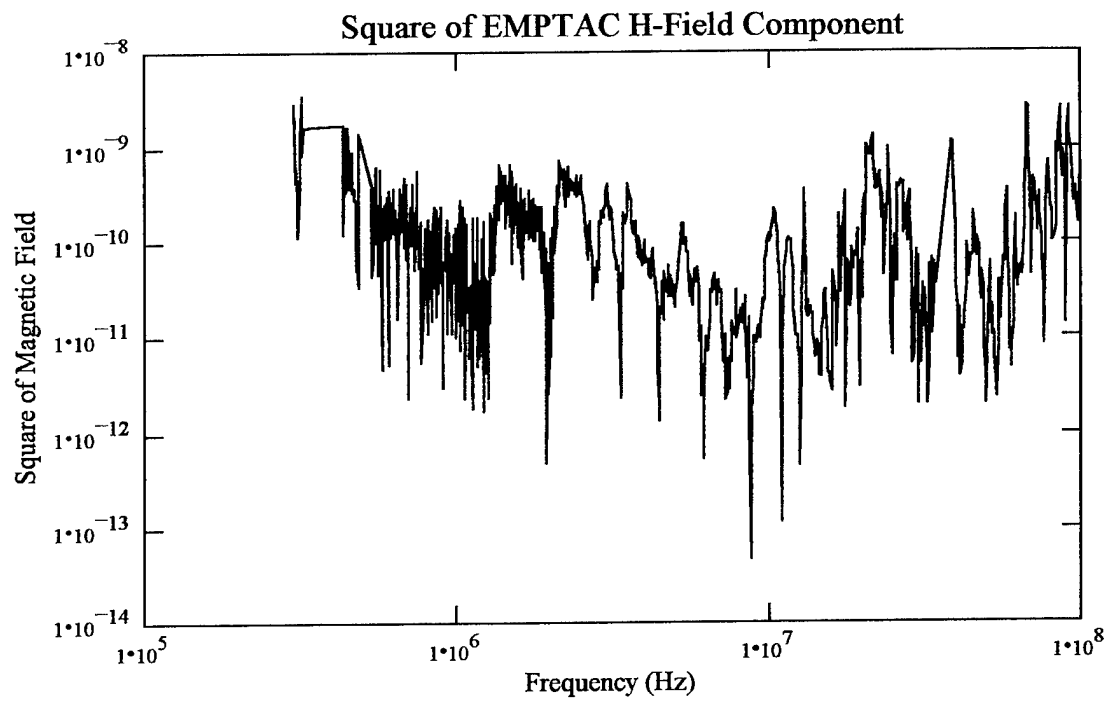


Figure 5.9. Square of magnetic field in the EMPTAC (300 kHz - 100 MHz low-frequency sweep of H_z , A050MBHZ).

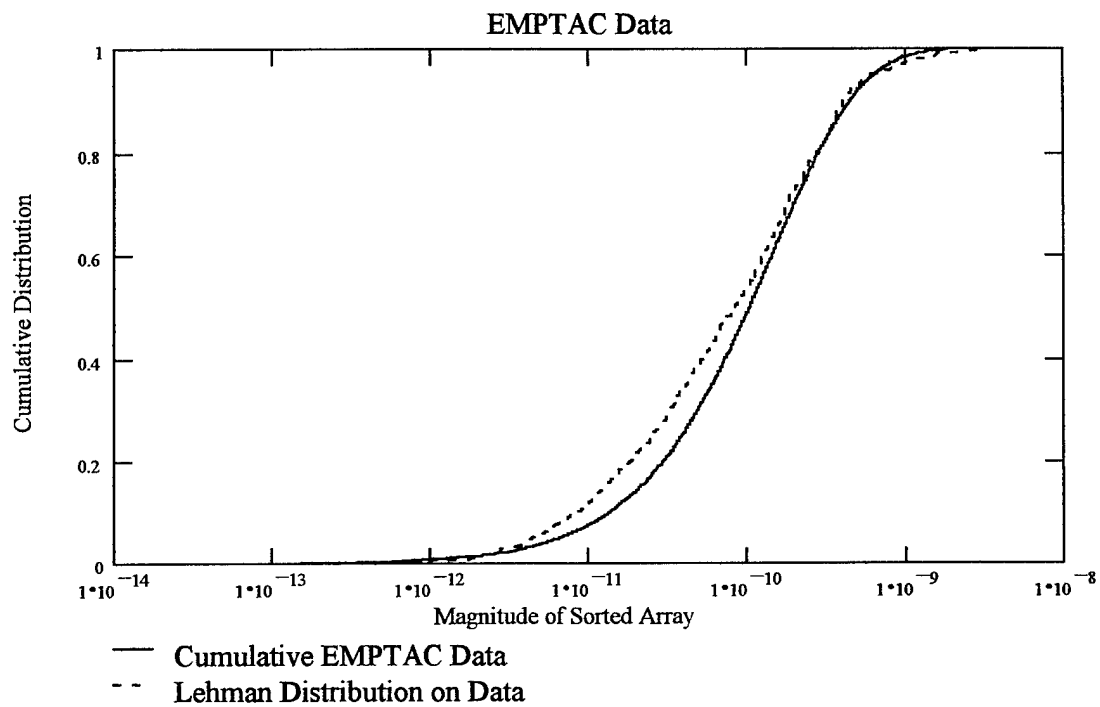


Figure 5.10. Lehman distribution (based on $\Lambda = 1.63e+10 = 3/\mu_{\text{data}}$) and EMPTAC data from 300 kHz to 100 MHz.

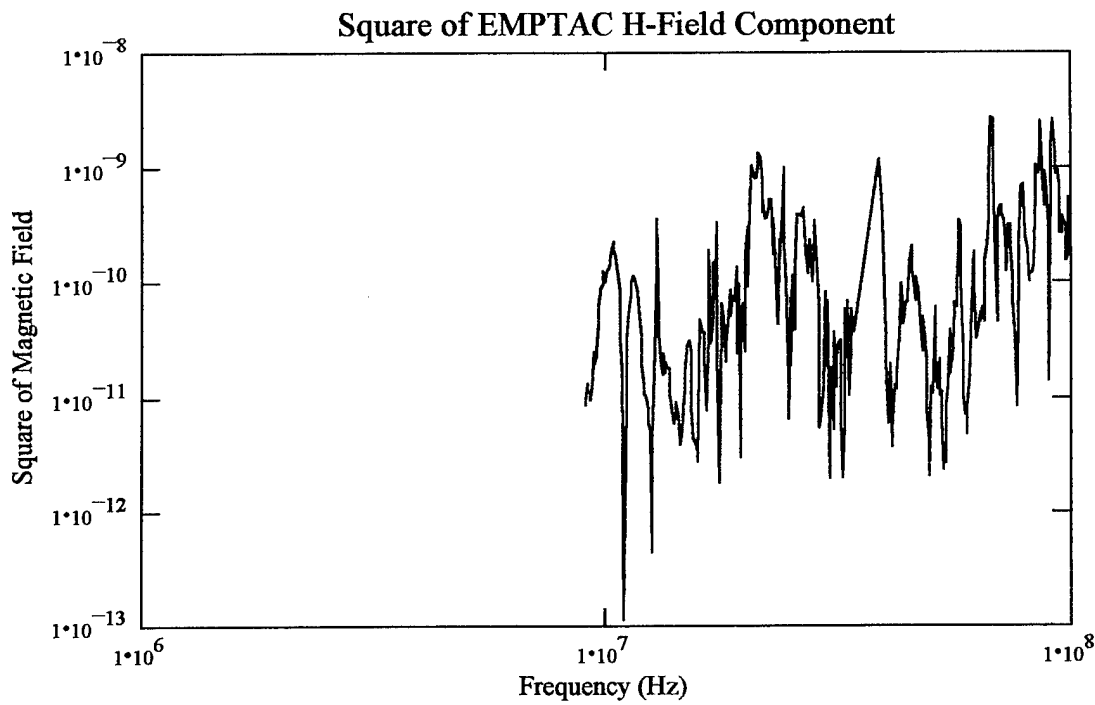


Figure 5.11. Square of magnetic field in the EMPTAC (9 MHz - 100 MHz low-frequency partial sweep of H_z , A050MBHZ).

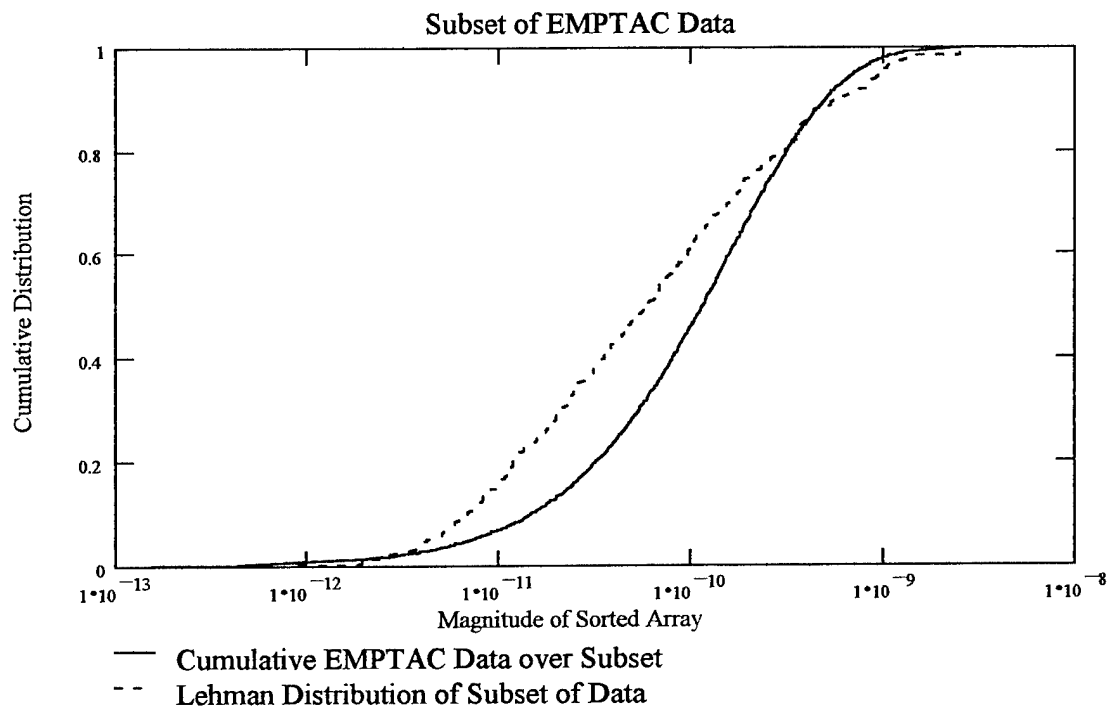


Figure 5.12. Lehman distribution (based on $\Lambda = 1.478\text{e}+10 = 3/\mu_{\text{data}}$) and EMPTAC data from 9 MHz to 100 MHz.

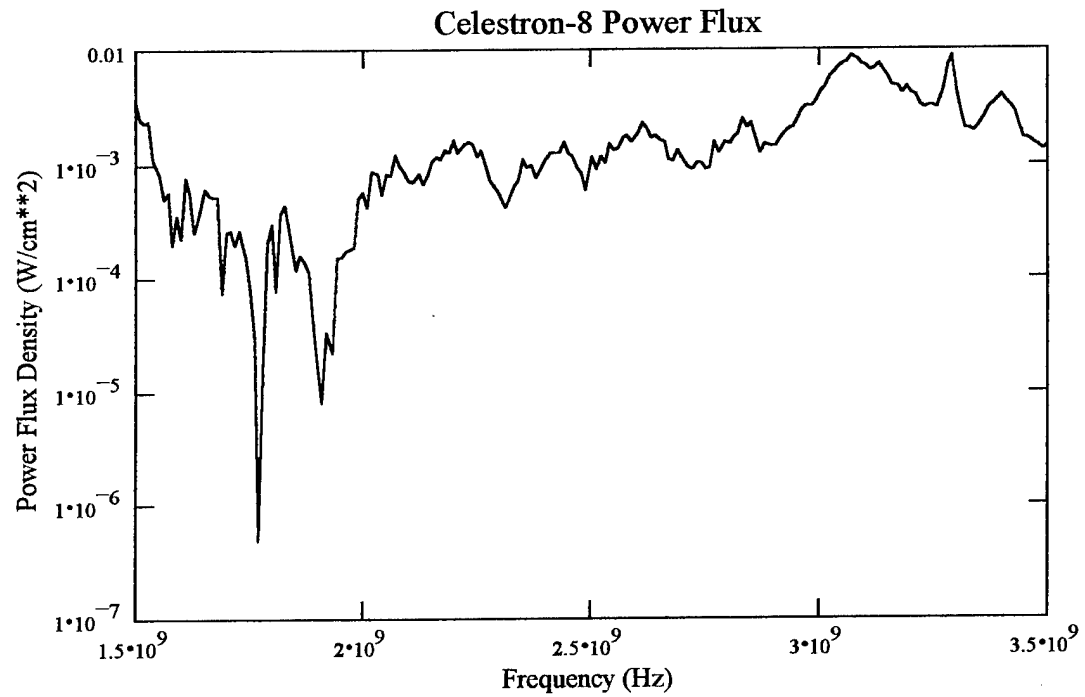


Figure 5.13. Power flux density at focal plane in Celestron 8 satellite telescope for 1.5 GHz - 3.5 GHz sweep.

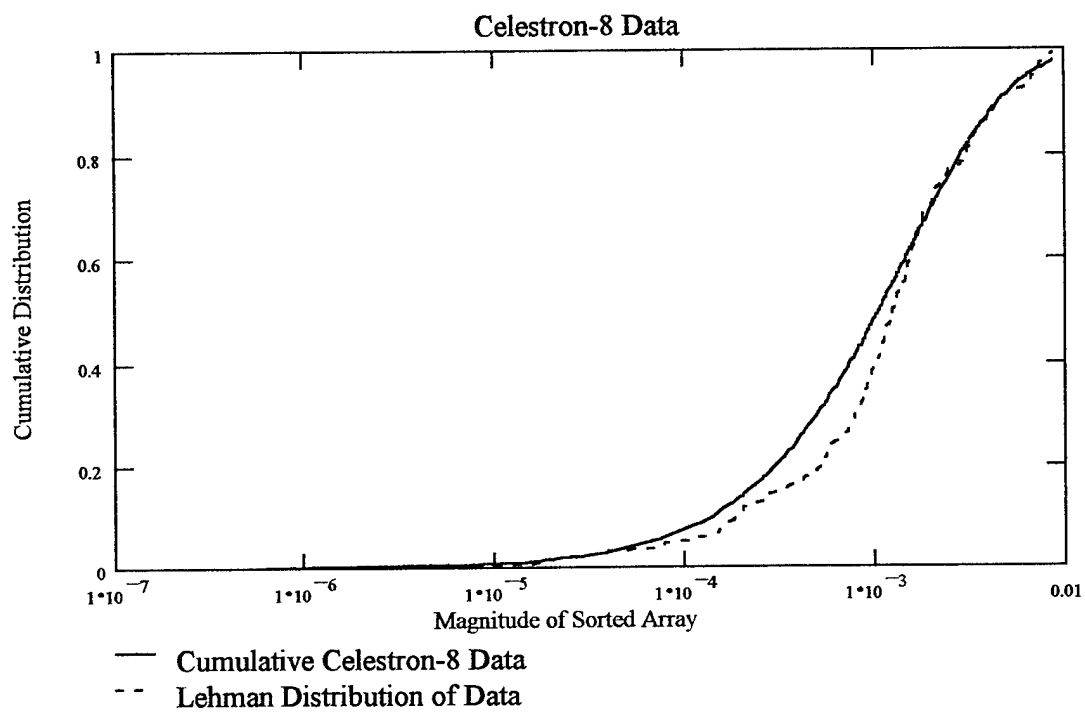


Figure 5.14. Lehman distribution (based on $\Lambda = 1.596e+3 = 3/\mu_{\text{data}}$) and Celestron 8 data from 1.5 to 3.5 GHz sweep.

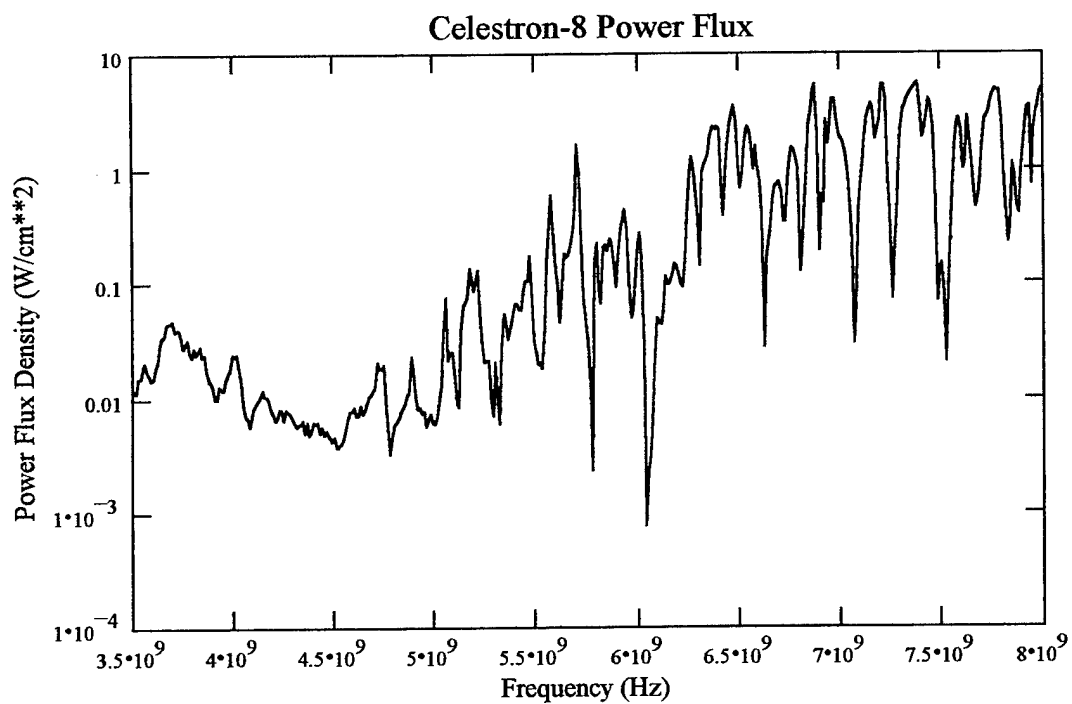


Figure 5.15. Power flux density at focal plane in Celestron 8 satellite telescope for 3.5 GHz - 8 GHz sweep.

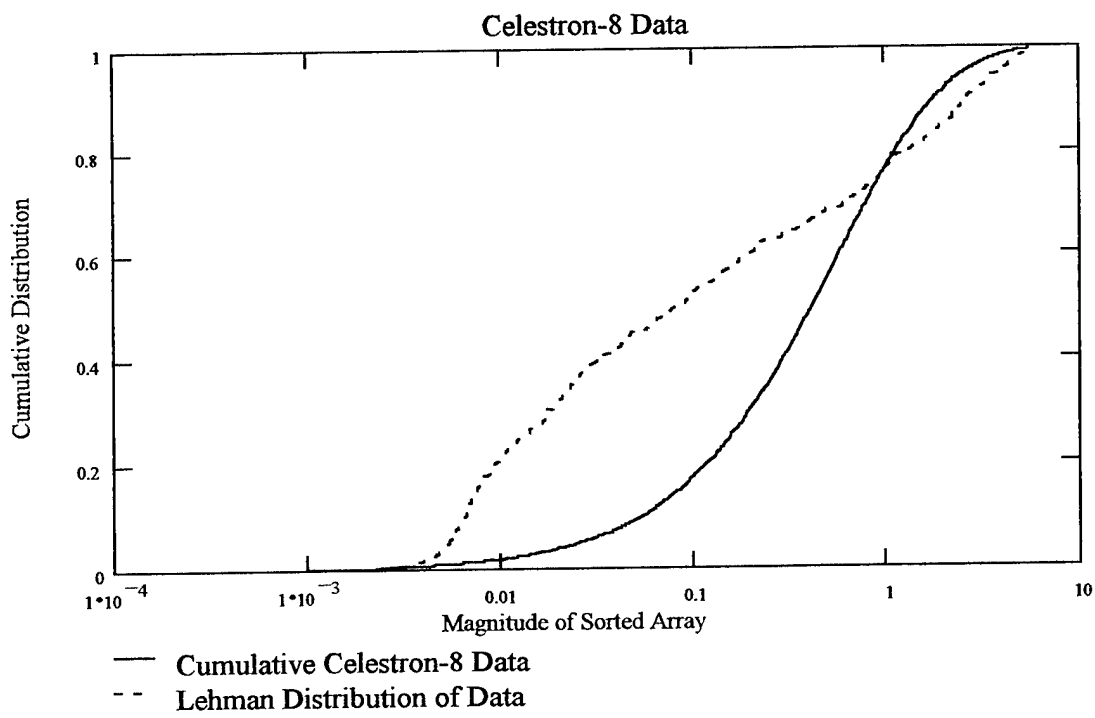


Figure 5.16. Lehman distribution (based on $\Lambda = 4.053 = 3/\mu_{\text{data}}$) and Celestron 8 data from 3.5 to 8 GHz sweep.

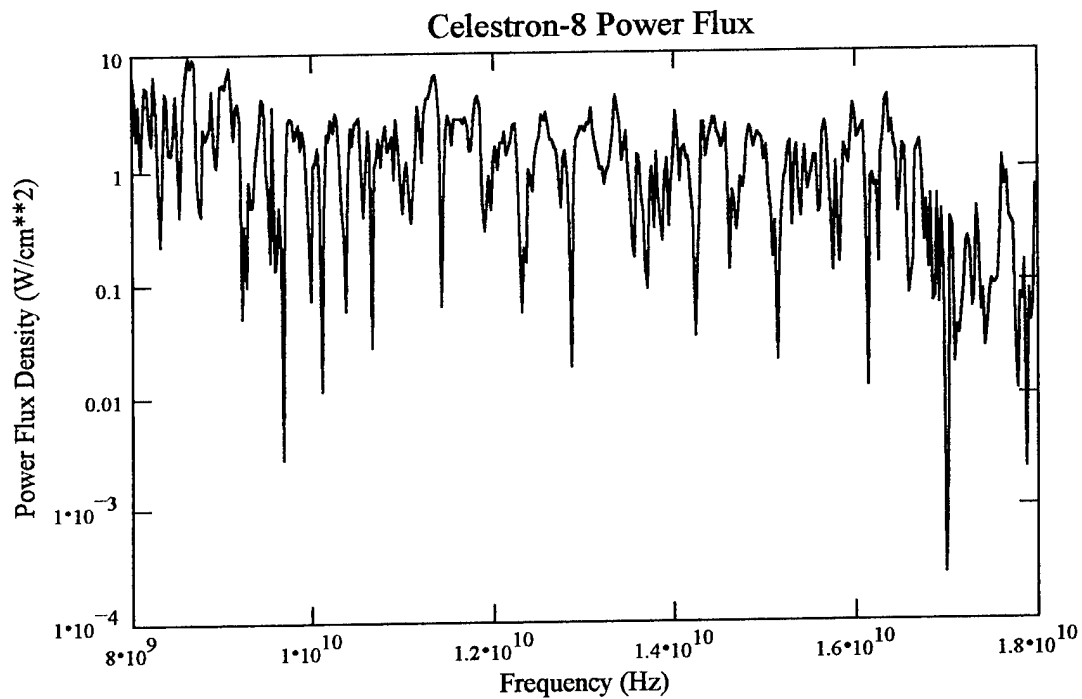


Figure 5.17. Power flux density distribution at focal plane in Celestron 8 satellite telescope for 8 GHz - 18 GHz sweep.

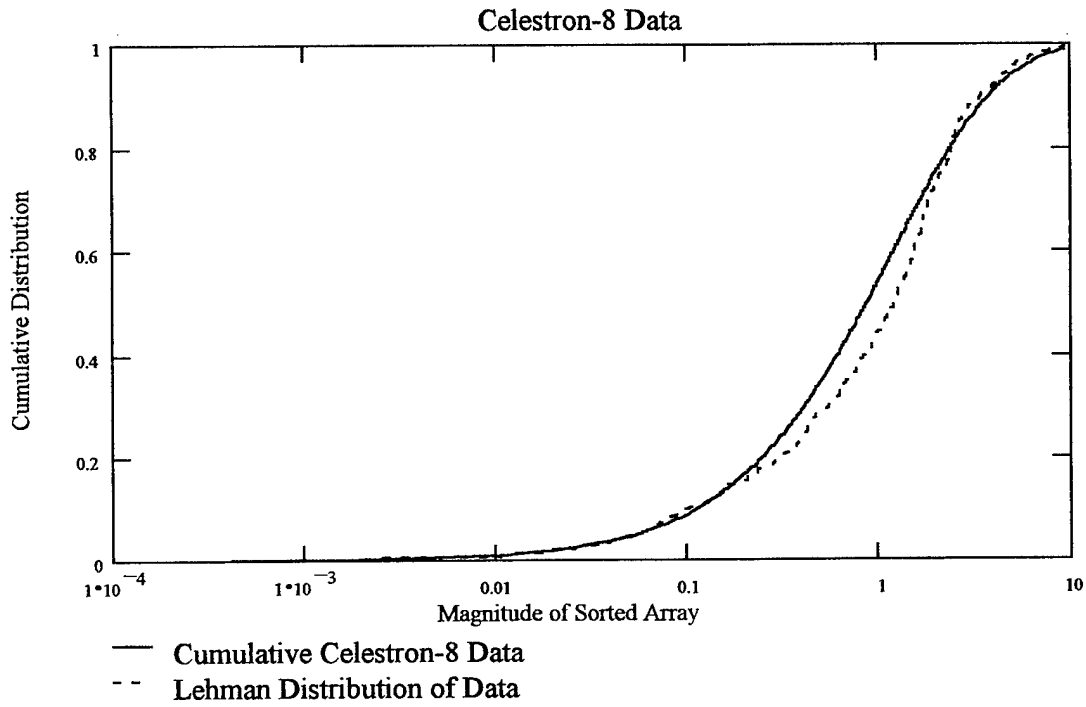


Figure 5.18. Lehman distribution (based on $\Lambda = 1.929 = 3/\mu_{\text{data}}$) and Celestron 8 data from 8 to 18 GHz sweep.

LEHMAN FIELD DECONVOLUTION: BRIEF OVERVIEW

The next objective is to find a probability density function $e_f(u) = e_f(v)$ which answers following question: if the probability density function of z is the Lehman probability density function (5-17), where z is related to u and v by (2-18), what is the probability density function $e_f(u)$? The solution of this problem is tedious, and will be given after this overview.

The answer proves to be

$$e_f(u) = \sqrt{\frac{\Lambda}{2\pi}} e^{-2\Lambda u^2} + \sqrt{\Lambda^3} u^2 e^{-2\sqrt{\Lambda}|u|} \quad -\infty < u < +\infty \quad (5-26)$$

and the corresponding cumulative distribution function $E_f(u)$ is

$$E_f(u) = \left\{ \frac{1}{2} \left[\frac{1}{2} + \frac{1}{\sqrt{\pi}} \int_0^{z\sqrt{2\Lambda}} e^{-u'^2} du' \right] + \left[\frac{1}{2} + \frac{1}{2} \frac{u}{|u|} \left(1 - e^{-2\sqrt{\Lambda}|u|} \sum_{k=0}^2 \frac{(2\sqrt{\Lambda}|u|)^k}{k!} \right) \right] \right\} \quad (5-27)$$

To demonstrate the use of this result, we generated two ensembles (one for each phase-quadrature field component) of 500 random numbers between 0 and 1. These random numbers correspond to probability, i.e., to R_{space} of (3-21). By means of (3-20) and (3-21), we introduced autocorrelation while generating the arrays. These probability arrays were next transformed to Lehman-distributed variate values for phase-quadrature field drivers by the use of the inverse Lehman-field operator, $E_l^{-1}(f_i)$ implied by (3-1) and (5-27). This operation is analogous to (3-1) - (3-3) for obtaining normally distributed drivers, except we are no longer dealing with the inverse normal operator $P^{-1}(f_i)$. One of the so-generated cumulative distributions, based upon $\Lambda = 10$, appears in Figure 5.19. A plot of $E_l(u)$ from (5-27) is overlaid on this figure. From this ensemble, we numerically found μ_l and σ_l as 0.34 and 0.46. Two more overlays were then placed on Figure 5.19, with Λ determined from the data through the relations of (5-25). All four plots may be seen to lie in excellent agreement.

(Before deriving his result, Lehman had observed that power flux data inside leaky chambers frequently had a σ/μ ratio of about $1.3 \approx \sqrt{15}/3$. Mention has been made that the Lehman distribution may have evolved from a mixture of physical insight and search for a distribution function with this property.)

We have measured EMPTAC cable current results available at four cable points for the high-frequency sweep (100 MHz to 1 GHz, see figure 4.17). Consequently, we next drove the EMPTAC cable model with Lehman-distributed fields. The Lehman parameter Λ was numerically deduced from the data appearing in Figure 5.4 by means of (5-25), and the fields so created were converted to cable currents according to the procedure outlined in (3-6) - (3-16). The three closely bunched measured current distributions are superimposed with two cable current computations in Figure 5.20. It may be seen that the modeled currents lie within or very close to the experimental spread. One of the computed currents was evaluated near the cable midpoint, and the other was evaluated near an end. The reason cable currents are not sensitive to separation from cable endpoints or to termination parameters, so long as the observation point is at least two wavelengths from the end, is discussed in great detail in Section 8.

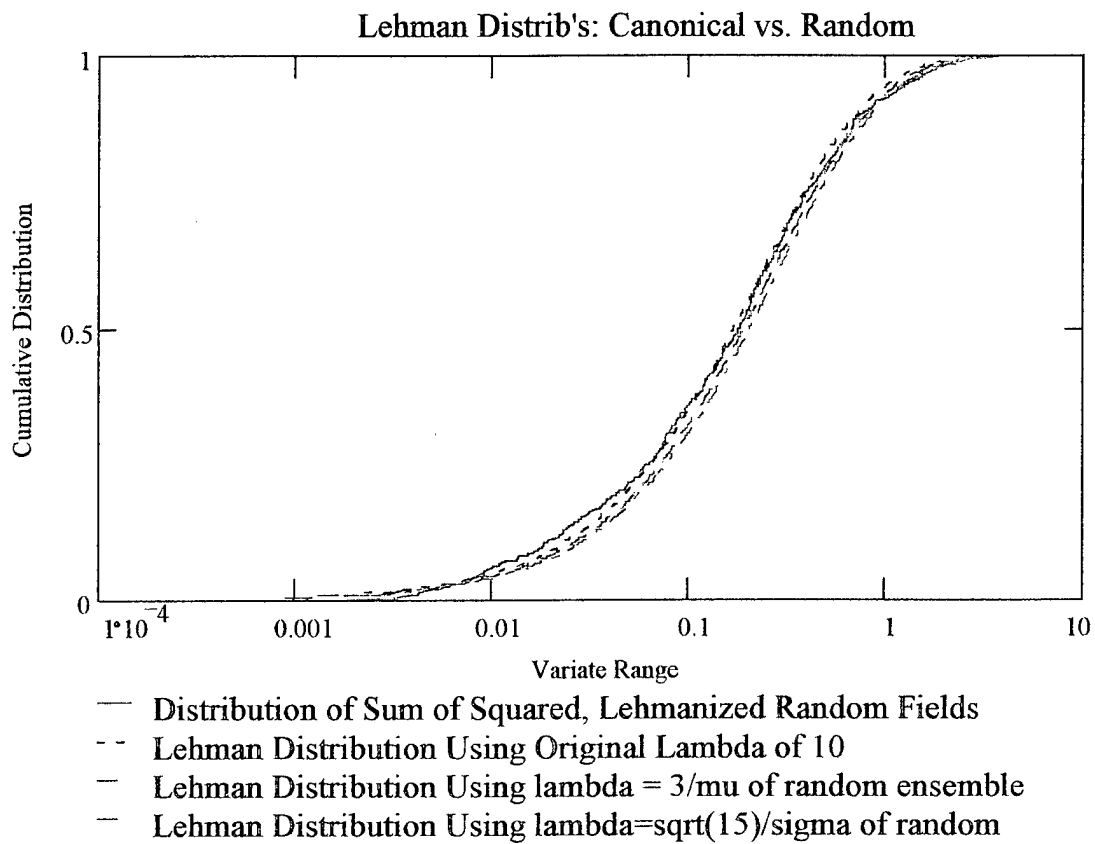


Figure 5.19. Overlay of 1) random field values, plotted as summed & squared components after Lehman rescaling according to (3-3) and (5-27) and based on $\Lambda = 10$, 2) values computed directly from the Lehman cumulative distribution function (5-22) with $\Lambda = 10$, 3) values computed directly from the Lehman cumulative distribution function with $\Lambda = 3/\mu$, where $\mu = 0.34$ was obtained from the random-rescaled ensemble, and 4) values computed directly from the Lehman cumulative distribution function with $\Lambda = \sqrt{15}/\sigma$, where $\sigma = 0.46$ was obtained from the random-rescaled ensemble.

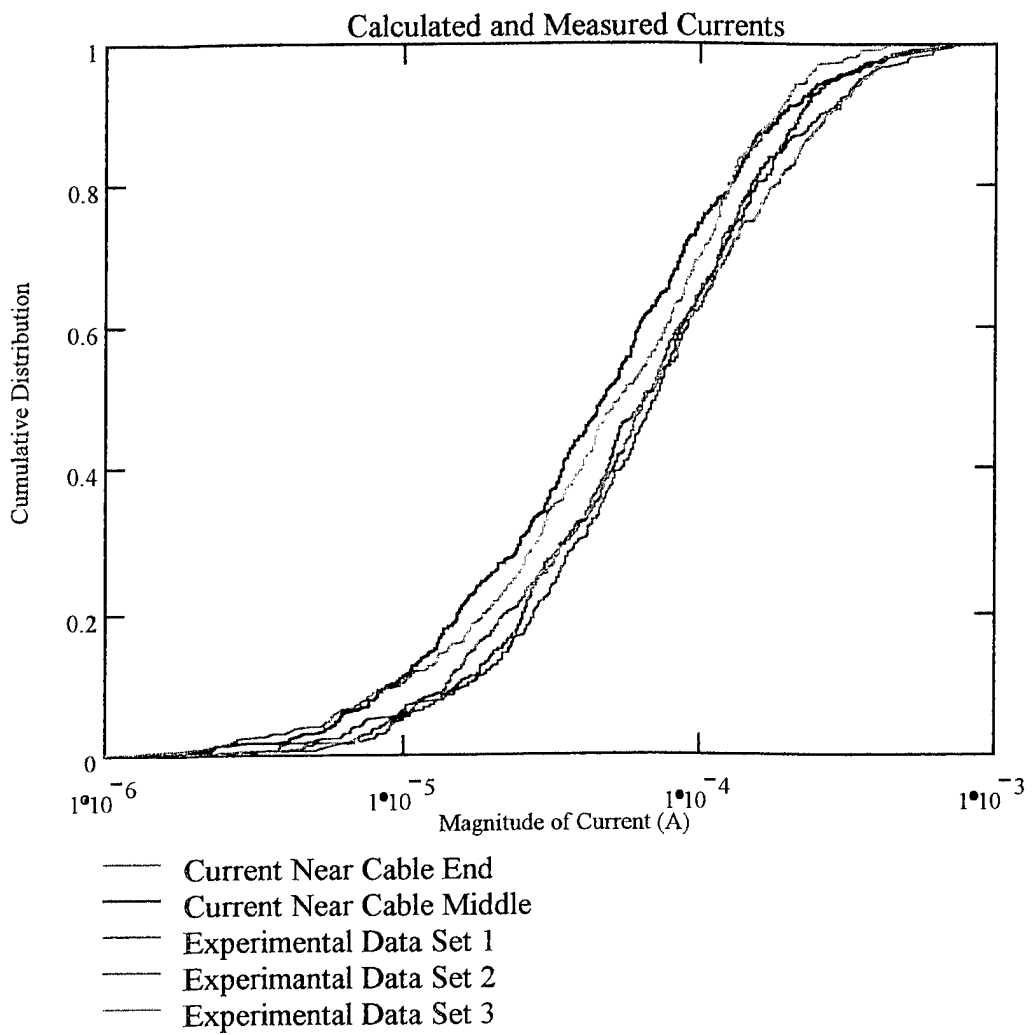


Figure 5.20. Two EMPTAC cable-current amplitude (unsquared) distributions based on cable model of (3-6) - (3-16) with the same parameters as those used to generate Figure 4.17, except that the Lehman electric-field distribution (5-27) was used instead of a chi square distribution. The Lehman parameter for the fields was determined from experimental data to be $\Lambda = 17600$. Also overlaid on this plot are the same three experimentally obtained EMPTAC current distributions used in Figure 4.17. The model cable current distributions lie close to or within the experimental spread, perhaps even more so than that in Figure 4.17, and also are relatively insensitive to distance from the cables ends.

LEHMAN FIELD DECONVOLUTION: IN-DEPTH DERIVATION

The explication which follows is due to the tenacity of the second author. It is not light reading, and, while significant to a full understanding of the field phase-quadrature Lehman distribution, is not vital to its use.

The Lehman Probability Density Function

The approximate form of the modified Bessel function of the second kind, of order v , is, for large arguments,

$$K_v(z) \approx f_{large}(z, v) \approx \sqrt{\frac{\pi}{2z}} e^{-z} \left[1 + \frac{\mu(v) - 1}{8z} + \frac{(\mu(v) - 1)(\mu(v) - 9)}{2(8z)^2} \right] \quad (5-28)$$

$$\mu(v) = 4v^2$$

and for small arguments,

$$K_v(z) \approx f_{small}(z, v) \approx \frac{\Gamma(v)}{2} \left(\frac{2}{z} \right)^v \quad (5-29)$$

If v is 2, the above reduces to

$$K_v(z) \approx f_{large}(z, v) \approx \sqrt{\frac{\pi}{2z}} e^{-z} \left[1 + \frac{3}{8z} - \frac{3}{2(8z)^2} \right] \quad (5-30)$$

Figure 5.21 illustrates the fit of the approximation

$$K_2(z) \approx f_{large}(z) (1 - e^{-\sqrt{z}}) + f_{small}(z) e^{-z} \quad (5-31)$$

to the desired function $K_2(z)$. Figure 5.22 illustrates the Lehman probability density function (5-17) for $\Lambda = 1$ and 10, and also the cumulative distribution.

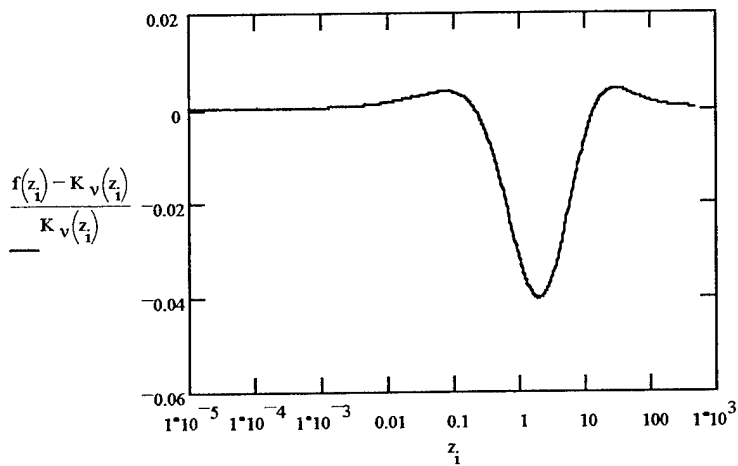


Figure 5.21. Comparison of $K_2(z)$ and the approximate fit of (5-32).

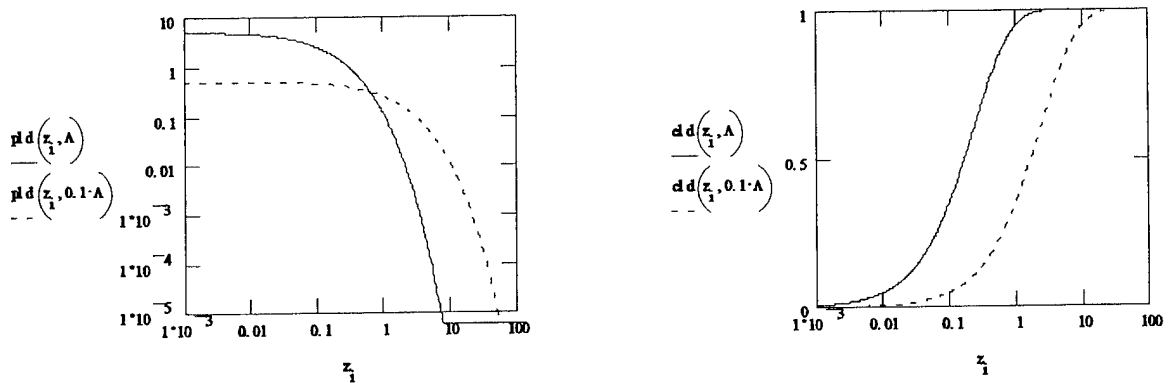


Figure 5.22. Lehman probability density function and cumulative distribution for $\Lambda = 10$ (solid) and 1 (dashed).

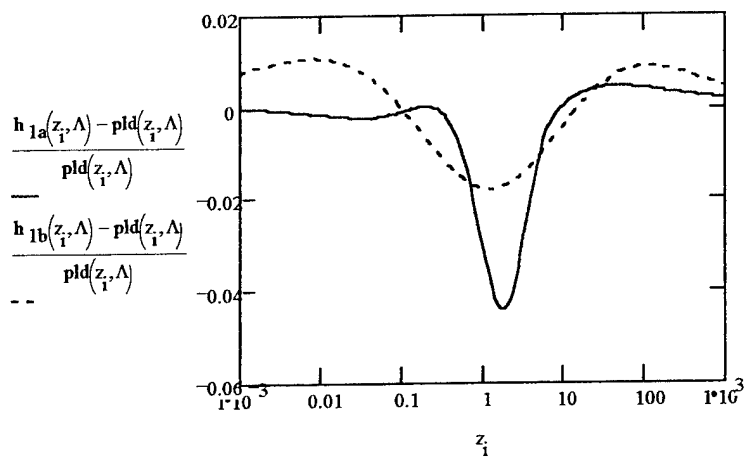


Figure 5.23. Error in approximations $h_{1a}(z, \Lambda)$ and $h_{1b}(z, \Lambda)$ [(5-32) and (5-33)] to the Lehman pdf.

Using the f_{large} and f_{small} expressions above give two approximate Lehman probability distributions:

$$h_{la}(z, \Lambda) = \Lambda^2 z \sqrt{\frac{\pi}{4\sqrt{\Lambda z}}} \cdot e^{-2\sqrt{\Lambda z}} \cdot \left(1 + \frac{1}{\sqrt{\Lambda z}} \right) \cdot (1 - e^{-\Lambda z}) + \frac{\Lambda}{2} e^{-\frac{5}{3}\Lambda z} \quad (5-32)$$

and

$$h_{lb}(z, \Lambda) = \Lambda^2 z \sqrt{\frac{\pi}{4\sqrt{\Lambda z}}} \cdot e^{-2\sqrt{\Lambda z}} \cdot \left(1 + \frac{1}{\sqrt{\Lambda z}} \right) \cdot (1 - e^{-\sqrt{2}\sqrt{\Lambda z}}) + \frac{\Lambda}{2} e^{-2\sqrt{\Lambda z}} \quad (5-33)$$

These forms differ from each other in the auxiliary functions multiplying f_{large} and f_{small} terms required to minimize the effects of the f_{large} function in the f_{small} domain, and vice-versa. Figure 5.23 shows how these two approximations fit the actual Lehman probability density function.

Now we introduce integral and summation expressions for $K_2(z)$ which can be numerically evaluated. These v -dependent forms can be used to evaluate noninteger, modified Bessel functions. The integral form is

$$K_i(v, z) = \int_0^{\ln\left(\frac{100}{z}\right) + 1} e^{-z \cosh z'} \cosh(vz') dz' \quad (5-34)$$

and the summation form is

$$K_f(v, z) = K_{small}(v, z) + K_{large}(v, z) \quad (5-35)$$

where

$$K_{small}(v, z) = \frac{\Gamma(v)}{2} \left(\frac{2}{z} \right)^v \cdot e^{-z \frac{v+1.5}{v+1}} \quad (5-36)$$

and

$$K_{large}(v, z) = \sqrt{\frac{\pi}{2z}} e^{-z} \left[1 + \sum_{n=1}^{v+2} \frac{1}{n! (8z)^n} \prod_{m=1}^n (\mu(v) - (2m-1)^2) \right] \cdot (1 - e^{-z^{v+2.5}}) \quad (5-37)$$

where, if v is not an integer, it is rounded up to the next higher integer. Figure 5.24 illustrates the fit of these approximations to $K_5(z)$. The integral fit may be seen to be superior, but it takes much longer to evaluate.

The Lehman-Associated Field-Component-Squared Probability Density Function

The next step is determining the form of the function $f_l(x)$ which, when convolved upon itself as in (2-86) or (4-5), gives back the Lehman pdf (5-17). In the low- z limit, the autoconvolution must be the same as the Lehman pdf, which may be evaluated from (5-17) as $\Lambda/2$. The square root of the Laplace transform of the low- z limit is $(\Lambda/2s)^{1/2}$, which has an inverse of $[\Lambda/(2\pi x)]^{1/2}$. Thus, the small- x form for $f_l(x)$ is

$$f_{l0}(x, \Lambda) = \sqrt{\frac{\Lambda}{2\pi x}} \quad (5-38)$$

which corresponds to a small- z approximation for $h_{l0}(z)$ of

$$h_{l0}(z, \Lambda) = \int_0^z f_{l0}(z - x, \Lambda) f_{l0}(x, \Lambda) dx \quad (5-39)$$

Figure 5.25 illustrates the error of (5-38) and (5-39) as a function of z for $\Lambda = 1$.

A general form which yields the same low- x limit is

$$f_{l1}(x, \Lambda, \alpha, \beta, \gamma) = \sqrt{\frac{\Lambda}{2\pi}} \left(\frac{\gamma^{v(\alpha, \beta)} K_{v(\alpha, \beta)}(\gamma x^\beta)}{2^{v(\alpha, \beta) - 1} \Gamma(v(\alpha, \beta))} \right)^\alpha \quad v(\alpha, \beta) = \frac{1}{2\alpha\beta} \quad (5-40)$$

This corresponds to a Lehman distribution approximation of

$$h_{l1}(z, \Lambda, \alpha, \beta, \gamma) = \int_0^z f_{l1}(z - x, \Lambda, \alpha, \beta, \gamma) f_{l1}(x, \Lambda, \alpha, \beta, \gamma) dx \quad (5-41)$$

Figure 5.26 compares the (5-41) approximation to the actual Lehman pdf for $\Lambda = 1$. This fit is based on minimizing the mean square error of the approximate fit, which leads (for $\Lambda = 1$) to $(\alpha, \beta, \gamma) = (1.02, 0.578, 1.056)$. The optimized parameters look like they might be pointing to $(1, 1/2, 1)$, but these numbers don't actually yield a very good match. The fit is sufficiently bizarre that it probably has no real implication of Bessel functions being in the solution for $f_l(x)$ beyond the fact that they happen to give a reasonable overlay.

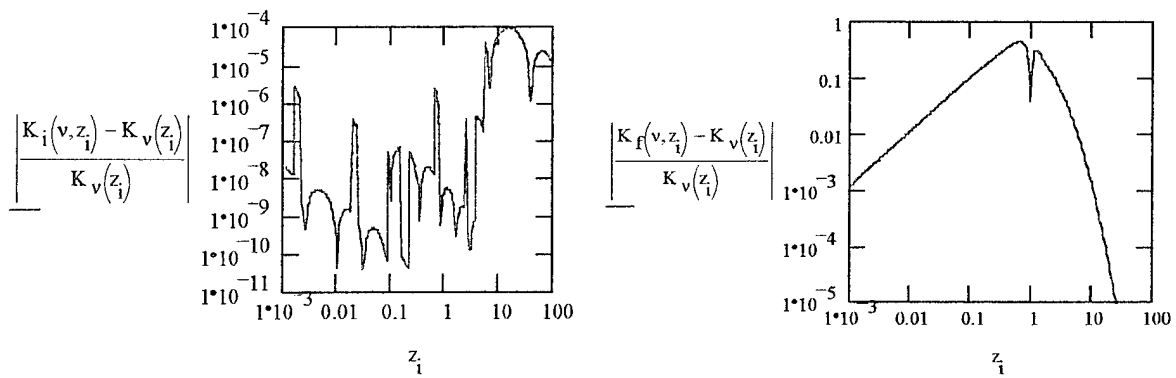


Figure 5.24. Integral (5-34) and high-low asymptotic (5-35) approximations to $K_5(z)$.

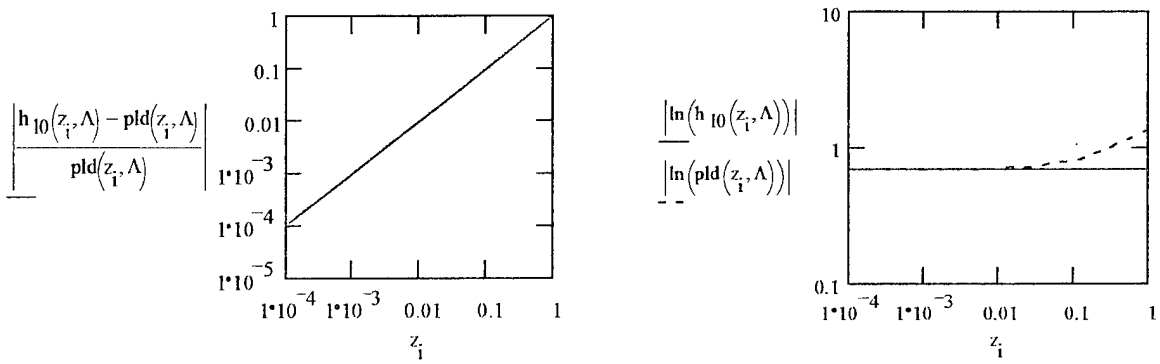


Figure 5.25. Deviation from Lehman pdf of low-z limit (5-39) of $h_{10}(z)$, based on low- z approximation $f_{10}(z, \Lambda)$ of (5-38), for $\Lambda = 1$.

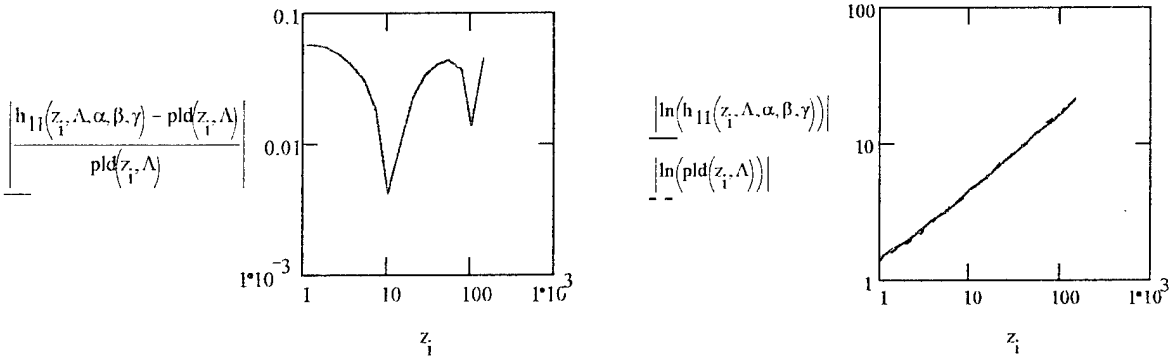


Figure 5.26. Deviation of $h_{11}(z, \Lambda, \alpha, \beta, \gamma)$ of (5-41) from Lehman pdf based on $\Lambda = 1$.

The actual dependence of $f_{l1}(x, \Lambda)$ on Λ can be determined from (5-40) in such a way that (α, β, γ) does not have to be recomputed every time Λ is changed. In particular, (5-39) can be manipulated to show

$$\begin{aligned} h_{l1}(\Lambda z, 1) &= \int_0^{\Lambda z} f_{l1}(\Lambda z - x, 1, \alpha, \beta, \gamma) f_{l1}(x, 1, \alpha, \beta, \gamma) dx \\ &= \Lambda \int_0^{\Lambda z} f_{l1}(\Lambda(z - x), 1, \alpha, \beta, \gamma) f_{l1}(\Lambda x, 1, \alpha, \beta, \gamma) dx \end{aligned} \quad (5-42)$$

For simplicity, let us call

$$f_{l1}(\Lambda x) = f_{l1}(\Lambda x, 1, \alpha, \beta, \gamma) \quad (5-43)$$

and

$$f_{l1}(x, \Lambda) = f_{l1}(x, \Lambda, \alpha, \beta, \gamma) \quad (5-44)$$

where, in this notation, it is implied that $(\alpha, \beta, \gamma) = (1.02, 0.578, 1.056)$.

The above definitions, along with (5-42), then lead to the result

$$f_{l1}(x, \Lambda) = \Lambda^{\nu} f_{l1}(\Lambda x) \quad (5-45)$$

or

$$f_{l1}(x, \Lambda) = \frac{\Lambda}{\sqrt{2\pi}} \left(\frac{\gamma^{v(\alpha, \beta)} K_{v(\alpha, \beta)}(\gamma[\Lambda x]^{\beta})}{2^{v(\alpha, \beta) - 1} \Gamma(v(\alpha, \beta))} \right)^{\alpha} \quad (5-46)$$

Let us define a misfit function for $h_{l1}(z, \Lambda)$ as $M_1(z, \Lambda)$ as

$$M_1(z, \Lambda) = \log \left(\left| \frac{h_{l1}(z, \Lambda) - \text{pld}(z, \Lambda)}{\text{pld}(z, \Lambda)} \right| \right) \quad (5-47)$$

with $h_{l1}(z, \Lambda)$ defined by (5-41) and (5-46). Figure 5.27 shows contour plots of $M_1(z, \Lambda)$ as functions of z and Λ . This misfit is roughly dependent on the product $z\Lambda$. (Log z plus log Λ = a straight line with a negative 45° slope.) The misfit does not exceed 20% for $z\Lambda < (15)^2$, and

generally is well below 5%. Review of Figures 5.1 - 5.20 indicates that this is an acceptable dynamic range.

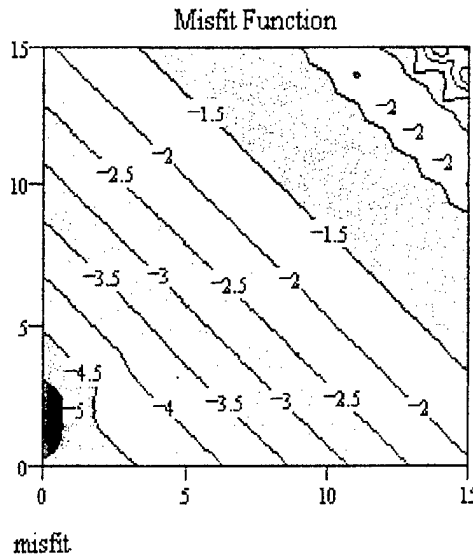


Figure 5.27. Contour plot of the misfit function $M_1(z, \Lambda)$ (5-47) for the $h_{l1}(z, \Lambda)$ (5-46) approximation to the Lehman distribution.

The Lehman-Associated Field-Component Probability Density Function

At this point, we have obtained a reasonable approximation for $f(x, \Lambda)$, the distribution of the square of the phase-quadrature field components [see (2-80) and (2-81)]. What we actually need is the distribution of the phase-quadrature of the field components themselves, $e_f(u, \Lambda) = e_f(v, \Lambda)$. Given the distribution of x , finding the distribution of u (or its generation by random numbers) should be easily accomplished from the relationships in Section 2 [(2-54) to (2-61)], of which (2-59) is the linchpin.

Here, we have, $x = u^2$, and g^{-1} of (2-58) is $(\cdot)^2$. Thus, the distribution of $e_f(u, \Lambda) = e_f(v, \Lambda)$ is

$$e_{l1}(u, \Lambda) = f_{l1}(g^{-1}(u), \Lambda) \left| \frac{dg^{-1}(u)}{du} \right| \quad (5-48)$$

This relationship transforms (5-46) into the desired formula,

$$e_{l1}(u, \Lambda) = \frac{2\Lambda u}{\sqrt{2\pi}} \left(\frac{\gamma^{v(\alpha, \beta)} K_{v(\alpha, \beta)}(\gamma[\Lambda u^2]^\beta)}{2^{v(\alpha, \beta)-1} \Gamma(v(\alpha, \beta))} \right)^\alpha \quad (5-49)$$

where this distribution is on amplitude from 0 to ∞ . If the distribution is on value, from $-\infty$ to $+\infty$, the probability density function must be divided by 2, and u replaced by $|u|$. Figure 5.28 illustrates the pdf, $e_{l1}(u)$, and the cdf, $E_{l1}(u)$, both based on $\Lambda = 10$.

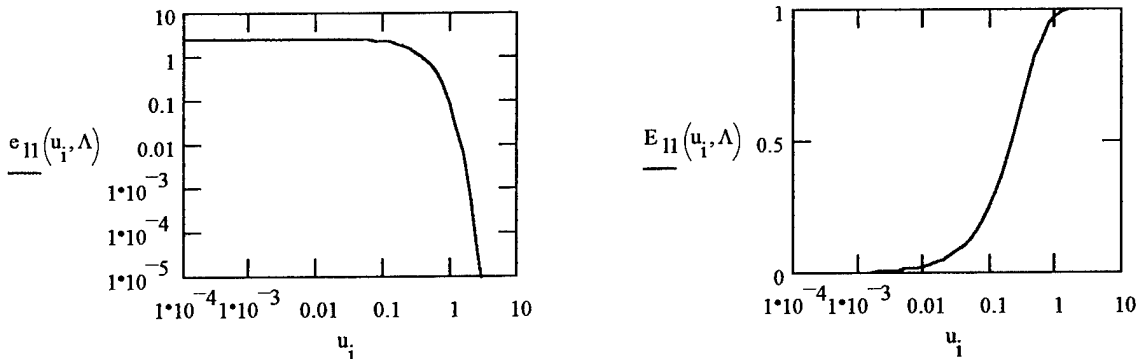


Figure 5.28. The pdf and cdf approximations, $e_{l1}(u, \Lambda)$ and $E_{l1}(u, \Lambda)$, to the Lehman-associated field amplitude distribution (5-49), based on $\Lambda = 10$.

FASTER LEHMAN FIELD DECONVOLUTION: IN-DEPTH DERIVATION

There are other ways to approximate the phase-quadrature Lehman-based field drive which are easier and faster to compute, although not so accurate as the preceding. An alternative way, which we shall now present, is faster, primarily because it does not involve the use of Bessel functions.

Alternative Lehman-Associated Field-Component-Squared Probability Density Function

We again begin by assuming (5-38) and (5-39) hold for small z . Similarly, at large z ,

$$h_{l2}(z, \Lambda) = \int_0^{\infty} f_{l2}(z - x, \Lambda) f_{l2}(x, \Lambda) dx \approx f_{l2}(z, \Lambda) \int_0^{\infty} f_{l2}(x, \Lambda) dx \approx f_{l2}(z, \Lambda) \quad (5-50)$$

where the last integral to the right must be unity because it is the integral of pdf over its entire domain. At large x , we thus obtain, in analogy with (5-32) or (5-33),

$$f_{l2}(x, 1) = x \sqrt{\frac{\pi}{4\sqrt{x}}} \cdot e^{-2\sqrt{x}} \quad (5-51)$$

If we multiply the small- x approximation (5-38) by e^{-x} to make it vanish at large x , and add it to the large- x form, we obtain

$$f_{l2}(x,1) = \frac{e^{-x}}{\sqrt{2\pi x}} + x \sqrt{\frac{\pi}{4\sqrt{x}}} \cdot e^{-2\sqrt{x}} \quad (5-52)$$

Autoconvolution of (5-52) upon itself then should give an approximation to $h_n(z,1)$. Figure 5.29 illustrates the replication of the exact $h_n(z,1)$ from (5-17) with that obtained from autoconvolution of (5-52).

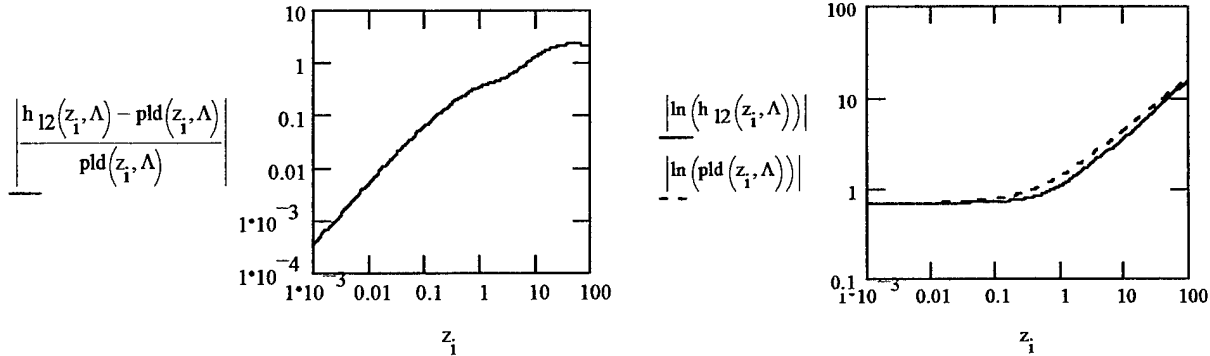


Figure 5.29. Comparison of the exact Lehman probability density function (5-17) and the approximate probability density function $h_n(z,1)$ obtained from autoconvolution of (5-52).

We now do some fine-tuning of $f_n(z,1)$ from (5-52). In particular, assume $f_n(z,1)$ can be expressed in the form

$$f_{l2}(x,1,\alpha,\beta,\gamma) = \frac{e^{-\beta x}}{\sqrt{2\pi x}} + \gamma x^\alpha e^{-2\sqrt{x}} \quad (5-53)$$

and that, in analogy with (5-42), we can define

$$h_{l2}(z,\Lambda,\alpha,\beta,\gamma) = \int_0^z f_{l2}(z-x,\Lambda,\alpha,\beta,\gamma) f_{l2}(x,\Lambda,\alpha,\beta,\gamma) dx \quad (5-54)$$

where, for the time being, we shall assume $\Lambda = 1$. Performing a least-squares fit like that utilized in (5-40) and (5-41) results in $(\alpha, \beta, \gamma) = (0.553, 1.396, 0.771)$. These values produce a fit which is, at worst, 10% off (see Figure 5.30).

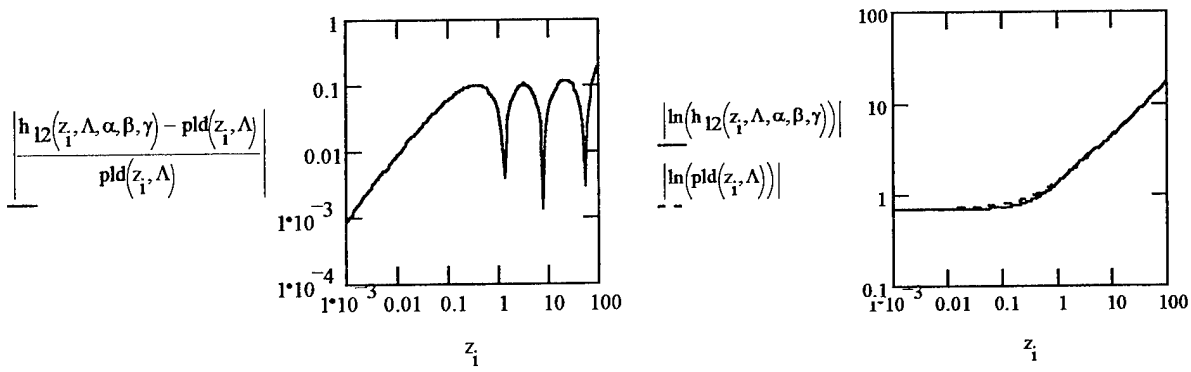


Figure 5.30. Comparison of the exact Lehman probability density function (5-17) and the approximate probability density function $h_{l2}(z, 1, \alpha, \beta, \gamma)$ obtained from (5-54). This figure is based upon optimized selection of (α, β, γ) as $(0.553, 1.369, 0.771)$.

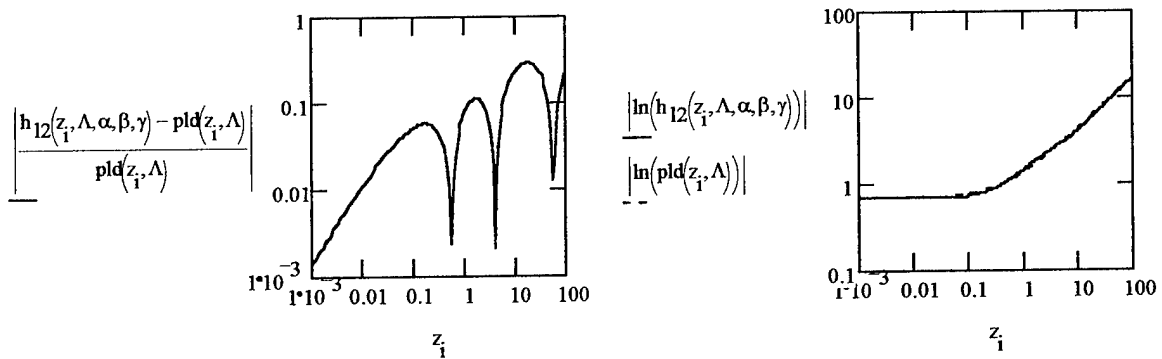


Figure 5.31. Comparison of the exact Lehman probability density function (5-17) and the approximate probability density function $h_{l2}(z, 1, \alpha, \beta, \gamma)$ obtained from (5-55). This figure is based upon integerized selection of (α, β, γ) as $(\frac{1}{2}, 2, 1)$.

Fitting (α, β, γ) with integers or inverses of integers leads to, for $\Lambda = 1$,

$$f_{l2}(x, 1, \alpha, \beta, \gamma) = \frac{e^{-2x}}{\sqrt{2\pi x}} + x^{\frac{1}{2}} e^{-2\sqrt{x}} \quad (5-55)$$

with $f_{l2}(x, \Lambda, \alpha, \beta, \gamma)$ still related to $h_{l2}(z, \Lambda, \alpha, \beta, \gamma)$ by (5-54). Figure 5.31 illustrates the agreement between autoconvolved (5-55) and the canonical pdf from (5-17).

The dependence of $f_{l2}(x, \Lambda)$ on Λ can be introduced into (5-55) exactly as was introduced into (5-46), with the result

$$f_{l2}(x, \Lambda) = \Lambda \left(\frac{e^{-2\Lambda x}}{\sqrt{2\pi\Lambda x}} + (\Lambda x)^{\frac{1}{2}} e^{-2\sqrt{\Lambda x}} \right) \quad (5-56)$$

where $f_{l2}(x, \Lambda)$ is $f_{l2}(x, \Lambda, \alpha, \beta, \gamma)$ with (α, β, γ) set to $(\frac{1}{2}, 2, 1)$. A misfit function for $h_{l2}(z, \Lambda), M_2(z, \Lambda)$, can then be given the same definition as $M_1(z, \Lambda)$ in (5-48), except that $f_{l2}(x, \Lambda)$ and $h_{l2}(x, \Lambda)$ now come from (5-56) instead of from (5-46). Figure 5.32, corresponding to Figure 5.27, shows contour plots of $M_2(z, \Lambda)$ as functions of z and Λ . The misfit also is roughly dependent on the product $z\Lambda$. It is mostly less than 10%, but does reach 50% for $z\Lambda = (15)^2$.

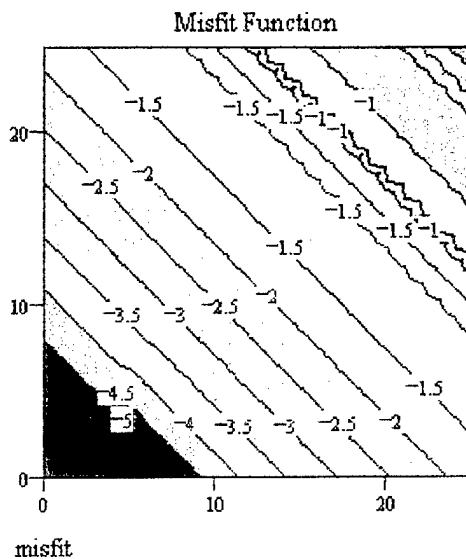


Figure 5.32. Contour plot of the second misfit function $M_2(z, \Lambda)$ for the $h_{l2}(z, \Lambda)$ (5-56) approximation to the Lehman distribution.

It is possible to integrate (5-56) from 0 to x using known forms [8]:

$$F_{l2}(x, \Lambda) = [P(t) - \frac{1}{2}] + \frac{1}{2} \left(1 - e^{-t} \sum_{k=0}^2 \frac{t^k}{k!} \right) \quad \text{with } t = \sqrt{4\Lambda x} \quad (5-57)$$

where $P(t)$ is still the cumulative normal distribution (2-24). Figure 5.33 illustrates $F_{l2}(x, \Lambda)$ for $\Lambda = 10$.

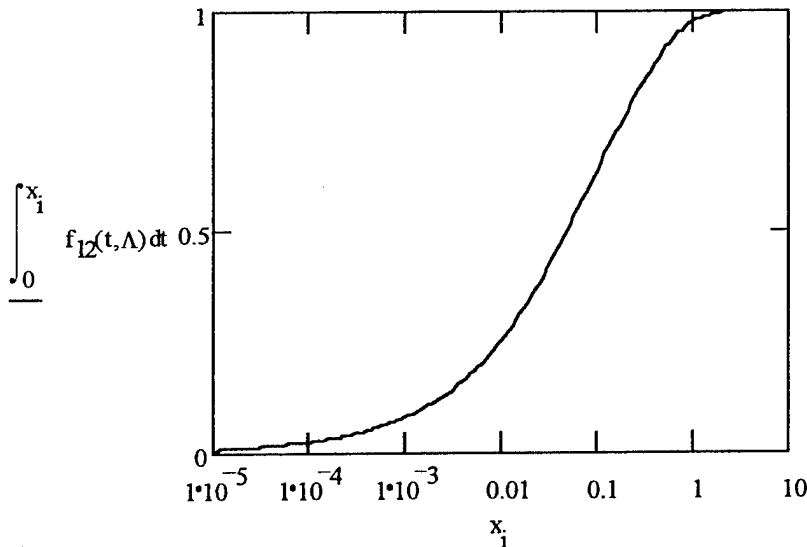


Figure 5.33. The cdf for the phase-quadrature components squared, based on $F_n(x, \Lambda)$ for $\Lambda = 10$, from (5-57).

Alternative Lehman-Associated Field-Component Probability Density Function

At this point, we have obtained a another reasonable approximation for $f_n(x, \Lambda)$, the distribution of the square of the phase-quadrature field components [see (2-80) and (2-81)]. Again, what we actually need is the distribution of the phase-quadrature of the field components themselves, $e_{l2}(u, \Lambda) = e_{l2}(v, \Lambda)$. Given the distribution of x , finding the distribution of u (or its generation by random numbers) should be easily accomplished from the above-cited relationships in Section 2.

In particular, (5-49) still applies, with g^{-1} of (2-57) remaining ()². These relationships transform (5-56) into the desired formula,

$$e_{l2}(u, \Lambda) = \sqrt{\frac{2\Lambda}{\pi}} e^{-2\Lambda u^2} + 2\sqrt{\Lambda^3} u^2 e^{-2\sqrt{\Lambda}u} \quad 0 \leq u < \infty \quad (5-58)$$

where this distribution is on amplitude. If the distribution is on value, from $-\infty$ to $+\infty$, the probability density function must be divided by 2, and u replaced by $|u|$

$$e_{l2}(u, \Lambda) = \sqrt{\frac{\Lambda}{2\pi}} e^{-2\Lambda u^2} + \sqrt{\Lambda^3} u^2 e^{-2\sqrt{\Lambda}u} \quad -\infty < u < \infty \quad (5-59)$$

This probability density function can also be expressed as

$$e_{l2}(u, \Lambda) = \frac{1}{2} e_g(u, \sigma_g) + \frac{1}{4} \left(4\sqrt{\Lambda} h_{\chi_6^2}(4\sqrt{\Lambda}|u|) \right) \quad \sigma_g = \frac{1}{2\sqrt{\Lambda}} \quad (5-60)$$

where $e_g(u, \sigma_g)$ is the normal probability density function (2-34), and $h_{\chi^2}(6, u)$ is the chi square probability density function with six degrees of freedom (5-6) - (5-9), which leads to a cdf of the form

$$E_{l2}(u, \Lambda) = \frac{1}{2}E_g(u, \sigma_g) + \frac{1}{4} \left(1 + H_{\chi^2}(4\sqrt{\Lambda}|u|) \frac{u}{|u|} \right) \quad (5-61)$$

Equation (5-59), finally yields the probability density function (5-26) given in the Brief Overview Subsection. Moreover, (5-59) can, alternatively to (5-61), be integrated over u to give the associated cdf, $E_{l2}(u, \Lambda)$ of (5-27). Figure 5.34 illustrates this $e_{l2}(u, \Lambda)$ and the associated cdf, $E_{l2}(u, \Lambda)$, both based on $\Lambda = 10$. This cdf converges to unity because its integral is just represents a change of variables from (5-57). The standard deviation of $e_{l2}(u, \Lambda)$ over u may be shown to be $[13/(8\Lambda)]^{1/2}$. Figure 5.35 illustrates how the normal and chi square parts of the cdf contribute as functions of u , and Figure 5.36 illustrates the inverses of $E_g(u, \sigma_g)$ and $H_{\chi^2}(6, 4\Lambda^{1/2}u)$, based on $\Lambda = 10$.

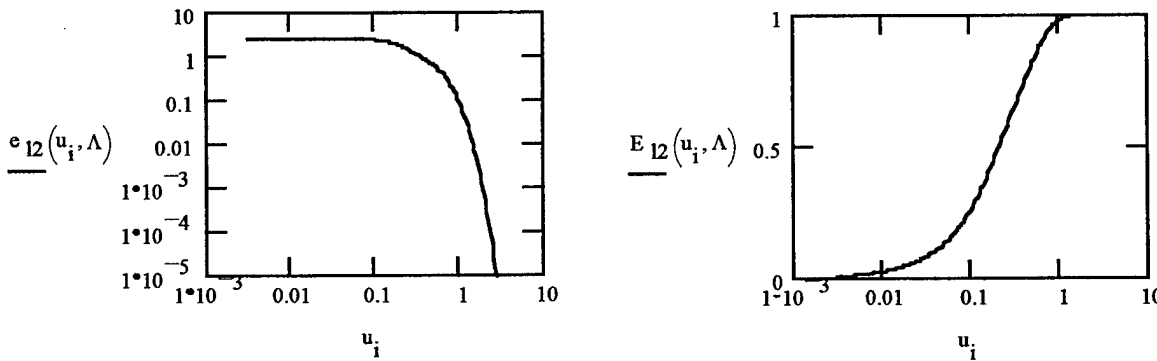


Figure 5.34. The pdf and cdf approximations, $e_{l2}(u, \Lambda)$ and $E_{l2}(u, \Lambda)$, to the Lehman-associated field amplitude distribution (5-26) and (5-27) or (5-59) and (5-60), based on $\Lambda = 10$.

Numerical testing shows that, for Λ fixed, the inverse of $E_{l2}(u, \Lambda)$ lies between the inverse of $E_g(u, \sigma_g)$ and the inverse of $H_{\chi^2}(6, 4\Lambda^{1/2}u)$. Thus, the first step in inverting $E_{l2}(u, \Lambda)$ is to invert the other two distributions (both of which are automated in Mathcad[®]) and take the average. A process along these lines is implemented in our software, and leads to the respectable result shown in Figure 5.37 for the difference between u and $E_{l2}[E_{l2}^{-1}(u)]$. Of course, the final check on this work is the generation of two unsquared phase-quadrature components, which may then be squared, summed, and compared to the Lehman distribution. Figure 5.38 shows two such ensembles, each consisting of 500 values and based on $\Lambda = 10$. Autocorrelation has not been added to these ensembles. They return squared-and-summed values of $3/\mu_i = 8.959$, $\sqrt{15}/\sigma_i = 9.359$, and $\sigma_i/\mu_i = 1.236$, which are respectably in agreement with the proper values [see (5-25)] of Λ , Λ , and 1.29. These are the ensembles upon which Figure 5.19 was based.

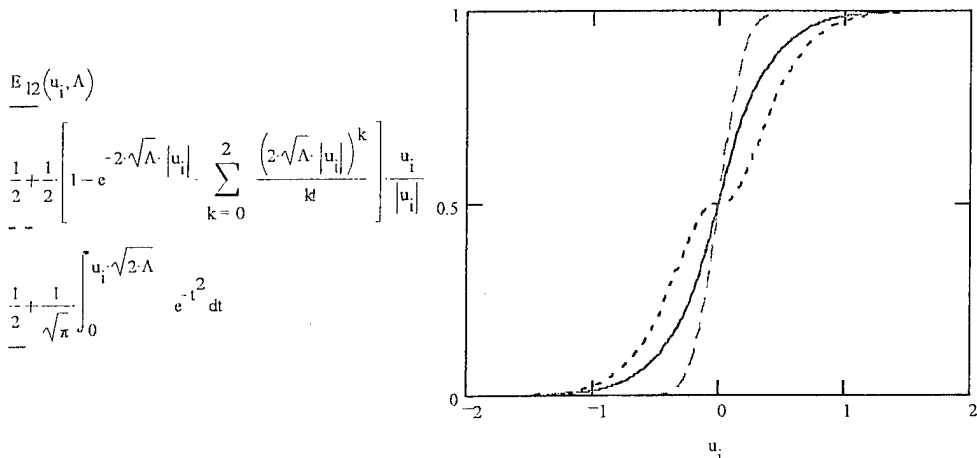


Figure 5.35. Contributions of the Gaussian-like and χ^2 -like parts of the phase-quadrature cdf.

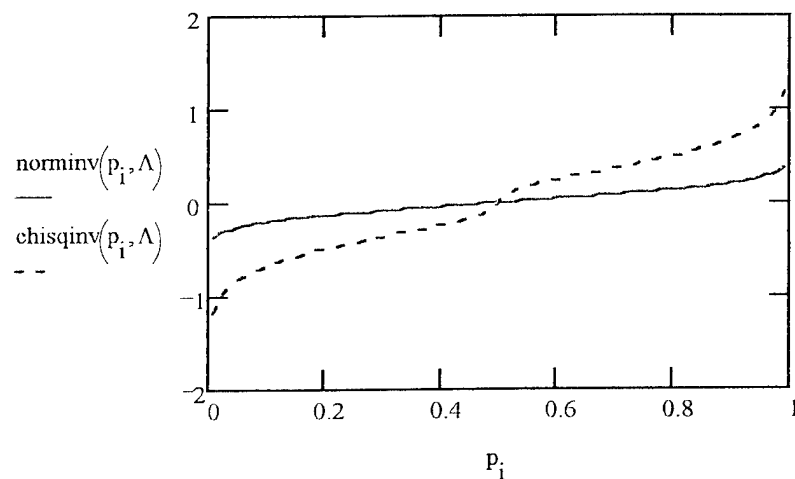


Figure 5.36. Inverses of $E_g(u, \sigma_g)$ and $H_{\chi^2}(6, 4\Lambda^{\nu/2}|u|) \cdot (u/|u|)$ [see (5-61)] for $\Lambda = 10$. These inverses are directly accessible from Mathcad®. The inverse of $F_{\nu}(x, \Lambda)$ has been found always to lie between these two inverses. Thus, the average of these two inverses is a fair and easy first guess for a binary fit to $F_{\nu}^{-1}(p, \Lambda)$.

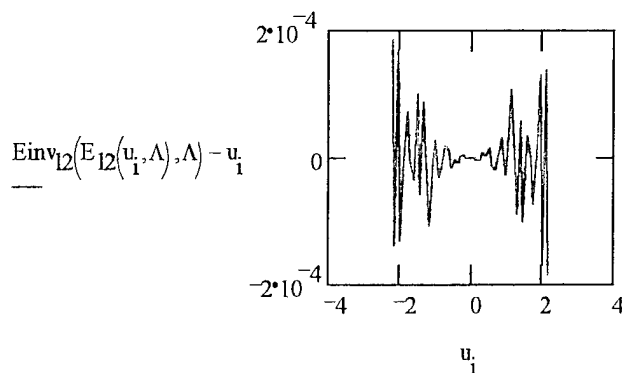


Figure 5.37. Evaluation of the fidelity of our algorithm for finding $F_B(x, \Lambda)$ and its inverse. This figure is based on $\Lambda = 10$, and indicates accuracy to a part in 10^{-4} .

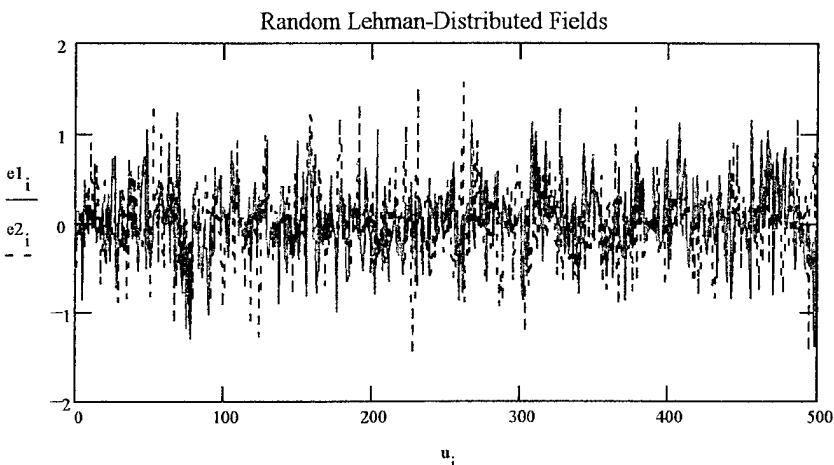


Figure 5.38. Two 500-point ensembles of Lehman-distribution-related phase-quadrature random variables, based on (5-60), with $\Lambda = 10$.

To test our process further, a total of seven such 500-point ensemble pairs were generated using $\Lambda = 10$. Table 5.1 presents the resulting squared-and-summed $3/\mu_i$, $\sqrt{15}/\sigma_i$, and σ/μ_i .

Table 5.1. Results of Lehman-Distributed Random Variable Ensemble Parameters

Test Number	$3/\mu_i$	$\sqrt{15}/\sigma_i$	σ/μ_i
1	8.959	9.359	1.236
2	8.180	8.726	1.210
3	9.434	9.884	1.232
4	9.234	8.973	1.329
5	8.519	8.262	1.331
6	10.196	9.072	1.451
7	9.073	10.249	1.143

FIELD AND CABLE CURRENT DISTRIBUTION IN SUBENCLOSURES

For a topologically simple enclosure driven by an internal source, the power flux probability density function $h(z)$ has been well documented, both theoretically and observationally, to be chi square with two degrees of freedom, (2-89) [3,5,6,10-15]

$$h(z) = h_{\chi^2_2}(z) \quad (5-62)$$

If the enclosure is driven by an external plane wave with EM energy leaking in through apertures or other p.o.e.'s, the power flux in the enclosure becomes, as we have just finished describing, the product of two variates, (5-1). One variate has a chi square distribution with two degrees of freedom, and the other is chi square with six degrees of freedom. This conclusion was originally deduced by Lehman.[1,2] To review, the reasoning for the distribution of the second variate was that the apertures could be driven by fields having three possible axes of propagation, each accompanied by two possible independent polarizations.¹

The power flux probability density function for an externally illuminated leaky chamber, in terms of the two variates, thus becomes representable as (5-2), which leads to the Lehman distribution, (5-6).

Using the above reasoning, for nested leaky chambers with drive from outside the outer chamber, the fields at the apertures of the inner chamber should have a Lehman-distributed power flux driving their $h_{\chi^2_2}(6,z)$ physical attribute, and the inner chamber itself should have its own $h_{\chi^2_2}(2,z)$ property. These statements imply that, after working our way down through the two topologies, we find the power-flux probability density function in the inner chamber to be the product of four variates,

$$z = z_1 z_2 z_3 z_4 \quad (5-63)$$

¹ The energy density inside a chamber is the sum of the two phase-quadrature components squared and resummed over the three physical axes; i.e., it is the sum of six squares, and thus will have distributional attributes reminiscent of chi square with six degrees of freedom. It may seem that this energy probability density function is the origin of the $h_{\chi^2_2}(6,z)$ attribute of (5-2) (as opposed to its origin being a consequence of aperture physics). This viewpoint is demonstrably incorrect, however, as the power-flux probability density function for internal illumination (5-1) also stems from an energy probability density function which is the sum of the same six squares. Yet (5-1) has no $h_{\chi^2_2}(6,z)$ constituent.

where z_1 and z_3 are χ^2 with two degrees of freedom, while z_2 and z_4 are χ^2 with six degrees of freedom.² This expression may be reorganized by recognizing that the product of the z_1 and z_2 variates, z_{12} , is a variate with a Lehman distribution, as is the product of the z_3 and z_4 variates, z_{34} .

$$z = z_{12} z_{34} \quad (5-64)$$

The overall probability density function of the power flux in the inner chamber may thus be obtained, in analogy with (5-6) or (5-8), as the logarithmic convolution of the inner and outer Lehman probability density functions:

$$\begin{aligned} h_{\text{inner}}(z) dz &= \int_0^\infty h_{l_{12}}(z'_{12}, \Lambda_{12}) h_{l_{34}}(z/z'_{12}, \Lambda_{34}) d(\ln z'_{12}) dz \\ &= \int_0^\infty [\Lambda_{12}^2 z'_{12} K_2(2\sqrt{\Lambda_{12} z'_{12}})] [\Lambda_{34}^2 (z/z'_{12}) K_2(2\sqrt{\Lambda_{12} z/z'_{12}})] \frac{dz'_{12}}{z'_{12}} dz \end{aligned} \quad (5-65)$$

If it proves that z_1 is properly omitted from (5-63), (5-64) will be replaced by

$$z = z_2 z_{34} \quad (5-66)$$

and the first bracket in (5-65), containing the outer Lehman probability density function, will be replaced by the chi square distribution with six degrees of freedom,

$$h_{\chi_6^2}(z'_2) = \gamma_6^3 (z'_2)^2 e^{-\gamma_6 z'_2} \quad (5-67)$$

FIELDS IN ENCLOSURES WITHIN MODE-STIRRED CHAMBERS

The power-flux probability density function inside a mode-stirred chamber at a fixed point and frequency is chi square with two degrees of freedom. Thus, the power flux probability density function in a leaky enclosure illuminated by the fields of a mode-stirred chamber differs from that present when illumination is plane wave by the addition of a third variate to (5-1),

$$z = z_0 z_1 z_2 \quad (5-68)$$

² There is another line of reasoning which eliminates one of the variates with two degrees of freedom from (12). While more thought (and probably testing against experiment) will be required to sort out this choice, the procedure used to reach an ultimate mathematical expression for the inner-chamber power-flux distribution is independent of this choice.

where z_0 is χ^2 with two degrees of freedom. For simplification and conformity with previous notation, let us redefine the variate factors of (5-68) as follows

$$z = z_1 z_3 z_4 \quad (5-69)$$

Then, the power-flux probability density function inside the inner chamber becomes of the form of (5-65), with

$$h(z'_1) = h_{\chi^2}(z'_1) \quad (5-70)$$

replacing the outer Lehman distribution in (5-65); i.e., with $h_{\chi^2}(2,z)$ replacing $h_{\chi^2}(6,z)$ in (5-67),

An item of additional concern with all these issues is that of how many independent variables are needed to define the probability density function. In the original Lehman distribution (5-17), only the mean power flux (μ or Λ) inside the enclosure must be found. For nested enclosures, the mean power fluxes (Λ_{12} and Λ_{34}) in both the inner and outer regions appear, although we speculate that there will be some way to eliminate the outer Lehman parameter Λ_{12} when attempting to determine the inner enclosure power-flux probability density function.

The same is probably true for enclosures nested in mode-stirred chambers: (5-67) implies that γ_6 and Λ_{34} , are both required, but we are sure there is a way to eliminate λ_6 when computing the power-flux and electric-field distribution densities inside the cavity.

EXTRAPOLATION OF PLANE-WAVE RESPONSE FROM MODE-STIRRED MEASUREMENTS

As indicated by (5-68), the power-flux probability density function of an enclosure in a mode-stirred chamber is obtained as the product of three variates, where z is the actual final result. However, (5-68) can be reversed to demonstrate that the associated plane-wave power-flux probability density function inside the enclosure can be expressed as the quotient of two variates,

$$z_3 z_4 = z_{pw} = z_0 / z_1 \quad (5-71)$$

where z_0 represents the mode-stirred power-flux probability density function variate within the enclosure, and z_1 is a generic chi-square variate with two degrees of freedom. The probability density function of z_0 is what would be measured in a mode-stirred chamber. What we actually want is the probability density function of the power-flux within the chamber when plane-wave illuminated, z_{pw} .

The power-flux probability density function inside the chamber for hypothetical plane-wave illumination on the outside thus becomes

$$h_{\text{meas}}(z_0) h_{\chi_2^2}(z_1) dz_0 dz_1 \quad (5-72)$$

where this expression gives the probability that z_0 is between z_0 and $z_0 + dz_0$, while z_1 is between z_1 and $z_1 + dz_1$. However, z_0 , z_1 , and z_{pw} are not all independent variates. If (5-72) holds, the probability that z_1 is between z_1 and $z_1 + dz_1$, while z_{pw} is between z_{pw} and $z_{\text{pw}} + dz_{\text{pw}}$ is obtained from the variate transformation

$$\begin{aligned} z_1 &= z_1' \\ z_0 &= z_1 z_{\text{pw}} \end{aligned} \quad (5-73)$$

The two-dimensional probability density function then becomes

$$h_{\text{meas}}(z_1', z_{\text{pw}}) h_{\chi_2^2}(z_1') \frac{\partial(z_1, z_0)}{\partial(z_1', z_{\text{pw}})} dz_1' dz_{\text{pw}} \quad (5-74)$$

where

$$\frac{\partial(z_1, z_0)}{\partial(z_1', z_{\text{pw}})} = \begin{vmatrix} \partial z_1 / \partial z_1' & \partial z_0 / \partial z_1' \\ \partial z_1 / \partial z_{\text{pw}} & \partial z_0 / \partial z_{\text{pw}} \end{vmatrix} = \begin{vmatrix} 1 & z_{\text{pw}} \\ 0 & z_1' \end{vmatrix} = z_1' \quad (5-75)$$

is the Jacobian of the (5-73) variate transformation. We now wish to find the probability that z_{pw} is between z_{pw} and $z_{\text{pw}} + dz_{\text{pw}}$ regardless of z_1' . This 1D probability differential is obtained as in previous situations [(2-86) and (5-6)], by summing all the 2D probability differentials of z_1' and z_{pw} over z_1' ; i.e., by integrating (5-75) over all possible z_1'

$$h(z_{\text{pw}}) dz_{\text{pw}} = \int_0^{\infty} h_{\text{meas}}(z_1' z_{\text{pw}}) h_{\chi_2^2}(z_1') z_1' dz_1' dz_{\text{pw}} \quad (5-76)$$

Equation (5-76) is the desired formula for extracting a predicted plane-wave power-flux probability density function $h(z_{\text{pw}})$ from a measured mode-stirred data set $h_{\text{meas}}(z_0)$. This equation can be used, for example, to relate the experimental results from the PLEXIS electronic mode-stirred chamber (being developed at the Air Force Phillips Laboratory) to the radiated susceptibility limits of standards such as MIL-STD-461D, SAE J 1113 and 1338, and the European IEC 801-3 - based EN 50082-1 and IEC 1000-4-3 (now under development). All these standards specify transmission-line excitation, and IEC 801-3 notes that, "The use of shielded enclosures has always caused a high degree of controversy..."

There is a variable γ_2 in $h_{\chi_2}(2, z_1)$ which needs to be eliminated from (5-76). Again, although we have not yet worked through the relevant derivation, we assume all powers of γ_2 in (5-76) will cancel upon actual implementation.

REFERENCES

- [1]. T. H. Lehman and R. M. Marshall, "Application of statistical physics to derivation of stress and strength distributions," Ball Systems Engineering Division, Albuquerque, NM, September 26, 1991.
- [2]. T. H. Lehman, "A statistical theory of electromagnetic fields in complex cavities," Air Force Phillips Laboratory, Interaction Note 494, May 1993.
- [3]. R. Holland & R. St. John, "Statistical Coupling of EM Fields to Cables in an Overmoded Cavity," *Conference Proceedings, 12th Annual Review of Progress in Applied Computational Electromagnetics*, Monterey, CA, Vol. II, pp. 877-887, 18-22 March 1996.
- [4]. R. Holland & R. St. John, "Statistical Description of Cable Current Response Inside a Leaky Enclosure," *Conference Proceedings, 13th Annual Review of Progress in Applied Computational Electromagnetics*, Monterey, CA, Vol. II, pp. 877-887, 17-21 March 1997.
- [5]. R. H. Price, *et al*, "Determination of the Statistical Distribution of Electromagnetic Field Amplitudes in Complex Cavities," 88JAL129, JAYCOR, 1 June 1988.
- [6]. R. H. Price, H. T. Davis, and E. P Wenaas, "Determination of the Statistical Distribution of Electromagnetic-Field Amplitudes in Complex Cavities," *Phys. Rev. E*. Vol. 48, pp. 4716-4729, December 1993.
- [7]. I. S. Gradshteyn and I. M. Ryzhik, *Tables of Integrals, Series, and Products*. New York: Academic Press, 1965, p. 307, Eq. (3.324.1) and p. 684, Eq. (6.561.16),
- [8]. *Ibid*, p. 306, Eq. (3.321.2); p. 310, Eq. (3.351.1); and p. 930, Eq. (8.250.1).
- [9]. *Users' Guide Mathcad®*. Cambridge MA: MathSoft, 1986-1995.
- [10]. Holland, R. and R. St. John, "Coupling of Statistical EM Field Models to Cables in an Overmoded Cavity," submitted to *IEEE Trans. Electromagn. Compat.*

- [11]. Holland, R. and R. St. John, "Statistical Response of EM-Driven Cables Inside an Overmoded Enclosure," submitted to *IEEE Trans. Electromagn. Compat.*
- [12]. Holland, R. and R. St. John, "Statistical HPM Satellite Survivability Modeling," PL-TR-96-1181, Air Force Phillips Laboratory, Kirtland Air Force Base, NM, 1996.
- [13]. Holland, R. and R. St. John, "Enforcing Correlation of Statistically Generated EM Cable Drivers," *Conference Proceedings*, Vol. 1, pp. 308-320, 11th Annual Review of Progress in Applied Computational Electromagnetics, Monterey, CA, 20-25 March 1995.
- [14]. Holland, R. and R. St. John, "Statistical Response of Enclosed Systems to HPM Environments," PL-TR-94-1006, Air Force Phillips Laboratory, Kirtland Air Force Base, NM, 1994.
- [15]. Holland, R. and R. St. John, "Statistical Responses of Enclosed Systems to HPM Environments," *Conference Proceedings*, Vol. 2, pp. 554-568, 10th Annual Review of Progress in Applied Computational Electromagnetics, Monterey, CA, 21-26 March 1994.

Chapter 6. FIELD-TESTS OF LEHMAN-MODELED CABLE CURRENTS, THE BETA DISTRIBUTION, AND ACCEPTANCE LIMITS

In addition to having data available from the EMPTAC facility and the Celestron 8 satellite telescope, we had the opportunity to make our own measurements with a waveguide-cavity approximately $1\text{m} \times 1\text{m} \times 8\text{m}$, and a Global Positioning Satellite (GPS) bus, the latter provided by the Air Force Phillips Laboratory. In this section, we shall describe testing done on these systems. Additionally, we shall here work through the (3-7) - (3-12) field-to-current algorithm to evaluate cable current distributions ensuing from Lehman-modeled field distributions. (In the previous section, we only developed and tested EM-field models.)

MEASUREMENTS IN THE WAVEGUIDE CHAMBER

We first measured electric fields at 401 frequencies from 300 MHz to 3 GHz using an EG&G ACD-4 \vec{D} -sensor connected to an HP8753 network analyzer. The waveguide cavity (see Figure 6.1) was illuminated by a log-periodic antenna (see Figure 6.2) driven by the network analyzer in tandem with an amplifier, which boosted the total antenna input to 1 W. The cavity configuration was approximately J-shaped, with the "J" lying in a plane parallel to the ground, and leakage mostly at the crown of the "J", which was also the surface facing the antenna. Current was observed on the shield of a coaxial cable, which was placed in a variety of orientations in the chamber. The currents were measured by the network analyzer through a Fischer PNF-65 $\oint \vec{B} \cdot d\vec{s}$ probe. Placement of the current probe was at the cable midpoint.

The \vec{D} -sensor was moved around within the chamber volume to obtain the four sets of data we will cite. A distance of 1 - 2 m was maintained between the probe and the cable. Orientation of the illuminating antenna was also a variable.

We made two comparisons between model values and experimental results: 1) Lehman statistics were checked against the measured field distributions, and 2) modeled currents were compared to observation. Figure 6.3 presents the average cumulative distributions of four 401-frequency-point electric-field sweeps. The comparison is between the normalized and averaged squares of the magnitude of the electric field data and the Lehman cumulative distribution function (cdf) (5-22). Normalization was performed by dividing each of the four data sets (squared), by the four individual averages of the squared data:

$$z_i = \frac{1}{4}[z_{i1}/\mu_1 + z_{i2}/\mu_2 + z_{i3}/\mu_3 + z_{i4}/\mu_4] \quad (6-1)$$

This normalization permitted combined use of data from different observation points (where the fields might have different average values), without superimposing possibly different spatial distribution functions of the frequency distribution functions of immediate concern. (The spatial distribution functions *should* also be Lehman, but we did not want to test two hypotheses at once.) Also shown in Figure 6.3 is the chi square (with two degrees of freedom) cdf, $H_{\chi^2}(2, z)$,

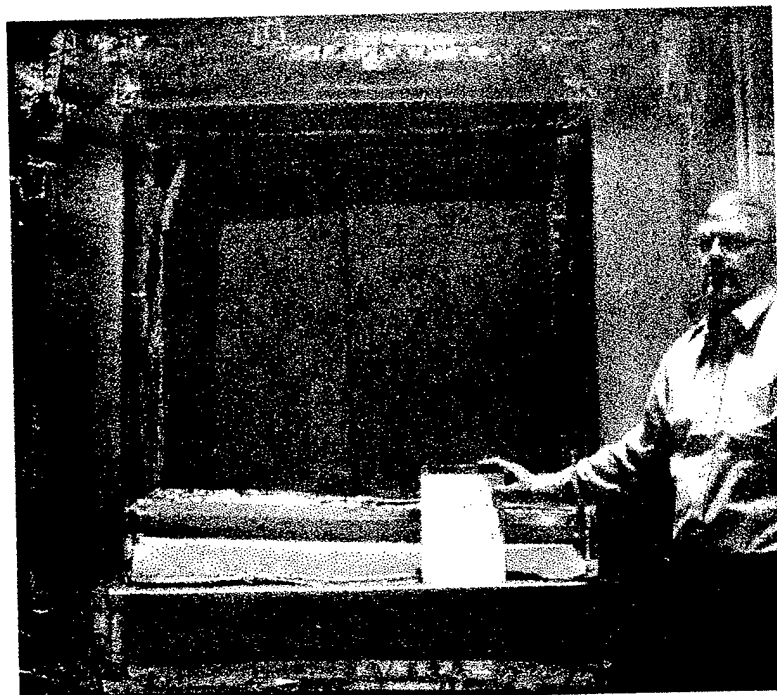


Figure 6.1. Top (front) of the J-shaped microwave chamber used for field- and current-distribution testing.

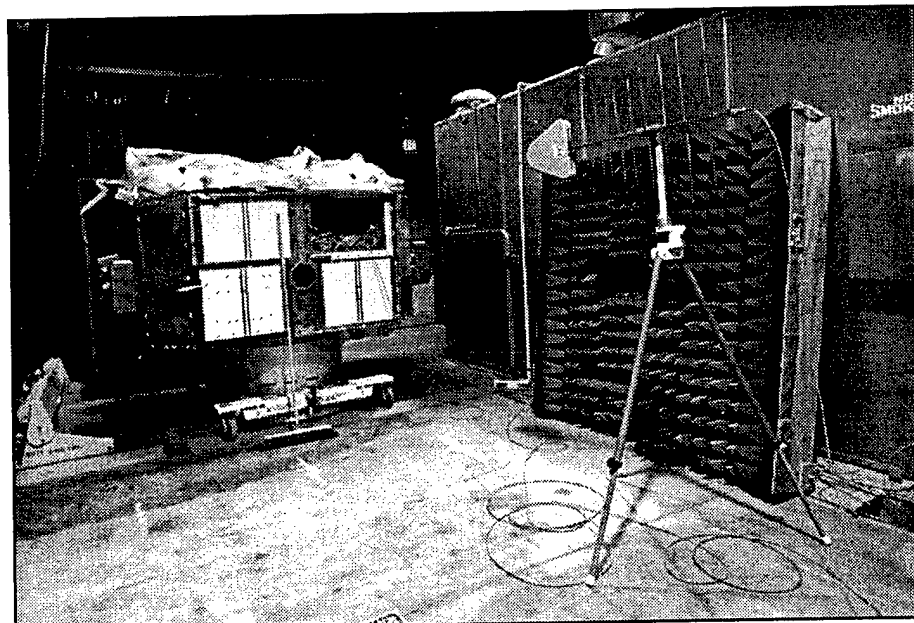


Figure 6.2. GPS bus (less antenna and solar panels) illuminated by log-periodic antenna (right). Note dust mop (in front of bus) to give size perspective.

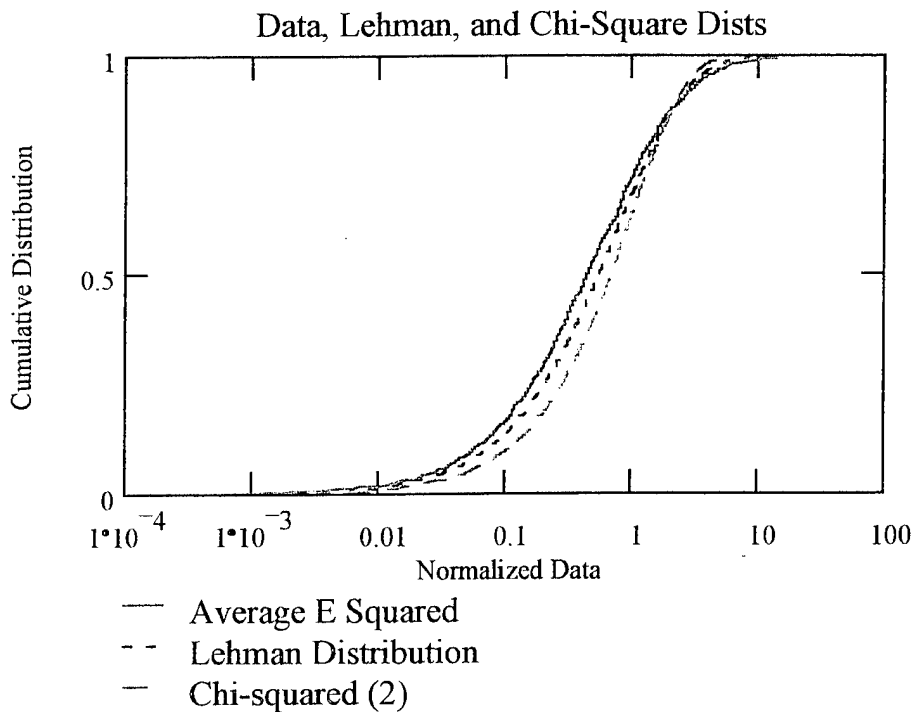


Figure 6.3. Cumulative distributions of averaged, normalized waveguide-chamber electric fields (measured), compared with those predicted from Lehman (5-22) and χ^2 (2-89) models. All curves are normalized so $\mu = 1$.

(2-89). The Lehman distribution may be seen consistently to hug the experimental data more closely than the chi square distribution.

The second comparison was made between modeled and measured currents. Using the Λ parameters from the four sets of measured electric fields before normalization, four sets of Lehman-distributed phase-quadrature fields were generated from random numbers between 0 and 1 using the inverse Lehman operator associated with (5-27) or (5-61). These fields were then input to the (3-7) - (3-12) field-to-current algorithm to obtain model currents on the cable. The magnitudes of the four sets of measured and modeled currents were then normalized by the means of the associated measured-current sets. (The modeled-current sets were not normalized by their own means, thus preserving possible systematic discrepancies between the measured and modeled results.) Cumulative distributions of the eight resulting normalized current magnitudes appear in Figure 6.4. The four normalized, measured currents all cluster very tightly to the left (smaller) side. Three of the predicted data sets also overlay very tightly; there is a single high-value outlier. The modeled currents are consistently larger than the observed, although never by more than a factor of two. There are two possible sources of this disagreement: the driving-field model and the field-to-current algorithm. Because of the excellent agreement between measured and modeled fields in Figure 6.3, it is probable that most of the error occurs in the second of the above.

At this point, electric fields were monitored at two additional sites inside the waveguide chamber. Figures 6.5 and 6.6 illustrate the observed cumulative E^2 distribution, along with the Lehman cdf. The Lehman parameter was determined from the measured E^2 mean, $\Lambda = 3/\mu$. The associated Lehman phase-quadrature field distributions (autocorrelated) from (5-27) were then input to the field-to-current algorithm of (3-7) to (3-12), leading to the midpoint cable current distributions shown in Figures 6.7 and 6.8. So far, all Lehman-based cable current calculations exceed what was measured. While this seems to occur regularly for the waveguide chamber, it does not always hold for GPS cable current models.

In this series of tests, we also first looked at fields and cable currents inside the GPS bus. Figures 6.9 and 6.10 show two typical cumulative E^2 distributions and the associated Lehman fits. These Lehman fits then gave current drivers (autocorrelated) from (5-27) to model GPS cable response according to the (3-7) to (3-12) formulation. Resulting modeled and measured currents appear in Figures 6.11 and 6.12. One may see here that the currents are no longer consistently over predicted, although deviation between model and measurement remains within a factor of 2.

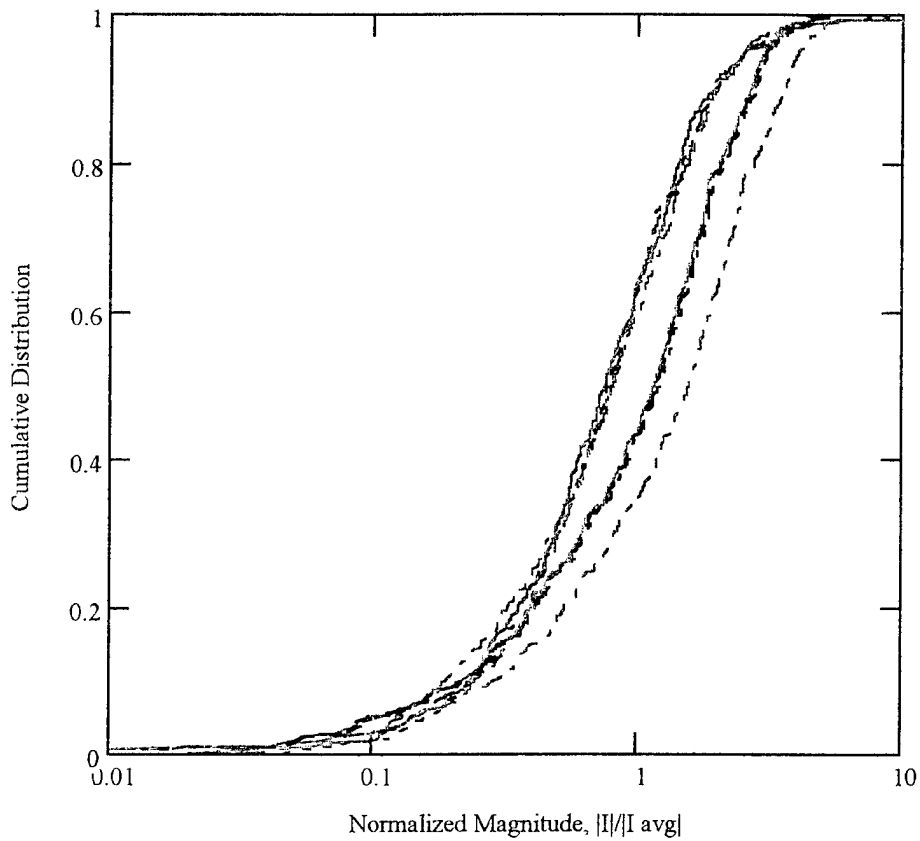


Figure 6.4. Overlay of four cable current measurements (cluster of four left traces), and four cable-model predictions (cluster of three middle traces and right outlier). Each modeled cable current distribution is normalized by the mean of the associated measured distribution.

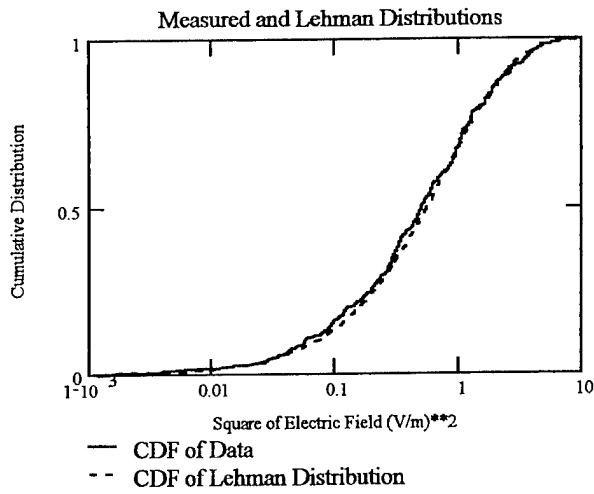


Figure 6.5. CDF of E^2 at Loc. 1 inside the waveguide chamber. Based on measured $\Lambda = 2.986$. (f9)

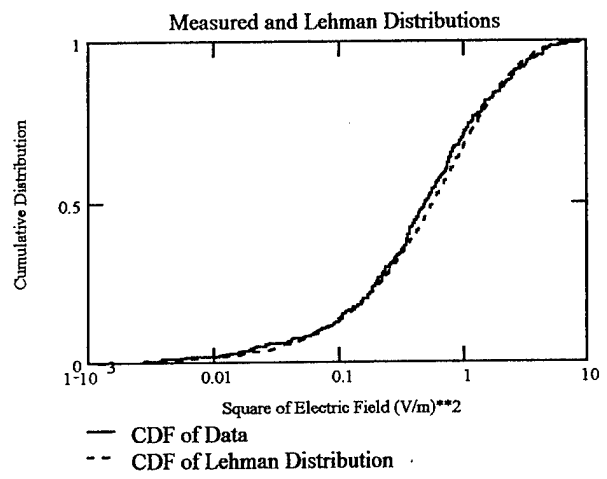


Figure 6.6. CDF of E^2 at Loc. 2 inside the waveguide chamber. Based on measured $\Lambda = 2.954$. (f10)

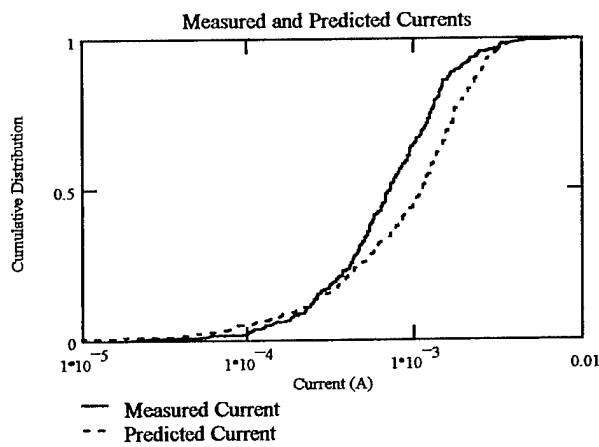


Figure 6.7. CDF of $ABS(I)$ at Loc. 1 inside the waveguide chamber. Based on Lehman E -field distribution of Figure 6.5. (f1 and f2)

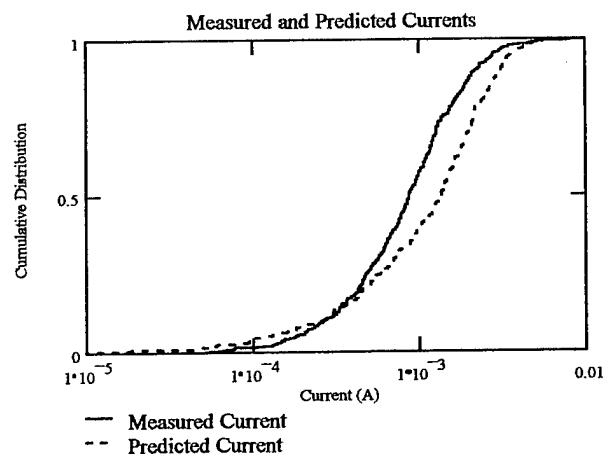


Figure 6.8. CDF of $ABS(I)$ at Loc. 2 inside the waveguide chamber. Based on Lehman E -field distribution of Figure 6.6. (f3 and f4)

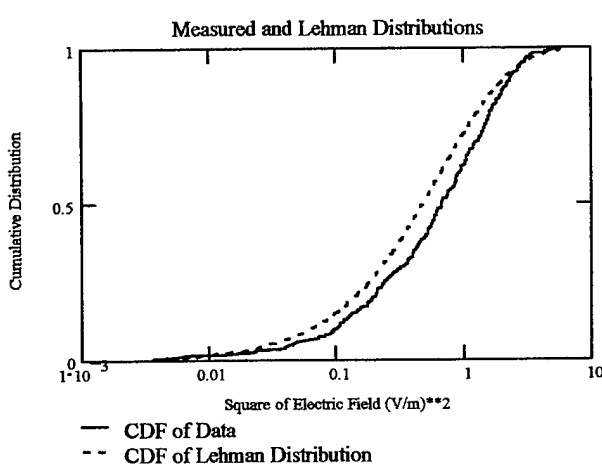


Figure 6.9. CDF of E^2 in lower Bay 1 of GPS.
Based on measured $\Lambda = 3.486$. (f5)

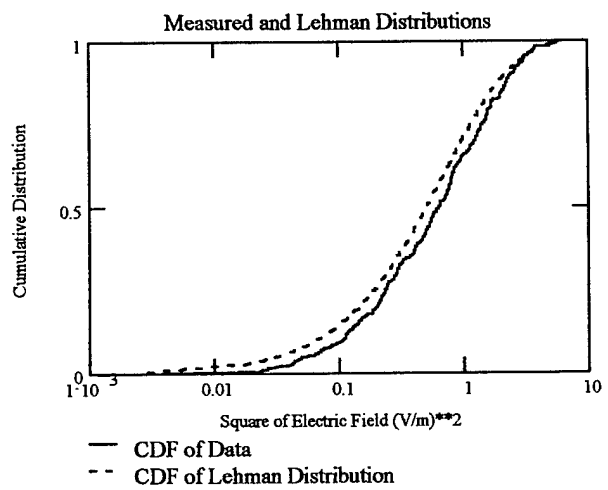


Figure 6.10. CDF of E^2 in lower Bay 2 of GPS.
Based on measured $\Lambda = 3.344$. (f6)

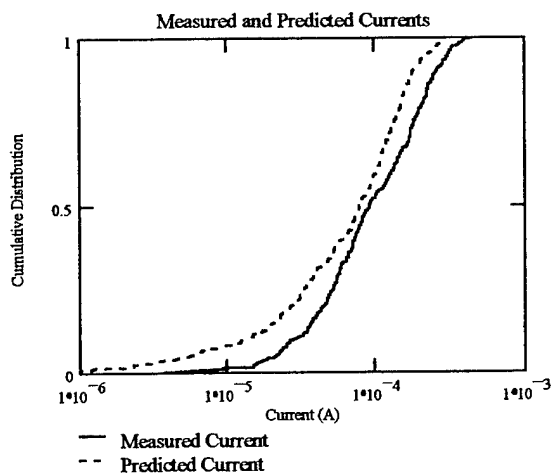


Figure 6.11. CDF of $ABS(I)$ on cable bundle in lower Bay 1 inside the GPS. Based on Lehman E -field distribution of Figure 6.9. (f7 and f8)

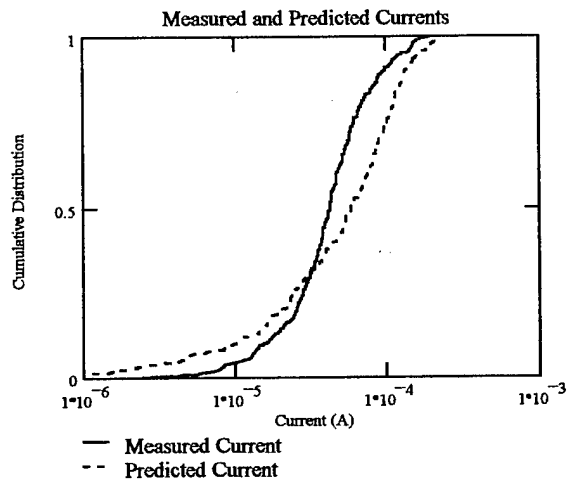


Figure 6.12. CDF of $ABS(I)$ on cable bundle in lower Bay 2 inside the GPS. Based on Lehman E -field distribution of Figure 6.10. (f11 and f12)

THE BETA DISTRIBUTION

For compatibility with some other statistical EM survivability/vulnerability (S/V) software, requests have been made that we look into the beta distribution as a possible designator of field or power-flux distributions. The beta distribution cdf is defined as

$$H_\beta(z, a, b) = \frac{1}{B(a, b)} \int_0^z z'^{a-1} (1 - z')^{b-1} dz' \quad 0 \leq z \leq 1 \quad (6-2)$$

where $B(a, b)$ is the beta function with a and b both positive

$$B(a, b) = \int_0^1 z'^{a-1} (1 - z')^{b-1} dz' \quad (6-3)$$

The beta function is best evaluated by expressing it in a gamma function expansion:

$$B(a, b) = \frac{\Gamma(a)\Gamma(b)}{\Gamma(a+b)} \quad (6-4)$$

It can be seen that the variate values of the beta distribution range from 0 to 1. Thus, in addition to the a and b parameters, the values of the data to be compared to the beta distribution must be scaled and shifted so they lie in the unit interval. Hence, the beta distribution has four parameters: scale, shift, a , and b , as opposed to the single parameter Λ of the Lehman distribution.

Three of the four parameters are found using the mean μ_β , the standard deviation σ_β , and the coefficient of skewness κ_β . We will assume the fourth parameter, offset, is zero as it would be a fairly bizarre random power flux distribution that did not permit values below some threshold. (In point of fact, one of the reasons for even considering a beta distribution is that it does not permit random numbers between 0 and 1, after passing through its inverse operator, ever to exceed some finite value. For zero offset, this value is just the scale factor. Here is a basic difference from all the other distributions we have considered; they all have some small, but nonzero probability that any value, no matter how ridiculously large, can be exceeded by the inverse operator's output.)

The coefficient of skewness is a third-order statistic. It is based on the third moment of the data about its average, normalized by the standard deviation

$$\kappa_\beta = \frac{1}{N\sigma_\beta^3} \sum_{i=1}^N (z_i - \mu_\beta)^3 \quad (6-5)$$

It is related to the beta distribution a and b by

$$\kappa_\beta = \frac{2(b-a)}{(a+b+2)} \sqrt{\frac{(a+b+1)}{ab}} \quad (6-6)$$

The coefficient of skewness can be used to find a scaling factor s which translates the data to values between 0 and 1,

$$\frac{s}{\mu_\beta} = \frac{\kappa_\beta \left(\frac{\mu_\beta}{\sigma_\beta} - \frac{\sigma_\beta}{\mu_\beta} \right) - 4}{\frac{\kappa_\beta \mu_\beta}{\sigma_\beta} - 2} \quad (6-7)$$

The remaining parameters of the beta distribution are then given by

$$a = \left(\frac{\mu_\beta}{\sigma_\beta} \right)^2 \left(1 - \frac{\mu_\beta}{s} \right) - \frac{\mu_\beta}{s} \quad b = a \left(\frac{s}{\mu_\beta} - 1 \right) \quad (6-8)$$

The coefficient of skewness is, of course, subject to a variation on a finite sample. That is, if one generates an infinite data set with a given κ_β , the evaluation of the skewness from a finite sample of the data will not give back exactly the value used to generate the data set.

To maintain values of a and b which are both positive, the coefficient of skewness is constrained to certain values,

$$\frac{\sigma_\beta}{\mu_\beta} - \frac{\mu_\beta}{\sigma_\beta} < \kappa_\beta < \frac{2\sigma_\beta}{\mu_\beta} \quad (6-9)$$

In other words, certain data sets cannot be fit to a beta distribution.

The probability density function (pdf) associated with the beta cdf (6-2) is

$$h_\beta(z, a, b) = \frac{1}{B(a, b)} z^{a-1} (1-z)^{b-1} \quad 0 \leq z \leq 1 \quad (6-10)$$

We, however, now have an interesting choice. The general assumption was that the beta function of (6-2) would describe the squared fields or power flux distribution. Extraction of the phase-quadrature field components would then involve very tedious manipulations like those applied to the Lehman power density pdf in Section 5. There was a strong physical argument in Section 5 for associating the Lehman distribution with power flux. There is no such compelling physical

argument in the case of the beta distribution. Its primary attraction is that of absolutely forbidding cable-drive model fields to exceed some selected ceiling.

However, this objective is equally satisfied by making the intermediate quantity, the phase-quadrature fields squared, but unsummed, be the quantity which is beta distributed. If we make this choice, (6-10) actually becomes replaced by

$$f_{\beta'}(x, a, b) = \frac{1}{B(a, b)} x^{a-1} (1-x)^{b-1} \quad 0 \leq x \leq 1 \quad (6-11)$$

in keeping with the convention of (2-86), (4-6), and (5-41). Now, instead of having to deconvolve $h_{\beta}(z, a, b)$ to find $f_{\beta}(x, a, b)$, we have the far easier task of autoconvolving $f_{\beta'}(z, a, b)$ to find $h_{\beta'}(x, a, b)$:

$$h_{\beta'}(z, a, b) = \int_0^z f(x', a, b) f_{\beta'}(z - x', a, b) dx' =$$

$$\frac{1}{B(a, b)^2} \int_0^z x'^{a-1} (1-x')^{b-1} (z-x')^{a-1} (1-(z-x'))^{b-1} dx' \quad (6-12)$$

$$0 \leq z \leq 1$$

Generation of the actual phase-quadrature field components now follows simply from (2-103),

$$e_{\beta'}(u, a, b) = |u| f_{\beta'}(u^2, a, b) = \frac{|u|}{B(a, b)} u^{2(a-1)} (1-u^2)^{b-1} \quad -1 \leq u \leq 1 \quad (6-13)$$

A DETAILED LOOK AT A GPS RESPONSE

In this subsection, we shall take a close look at the fields and cable currents predicted by our models and verified or rejected experimentally by the Figure 6.2 setup of a log periodic antenna illuminating the GPS. First, the electric field (actually \vec{D}), was measured at a fixed location in the 5BH bay on the lower dark-side of the GPS as frequency was swept in 401 steps from 600 MHz to 2 GHz. The result of squaring this field is plotted in Figure 6.13. Figure 6.14 illustrates the autocorrelation of this data. It bears a not unreasonable resemblance to autocorrelation of other experimental data taken on the EMPTAC (see Figures 2.7-2.9).

The data was first compared to a chi square distribution. Figure 6.15 shows the result plotted against a Kolmogorov-Smirnov test for 90% confidence of fit. The test is obviously failed. The confidence limits here are obtained by plotting (2-89), and then shifting the curves up and down by D , which for 401 points and 90 % confidence is 0.02385 (see Section 9). We then

tested the data against a Lehman distribution, with Figure 6.16 resulting. This test fit, while not actually passing, comes quite close. Next, the data was tested against a beta distribution, with $(\mu, \sigma, \kappa) = (0.0170, 0.0213, 1.98)$ implying $(a, b, s) = (0.497, 5.30, 0.198)$. Figure 6.17 indicates this test is rather spectacularly failed at the low ranges, where a statistics breakdown doesn't have implications on a system S/V analysis. For the upper 65% of variate values, the fit is fine, especially so at the top of the plot where legitimate S/V concerns would be focussed. It is our conclusion that the beta distribution test is passed in the way that matters. Finally, Figure 6.18 illustrates the results of a log normal test fit. This fit is perhaps best characterized as everywhere mediocre.

Square of Magnitude

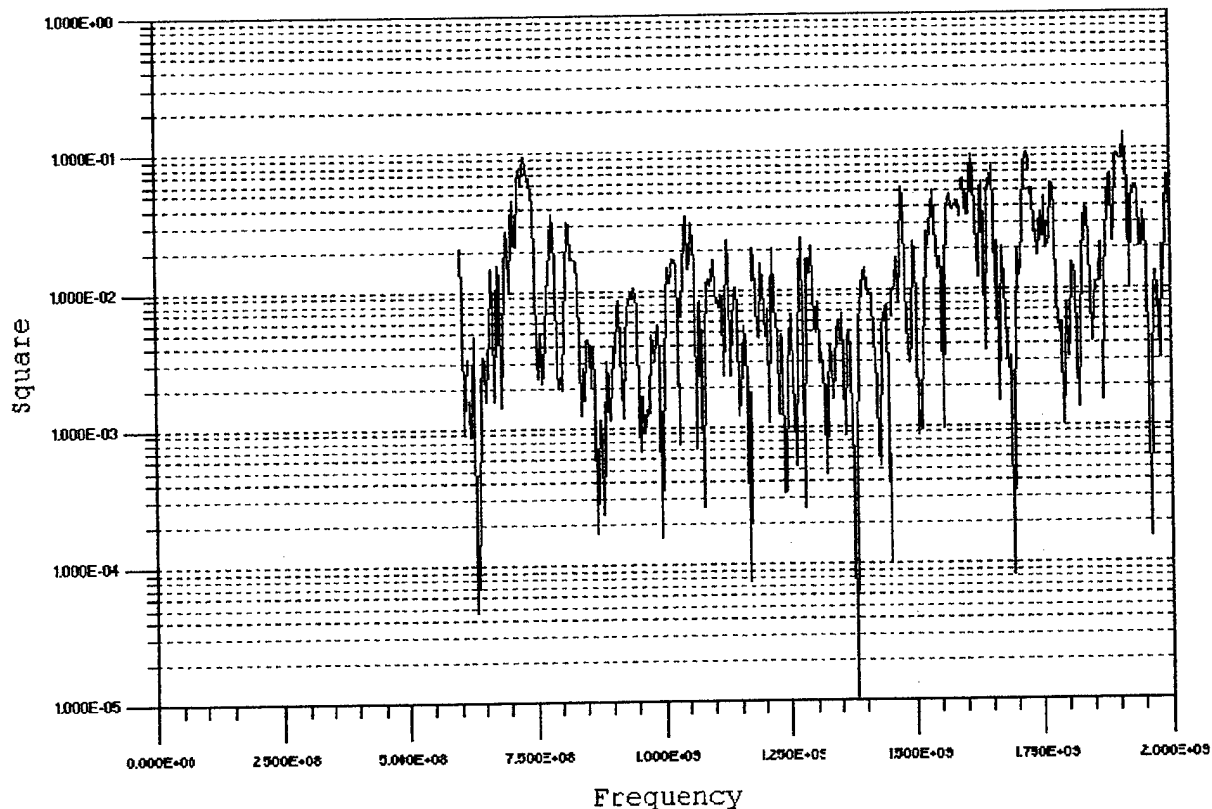


Figure 6.13. Observed E^2 at a fixed point in the 5BH bay on the lower dark-side of the GPS as frequency is stepped from 600 MHz to 2 GHz. Mean μ , standard deviation σ , and coefficient of skewness κ were found to be $(0.0170, 0.0213, 1.98)$.

Correlation of Data

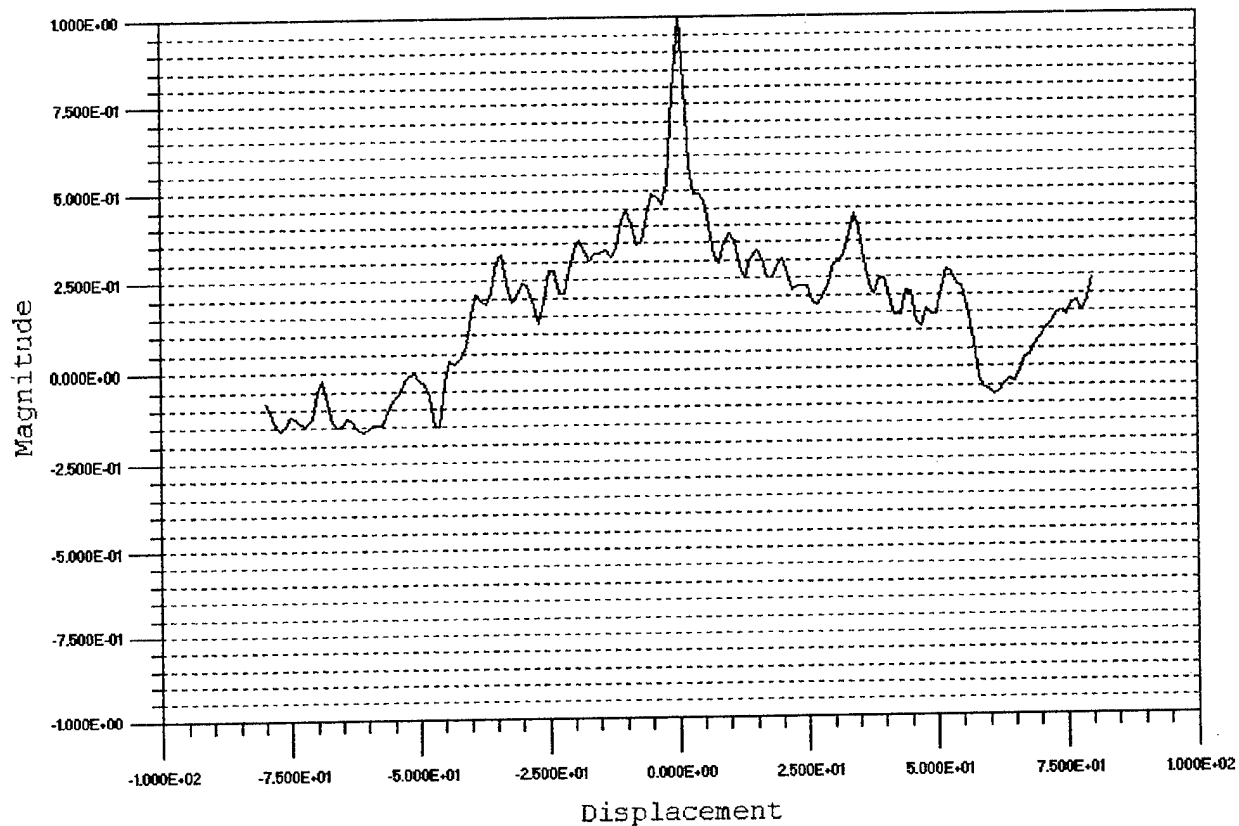


Figure 6.14. Autocorrelation of data appearing in Figure 6.17. Displacement is in units of frequency steps. This plot resembles Figures 2.7--2.9 taken on the EMPTAC facility, except the scale has been linearly stretched to go from -1 to 1 instead of 0 to 1.

K-S Comparison

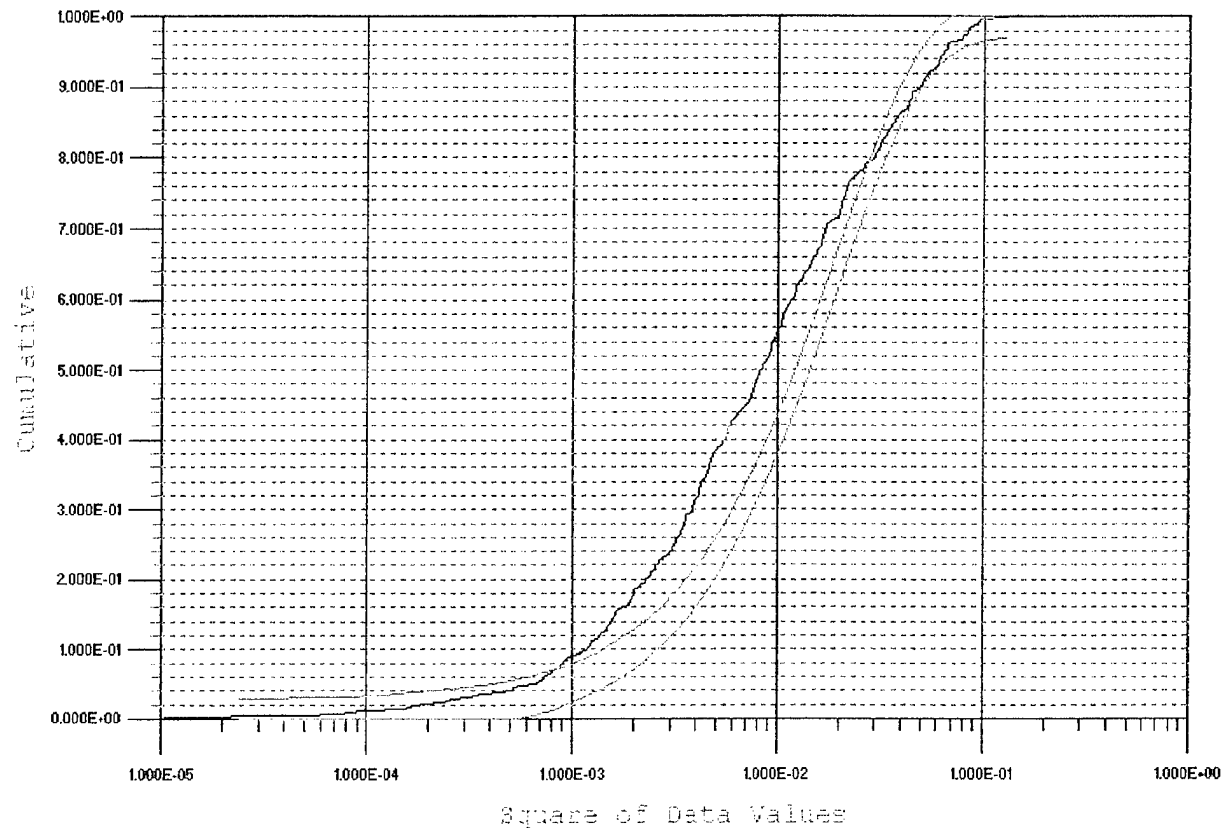


Figure 6.15. The Figure 6.13 data fails a 90% K-S confidence test for fitting a chi square (two degrees of freedom) distribution, especially at midrange. This plot is based on $\mu_c = 0.0170$.

K-S Comparison

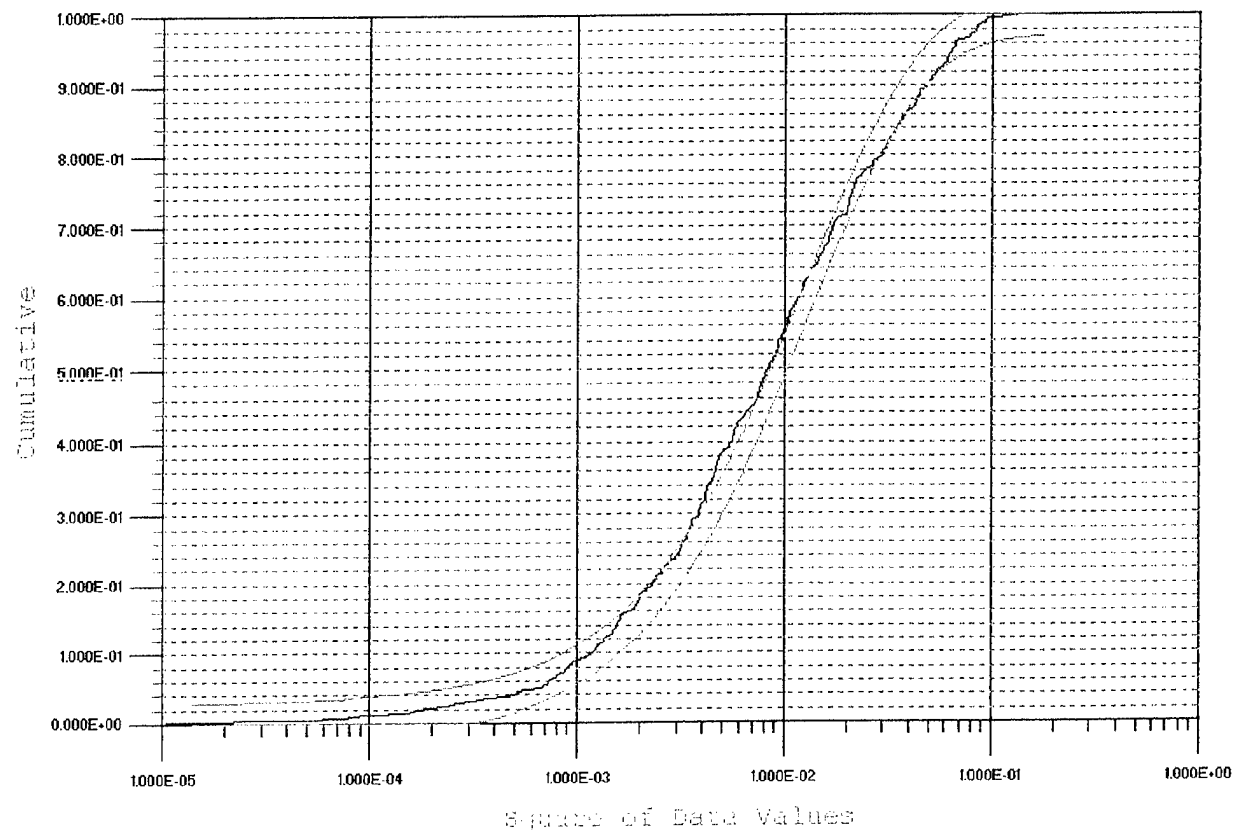


Figure 6.16. The Figure 6.13 data narrowly misses a 90% K-S confidence test for fitting a Lehman distribution. This plot is based on $\Lambda = 176.4$.

K-S Comparison

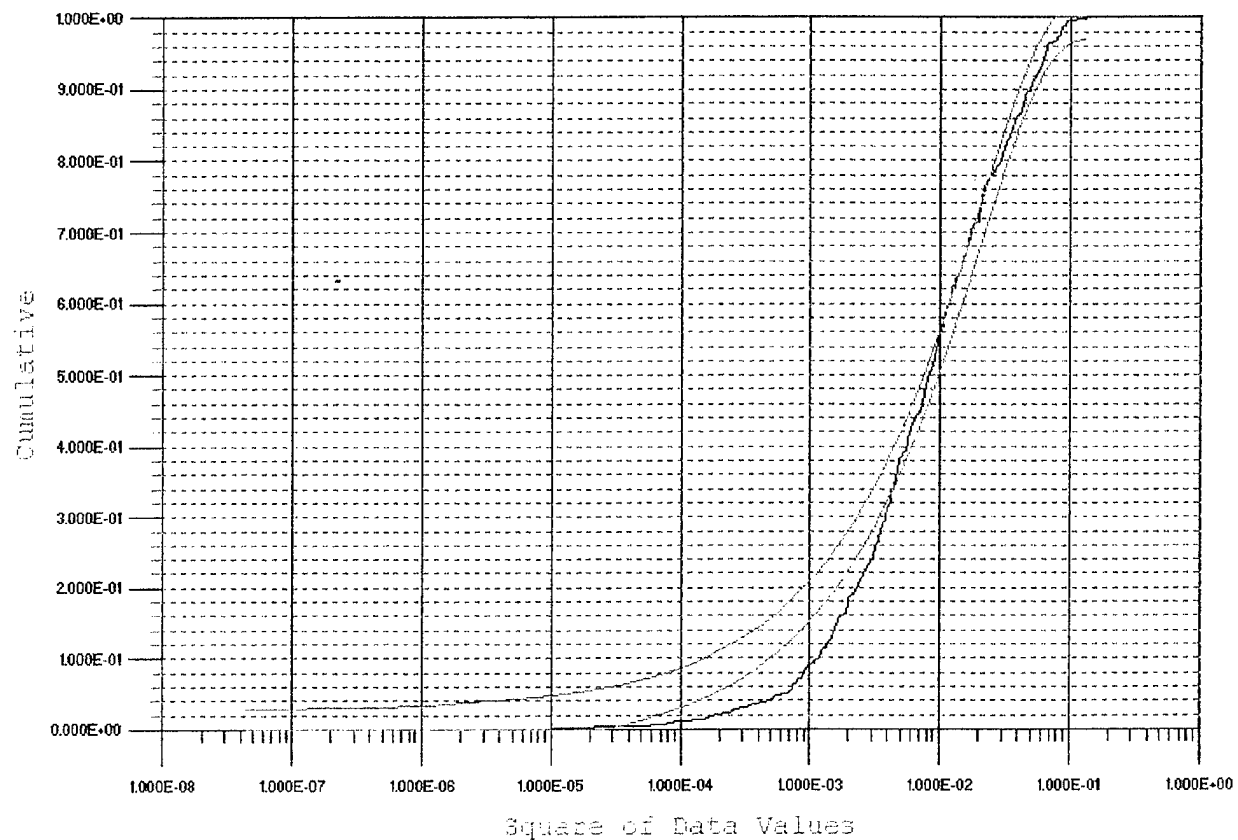


Figure 6.17. The upper 65% of the Figure 6.13 data passes 90% K-S confidence test for fitting a beta distribution. This plot is based on $(\mu, \sigma, \kappa) = (0.0170, 0.0213, 1.98)$, implying $(a, b, s) = (0.497, 5.30, 0.198)$. Despite the severe excursion on the lower tail, this fit is considered acceptable for practical (as opposed to purist) concerns.

K-S Comparison

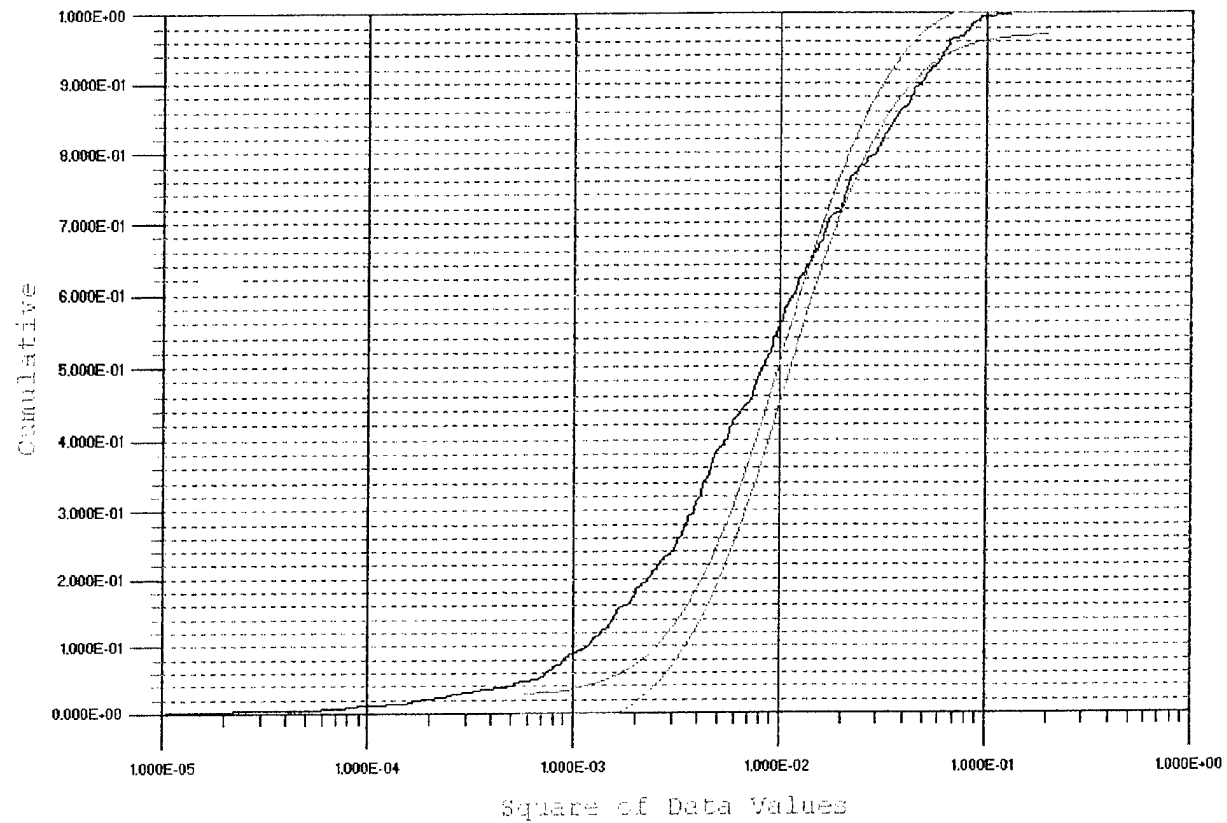


Figure 6.18. The Figure 6.13 data does not fit a 90% K-S confidence test for being log normal; the deviation is bipolar. This plot is based on $(\mu_{lg}, \sigma_{lg}) = (-4.546, 0.972)$.

ACCEPTANCE LIMITS

While the Kolmogorov-Smirnov test is a nice, rigorous way for checking distribution models, it does not give the information which is really wanted for a S/V analysis. In particular, it applies confidence limits or intervals along the probability axis. What we really need to know is, are our conclusions reliable within some fixed magnitude error (say, $\pm 50\%$)? If we, for example, examine the K-S plot in Figure 6.15, we see that the K-S test provides absolutely no information of the model's reliability for the fraction of results (or predictions) which are in the top $100 \times D\%$, where, in this case, $D = 0.02385$ (see Section 9). In other words, the K-S test is no help in determining if our model works at the extreme upper tail, where killer responses occur. The failure of the K-S test to give this information is even more graphically displayed in the original SEM work by Price and Davis, where the K-S limits are superimposed on probability plots.[1,2]

To address this problem more appropriately, we introduce the concept of the *acceptance limit* or interval.[3] This interval is usually defined as the spread between the confidence curves along the axis perpendicular to probability or cdf, and thus is narrow at midrange, but broad at the distribution tails, and infinite above $p = 1 - D$. As such, it, thus, gives no more help where help is needed. We chose to define the acceptance limits as the result of taking the model result and shifting it (say $\pm 50\%$) along the axis perpendicular to the cdf. Figure 6.19 is the result of applying this procedure to the chi square model of the Figure 6.12 data. Our acceptance interval definition may be seen to be especially tidy if the axis along which model displacement occurs is logarithmic.

Figure 6.20 is a similar acceptance interval plot for the Lehman distribution model, and Figure 6.21 treats the beta distribution acceptance interval. Finally, Figure 6.22 treats the log normal representation. While all four models pass the acceptance interval test over the top 50% of the probability domain, only the Lehman model works everywhere. The beta model is considered an interesting alternative due to its remarkable fidelity at the very top of the domain. The chi square and log normal models give poorer accountings for themselves.

Of course, the real test of a field model is whether its inverse operator yields random-number field drivers which produce cable current distributions in agreement with measured cable currents. We first used the inverse Gaussian operator, (2-28), (2-36) and (2-104), to generate phase-quadrature cable drivers corresponding to a chi square power flux distribution. Autocorrelation was included in the cable-drive ensemble according to (3-28) and (3-29), and converted to cable currents as outlined in (3-7) to (3-12). Results appear in Figure 6.23, plotted in comparison with a $\pm 50\%$ acceptance interval. (Only data for response from 600 MHz to 1 GHz is included, as we do not have a current probe which performs above 1 GHz.)

At present, we do not have a phase-quadrature model cable driver operational which is based of a beta distribution for the squared field components (summed or unsummed). Consequently, the next test was performed using the inverse Lehman phase-quadrature field generator (5-27) or (5-61) (see Figure 6.24). Lastly, the cable model was tested using the inverse log normal phase-quadrature field generator of (4-22), with the result displayed in Figure 6.25.

The log normal field model yields cable current predictions which are incompatible with observed cable currents at the $\pm 50\%$ acceptance level. The chi square and Lehman models predict cable currents with $\pm 50\%$ acceptance intervals which contain the measured cable currents, although the Lehman model yields cable current predictions which are much closer to the acceptance interval midline.

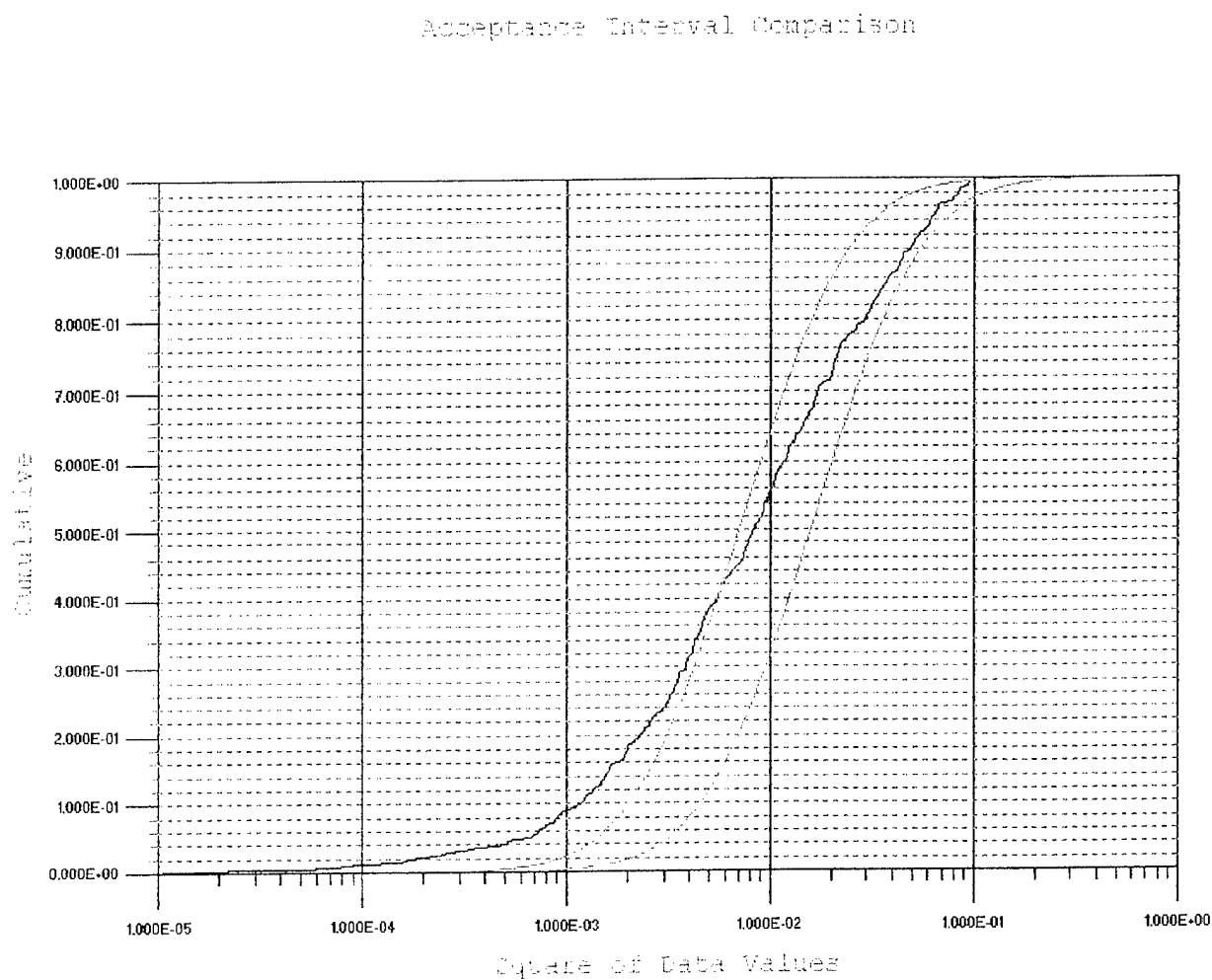


Figure 6.19. The Figure 6.13 data lies within a $\pm 50\%$ acceptance interval for fitting a chi square (two degrees of freedom) distribution, over the upper half of its domain. This means the chi square model is probably an acceptable, even if not ideal, representation of the data. This plot is based on $\mu_c = 0.0170$.

Acceptance Interval Comparison

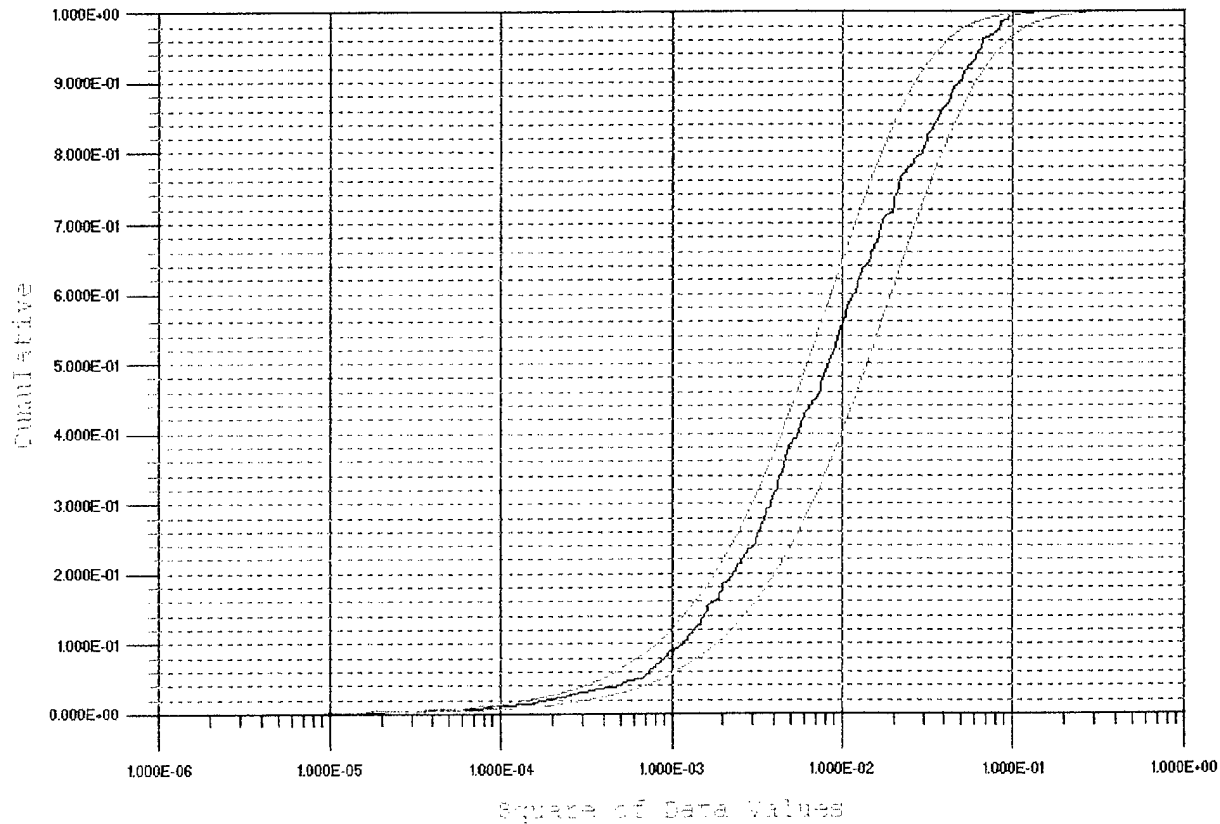


Figure 6.20. The Figure 6.13 data lies well within a $\pm 50\%$ acceptance interval for fitting a Lehman distribution over its entire domain. This means the Lehman model is an excellent replication of reality. This plot is based on $\Lambda = 176.4$.

Acceptance Interval Comparison

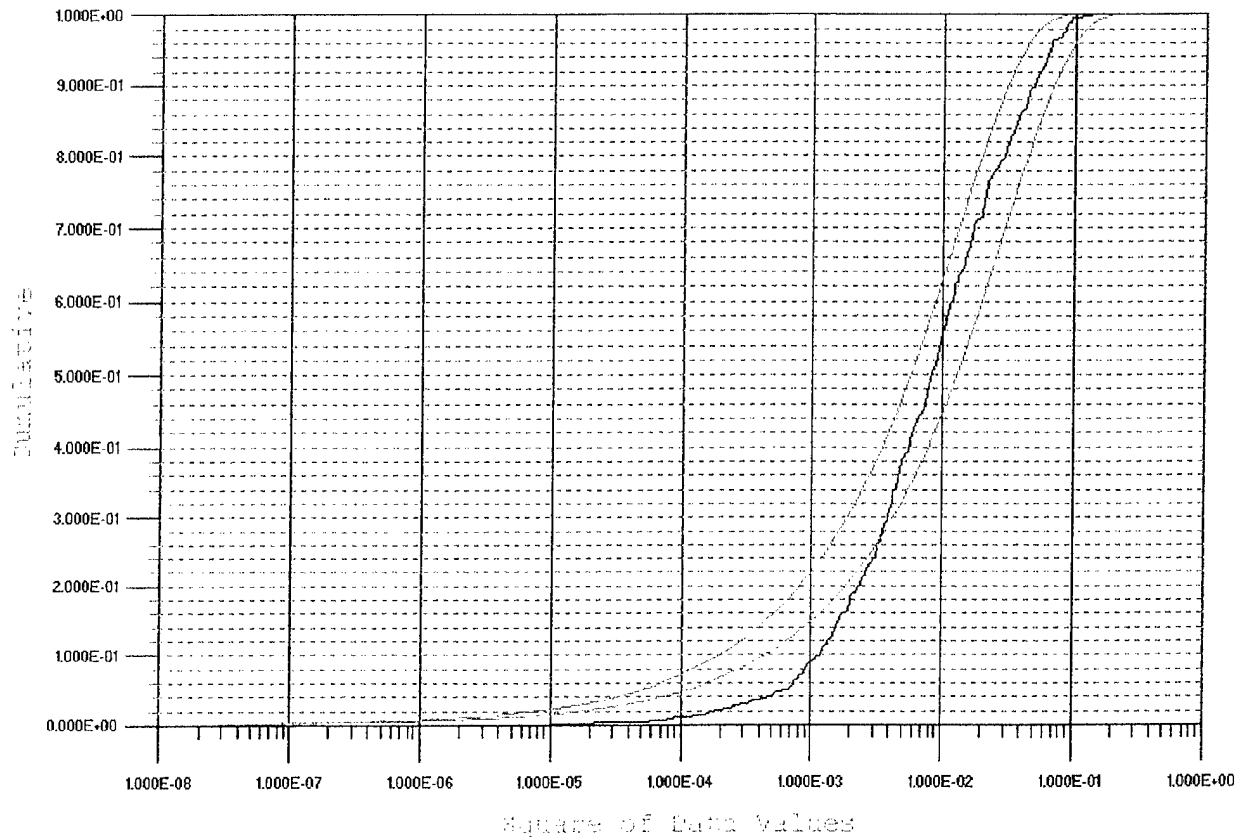


Figure 6.21. The Figure 6.13 data lies within a $\pm 50\%$ acceptance interval for fitting a beta distribution, over the upper 75% of its domain. This means the beta model is an acceptable representation of the data. The tendency of the beta distribution model to split, almost perfectly, the acceptance interval over the top 15% of its domain is especially valuable.

Acceptance Interval Comparison

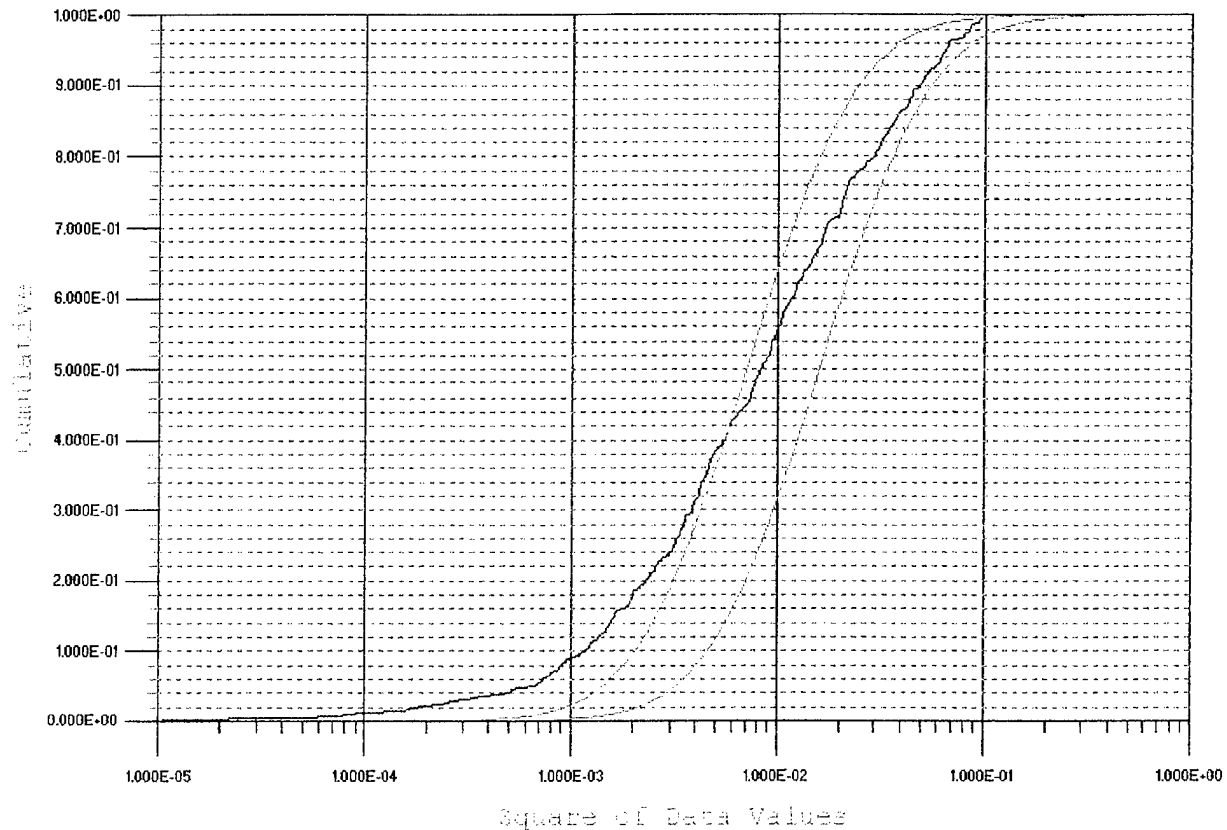


Figure 6.22. The Figure 6.13 data lies within a $\pm 50\%$ acceptance interval for fitting a chi square (two degrees of freedom) distribution, over the upper half of its domain. This means the log normal model is conditionally acceptable, although the close brushes with both sides of the acceptance interval near the top of its domain make it the least desirable of the four choices.

Acceptance-Limit Comparison of CDF Data

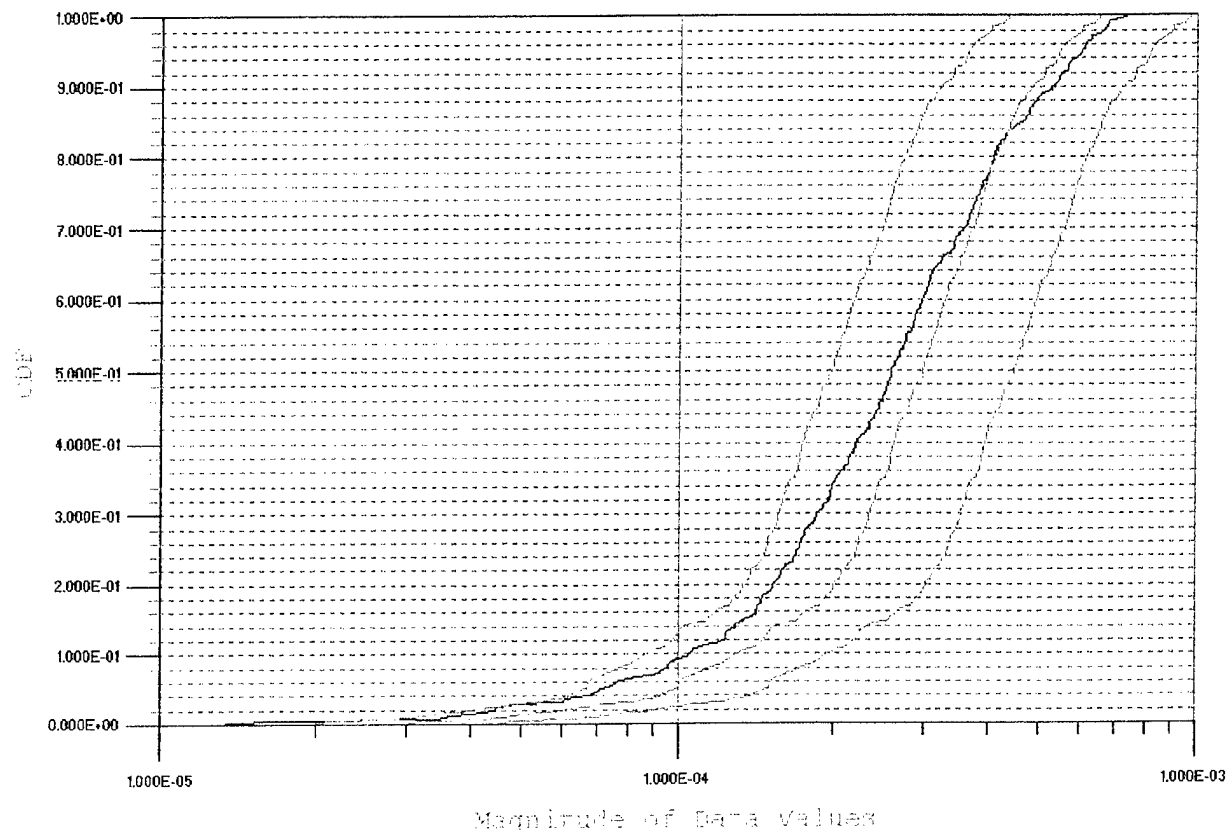


Figure 6.23. The Figure 6.13 field data, when modeled as chi square (with two degrees of freedom), leads to a modeled cable current which, given a $\pm 50\%$ acceptance interval, everywhere brackets the measured cable current. The field model is based on $\mu_c = 0.0170$.

Acceptance-Limit Comparison of CDF Data

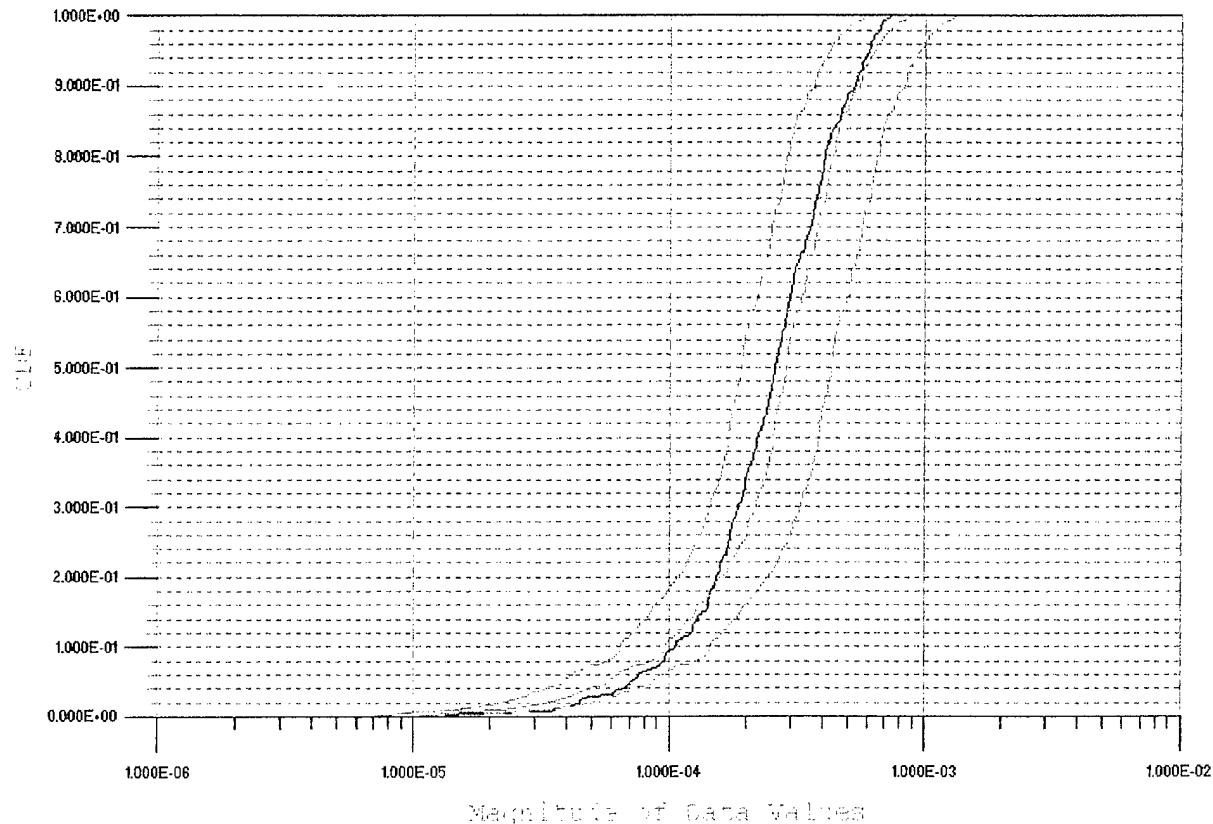


Figure 6.24. The Figure 6.13 field data, when represented as a Lehman distribution, leads to a modeled cable current which, given a $\pm 50\%$ acceptance interval, everywhere brackets the measured cable current. Moreover, this model hugs the measured current at the upper part of the domain better than the chi-square-based model in Figure 6.23. This field model is based on $\Lambda = 176.4$.

Acceptance-Limit Comparison of CDF Data

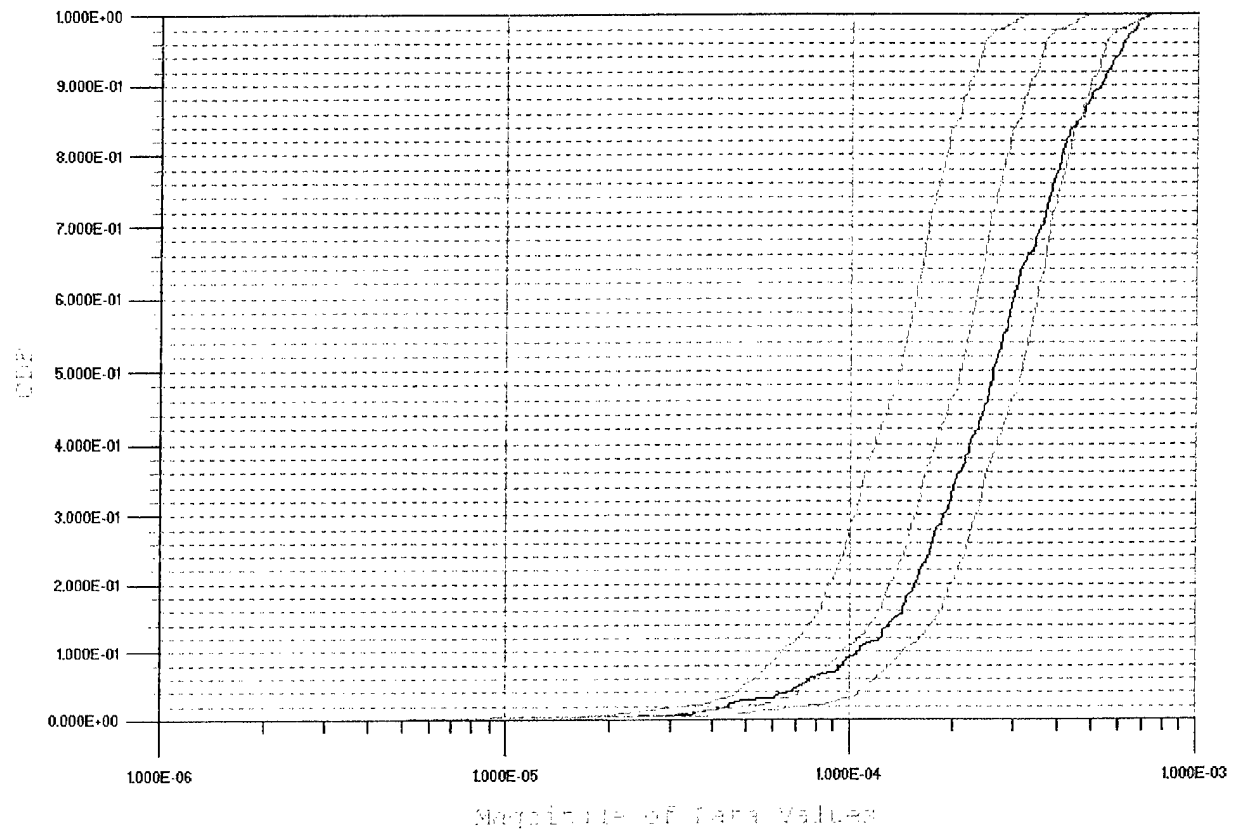


Figure 6.25. The Figure 6.13 field data, when represented as log normal, leads to a modeled cable current which, given a $\pm 50\%$ acceptance interval, fails to bracket the measured cable current. What is worse, the failure occurs at the upper part of the model domain. This figure is based on $(\mu_{lg}, \sigma_{lg}) = (-4.546, 0.972)$.

REFERENCES

- [1]. Price, R. H., *et al*, "Determination of the Statistical Distribution of Electromagnetic Field Amplitudes in Complex Cavities," 88JAL129, JAYCOR, 1 June 1988.
- [2]. Price, R. H., H. T. Davis, and E. P. Wenaas, "Determination of the Statistical Distribution of Electromagnetic-Field Amplitudes in Complex Cavities," *Phys. Rev. E*, Vol. 48, pp. 4716-4729, December 1993.
- [3]. Korn, G.A. and T.M. Korn, *Mathematical Handbook for Scientists and Engineers*, Second Edition, p. 692, McGraw-Hill Book Company, New York, New York, 1968.

Chapter 7. CAVITY EIGENMODES: THEIR EVALUATION, PROPERTIES, AND PERTURBATION BY DISSIPATION AND BY APERTURES

Statistical electromagnetics (SEM) in an enclosure is largely based on consideration of simultaneous excitation of a large number of enclosure eigenmodes. To this end, we shall begin with a review of eigenmode definitions and techniques for lossy, leaky cavities. In this section, we shall deal with cavities containing inhomogeneous fill which may be lossy, but not so lossy that Q is less than 6 or so. Apertures may also be present, further reducing the Q . It is our intent to begin with lossless, completely closed cavities, and then to introduce dissipation and apertures as perturbations. We shall, however, specifically include the case where the only cavity drive is through apertures.

Our discussion of the lossless case is fairly readily generalized to include anisotropy, provided ϵ and μ remain hermitian (lossless). Nevertheless, we shall not explicitly discuss anisotropy. At present, we have not considered anisotropic dissipation. What we discuss can, almost certainly be so-generalized, but this effort, which is based on a need to understand EM satellite damage or compromise, came with no cause to consider anisotropic dissipation.

EIGENMODE DEFINITION AND EXPANSION

Maxwell's equations in the presence of both electric and magnetic currents are

$$\nabla \times \mathbf{E} = -j\omega\mu\mathbf{H} - \mathbf{J}_m \quad (7-1)$$

$$\nabla \times \mathbf{H} = j\omega\epsilon\mathbf{E} + \mathbf{J} \quad (7-2)$$

where sinusoidal steady state is assumed. These equations can be manipulated to yield the vector wave equations for the fields

$$\nabla \times (\epsilon^{-1}\nabla \times \mathbf{H}) - \omega^2\mu\mathbf{H} = -j\omega\mathbf{J}_m + \nabla \times (\epsilon^{-1}\mathbf{J}) \quad (7-3)$$

$$\nabla \times (\mu^{-1}\nabla \times \mathbf{E}) - \omega^2\epsilon\mathbf{E} = -j\omega\mathbf{J} - \nabla \times (\mu^{-1}\mathbf{J}_m) \quad (7-4)$$

The ϵ and μ in (7-1) - (7-4), as in most of the formulas in this paper, can be viewed as tensors (matrices) if one wishes to interpret this formulation as anisotropic.

The eigenmodes of a cavity can be expressed either in terms of the \mathbf{E} -fields or the \mathbf{H} -fields. They can be defined with loss present (in which case the eigen frequencies come out complex) or with loss absent. As mentioned above, our experience is that less confusion results if the eigenmodes are initially defined without loss, and loss is subsequently implemented as a perturbation.

Let us express the real and imaginary parts of ϵ and μ as

$$\epsilon = \epsilon' - j\epsilon'' \quad (7-5)$$

$$\mu = \mu' - j\mu'' \quad (7-6)$$

where any conductive loss, σ or σ_m , is incorporated into ϵ'' or μ'' . Then the E -field eigenmodes obey the homogeneous, lossless version of (7-4):

$$\nabla \times (\mu'^{-1} \nabla \times \mathbf{E}_n) - \omega_n^2 \epsilon' \mathbf{E}_n = 0 \quad (7-7)$$

A bit of vector analysis manipulation (dot \mathbf{E}_p into (7-7) for \mathbf{E}_n , dot \mathbf{E}_n into (7-7) for \mathbf{E}_p , and subtract the second result from the first), shows that two eigenmodes with different eigen frequencies must be orthogonal with respect to ϵ' . In this article, we shall assume no modes are degenerate. The normalization convention we shall use is

$$\iiint \mathbf{E}_p \cdot \epsilon' \mathbf{E}_n dV = \delta_{pn} \quad (7-8)$$

The boundary condition at the cavity walls is invoked in deriving (7-8)

$$\mathbf{n} \times \mathbf{E}_n = 0 \quad (7-9)$$

where \mathbf{n} points outward (into the cavity wall from the interior). More vector manipulation can show that $\nabla \times \mathbf{E}_p$ and $\nabla \times \mathbf{E}_n$ are also orthogonal with respect to μ'^{-1}

$$\frac{1}{\omega_p^2} \iiint \nabla \times \mathbf{E}_p \cdot \mu'^{-1} \nabla \times \mathbf{E}_n dV = \delta_{pn} \quad (7-10)$$

If a cavity is driven by \mathbf{J} and \mathbf{J}_m , \mathbf{E} can be expanded in terms of the eigenmodes:

$$\mathbf{E} = \sum_n B_n \mathbf{E}_n \quad (7-11)$$

Substitution of (7-11) into (7-4) yields

$$B_n = \frac{1}{\omega_n^2 - \omega^2} \left[-j\omega \iiint \mathbf{E}_n \cdot \mathbf{J} dV - \iiint \nabla \times \mathbf{E}_n \cdot \mu'^{-1} \mathbf{J}_m dV \right] \quad (7-12)$$

where (7-9) is again used.

The \mathbf{H} -field eigenmodes obey the homogeneous, lossless version of (7-3), which is dual to (7-7).

$$\nabla \times (\epsilon'^{-1} \nabla \times \mathbf{H}_n) - \omega_n^2 \mu' \mathbf{H}_n = 0 \quad (7-13)$$

As we have eliminated all imaginary terms from (7-7) and (7-13), all unperturbed eigenfunctions, \mathbf{E}_n and \mathbf{H}_n , will be pure real. The \mathbf{H}_n modes are orthogonal with respect to μ' , and are normalized as follows

$$\iiint \mathbf{H}_p \cdot \mu' \mathbf{H}_n dV = \delta_{pn} \quad (7-14)$$

The boundary condition on \mathbf{H} at the cavity walls is a necessary part of the derivation of (7-14)

$$\mathbf{n} \times \nabla \times \mathbf{H}_n = 0 \quad (7-15)$$

We can also demonstrate that $\nabla \times \mathbf{H}_p$ and $\nabla \times \mathbf{H}_n$ are orthogonal with respect to ϵ'^{-1}

$$\frac{1}{\omega_p^2} \iiint \nabla \times \mathbf{H}_p \cdot \epsilon'^{-1} \nabla \times \mathbf{H}_n dV = \delta_{pn} \quad (7-16)$$

The driven \mathbf{H} field inside a cavity can be expressed in terms of the \mathbf{H} -field eigenmodes:

$$\mathbf{H} = \sum_n A_n \mathbf{H}_n \quad (7-17)$$

Substitution of (7-17) into (7-3) yields

$$A_n = \frac{1}{\omega_n^2 - \omega^2} \left[-j\omega \iiint \mathbf{H}_n \cdot \mathbf{J}_m dV + \omega_n \iiint \mathbf{E}_n \cdot \mathbf{J} dV \right] \quad (7-18)$$

where a boundary condition similar to (7-15) is again required.

There are apparently several ways to relate \mathbf{E}_n and \mathbf{H}_n (which do have the same eigen frequency and are merely different representations of the same mode). One verified convention is

$$\epsilon'^{-1} \nabla \times \mathbf{H}_n = \omega_n \mathbf{E}_n \quad (7-19)$$

$$\mu'^{-1} \nabla \times \mathbf{E}_n = \omega_n \mathbf{H}_n \quad (7-20)$$

There are also options with judiciously placed factors of j and -1 . In this article, we shall work with (7-19) and (7-20). In view of (7-20), it is possible to rewrite (7-12) for B_n as

$$B_n = \frac{1}{\omega_n^2 - \omega^2} \left[-j\omega \iiint E_n \cdot J dV - \omega_n \iiint H_n \cdot J_m dV \right] \quad (7-21)$$

ENERGY AND POWER DISSIPATION PARTITIONING BETWEEN MODES

The total magnetic time-average energy in the cavity is

$$E_m = \iiint \frac{1}{4} \mathbf{H} \cdot \mu' \mathbf{H}^* dV = \frac{1}{4} \sum_p |A_p|^2 \quad (7-22)$$

where (7-14) for normalizing the \mathbf{H}_p is applied. The total electric time-average energy in the cavity is

$$E_e = \iiint \frac{1}{4} \mathbf{E} \cdot \epsilon' \mathbf{E}^* dV = \frac{1}{4} \sum_p (\omega_p^2 / \omega) |A_p|^2 \quad (7-23)$$

where (7-8), (7-16), and (7-19) are utilized. Dual formulas for partitioning the energy in terms of the B_n electric-eigenmode amplitudes flow easily from (7-22) and (7-23). Note that at $\omega = \omega_p$ mode p contains equal electric and magnetic average energy.

Partitioning of the power dissipation between modes is not so clear. The power flux or Poynting vector in the frequency domain is

$$\mathbf{S} = \frac{1}{2} \operatorname{Re}(\mathbf{E} \times \mathbf{H}^*) \quad (7-24)$$

The net power loss by the cavity is the negative divergence of \mathbf{S} integrated over the cavity. At steady state, this must be zero:

$$P_{loss} = - \frac{1}{2} \operatorname{Re} \iiint \nabla \cdot (\mathbf{E} \times \mathbf{H}^*) dV = 0 \quad (7-25)$$

A fair amount of vector analysis and use of Maxwell's equations permits re-expression of (7-25) as

$$\begin{aligned} & \frac{1}{2} \operatorname{Re} \iiint \left(\mathbf{H}^* \cdot \mathbf{J}_m - \frac{1}{j\omega} \epsilon^{-1} \nabla \times \mathbf{H}^* \right) dV \\ & + \frac{1}{2} \operatorname{Re} \iiint \left(j\omega \mathbf{H} \cdot \mu \mathbf{H}^* + \frac{1}{j\omega} \nabla \times \mathbf{H} \cdot \epsilon^{-1} \nabla \times \mathbf{H}^* \right) dV = P_{in} + P_{diss} = 0 \end{aligned} \quad (7-26)$$

where, since we are now considering dissipation, Maxwell's equations are now used in their source-present, lossy form, (7-1) and (7-2). It is easy to identify the first part of (7-26) as power in and the second part as power dissipated.

The power-dissipated term can be manipulated to yield, from the expansion of (7-17),

$$\begin{aligned} P_{diss} &= \frac{1}{2} \iiint \left(\omega \mu'' |\mathbf{H}|^2 + \frac{\epsilon''}{\omega |\epsilon|^2} |\nabla \times \mathbf{H}|^2 \right) dV \\ &= \frac{1}{2} \iiint \left(\omega \mu'' \sum_n A_n \mathbf{H}_n \cdot \sum_p A_p^* \mathbf{H}_p + \frac{\epsilon''}{\omega |\epsilon|^2} \sum_n A_n \nabla \times \mathbf{H}_n \cdot \sum_p A_p^* \nabla \times \mathbf{H}_p \right) dV \end{aligned} \quad (7-27)$$

(Complex conjugate operators are not expressed on the unperturbed eigenfunctions as they are pure real.) We now have a problem: the power dissipation does not readily partition between eigenmodes, as the eigenmodes are orthogonal with respect to μ' and ϵ'^{-1} , not μ'' and $\epsilon''/|\epsilon|^2$. This is manifested in (7-27) by the presence of modal cross-terms.

There is, however, a presumption we can make which is probably valid in most cases. Especially for a rather accidentally penetrated satellite, the different modal coefficients are uncorrelated. In this case, the expectancy of each of the coefficients will be zero (unless they are squared), and the expectancy of P_{diss} will drop the cross-terms:

$$E[P_{diss}] = \frac{1}{2} \sum_n E[|A_n|^2] \iiint \left(\omega \mu'' H_n^2 + \frac{\omega_n^2}{\omega} \epsilon'' E_n^2 \right) dV \quad (7-28)$$

where we have again used (7-10). In the future, we shall replace the expectancy of $|A_n|^2$ and P_{diss} just with $|A_n|^2$ and P_{diss} .

The part of (7-26) associated with input power, or drive, can be manipulated to the form

$$P_{dr} = P_{in} = \frac{1}{2} \operatorname{Re} \iiint (\mathbf{H}^* \cdot \mathbf{J}_m + \mathbf{E}^* \cdot \mathbf{J}) dV \quad (7-29)$$

The $\mathbf{E}^* \cdot \mathbf{J}$ term in (7-29) is the complex conjugate of what we usually see at this point, and may indicate an algebraic error. We are disinclined to check this out, however, as taking the real part of (7-29) makes the issue moot, and we can think of no way to test a discarded, nonphysical part of a formula for a mistake.

CONSIDERATION OF Q

The Q associated with magnetic aspects of the cavity is defined at mode n as

$$Q_{mn} = \frac{\omega_{nR} E_{mn}}{P_{mn}} \quad (7-30)$$

where ω_{nR} is the real part of ω_n , E_{mn} is the magnetic energy stored in mode n , and P_{mn} is the magnetic energy dissipated by mode n . (Since we are now dealing with loss, ω_n unsubscripted by R , is no longer unambiguous.) If μ'' is just μ' times a scale factor, (7-27) and (7-28) indicate

$$Q_{mn} = \frac{\omega_{nR} \cdot \frac{1}{4} |A_n|^2}{\omega \cdot \frac{1}{2} \iiint \mu'' H_n^2 dV} = \frac{\mu'}{2\mu''} \quad (7-31)$$

is just $\frac{1}{2}$ the reciprocal of that scale factor. This result is known to be correct.

An exactly dual argument establishes the same fact about the electrical Q of the cavity

$$Q_{en} = \frac{\epsilon'}{2\epsilon''} \quad (7-32)$$

It is also true that the overall Q_n (not including apertures) is related to Q_{mn} and Q_{en} by

$$\frac{1}{Q_n} = \frac{1}{2Q_{mn}} + \frac{1}{2Q_{en}} = \frac{\mu''}{\mu'} + \frac{\epsilon''}{\epsilon'} \quad (7-33)$$

and that Q_n is related to ω_{nR} and ω_{nI} by

$$Q_n = \frac{\omega_{nR}}{2\omega_{nI}} \quad (7-34)$$

START-UP TRANSIENTS

When a cw source is initiated, start-up transients in the cavity will have to ring out. The evaluation of these transients and their behavior is simple, but quite tedious.

Impulse Response

The frequency-domain cw behavior of the cavity is

$$\mathbf{H}(\mathbf{r}, \omega) = \sum_n \frac{\mathbf{H}_n(r)}{\omega_n^2 - \omega^2} (-j\omega F_n + G_n) \quad (7-35)$$

where F_n and G_n are easily picked off by association with (7-18):

$$F_n = \iiint \mathbf{H}_n \cdot \mathbf{J}_m dV \quad (7-36)$$

$$G_n = \omega_n \iiint E_n \cdot J dV \quad (7-37)$$

The associated time-domain impulse response is

$$\begin{aligned} h(r, \tau) &= \frac{1}{2\pi} \int_{-\infty}^{\infty} H(r, \omega) e^{j\omega\tau} d\omega = \frac{1}{2\pi} \int_{-\infty}^{\infty} \sum_n \frac{(j\omega F_n - G_n) H_n(r) e^{j\omega\tau} d\omega}{(\omega - \omega_{nR} - j\omega_{nI})(\omega + \omega_{nR} - j\omega_{nI})} \\ &= \sum_n \left[F_n \left(-\cos \omega_{nR}\tau + \frac{1}{2Q_n} \sin \omega_{nR}\tau \right) + \frac{G_n}{\omega_{nR}} \sin \omega_{nR}\tau \right] H_n(r) e^{-\omega_{nI}\tau} \end{aligned} \quad (7-38)$$

CW Start-Up Transient

If, instead of being a delta function or impulse, the drive is a cw signal turned on at $\tau = 0$

$$f(\tau) = e^{j\omega'\tau} u_{-1}(\tau) \quad (7-39)$$

we find that $f(\tau)$ has a frequency domain representation

$$F(\omega) = \frac{-j}{\omega - \omega'} \quad (7-40)$$

The overall response in the frequency domain is then

$$\begin{aligned} R(r, \omega) &= \frac{-j}{(\omega - \omega')} \sum_n \frac{H_n(r)}{\omega^2 - \omega_n^2} (j\omega F_n - G_n) \\ &= \sum_n \frac{H_n(r)(\omega F_n + jG_n)}{(\omega - \omega')(\omega - \omega_{nR} - j\omega_{nI})(\omega + \omega_{nR} - j\omega_{nI})} \end{aligned} \quad (7-41)$$

The associated time-domain response is

$$r(r, \tau) = \sum_n \int_{-\infty}^{\infty} \frac{(\omega F_n + jG_n) e^{j\omega\tau} d\omega}{2\pi(\omega - \omega')(\omega - \omega_{nR} - j\omega_{nI})(\omega + \omega_{nR} - j\omega_{nI})} \quad (7-42)$$

This expression can be factored as

$$\mathbf{r}(\mathbf{r}, \tau) = \sum_n \int_{-\infty}^{\infty} \left(\frac{\mathbf{a}_n}{\omega - \omega'} + \frac{\mathbf{b}_n}{\omega - \omega_{nR} - j\omega_{nI}} + \frac{\mathbf{c}_n}{\omega + \omega_{nR} - j\omega_{nI}} \right) d\omega \quad (7-43)$$

where

$$\mathbf{a}_n = \frac{(\omega' F_n + jG_n) \mathbf{H}_n(\mathbf{r}) e^{j\omega' \tau}}{2\pi(\omega' - \omega_{nR} - j\omega_{nI})(\omega' + \omega_{nR} - j\omega_{nI})} \quad (7-44)$$

$$\mathbf{b}_n = \frac{[(\omega_{nR} + j\omega_{nI})F_n + jG_n] \mathbf{H}_n(\mathbf{r}) e^{j(\omega_{nR} + j\omega_{nI})\tau}}{2\pi(-\omega_{nR} + j\omega_{nI} - \omega')(2\omega_{nR})} \quad (7-45)$$

$$\mathbf{c}_n = \frac{[(\omega_{nR} - j\omega_{nI})F_n - jG_n] \mathbf{H}_n(\mathbf{r}) e^{j(-\omega_{nR} + j\omega_{nI})\tau}}{2\pi(-\omega_{nR} + j\omega_{nI} - \omega')(2\omega_{nR})} \quad (7-46)$$

Following a formidable amount of symbol manipulation, $\mathbf{r}(\mathbf{r}, \tau)$ is evaluated as a sum of 8 terms, including all combinations of (start-up transients vs cw response), (electric drive response vs magnetic drive response) and (sine drive vs cosine drive, as $f(\tau) = e^{j\omega' \tau} u_{-1}(\tau)$ has a real cosine part and an imaginary sine part). The transient part of the response is

$$\begin{aligned}
\mathbf{r}_{trans}(\mathbf{r}, \tau) = & \sum_n \frac{f_n \mathbf{H}_n(\mathbf{r}) e^{-\omega_{nl}\tau}}{[(\omega_{nR} - \omega')^2 + \omega_{nl}^2]} & \text{electric drive} \\
& \cdot \left[\left(-\frac{(\omega_{nR} - \omega')}{2} \sin \omega_{nR} \tau + \frac{\omega'}{4Q_n} \cos \omega_{nR} \tau \right) \right. & \text{cosine drive} \\
& \left. + j \left(\frac{\omega'(\omega_{nR} - \omega')}{2\omega_{nR}} \cos \omega_{nR} \tau + \frac{\omega_{nR}}{4Q_n} \sin \omega_{nR} \tau \right) \right] & \text{sine drive} \\
& + \sum_n \frac{G_n \mathbf{H}_n(\mathbf{r}) e^{-\omega_{nl}\tau}}{[(\omega_{nR} - \omega')^2 + \omega_{nl}^2]} & \text{magnetic drive} \quad (7-47) \\
& \cdot \left[\left(-\frac{(\omega_{nR} - \omega')}{2\omega_{nR}} \cos \omega_{nR} \tau - \frac{1}{4Q_n} \frac{\omega'}{\omega_{nR}} \sin \omega_{nR} \tau \right) \right. & \text{cosine drive} \\
& \left. + j \left(-\frac{(\omega'/\omega_{nR})(\omega_{nR} - \omega')}{2\omega_{nR}} \sin \omega_{nR} \tau + \frac{1}{4Q_n} \cos \omega_{nR} \tau \right) \right] & \text{sine drive}
\end{aligned}$$

The cw part of the response is

$$\begin{aligned}
\mathbf{r}_{cw}(\mathbf{r}, \tau) = & \sum_n \frac{F_n \mathbf{H}_n(\mathbf{r})}{[(\omega_{nR} - \omega')^2 + \omega_{nl}^2]} & \text{electric drive} \\
& \cdot \left[\left(\frac{(\omega_{nR} - \omega')(\omega'/\omega_{nR})}{2} \sin \omega' \tau - \frac{\omega'}{4Q_n} \cos \omega' \tau \right) \right. & \text{cosine drive} \\
& \left. + j \left(-\frac{\omega'(\omega_{nR} - \omega')}{2\omega_{nR}} \cos \omega' \tau - \frac{\omega'}{4Q_n} \sin \omega' \tau \right) \right] & \text{sine drive} \\
& + \sum_n \frac{G_n \mathbf{H}_n(\mathbf{r})}{[(\omega_{nR} - \omega')^2 + \omega_{nl}^2]} & \text{magnetic drive} \quad (7-48) \\
& \cdot \left[\left(\frac{(\omega_{nR} - \omega')}{2\omega_{nR}} \cos \omega' \tau + \frac{1}{4Q_n} \sin \omega' \tau \right) \right. & \text{cosine drive} \\
& \left. + j \left(\frac{(\omega_{nR} - \omega')}{2} \sin \omega' \tau - \frac{1}{4Q_n} \cos \omega' \tau \right) \right] & \text{sine drive}
\end{aligned}$$

Note that

$$\mathbf{r}(\mathbf{r}, \tau) = \mathbf{r}_{trans}(\mathbf{r}, \tau) + \mathbf{r}_{cw}(\mathbf{r}, \tau) \quad (7-49)$$

starts off everywhere zero at $\tau = 0$.

Very-Low Frequency Response

We shall next consider some limiting cases of the cw start-up transient response. If we assume ω' is very small, we drop all terms that are linear in ω' or contain $\sin \omega' \tau$. In this case, the cosine-drive part of (7-48) and (7-49) becomes

$$\begin{aligned} \mathbf{r}_{cos}(\mathbf{r}, \tau) = & \sum_n \left[\frac{F_n \mathbf{H}_n(\mathbf{r}) e^{-\omega_n \tau}}{\omega_{nR}} \left(-\frac{1}{2} \sin \omega_{nR} \tau \right) \right. \\ & \left. + \frac{G_n \mathbf{H}_n(\mathbf{r})}{\omega_{nR}^2} \left(\frac{1}{2} \cos \omega' \tau - \frac{e^{-\omega_n \tau}}{2} \cos \omega_{nR} \tau \right) \right] \end{aligned} \quad (7-50)$$

This quantity also may be seen to vanish at $\tau = 0$.

The sine-drive part of (7-48) and (7-49) is

$$\begin{aligned} \mathbf{r}_{sin}(\mathbf{r}, \tau) = & \sum_n \left[\frac{F_n \mathbf{H}_n(\mathbf{r}) e^{-\omega_n \tau}}{\omega_{nR}} \left(\frac{1}{4Q_n} \sin \omega_{nR} \tau \right) \right. \\ & \left. + \frac{G_n \mathbf{H}_n(\mathbf{r})}{\omega_{nR}^2} \left(\frac{1}{4Q_n} e^{-\omega_n \tau} - \frac{1}{4Q_n} \cos \omega' \tau \right) \right] \end{aligned} \quad (7-51)$$

This response is also zero initially, and never departs from zero in the lossless ($Q_n = \infty$) case.

Drive At Resonance

If the cavity is driven at one of its resonant frequencies ($\omega' = \omega_{nR}$), the response of mode n is, including start-up transients,

$$\begin{aligned}
\mathbf{r}_n(\mathbf{r}, \tau) = & \\
& \left[-F_n \mathbf{H}_n(\mathbf{r}) \cos \omega_{nR} \tau + G_n \mathbf{H}_n(\mathbf{r}) \frac{\sin \omega_{nR} \tau}{\omega_{nR}} \right] \quad \text{cosine drive} \\
& \left[-F_n \mathbf{H}_n(\mathbf{r}) \sin \omega_{nR} \tau + G_n \mathbf{H}_n(\mathbf{r}) \frac{\cos \omega_{nR} \tau}{\omega_{nR}} \right] \quad \text{sine drive} \quad (7-52) \\
& \cdot \frac{Q_n}{\omega_{nR}} (1 - e^{-\omega_{nR} \tau})
\end{aligned}$$

It is most interesting to note that the time-average energy in cavity mode n builds up as $(1 - e^{-\omega_{nR} \tau})^2$:

$$\iiint \frac{1}{2} \mu' \mathbf{H}(\mathbf{r}) \cdot \mathbf{H}(\mathbf{r})^* dV = \frac{1}{4} \sum_n \frac{Q_n^2}{\omega_{nR}^2} |F_n + G_n/\omega_{nR}|^2 (1 - 2e^{-\omega_{nR} \tau} + e^{-2\omega_{nR} \tau}) \quad (7-53)$$

This expression not only starts off at zero, but with a zero derivative. In other words, energy cannot be pumped into an eigenmode until there is already energy present, providing fields for the drive to push against and perform work.

APERTURE DRIVE

Drive by aperture leakage turns out to be more complex than one might expect. What we would have liked to do is apply the equivalence principle: foil over the apertures, see what surface current density \mathbf{K} flows over the foil exteriors, remove the foils, and drive the cavity behind the apertures by forcing the foil surface currents across the open apertures [1-4]. The problem with this approach is readily apparent from (7-9) and (7-18) or (7-21): the unperturbed electric eigenmodes have no tangential component at the cavity surface (which includes the foil for evaluation of the unperturbed modes). Thus, $\mathbf{E}_n \cdot \mathbf{K}$ will everywhere be zero, and this model will never give a cavity response.

(Were we to deal with the perturbed eigenmodes \mathbf{E}'_n , evaluated with the apertures open, $\mathbf{E}'_n \cdot \mathbf{K}$ would not vanish everywhere, and the desired approach would work. However, the perturbed eigenmodes are generally hard to evaluate, and do not even have real eigenvalues, as they must allow energy to escape the cavity. Also, it is not obvious that the radiating parts of the perturbed eigenmodes do not destroy their orthogonality; at the very least, the radiating fields greatly complicate the eigenmode normalization procedure.)

An alternative approach, which will work but is more difficult involves use of Babinet's principle [5]. Replace the aperture by a conducting patch, remove everything else, illuminate the patch, and see what surface current \mathbf{K} flows on its illuminated surface (using FDTD if necessary). Then close the aperture, and place an internal magnetic surface current \mathbf{K}_m equal to \mathbf{K} over the patch where the aperture had been. As (7-18) and (7-21), together with the boundary condition (7-15), on the \mathbf{H}_a , show, this magnetic surface current will couple to and drive the magnetic representation of the eigenmodes. Specifically (7-18) for instance, now is replaced by

$$A_n = \frac{1}{\omega_n^2 - \omega^2} \left[-j\omega \iiint H_n \cdot J_m dV - j\omega \iint_{\text{aperture}} \mathbf{H}_n \cdot \mathbf{K}_m dS + \omega_n \iiint E_n \cdot J dV \right] \quad (7-54)$$

Equation (7-21) for B_n is identically modified.

It may occur that one is able to determine the electric field across the aperture \mathbf{E}_a in the presence of the satellite. If this is the case, one can approximate the magnetic surface current \mathbf{K}_m to apply across the aperture without explicitly appealing to Babinet's principle:

$$\mathbf{K}_m = \mathbf{n} \times \mathbf{E}_a \quad (7-55)$$

(In some formulations, \mathbf{K}_m is divided by 2, as half of \mathbf{K}_m radiates into the cavity and half radiates back to the outside world [6].)

In either case, one fact remains true: a magnetic surface current inside the cavity looks like a zero-impedance source, and thus matches the unperturbed eigenmode boundary conditions. The equivalence principle, with its electric current across an open aperture, does not do this. Thus, the approach of using magnetic instead of electric equivalent current is much more compatible with our philosophy of avoiding aperture-perturbed eigenmodes.

The use of equivalent magnetic currents to describe aperture penetration is a generalization of Bethe hole theory [7], which itself is applicable only to apertures small compared to a wavelength. Magnetic currents have long been used to describe leakage through long slots or cracks [8, 9].

LAGRANGIAN REPRESENTATION AND TECHNIQUES

The use of a Lagrangian is a handy technique for manipulating Maxwell's equations, especially when energy densities are involved and one has not yet reached the stage of introducing loss. If one wishes to work with \mathbf{E} -fields, there are three common variants of the Lagrangian. If one is trying to find eigenmodes (no drive present), and one is using trial functions which satisfy the \mathbf{E} -field boundary condition (7-9), the appropriate Lagrangian is [10]

$$L_1 = \iiint \nabla \times \mathbf{E} \cdot \mu^{-1} \nabla \times \mathbf{E} dV - \omega^2 \iiint \mathbf{E} \cdot \epsilon \mathbf{E} dV \quad (7-56)$$

If there is no drive, but the trial functions do not satisfy (7-9), the appropriate Lagrangian is

$$L_1 = \iiint \nabla \times \mathbf{E} \cdot \mu^{-1} \nabla \times \mathbf{E} dV - 2 \oint \oint \mathbf{n} \cdot (\mathbf{E} \times (\mu^{-1} \nabla \times \mathbf{E})) dS - \omega^2 \iiint \mathbf{E} \cdot \epsilon \mathbf{E} dV \quad (7-57)$$

If electric and magnetic current drives are present and the trial functions do not satisfy (7-9), the appropriate Lagrangian is

$$\begin{aligned} L_1 = & \iiint \nabla \times \mathbf{E} \cdot \mu^{-1} \nabla \times \mathbf{E} dV - 2 \oint \oint \mathbf{n} \cdot (\mathbf{E} \times (\mu^{-1} \nabla \times \mathbf{E})) dS \\ & - \omega^2 \iiint \mathbf{E} \cdot \epsilon \mathbf{E} dV + 2 \iiint \mathbf{E} \cdot \nabla \times (\mu^{-1} \mathbf{J}_m) dV + 2 \iiint \mathbf{E} \cdot \mathbf{J} dV \end{aligned} \quad (7-58)$$

A bit of vector calculus shows that this last expression is stationary only when (7-4) and (7-9) hold.

Similar (but not identical) Lagrangians apply if one is working with the \mathbf{H} -field based Lagrangian. Specifically, if one is looking for \mathbf{H} -field eigenmodes (no drive present), the appropriate Lagrangian is [10]

$$L_2 = \iiint \nabla \times \mathbf{H} \cdot \epsilon^{-1} \nabla \times \mathbf{H} dV - \omega^2 \iiint \mathbf{H} \cdot \mu \mathbf{H} dV \quad (7-59)$$

whether or not the trial functions obey (7-15), the \mathbf{H} -field boundary condition.

If electric and magnetic drives are present, the appropriate \mathbf{H} -field Lagrangian is

$$\begin{aligned} L_2 = & \iiint \nabla \times \mathbf{H} \cdot \epsilon^{-1} \nabla \times \mathbf{H} dV - \iiint \omega^2 \mathbf{H} \cdot \mu \mathbf{H} dV \\ & - 2 \iiint \mathbf{H} \cdot \nabla \times (\epsilon^{-1} \mathbf{J}) dV + 2 \iiint \mathbf{H} \cdot \mathbf{J}_m dV \end{aligned} \quad (7-60)$$

The variation of L_2 in (7-60) is

$$\begin{aligned}
\delta L_2 = & 2 \iiint \nabla \cdot (\delta \mathbf{H} \times (\epsilon^{-1} \nabla \times \mathbf{H})) dV + 2 \iiint \delta \mathbf{H} \cdot \nabla \times (\epsilon^{-1} \nabla \times \mathbf{H}) dV \\
& - 2\omega^2 \iiint \delta \mathbf{H} \cdot \mu \mathbf{H} dV - 2 \iiint \delta \mathbf{H} \cdot \nabla \times (\epsilon^{-1} \mathbf{J}) dV + 2 \iiint \delta \mathbf{H} \cdot \mathbf{J}_m dV \\
= & - 2 \oint \oint \epsilon^{-1} \delta \mathbf{H} \cdot [\mathbf{n} \times \nabla \times \mathbf{H}] dS \\
& + 2 \iiint \delta \mathbf{H} \cdot [\nabla \times (\epsilon^{-1} \nabla \times \mathbf{H}) - \omega^2 \mu \mathbf{H} - \nabla (\epsilon^{-1} \mathbf{J}) + \mathbf{J}_m] dV
\end{aligned} \tag{7-61}$$

For an arbitrary $\delta \mathbf{H}$, this Lagrangian is stationary only if (7-15), the first bracketed term of (7-61), is everywhere obeyed at the cavity boundary, and if the wave equation (7-3), which is the second bracketed term of (7-61), is obeyed everywhere within the cavity. The Lagrangians of (7-56) - (7-59) are verified in the same way as we just validated (7-60).

EXPANSION OF RESPONSE OF APERTURE DRIVE

The electric-mode expansion (7-11) and (7-12), may be expressed as

$$\begin{aligned}
\mathbf{E} = \sum_n B_n \mathbf{E}_n &= \sum_n \frac{\mathbf{E}_n}{\omega_n^2 - \omega^2} [d_{m,n} + d_{e,n}] \\
&= \sum_n \frac{\mathbf{E}_n}{\omega^2 - \omega_n^2} \left[\iiint \nabla \times \mathbf{E}_n \cdot \mu'^{-1} \mathbf{J}_m dV + \iiint \mathbf{E}_n \cdot \mathbf{J} dV \right]
\end{aligned} \tag{7-62}$$

where this formula serves to define the magnetic and electric parts, $d_{m,n}$ and $d_{e,n}$, of the electric eigenmode drive.

Similarly, the magnetic mode expansion (7-17) and (7-18) are

$$\begin{aligned}
\mathbf{H} = \sum_n A_n \mathbf{H}_n &= \sum_n \frac{\mathbf{H}_n}{\omega_n^2 - \omega^2} [D_{e,n} - D_{m,n}] \\
&= \sum_n \frac{\mathbf{H}_n}{\omega^2 - \omega_n^2} \left[\iiint \mathbf{H}_n \cdot \mathbf{J}_m dV - \iiint \nabla \times \mathbf{H}_n \cdot \epsilon'^{-1} \mathbf{J} dV \right]
\end{aligned} \tag{7-63}$$

where this formula serves to define the magnetic and electric parts, $D_{m,n}$ and $D_{e,n}$ of the magnetic eigenmode drive.

If the cavity is driven entirely by apertures, the \mathbf{E} -field across the aperture becomes the drive. (This approach works with Bethe hole theory [7], Babinet's principle [5], and the Karzas (high-frequency) approximation [11], but not in conjunction with the equivalence principle [1-4].) In this case, we have

$$\begin{aligned}\mathbf{E} &= \sum_n \frac{\mathbf{E}_n}{\omega^2 - \omega_n^2} \iint_{\text{aperture}} \nabla \times \mathbf{E}_n \cdot \mu'^{-1} \mathbf{K}_m dS \\ &= \sum_n \frac{\mathbf{E}_n}{\omega^2 - \omega_n^2} \iint_{\text{aperture}} \nabla \times \mathbf{E}_n \cdot \mu'^{-1} (\mathbf{E}_o \times \mathbf{n}) dS\end{aligned}\quad (7-64)$$

where \mathbf{E}_o is the field in the aperture. Alternatively, we can use the magnetic-mode expansion

$$\mathbf{H} = \sum_n \frac{\mathbf{H}_n}{\omega^2 - \omega_n^2} \iint_{\text{aperture}} \mathbf{H}_n \cdot \mathbf{K}_m dS = \sum_n \frac{\mathbf{H}_n}{\omega^2 - \omega_n^2} \iint \mathbf{H}_d \cdot \mathbf{n} \times \mathbf{E}_o dS \quad (7-65)$$

Use of (7-19) and (7-20), relating \mathbf{E}_n and \mathbf{H}_n , will restore (7-63) and (7-64) to their previous form, (7-18) and (7-21).

GREEN'S FUNCTIONS

Equation (7-62) for \mathbf{E} can also be written

$$\mathbf{E}(\mathbf{r}) = \sum_n \frac{1}{\omega^2 - \omega_n^2} \iiint \left[\mathbf{E}_n(\mathbf{r}) \nabla \times \mathbf{E}_n(\mathbf{r}') \mu^{-1} \cdot \mathbf{J}_m(\mathbf{r}') + \mathbf{E}_n(\mathbf{r}) \mathbf{E}_n(\mathbf{r}') \cdot \mathbf{j} \right] dV \quad (7-66)$$

Consequently, the Green's function relating magnetic sources to electric fields is

$$\underline{\mathbf{G}}_1(\mathbf{r}, \mathbf{r}') = \sum_n \frac{1}{\omega^2 - \omega_n^2} \mathbf{E}_n(\mathbf{r}) \mu^{-1} \nabla \times \mathbf{E}_n(\mathbf{r}') = \sum_n \frac{\omega_n}{\omega^2 - \omega_n^2} \mathbf{E}_n(\mathbf{r}) \mathbf{H}_n(\mathbf{r}') \quad (7-67)$$

and the Green's function relating electric sources to electric fields is

$$\underline{G}_2(\mathbf{r}, \mathbf{r}') = \sum_n \frac{1}{\omega^2 - \omega_n^2} \mathbf{E}_n(\mathbf{r}) \mathbf{E}_n(\mathbf{r}') \quad (7-68)$$

Equation (7-68) is the familiar form of the Green's function for the wave equation where the result is a summation of the eigenmode products expressed at the source and the observer, and divided by a factor to describe the resonances [12, 13]. Equation (7-67) is a variation on this form necessitated by the other kind of drive (magnetic) which the cavity can see.

Similarly, (7-63) for \mathbf{H} can be expanded

$$\mathbf{H}(\mathbf{r}) = \sum_n \frac{1}{\omega^2 - \omega_n^2} \iiint [\mathbf{H}_n(\mathbf{r}) \mathbf{H}_n(\mathbf{r}') \cdot \mathbf{J}_m - \mathbf{H}_n(\mathbf{r}) \epsilon^{-1} \nabla \times \mathbf{H}_n(\mathbf{r}') \cdot \mathbf{J}] dV \quad (7-69)$$

Consequently, the Green's function relating electric sources to magnetic fields is

$$\underline{G}_3(\mathbf{r}, \mathbf{r}') = - \sum_n \frac{1}{\omega^2 - \omega_n^2} \mathbf{H}_n(\mathbf{r}) \epsilon^{-1} \nabla \times \mathbf{H}_n(\mathbf{r}') = - \sum_n \frac{\omega_n}{\omega^2 - \omega_n^2} \mathbf{H}_n(\mathbf{r}) \mathbf{E}_n(\mathbf{r}') \quad (7-70)$$

and the Green's function relating magnetic sources to magnetic fields is

$$\underline{G}_4(\mathbf{r}, \mathbf{r}') = \sum_n \frac{1}{\omega^2 - \omega_n^2} \mathbf{H}_n(\mathbf{r}) \mathbf{H}_n(\mathbf{r}') \quad (7-71)$$

Equations (7-70) and (7-71) consist of eigenmode products summed over the modes and modified by resonance factors just as (7-67) and (7-68) did.

EIGENMODE EXPANSION OF POWER INPUT THROUGH AN APERTURE

In general, the power flowing through an aperture into a cavity can be viewed as the equivalent aperture magnetic surface current \mathbf{K}_m pushing against the magnetic field existent in the cavity (see (7-65))

$$P_{in} = \frac{1}{2} \operatorname{Re} \iint_{\text{aperture}} \mathbf{H}^* \cdot \mathbf{K}_m dS \quad (7-72)$$

Use of (7-63) or (7-65) permits expansion of (7-72) as

$$P_{in} = \frac{1}{2} \operatorname{Re} \sum_n A_n^* \iint \mathbf{H}_n \cdot \mathbf{K}_m dS \quad (7-73)$$

where now, in the absence of internal sources, (7-18) for A_n becomes

$$A_n = \frac{1}{\omega^2 - \omega_n^2} \iint_{\text{aperture}} \mathbf{H}_n \cdot \mathbf{K}_m dS \quad (7-74)$$

Consequently, the overall power input becomes

$$\begin{aligned} P_{in} &= \frac{1}{2} \operatorname{Re} \left\{ \sum_n \left[\frac{-j\omega}{\omega^2 - \omega_n^2} \right] \left| \iint_{\text{aperture}} \mathbf{H}_n \cdot \mathbf{K}_m dS \right|^2 \right\} \\ &= \frac{1}{2} \sum_n |L_n|^2 \operatorname{Re} \left[\frac{-j\omega}{(\omega - j\omega_{nl})^2 - \omega_{nR}^2} \right] \end{aligned} \quad (7-75)$$

where (7-75) serves to define L_n as the eigenmode expansion component of \mathbf{K}_m over the aperture. The L_n are like the $D_{m,n}$ of (7-63), except a $j\omega$ term has been factored out, and the volume integral of (7-63) reduces to an aperture integral. Additional manipulations permit re-expression of the input power as

$$P_{in} = \frac{1}{2} \sum_n \frac{|L_n|^2 \omega_{nl}}{4(\omega - \omega_{nR})^2 - (\omega_{nR}/Q_n)^2} \quad (7-76)$$

where use is made of (7-34), terms in Q_n^{-2} are dropped, and it is assumed that ω and ω_{nR} are fairly similar for terms that make a significant contribution to the summation. Note that the modal partition of aperture power input is free of cross-modal terms, like (7-22) and (7-23) for the energy partition, but unlike (7-27) for dissipation partition.

EIGENMODE EXPANSION OF POWER LOSS THROUGH AN APERTURE

While power in and power loss via an aperture may seem like similar phenomena, actually there is a great amount of difference. Partly this occurs because power out never bounces back to behave reactively. Perhaps another way of saying the same thing is to state that power out eventually reaches a far-field characterization, which power in does not.

Unlike power input, power output is amenable to description using the equivalence principle [1, 2]: foil over the aperture, and let \mathbf{K} be the surface current flowing on the foil. Then remove the foil. The far-field magnetic vector potential produced by \mathbf{K} becomes, assuming the aperture lies in the xy plane,

$$A(x, y, z) = \frac{\mu_0 e^{-jkz}}{4\pi r} \iint_{\text{aperture}} \mathbf{K}(x', y') e^{-jk(x'x + y'y)/r} dx' dy' \quad (7-77)$$

If $G(\omega)$ is the Fourier transform of $g(\tau)$, one can demonstrate that energy is similarly expressed in either the time or the frequency domain:

$$\int_{-\infty}^{\infty} G(\omega) G^*(\omega) d\omega = 2\pi \int_{-\infty}^{\infty} g^2(\tau) d\tau \quad (7-78)$$

A similar 2D theorem applies to (7-77): The electric far field associated with $A(x, y, z)$ is

$$\mathbf{E}(x, y, z) = -j\omega \mathbf{A}_t(x, y, z) = -\frac{jkZ_o e^{-jkz}}{4\pi r} \iint_{\text{aperture}} \mathbf{K}(x', y') e^{-j\left(\frac{k}{r}(xx' + yy')\right)} dx' dy' \quad (7-79)$$

where \mathbf{A}_t is the magnetic vector potential less its radial component.

The total power reaching the far field and being lost through the aperture is

$$P_T = \frac{1}{2} \int_{-\infty}^{\infty} \int_{-\infty}^{\infty} \mathbf{i}_r \cdot \text{Re}[\mathbf{E}(x, y, z) \times \mathbf{H}^*(x, y, z)] dx dy = (y_o/2) \int_{-\infty}^{\infty} \int_{-\infty}^{\infty} |\mathbf{E}(x, y, z)|^2 dx dy \quad (7-80)$$

where all terms in (7-80) are evaluated in the far field. In view of (7-79), P_T can also be expressed as

$$\begin{aligned}
P_T = & \frac{\frac{1}{2}k^2 Z_o}{(4\pi r)^2} \iint_{\text{aperture}} \mathbf{K}(x', y') dx' dy' \cdot \iint_{\text{aperture}} \mathbf{K}^*(x'_1, y'_1) dx'_1 dy'_1 \\
& \cdot \int_{-\infty}^{\infty} \int_{-\infty}^{\infty} e^{j(\frac{k}{r})[x(x'_1 - x') + y(y'_1 - y')]} dx dy
\end{aligned} \tag{7-81}$$

The last double integral of (7-81) yields a double delta function,

$$I = (2\pi)^2 \delta\left[\frac{k}{r}(x'_1 - x')\right] \delta\left[\frac{k}{r}(y'_1 - y)\right] \tag{7-82}$$

Substitution of (7-82) in (7-81) and integration over (x'_1, y'_1) leaves

$$P_T = \frac{1}{2} Z_o \iint [\frac{1}{2} \mathbf{K}(x', y')] \cdot [\frac{1}{2} \mathbf{K}^*(x', y')] dx' dy' \tag{7-83}$$

where the factors of $\frac{1}{2}$ occur because the equivalence-principle surface current sends half its magnetic field discontinuity back into the cavity. Equations (7-80) - (7-83) are the two-dimensional generalization of the Fourier transform energy-conservation relationship (7-78) as applied to aperture radiation [14]. (Electron microscopes work on the principle that the diffracted far field is the Fourier transform of the field at the aperture or object under scrutiny.)

If the surface currents of (7-83) are referred back to the magnetic fields they represent in the cavity, P_T becomes

$$\begin{aligned}
P_T &= Z_o/2 \iint_{\text{aperture}} [-\frac{1}{2} \mathbf{n} \times \mathbf{H}(x', y')] \cdot [-\frac{1}{2} \mathbf{n} \times \mathbf{H}^*(x', y')] dx' dy' \\
&= Z_o/2 \iint_{\text{aperture}} \frac{1}{2} \sum_n A_n \mathbf{H}_n(x', y') \cdot \frac{1}{2} \sum_n A_p^* \mathbf{H}_p(x', y') dx' dy' \\
&\approx \frac{1}{2} \sum_n |A_n|^2 \iint_{\text{aperture}} \left(\frac{Z_o}{4}\right) |\mathbf{H}_n(x', y')|^2 dx' dy'
\end{aligned} \tag{7-84}$$

where the radiation aperture power loss has the same pesky cross-modal terms as the internal dissipation formula (7-27). These terms are again dropped in (7-84) by appeal to the same expectancy argument used in deducing (7-28) from (7-27).

In conclusion, we point out that the first expression of P_T in (7-84) is merely the integral of the Poynting vector over the aperture, and thus represents the aperture power leakage. This argument alone would serve to equate P_T of (7-80) and (7-84) on the basis of physics. In a sense, (7-80) - (7-84) do nothing more than demonstrate that Maxwell's equations conserve energy flux in free space between the near and far fields.

EFFECT ON Q OF APERTURES

If a cavity has apertures, but no internal loss, the Q for a given mode is obtained by dividing the energy stored in that mode (7-22) and (7-23) by (7-84)

$$Q_n' = \frac{4\omega_n}{Z_o \iint_{\text{aperture}} |\mathbf{H}(x', y')|^2 dx' dy'} \quad (7-85)$$

For electrically small apertures, (7-85) can give greatly differing values of Q_n for adjacent n . A somewhat less sensitive (and probably more useful) value of Q can be obtained by taking the sums of (7-22), (7-23) and (7-84) over the bandwidth of interest and performing division on the summations.

If both internal losses and apertures contribute to a reduced Q_n , Q_n^{-1} of (7-33) is augmented by $Q_n'^{-1}$ of (7-85) to obtain a reciprocal Q which includes combined effects.

REFERENCES

- [1] R. Holland, "Development of the equivalence principle for SGEMP and source-region EMP problems," *IEEE Trans. Electromagn. Compat.*, vol. ECM-37, pp. 84-88, February 1995.
- [2] R. Holland, "Two-pass finite-difference time-domain (FDTD) calculations on a fighter aircraft," *IEEE Trans. Ant. & Propagat.*, vol. AP-44, pp. 659-664, May 1996.
- [3] D. E. Merewether and R. Fisher, "Finite-difference analysis of EM fields inside complex cavities driven by large apertures," *IEEE Trans. Electromagn. Compat.*, vol. EMC-24, pp. 406-410, November 1982.
- [4] S. A. Schelkunoff, "Field equivalence theorems," *Commun. Pure Appl. Math.*, vol. 4, p. 43-59, June 1951.

- [5] S. Silver, *Microwave Antenna Theory and Design*, New York: McGraw Hill Book Company, 1949, pp. 167-168, sec. 5.15.
- [6] K. S. H. Lee (Ed.), *EMP Interaction: Principles, Techniques and Reference Data (A Compleat Concatenation of Technology from the EMP Interaction Notes*, Air Force Weapons Laboratory, AFWL-TR-80-402, Kirtland AFB, NM, December 1980, pp. 87-91, sec. 1.3.1.5, pp. 184-186, sec. 1.4.1.4.2, and pp. 436-445, sec. 2.1.3.2.2.
- [7] H. A. Bethe, "Theory of diffraction by small holes," *Phys. Rev.*, vol. 66, pp. 163-182, October and November, 1944.
- [8] D. J. Riley and C. D. Turner, "Hybrid thin-slot algorithm for the analysis of narrow apertures in finite-difference time-domain calculations," *IEEE Trans. Ant. Propagat.*, vol. AP-38, pp. 1943-1950, December 1990. See also Sandia National Laboratory Tech. Repts. SAND 89-3073, January 1990, SAND90-0519, April 1990, SAND91-1061, June 1991, and SAND93-0735, April 1993.
- [9] D. J. Riley and C. D. Turner, "The inclusion of wall loss in finite-difference time-domain thin-slot algorithms, *IEEE Trans. Electromagn. Compat.*, vol. EMC-33, pp. 304-311, November 1991.
- [10] A. D. Berk, "Variational principles for electromagnetic resonators and waveguides," *IRE Trans. Ant. Propagat.*, vol. AP-4, pp. 104-111, April 1956.
- [11] W. J. Karzas, Back Door Coupling of RF (Microwave) Energy to Spacecraft Interior Cabling, Air Force Phillips Laboratory, AFPL-TR-95-0475, Kirtland AFB, NM, June 1995.
- [12] P.M. Morse and H. Feshbach, *Methods of Theoretical Physics*, New York: McGraw Hill Book Company, 1953, pp. 849-851, sec. 7.3.
- [13] R. Holland and E. P. EerNisse, *Design of Resonant Piezoelectric Devices*, Cambridge, Mass: MIT Press, 1969, pp. 61-89, sec. 2.3.
- [14] R. Holland, "Optimization criterion for illuminating circular antenna apertures," *IEEE Trans. Ant. Propagat.*, vol. AP-19, pp.436-443, May 1971.

Chapter 8. EM PICKUP AND SCATTERING BY A WIRE

Since a major goal in the study of EM pickup (deterministic or statistical) by cables in an enclosure consists of understanding cable coupling, we now present a review of pickup and scattering by a single wire in free space or over a ground plane. The wire may be uniform and infinite or finite and nonuniform. Solutions based on Maxwell's equations directly are compared with solutions based on the telegrapher's equations; for 1 mm Cu wire at 1 GHz, equilibrium cw currents as computed from the two models differ by 6 dB. In general, the wire-current solutions are separated into a homogeneous part and a particular or driven part. The driven part couples and scatters fields, while, at least for an infinite wire in the far field, the homogeneous part does not. We also discuss the quality factor Q and indicate a manner in which its meaning is occasionally misinterpreted.

In this work we describe the development of statistical tools for evaluating field-induced currents on satellite wiring harnesses and similar cavity-enclosed systems which are too complex for deterministic techniques, such as FDTD, MoM, or finite elements to have any real prospect of success.[1,2] The statistical philosophy we employ is to divide up as much of the wiring as possible into small segments, then apply driving fields to each of the segments, and finally match current and potential at segment junctions. The cable model we use permits segments to be about $\lambda_0/4$ long. We do not explicitly include coupling between non-adjacent segments, but rather assume it is implicitly folded into the field statistics. This approach becomes more reasonable the more complex the wiring is; in fact, for most statistical problems, it is true that this sort of procedure introduces an error which, on the average, decreases as the square root of the number of segments. Thus, a statistical approach actually thrives on complexity. It also eliminates the need to manipulate any huge matrices, or even to track collaterally a myriad of variables in which we have no real interest (which could not be avoided using FDTD or FVTD).

The cable-driving fields are randomly generated, but filtered and weighted so they have some physically justifiable probability density function such as normal, log normal, or chi square with two degrees of freedom. In fact, a watchword of this work has been the inclusion into the statistics of as much EM physics as possible.

In this context, we have confronted the problem of an EM field coupling to a wire segment, and found that even some seemingly simple, canonical problems are apparently not well understood. With this background in mind, we here undertake a presentation of some ostensibly fundamental problems and their solutions which we have had to work out.

We also find it necessary to assume the behavior of an infinite wire (which we can usually determine) has characteristics which carry over to finite wire segments (which may be harder to describe). Basically, in our statistical modeling of wire segments, we think it better to use the EM physics of an infinite wire than to use no physics at all. We prefer not just to treat the statistics as a disembodied mathematical exercise.

In this section, we shall consider first the problem of determining the current on a wire driven by a plane-wave incident field. Initially we shall assume the wire is infinitely long, straight, uniform, and not backed by a ground plane. Later in the section, we will relax some of these assumptions. We shall, moreover, only consider the case where the wire and illumination parameters are such that non-axially symmetric portions of the solution of the fields and currents around the wire are negligible. (This assumption is clearly reasonable for our problem, given that we are going to use all quantities only statistically, and the spatial average of any asymmetric field component having a $\cos n\phi$ distribution, $n \neq 0$, will always be zero. We presume there are other real problems, such as asymptotic antenna theory for round wires[3] or the current on a conductor segment in a simple MoM model, for which our assumptions are also adequate.) At no point shall we relax azimuthal independence. Thus, phenomena such as creeping waves at a bend with bend radius not great compared to wavelength will be ignored. Also, when a ground plane is introduced, we shall assume that the wire radius a is so small compared to height h over the ground plane that current concentration on the side of the wire facing the ground plane is negligible. The wire will be required to have a small amount of resistivity ($\rho_{\text{Cu}} = 1.7 \text{ E-}8 \Omega/\text{m}$ will do nicely), as certain homogeneous solutions of Maxwell's equations are otherwise forbidden.

Our initial approach will be the direct solution of Maxwell's equations for an infinite, solitary wire. Such a problem is essentially an ordinary, hyperbolic, second-order differential equation, and as such has a homogeneous and an inhomogeneous wave solution for the current on the wire. The homogeneous solution is not driven by the incident field (nor does it radiate, at least not where the wire is uniform). This solution appears only where something nonuniform (such as a bend, shadow, or wire termination) occurs. At such points, its presence is required to match boundary conditions, and it can propagate away from such points, mixed and matched with the driven or inhomogeneous solution. We had long been perplexed by the seeming experimental paradox that cables in a region of well-randomized driving fields carry currents that are invariant to cable termination conditions, provided the observer is $3\lambda_0$ or more removed from the termination. On the other hand, currents coming into a shielded enclosure from an external connection can propagate, obviously, the entire length of an airplane and more. We now see that the first case is dominated by inhomogeneous currents, while the second is dominated by homogeneous currents; that the two kinds of current solutions have quite different properties; and that the paradox evaporates. Whatever we put into our statistical segment model, this ability to include both types of solutions is fundamentally obligatory.

Next, we shall compare the exact (in the azimuthally symmetric limit) solution of Maxwell's equations with a simpler, but approximate, model, specifically that based on the telegrapher's equations. Not surprisingly, the telegrapher's equation solution is fine in the low-frequency limit, but pulls away from the exact solution very gradually as wavelength decreases. Even for a single wire in free space, one can symbolically write the telegrapher's equations. In this case, however, the quantity identified with series resistance has some very peculiar properties. This, in turn, implies we probably should not use telegrapher's-equation-based transmission line models with fixed, frequency-independent (r, l, g, c) in our statistical formulation for cable

segments which are far from other conductors. In this case, it is preferable to use a model based more fundamentally on the exact solution of Maxwell's equations.

Our next step is to evaluate the effects of adding a ground plane. In a sense, this simplifies the problem, as the telegrapher's equations parameters (r, l, g, c) are now less exotically defined. The exact solution, however, becomes considerably more complicated, especially in the homogeneous case. Thus, for wires near a ground plane, statistical wire modeling by the telegrapher's equation makes more sense, and is the preferable approach. As most wires are near a ground plane or conducting wall, this is a conclusion of major significance.

Lastly, as an appendix, we discuss some aspects and interpretations of the quality factor Q in a resonant system. This is important to our statistical wire model because it dictates how and when we need to include terms such as radiation resistance. (While our statistical EM philosophy embraces the concept that we do not need to cross-couple cable segments, it does not embrace the concept that a segment cannot lose energy by radiation.) We also find it useful to examine different ways of inserting loss into our model enclosure, which is actually an interactive part of the wiring harness system. Finally, we point out that, while it is true that energy decays as a simple Q -dependent exponential when the drive is turned off, it does not follow that energy builds up as a simple exponential when a system is turned on. (The latter belief is a fairly commonly encountered mistake.[4])

HOMOGENEOUS SOLUTION FOR A WIRE

Let us begin with a solution having $e^{\gamma z}$ dependence along the wire, where γ must necessarily be complex and have a negative real part. For sinusoidal e^{st} conditions (s and $-j\omega$ will be interchangeable in this section; $e^{-j\omega t}$ time dependence insures Hankel functions of complex arguments asymptote properly), Maxwell's equations are of the form

$$\nabla \times \mathbf{E} = - \mu s \mathbf{H} \quad (8-1)$$

$$\nabla \times \mathbf{H} = \mathbf{J} + (\sigma + \epsilon s) \mathbf{E} \quad (8-2)$$

Because of the small-diameter assumption, $\partial/\partial\phi$ of scattered fields are zero by definition, and the partial differential equations specifically take the form

$$-\mu s H_\phi = \frac{\partial E_r}{\partial z} - \frac{\partial E_z}{\partial r} = \gamma E_r - \frac{\partial E_z}{\partial r} \quad (8-3)$$

plus two additional coupled equations coming from (8-2) and involving the same three fields. For the azimuth-independent case, the TE solutions (E_ϕ, H_r, H_z) decouple from the TM solutions (E_r, E_z, H_ϕ), and may be assumed to be absent.

If we call

$$k^2 = -\mu s(\sigma + \epsilon s) \quad (8-4)$$

manipulation of the partial differential equations yields the homogeneous circular cylinder wave equation for H_ϕ

$$\frac{\partial}{\partial r} \left(\frac{1}{r} \frac{\partial(rH_\phi)}{\partial r} \right) + (k^2 + \gamma^2)H_\phi = 0 \quad (8-5)$$

We next define the complex radial wavenumber by

$$(\kappa^{(h)})^2 = k^2 + \gamma^2 \quad (8-6)$$

which leads to the Bessel function solution for the homogeneous fields inside the wire (medium 1)

$$H_{\phi 1}^{(h)} = AJ_1(\kappa_1^{(h)}r) \quad (8-7)$$

$$E_{r1}^{(h)} = \frac{\mu_1 s \gamma}{k_1^2} AJ_1(\kappa_1^{(h)}r) \quad (8-8)$$

$$E_{z1}^{(h)} = -\frac{\mu_1 s \kappa_1^{(h)}}{k_1^2} AJ_0(\kappa_1^{(h)}r) \quad (8-9)$$

In (8-7) - (8-9), A is an undefined constant which can be related to the homogeneous solution for the current flowing on (and in) the wire as

$$I^{(h)} = \int_0^a 2\pi(\sigma + \epsilon s)E_z^{(h)}r dr = 2\pi a AJ_1(\kappa_1^{(h)}a) \quad (8-10)$$

Equations (8-6) - (8-10) can be manipulated to yield the homogeneous fields in terms of the homogeneous current in the wire

$$H_{\phi 1}^{(h)} = \frac{I^{(h)}}{2\pi a} \frac{J_1(\kappa_1^{(h)} r)}{J_1(\kappa_1^{(h)} a)} \quad (8-11)$$

$$E_{r1}^{(h)} = \frac{\mu_1 s \gamma I^{(h)}}{2\pi a k_1^2} \frac{J_1(\kappa_1^{(h)} r)}{J_1(\kappa_1^{(h)} a)} \quad (8-12)$$

$$E_{z1}^{(h)} = - \frac{\mu_1 s \kappa_1^{(h)} I^{(h)}}{2\pi a k_1^2} \frac{J_0(\kappa_1^{(h)} r)}{J_1(\kappa_1^{(h)} a)} \quad (8-13)$$

The fields outside the wire, in air, are obtained by replacing the region subscripts 1 with 2's and the Bessel functions with Hankel functions of the first kind in (8-11) - (8-13).

It remains to evaluate the elusive complex wavenumber $\gamma(s)$. This is done by requiring $H_{\phi}^{(h)}$ and/or $E_z^{(h)}$ to be continuous at the wire surface:

$$\frac{\mu_1 \kappa_1^{(h)}}{k_1^2} \frac{J_0(\kappa_1^{(h)} a)}{J_1(\kappa_1^{(h)} a)} = \frac{\mu_0 \kappa_2^{(h)}}{k_2^2} \frac{H_0^{(1)}(\kappa_2^{(h)} a)}{H_1^{(1)}(\kappa_2^{(h)} a)} \quad (8-14)$$

where γ enters (8-14) through (8-6), the definition of $\kappa_1^{(h)}$ and $\kappa_2^{(h)}$. Figure 8.1 illustrates the real and imaginary parts of γ as functions of frequency for a 1 mm radius copper wire. Note that the real part of γ everywhere possesses the required negative sign.

We next investigate the radiation resistance associated with the current $I^{(h)}$ corresponding to the homogeneous solution of Maxwell's equations. The power radiated per unit length by the wire is obtained by taking the radial component of the Poynting vector

$$S_{r2}^{(h)} = \frac{1}{2} \operatorname{Re}[E_{z2}^{(h)} H_{\phi 2}^{(h)*}] \quad (8-15)$$

and integrating it around the wire azimuth in the limit as r goes to infinity. Substitution of $E_{z2}^{(h)}$ and $H_{\phi 2}^{(h)}$ in the large- r limit yields

$$S_{r2}^{(h)} = \frac{|I^{(h)}|^2}{(2\pi a)^2} \cdot \frac{1}{\pi |\kappa_2^{(h)}| r} \cdot \frac{\mu_0}{|H_1(\kappa_2^{(h)} a)|^2} \operatorname{Re} \left[-\frac{j s \kappa_2^{(h)} e^{-2 \operatorname{Im}[\kappa_2^{(h)}] r}}{\omega \epsilon_0 \mu_0} \right] \quad (8-16)$$

From (8-4), we see that k_2^2 must be pure real and positive, while Figure 8.1 shows that γ^2 will normally have phase just over π (in the third quadrant). Thus, $\kappa_2^{(h)}$ will, from (8-6), normally have a positive imaginary part in (8-16), and the integral of $S_{r2}^{(h)}$ over the azimuth will have an exponentially decaying dependence on r .

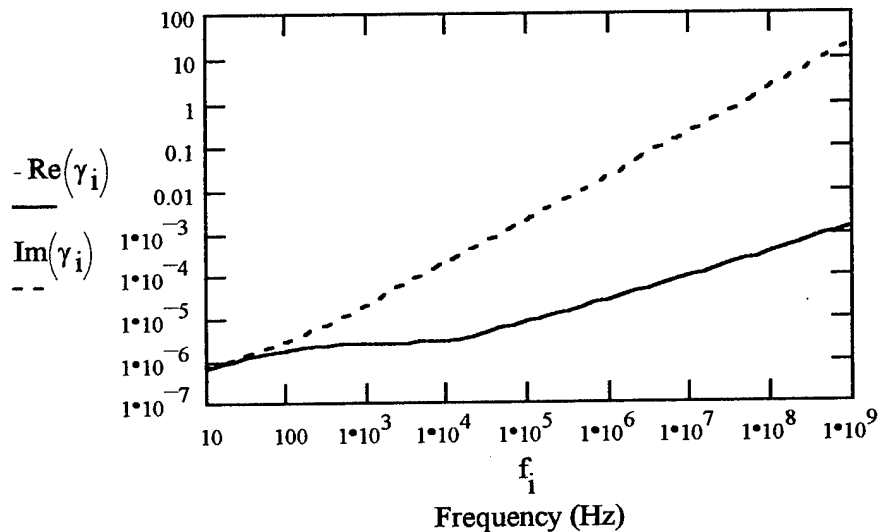


Figure 8.1. Real (attenuation) and imaginary (phase-velocity propagation) parts of $\gamma^{(h)}$ as functions of frequency for homogeneous-mode current on a 1 mm radius copper wire. Note $\operatorname{Re}[\gamma^{(h)}]$ is always negative.

This means that the homogeneous solution of the wire problem does not radiate power; i.e., at least in the infinite-wire case, it has no radiation resistance. In retrospect, this outcome could have been anticipated: since this solution is homogeneous, incident fields do not couple to or drive it. By reciprocity, it thus cannot radiate or scatter. This is the first of several conclusions we will point out which are both obvious and easy to overlook.

One should note that, if ρ_{Cu} were actually zero, (8-14) would have no solution with γ having a negative real part. The consequences of having $\operatorname{Re}[\gamma] = 0$ are that $\operatorname{Im}[\kappa_2^{(h)}] = 0$, the fields lose their decaying exponential dependence on r , and the amount of energy per unit length required to set up the fields associated with a nonzero current $I^{(h)}$ is infinite. In point of fact, with

$\rho = 0$, the TM solution corresponding to (8-11) - (8-13) collapses to a TEM solution with no fields in the wire and no $E_{z2}^{(h)}$ field in the air. This, in turn, implies the inward radial component of the Poynting vector vanishes everywhere, and, colloquially speaking, no glue remains to bind the fields to the wire. [Since (8-14) strictly pertains only to an infinite wire, the conclusions of this paragraph have only been proved for an infinite wire.]

We are not sure when this solution to Maxwell's equation was discovered: in 1941, Stratton [5, pp. 524-530] cited a 1927 treatment by Sommerfeld [6] who had stated that for 1 mm Cu wire at 1 GHz, a signal traveling in this mode will e -fold in 770 m. At times, this solution is referred to as a single-conductor or Goubau transmission line, although the actual Goubau line apparently consists of a wire coated with a dielectric, and depends on the dielectric, not the wire dissipation, to contain the wave.[7] Physically, this solution corresponds to the surface wave of the Sommerfeld problem[8], except here the propagation is axial, whereas in the Sommerfeld solution, propagation is along the earth's surface radially from a vertical source. One-dimensional surface waves of this type were described as early as 1907 by Zenneck.[9]

INHOMOGENEOUS SOLUTIONS FOR A WIRE

Let us now consider the wire to be driven by a plane wave

$$\mathbf{E}^i = \mathbf{E}_0^i e^{j\mathbf{k}_2 \cdot \mathbf{r}} = \mathbf{E}_0^i e^{(\gamma x + \beta y + \alpha z)} \quad (8-17)$$

where γ of (8-17) is not related to γ of the homogeneous case. We can re-express $\mathbf{k}_2 \cdot \mathbf{r}$ as

$$\mathbf{k}_2 \cdot \mathbf{r} \approx k_2(\gamma_x x + \gamma_y y + \gamma_z z) \quad (8-18)$$

with \mathbf{k}_2 given as

$$k_2^2 = \omega^2 \mu_0 \epsilon_0 = \omega^2 / c_0^2 \quad (8-19)$$

and $(\gamma_x, \gamma_y, \gamma_z)$ being the direction cosines between \mathbf{k}_2 and the cartesian axes. Note that \mathbf{E}_0^i and \mathbf{k}_2 must be orthogonal.

If the wire is assumed to lie on the z -axis, x and y will be zero, and the incident field parallel to the wire will be

$$\mathbf{E}^i \cdot \mathbf{i}_z = E_z^i e^{\alpha z} = E_z^i e^{j k_2 \gamma_z z} = E_z^i e^{j k_2 \cos \theta_z z} \quad (8-20)$$

with θ_z being the angle between the wavevector and the positive wire ($+z$) axis.

As in the homogeneous case, the fields scattered by the wire will be azimuth independent ($\partial/\partial\phi = 0$), since the wire has been postulated to be a small fraction of a wavelength. Scattered-

field and current dependence on z will be $e^{\alpha z}$ where, unlike γ in the homogeneous case, α is pure imaginary, and simply obtained from

$$\alpha = j\omega\gamma_z/c_0 \quad (8-21)$$

The radial wavenumber now becomes, instead of (8-6)

$$(\kappa^{(p)})^2 = k^2 + \alpha^2 \quad (8-22)$$

where α replaces γ in the wave equation (8-5) for H_ϕ

Thus, the inhomogeneous, or particular, solutions of Maxwell's equations in the wire are, instead of (8-11) - (8-13)

$$H_{\phi 1}^{(p)} = \frac{I^{(p)}}{2\pi\alpha} \frac{J_1(\kappa_1^{(p)}r)}{J_1(\kappa_1^{(p)}a)} \quad (8-23)$$

$$E_{r1}^{(p)} = \frac{\mu_1 s \alpha I^{(p)}}{2\pi a k_1^2} \frac{J_1(\kappa_1^{(p)}r)}{J_1(\kappa_1^{(p)}a)} \quad (8-24)$$

$$E_{z1}^{(p)} = - \frac{\mu_1 s \kappa_1 I^{(p)}}{2\pi a k_1^2} \frac{J_0(\kappa_1^{(p)}r)}{J_1(\kappa_1^{(p)}a)} \quad (8-25)$$

In (8-23) - (8-25), $I^{(p)}$ is the inhomogeneous solution for the current flowing on (and in) the wire. The fields in air are again obtained by replacing regional subscripts 1 with 2's and Bessel functions with Hankel functions of the first kind.

Now the driven or inhomogeneous wire current $I^{(p)}$ is the unknown to be obtained by matching boundary conditions just as the axial wavenumber γ was the unknown in the homogeneous case. Matching boundary conditions on $E_z^{(p)}$ at the interface

$$E_{z1}^{(p)} = E_{z2}^{(p)} + E_z^i = E_{z2}^{(p)} + E_0^i \sin \theta_z \quad (8-26)$$

gives

$$I^{(p)} = E_0^i \sin \theta_z \cdot \frac{2\pi a}{s} \left(\frac{\mu_0 \kappa_2^{(p)} H_0^{(1)}(\kappa_2^{(p)}a)}{k_2^2 H_1^{(1)}(\kappa_2^{(p)}a)} - \frac{\mu_1 \kappa_1^{(p)} J_0(\kappa_1^{(p)}a)}{k_1^2 J_1(\kappa_1^{(p)}a)} \right)^{-1} = I_0 \quad (8-27)$$

Figure 8.2 illustrates $I^{(p)}/(E_0^i \sin \theta_z)$ as a function of frequency for a 1 mm radius Cu wire based on broadside ($\theta_z = \pi/2$, $\gamma_z = \alpha = 0$, $\kappa_2 = k_2 = \omega/c_0$) illumination. [The quantity I_0 is introduced in (8-27) for later use and reference.]

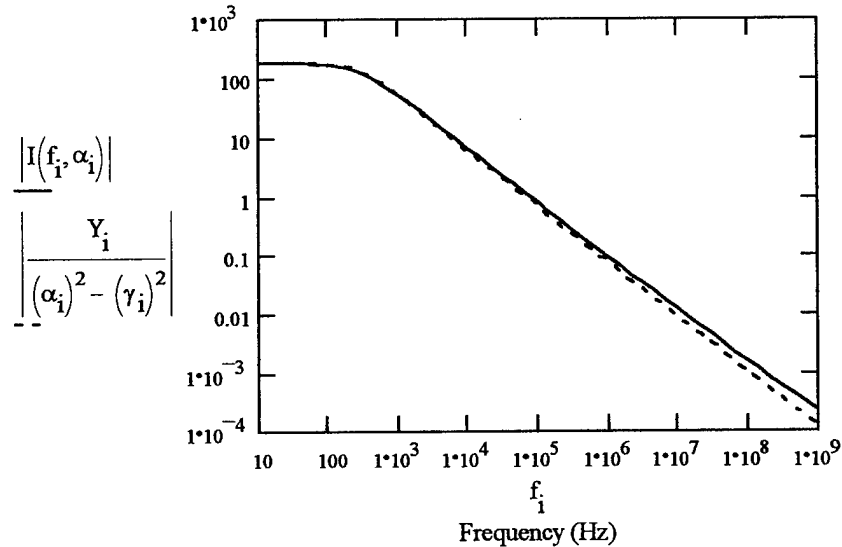


Figure 8.2. Normalized inhomogeneous current, $I^{(p)}/E_z^i$ as a function of frequency for inhomogeneous mode on a 1 mm radius copper wire as computed by exact solution of Maxwell's equations (8-27) and by solution of the approximate telegrapher's equations (8-53). Note the telegrapher's current is about 6 dB below the exact solution at 1 GHz. For a 5 mm copper wire, the disparity at 1 GHz increases to 8 dB. This figure is based on broadside illumination.

Since the inhomogeneous portion of the current on a wire is field driven, reciprocity requires it also to radiate. Let us now seek the radiation resistance associated with $I^{(p)}$. The radial component of the Poynting vector $S_{r2}^{(p)}$ associated with the driven (scattered) solution of Maxwell's equations in air becomes, in the large- r limit,

$$S_{r2}^{(p)} = \frac{1}{2} \operatorname{Re} [E_{z2}^{(p)} H_{\phi 2}^{(p)*}] = \frac{1}{2} \operatorname{Re} \left[\frac{2\mu_0 \omega |I^{(p)}|^2}{(2\pi k_2 a)^2 \pi r |H_1^{(1)}(\kappa_2^{(p)} a)|^2} \right] \quad (8-28)$$

where $E_{z2}^{(p)}$ and $H_{\phi 2}^{(p)}$ are obtained from (8-23) and (8-25). This expression represents the power scattered per unit length of wire, and the radiation resistance per unit length thus is

$$R_{rad} = \frac{2\pi r S_{r2}^{(p)}}{\frac{1}{2} |I^{(p)}|^2} = \frac{2\mu_0 \omega}{(2\pi k_2 a)^2 |H_1^{(1)}(\kappa_2^{(p)} a)|^2} = \frac{\mu_0 \omega}{8(k_2 / \kappa_2^{(p)})^2} \quad (8-29)$$

where the last expression in (8-29) is obtained by invoking the requirement that the wire diameter be a small fraction of a wavelength, so the Hankel functions can be evaluated as its small-argument limit

$$|H_1^{(1)}(\kappa_2^{(p)} a)| \approx \left(\frac{2}{\pi \kappa_2^{(p)} a} \right)^{\frac{1}{2}} \quad (8-30)$$

Evaluating (8-21) and (8-22) in air indicates that

$$(k_2 / \kappa_2^{(p)})^2 = 1 / \sin^2 \theta_z \quad (8-31)$$

so (8-29) for the radiation resistance can also be written

$$R_{rad} = \frac{\mu_0 \omega \sin^2 \theta_z}{8} \quad (8-32)$$

This formula is the same as that derived under quite different circumstances by Vance.[10]

We can now perform a most interesting computation: if a wire is not infinite, how far down the wire from a termination is the termination detectable in the driven current response? Consider for analogy a transmission line characterized by (r, l, g, c) . For a single-conductor transmission line, the concept of a shunt loss g is somewhat vague. Omitting g , the wavenumber for a lossy transmission line is

$$k_z = \omega \sqrt{lc} \left(1 + \frac{jr}{2\omega l} \right) = k_z' + jk_z'' = \frac{2\pi}{\lambda_z} \left(1 + \frac{jk_z''}{k_z'} \right) \quad (8-33)$$

Thus, in a homogeneous plane-wave field, the effects of any discontinuity on the driven-mode current will e -fold in a distance

$$\Delta = \frac{\lambda_z}{2\pi} \frac{k_z'}{k_z''} = \frac{\lambda_z}{2\pi} \cdot \frac{2\omega l}{r} \quad (8-34)$$

The inductance per unit length l of most free-space transmission lines differs from μ_0 only by a geometrical constant on the order of unity. (For a wire of radius a at height h over a ground plane, the constant is $[\ln(2h/a)]/(2\pi)$. For the present case, $2h$ is approximately replaced by λ_0 .) The radiation resistance of (8-32) corresponds to r in (8-34). Thus, we can evaluate Δ , the e -fold attenuation distance of termination effects along a wire, approximately as

$$\Delta \approx \frac{\lambda_0}{2\pi} \cdot \frac{16}{\sin^2 \theta_z} \approx \frac{2.5 \lambda_0}{\sin^2 \theta_z} \quad (8-35)$$

with respect to the driven current solution of Maxwell's equations. In other words, if one is more than three wavelengths away from the end of a cable, one probably cannot tell from the driven portion of the cable response what its termination is. This result is well-known throughout the HPM experimental community, although it is not always readily embraced by theorists.[11]

Having derived the radiated power by evaluating the radial component of the Poynting vector at larger r , we next look at the total power extracted (scattered or dissipated) from the incident field by the wire. This quantity can be written¹

$$P_{ex} = \frac{1}{2} \operatorname{Re}[E_z^i I^{(p)*}] = \frac{1}{2} \operatorname{Re}[E_0^i \sin \theta_z I^{(p)*}] \quad (8-36)$$

If (8-27) is solved for $E_0^i \sin \theta_z$, the result substituted in (8-36), and this result divided by $\frac{1}{2}|I^{(p)}|^2$, we obtain a formula for the total effective resistance describing the wire's behavior in extracting energy from the incident field:

$$\frac{P_{ex}}{\frac{1}{2}|I^{(p)}|^2} = R_{ex} = \operatorname{Re} \left[\frac{j\omega}{2\pi a} \left(\frac{\mu_0 \kappa_2^{(p)} H_0^{(1)}(\kappa_2^{(p)} a)}{k_2^2 H_1^{(1)}(\kappa_2^{(p)} a)} - \frac{\mu_1 \kappa_1^{(p)} J_0(\kappa_1^{(p)} a)}{k_1^2 J_1(\kappa_1^{(p)} a)} \right) \right] \quad (8-37)$$

This total effective resistance consists of two very distinct parts, the scattering or radiation resistance of (8-32) and the ohmic loss of the wire (which is enhanced by the skin effect when the skin depth becomes commensurate or short compared to the wire radius a). Figure 8.3 represents an overlay of R_{ex} , R_{rad} , and the ohmic loss. It may be seen that R_{ex} indeed, is the sum of its two constituents.

MATCHING THE HOMOGENEOUS AND INHOMOGENEOUS SOLUTIONS

Since the driven current on a wire only propagates a few wavelengths, the obvious question arises, how do incident field effects on a cable make their way any distance out of the driven region and into a shielded enclosure or asset? The obvious answer is that it is the

¹The time-domain version of this equation has some implications concerning energy buildup in a resonant system which are often misinterpreted (see previous section and Appendix 8A).

homogeneous current solution that actually penetrates. Any differential equation has a solution consisting of a particular part (the response to local drive) plus a homogeneous part (used to match boundary conditions). Thus, the general solution for current on a wire (finite or infinite) is

$$I = I^{(p)} + I^{(h)} = I^{(p)} + a_1 e^{\gamma z} + a_2 e^{-\gamma z} \quad (8-38)$$

In our statistical model, a_1 and a_2 are the parameters which are matched to obtain continuity of current and voltage at segment junctions. We have thus built into our statistical model the aforementioned requirement of being able to utilize both homogeneous and inhomogeneous solutions.

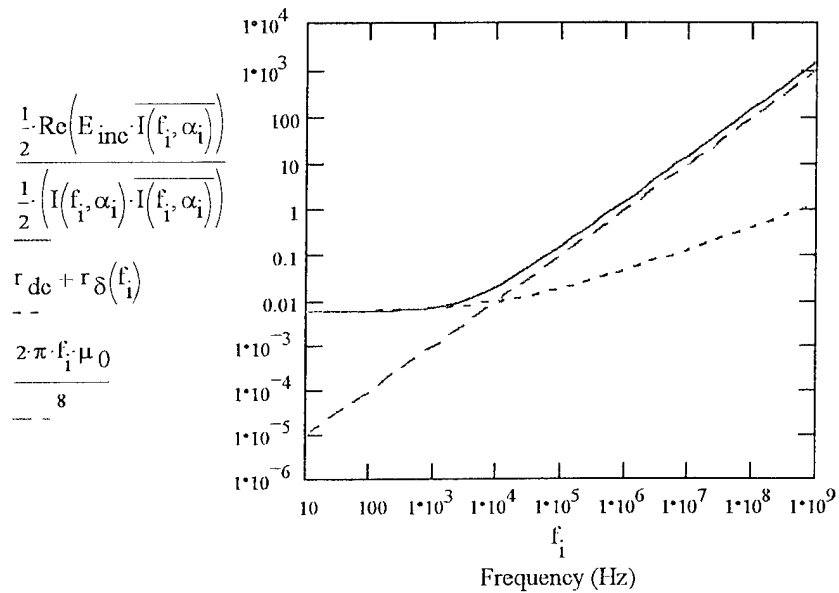


Figure 8.3. Comparison of 1) the total power extracted by a 1 mm radius copper wire from the incident plane wave according to (8-37), 2) the skin-effect-enhanced ohmic loss of the wire, and 3) the radiation or scattering resistance of the wire (8-32). Note that 1) is the (approximate) sum of 2) and 3). This figure is based on the plane wave being normally incident on the wire.

Consider, as a highly idealized model of the situation in the preceding paragraph, an infinite wire illuminated by the incident field for $z < 0$, but in a shadow for $z > 0$. (Assume whatever casts the shadow does not produce diffraction effects at its edge, and that it also does not act like ground plane which would modify the characteristic impedance of the wire.) Now the current on the negative portion of the wire will be given by the particular or driven solution (8-27) (with an $e^{\alpha z}$ multiplier), which we will call I_0 . On the positive (shadowed) portion of the wire there is no drive, and the particular or driven solution vanishes. However, current continuity must be maintained, so we require a nonzero homogeneous part to match this boundary condition at $z = 0$. Thus, the current on the positive portion of the wire will still be given by (8-27), with an

attenuating $e^{\gamma z}$ multiplier. In other words, to match continuity of current at $z \geq 0$, a_2 is zero, but a_1 is given by I_0 , the right side of (8-27), times $e^{\gamma z}$. There is no physical discontinuity in the wire at $z = 0$. Thus, there is no negative-going homogeneous-mode reflection, and a_2 is everywhere zero. The wire current solution is mathematically written

$$I = \begin{cases} I_0 e^{\alpha z} & z \leq 0 \\ I_0 e^{\gamma z} & z \geq 0 \end{cases} \quad (8-39)$$

(The preceding idealization could be rendered more physically possible by assuming there was some sort of physical discontinuity at $z = 0$, such as the introduction of a shadowing semi-infinite perfectly conducting plate. Unlike the initial model, this new conceptualization would reflect at the discontinuity, add an $e^{-\gamma z}$ term to the $z \leq 0$ region, with an unknown coefficient to be matched, and change the coefficient from I_0 in the $z \geq 0$ region.) This example explains how a cable which is partly illuminated and partly dark actually manages to transport energy from the excited region to the quiet region, as in the case of an external antenna cable running through a wall and into a shielded volume, such as an aircraft fuselage or satellite bus.

For a second example, let us consider a finite wire running from $z = -b$ to b where, to avoid complication and confusion, b is presumed much greater than the termination-effect penetration length Δ of (8-34). Here, the particular solution for the current on the wire is still given by (8-27), but we have physical discontinuities at $z = \pm b$, so, both a_1 and a_2 will be nonzero, in consequence of reflections occurring at both ends of the wire. We thus have

$$I = I_0 e^{\alpha z} + a_1 e^{\gamma z} + a_2 e^{-\gamma z} \quad -b \leq z \leq b \quad (8-40)$$

The boundary conditions are that I must vanish at $\pm b$. The solution of (8-40), with boundary conditions, is

$$I = I_0 \left(e^{\alpha z} - \frac{e^{(\alpha + \gamma)b} - e^{-(\alpha + \gamma)b}}{e^{2\gamma b} - e^{-2\gamma b}} e^{\gamma z} + \frac{e^{(\alpha - \gamma)b} - e^{-(\alpha - \gamma)b}}{e^{2\gamma b} - e^{-2\gamma b}} e^{-\gamma z} \right) \quad (8-41)$$

It may be seen that resonance is appropriately predicted when the wire-length is an integral multiple of homogeneous-solution half wavelengths,

$$\text{Re}[\gamma(\omega)] \cdot 2b = n\pi \quad (8-42)$$

[There is, of course, an additional approximation made here that the scattered field does not fringe past the wire end. If this approximation is not made, the first resonance of the wire segment occurs when the wire is a bit shorter than $\lambda_0/2$. For higher modes, the deviation of resonant wire length from $n\lambda_0/2$ diminishes rapidly with n . A reviewer has pointed out that, had we alternatively terminated the wire segment with conducting plates perpendicular to the wire, (8-42) would not be just an approximation. Also, we have previously stipulated that the wire

segment length $2b$ is greater than $2\Delta \approx 5\lambda_0$, or $n \geq 10$. Thus, for this example, the end-effect issue is somewhat moot anyway.]

The two examples presented here indicate obvious generalizations to wires with bends, discontinuous radii, point impedances, and any other sort of discontinuity, including passing through an opening from a system exterior to the interior. (These generalizations do, however, depend on our basic assumption of azimuthal independence. Obviously, this assumption will be violated to some extent at zero-radius bends and at wire junctions. In some applications, this approximation, which explicitly ignores creeping waves and differential-mode current concentration of facing sides of proximate cables, may not be tolerable. For our statistical cable work, however, where we are interested in spatial-average quantities, it is quite adequate. There are doubtless other situations, such as asymptotic antenna theory[3] or the current distribution on a conductor segment in a simple MoM model, which have similar toleration.)

The major impact of this section as pertaining to our statistical work is that we do not need to concern ourselves with cable termination conditions on cables inside overmoded chambers if we are more than $3\lambda_0$ from a given termination.

REVIEW OF TRANSMISSION LINES

Even the single-wire transmission line has some conventions in common with two-conductor systems; the second conductor is just removed to infinity, and the wire has to be infinitely long before the commonality is exact. Symbolically, one can still write the homogeneous telegrapher's equations

$$\frac{dV^{(h)}}{dz} = - ZI^{(h)} \quad (8-43)$$

$$\frac{dI^{(h)}}{dz} = - YV^{(h)} \quad (8-44)$$

For such lines, there are four parameters, γ , Y , Z , and Z_c , the last being the characteristic impedance

$$Z_c = \frac{1}{I^{(h)}} \int_a^{\infty} E_r^{(h)} dr = - \frac{\mu_0 s \gamma}{2\pi a k_2^2} \frac{H_0^{(1)}(\kappa_2^{(h)} a)}{\kappa_2^{(h)} H_1^{(1)}(\kappa_2^{(h)} a)} \quad (8-45)$$

Only two of these parameters are independent. Since we already know γ from (8-14) and Z_c from (8-45), we should be able to determine Y and Z from (8-43) and (8-44). Specifically, it is easy to show that

$$Z = -\gamma Z_c \quad Y = -\gamma/Z_c \quad Z_c = \sqrt{Z/Y} \quad \gamma^2 = YZ \quad (8-46)$$

Sometimes Z and Y are separated into their real and imaginary parts [see (8-33) and (8-34)]

$$Z = r - j\omega l = -\gamma Z_c \quad (8-47)$$

$$Y = g - j\omega c = -\gamma/Z_c \quad (8-48)$$

Let us consider an element dz of the wire. The net power entering dz is

$$P_{net}^{(h)} = \frac{1}{2} \operatorname{Re} \left[V_+^{(h)} I_+^{(h)*} - V_-^{(h)} I_-^{(h)*} \right] \quad (8-49)$$

where a + subscript indicates a $+z$ -going wave and a - subscript indicates a $-z$ -going wave. Equation (8-49) is a sort of generalized 1D divergence relation (in so far as "generalized 1D" is not an oxymoron).

Generous manipulations of (8-43) - (8-49) lead to the result

$$P_{net}^{(h)} = \frac{1}{2} (|I_+^{(h)}|^2 + |I_-^{(h)}|^2) (g|Z_c|^2 + r) \quad (8-50)$$

This is the power per unit length dissipated by the homogeneous mode. It is possible to extract r and g from (8-47) and (8-48). Results are plotted as functions of frequency in Figure 8.4 for a copper wire of 1 mm radius. This figure yields the curious result that the series resistance in this model is negative, and that $g|Z_c|^2$ cancels r to three orders of magnitude (even though the sum does remain positive, i.e., dissipative).

Our purpose of this exercise is to demonstrate that, while (8-43), (8-44), (8-47) and (8-48) are at least symbolically correct, use of (8-47) and (8-48) for representing the broad-band response of a single-wire transmission line seems unwise. (This is another example of a result one might not anticipate prior to undertaking an examination of the form presented here.) If they are used, one will generate some very curious intermediate values, and if they are subjected to FDTD representation, the negative nature of r at all but the lowest frequencies could lead to numerical instability. The foregoing discussion does not imply it is ever dangerous to use the equations preceding (8-47). (In geometries where more is present than a single wire, doing so may be needlessly difficult, but will not result in error.)

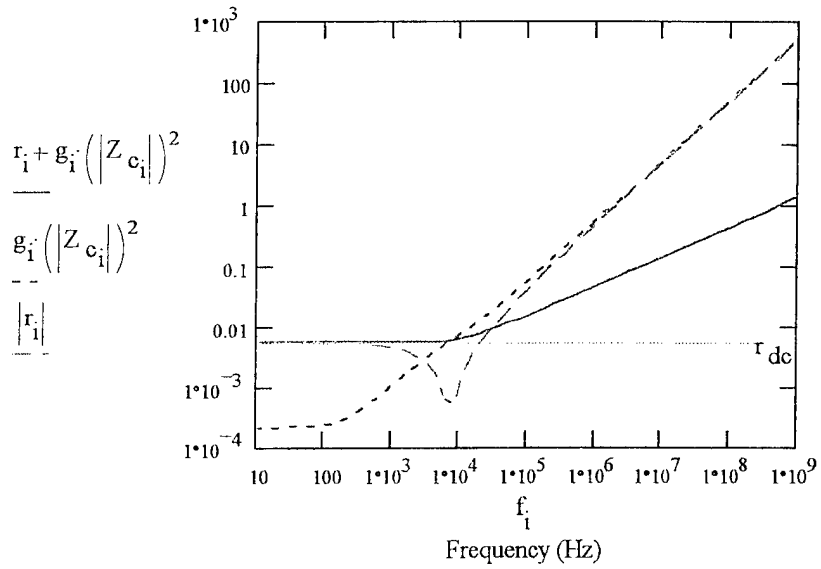


Figure 8.4. The total effective resistance per unit length for the single-conductor (1 mm radius Cu wire) homogeneous mode, broken down into 1) shunt and 2) series portions. This figure demonstrates the probable inappropriateness of using a lumped-parameter series-shunt model for partitioning the dissipation in this case: the model of the series dissipation r changes sign at the 10 kHz notch in the $|r|$ plot.

NUMERICAL COMPARISON WITH A SIMPLER MODEL

In most practical solutions of the wire problem, one works with the inhomogeneous telegrapher's equations

$$\frac{dV^{(p)}}{dz} = -ZI^{(p)} + E_z^i e^{\alpha z} \quad (8-51)$$

$$\frac{dI^{(p)}}{dz} = -YV^{(p)} \quad (8-52)$$

not the exact solution of Maxwell's equations (8-27). These equations may be combined with the useful definitions in (8-46) of the previous section on transmission lines to obtain the telegrapher's solution

$$I = a_1 e^{\gamma z} + a_2 e^{-\gamma z} + \frac{YE_z^i e^{\alpha z}}{\gamma^2 - \alpha^2} \quad (8-53)$$

$$V = -Z_c(a_1 e^{\gamma z} - a_2 e^{-\gamma z}) - \frac{\alpha E_z^i e^{\alpha z}}{\gamma^2 - \alpha^2} \quad (8-54)$$

where the general homogeneous solution has been added to the obviously particular term. In (8-53) and (8-54), γ is taken from the exact solution, (8-14) or Figure 8.1. The undetermined homogeneous solution coefficients a_1 and a_2 are again used to match continuity of current and voltage at each segment of the statistical model. Note that, like (8-38), this simplified telegrapher's model still retains the use of both homogeneous and particular solutions.

It is interesting to see how much the exact solution for I^p/E_z^i as given by (8-27) (see Figure 8.2) differs from the telegrapher's approximation as given by (8-53). Consequently, we have overlaid the result of (8-53) on (8-27) in Figure 8.2. It may be seen that for broadside illumination of a 1 mm radius copper wire, the telegrapher's equation does remarkably well at least up to 1 MHZ, although it does under predict driven current by about 6 dB at 1 GHz. (We consider (8-27) to be more accurate than (8-53) because (8-27) specifically takes into account subtle differences between the driven- and the homogeneous-mode solutions, while (8-53) is a mixture of their properties.)

Our statistical cable network model can be flagged to represent cable segments well-removed from other conductors either by formulas based on (8-53) and (8-54) or on (8-14) and (8-27), although the more exact and preferred selection in this case is the latter. [For cable segments close to a ground plane, however, we shall see that (8-53) and (8-54) become adequate, and are much easier to use.]

INTRODUCTION OF A GROUND PLANE

The last topic we shall consider in the body of this paper is the effect on the particular or driven wire solution of introducing a ground plane. Basically, we now let the driving field consist of 1) the old incident field, E_z^i , 2) the reflection of this field by the ground plane, and 3) an infinite sum of fields scattering between the cable and the ground plane. The idea behind the sum is first finding the scattered fields resulting from a particular solution driven by the incident field and its reflection. The scattered field is then reflected from the ground plane and used to reinforce the wire drive. This results in another scattered field which is then reflected from the ground plane and again used to drive the cable. This process is continued to form the infinite sum of driving/response terms.

The first quantity to find is the ratio of the scattered field to the incident field. Using (8-25) and (8-27), the relations between the scattered field to the wire current, and between the wire current to the incident field, we find the ratio of scattered to incident fields at a center line image separation of $2h$ is

$$\frac{E_{z2}^{(p)}}{E_z^i} = \left[\frac{\mu_1 \kappa_1^{(p)} k_2^2 J_0(\kappa_1^{(p)} a) H_1^{(1)}(\kappa_2^{(p)} a)}{\mu_0 \kappa_2^{(p)} k_1^2 J_0(\kappa_1^{(p)} a) H_0^{(1)}(2h\kappa_2^{(p)})} - \frac{H_0^{(1)}(\kappa_2^{(p)} a)}{H_0^{(1)}(2h\kappa_2^{(p)})} \right]^{-1} = S_c^{(p)} \quad (8-55)$$

The next scattering parameter to determine is the ratio of the incident field to the field first reflected by the ground plane. This is just

$$S_g^{(p)} = RD_g^{(p)} = -e^{j2h\kappa_2^{(p)}} \quad (8-56)$$

which is simply a delay time or phase difference times a -1 reflection coefficient R . Thus, the non-scattered field driving the wire is

$$E_z^{i'} = E_z^i(1 + RD_g^{(p)}) \quad (8-57)$$

The driving field from the second reflection is

$$E_z^{i''} = -E_z^i(1 + RD_g^{(p)})S_c^{(p)} \quad (8-58)$$

and the total field driving the wire is

$$E_z^{(p)tot} = E_z^i(1 + RD_g^{(p)})(1 - S_c^{(p)} + S_c^{(p)2} - S_c^{(p)3} \dots) = E_z^i \frac{(1 + RD_g^{(p)})}{(1 - RS_c^{(p)})} \quad (8-59)$$

Consequently, the net effect on the particular current solution $I^{(p)}$ of adding a ground plane is to replace (8-27) by

$$I^{(p)} = E_0^i \sin \theta_z \cdot \frac{2\pi a}{s} \left(\frac{\mu_0 \kappa_2^{(p)} H_0^{(1)}(\kappa_2^{(p)} a)}{k_2^2 H_1^{(1)}(\kappa_2^{(p)} a)} - \frac{\mu_1 \kappa_1^{(p)} J_0(\kappa_1^{(p)} a)}{k_1^2 J_1(\kappa_1^{(p)} a)} \right)^{-1} \left(\frac{1 + RD_g^{(p)}}{1 - RS_c^{(p)}} \right) \quad (8-60)$$

Figure 8.5 compares $S_c^{(p)}$, $1 + RD_g^{(p)}$ and $(1 + RD_g^{(p)})/(1 - RS_c^{(p)})$ for 1 mm radius copper wire as a function of frequency for the wire 10 cm above the ground plane ($h = .1$).

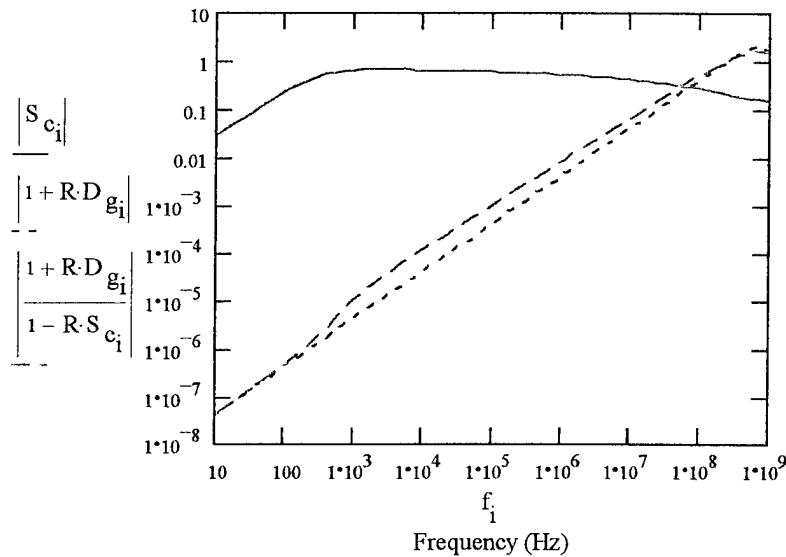


Figure 8.5. The scattering coefficient $S_c^{(p)}$ (8-55), the incident-plus-reflection coefficient $(1 + RD_g^{(p)})$ (8-56), and the overall coefficient of reflection/scattering enhancement $(1 + RD_g^{(p)})/(1 - RS_c^{(p)})$ (8-59), all based on a 1 mm radius copper wire elevated $h = 10$ cm over a ground plane.

More numerical results appear in Figure 8.6, which shows $|(I_0/E_z) \cdot (1 + RD_g^{(p)})|$, the normalized current predicted with the ground-plane reflection added to the exact free-space solution, but with multiple scattering and effects of the ground plane on the exact homogeneous parameters I_0 , $Y = -\gamma/Z_c$, and γ ignored. Also shown in this figure is $|Y(1 + RD_g^{(p)})/(\alpha^2 - \gamma^2)|$, a version of the first curve including the additional approximations of the telegrapher's equations (8-53). (Remember α is zero for broadside illumination, so in this case (8-53) reduces to the fourth of (8-46).) Lastly, this figure presents $|(I_0/E_z) \cdot (1 + RD_g^{(p)})/(1 - RS_c^{(p)})|$, which is the same as the first curve, but with the infinite series of wire/ground-plane scattering terms restored (8-60). All these approximations are plotted as functions of frequency, with I_0 , $Y = -\gamma/Z_c$, and γ all pertaining to the ground-plane-absent case.

For wires close to a ground plane, the statistical cable model we use for each segment is based on the Maxwell-like solution (8-60) or, alternatively, on the simpler telegrapher's solution, (44) and (45). In this situation, (8-47) and (8-48) usually suffice, and application of the more general equations preceding (8-47) is an unnecessary complication. As most wires are near a ground plane or conducting wall, this is a conclusion of major significance. In fact, this is the case where, if the wire elevation h does not exceed $\lambda_0/16$, one can replace l and c in (8-47) and (8-48) by their dc values, $l = \mu_0 \ln[(2h/a)]/(2\pi)$ and $c = 2\pi\epsilon_0/\ln[(2h/a)]$, so that $Z \approx -j\omega l$, $Y \approx -j\omega c$, $\gamma^2 \approx -\omega^2 lc$, and $Z_c \approx (\mu_0/\epsilon_0)^{1/2} \ln[(2h/a)]/(2\pi)$.

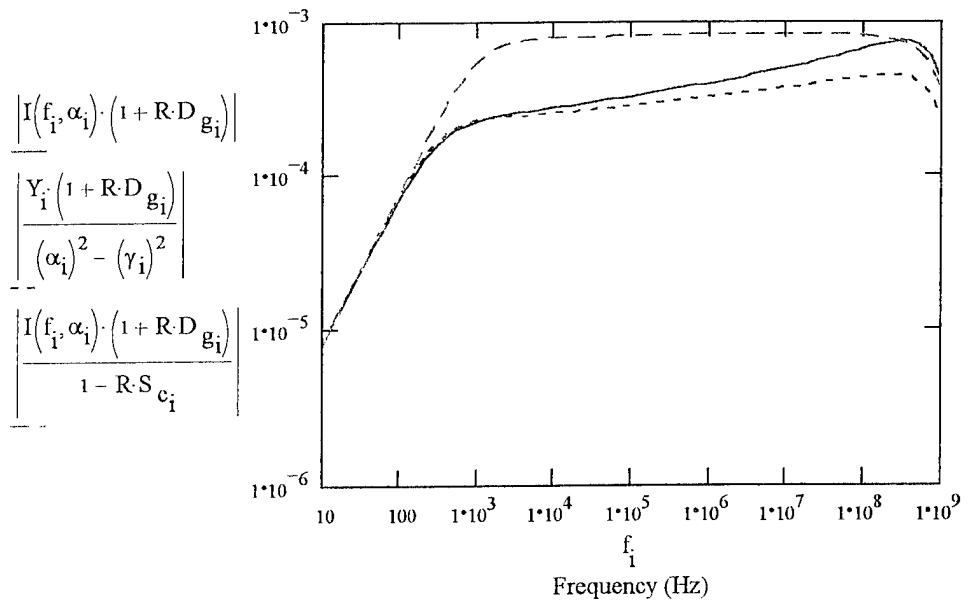


Figure 8.6. Normalized approximate currents for a 1 mm radius Cu wire 10 cm over a ground plane a) based on the exact free-field solution of Maxwell's equations, with the field reinforced by the ground-plane reflection but not by multiple scattering (8-57), b) based on the telegrapher's equations, but otherwise unchanged from a) (8-54), and c) based on the exact free-field solution of Maxwell's equations, with the driving field reinforced by the ground-plane reflection and by multiple scattering (8-60). All curves assume broadside illumination and use the approximation that the ground plane does not alter I_0 , $Y = -\gamma/Z_c$, or γ .

As one would expect, the two curves in Figure 8.6 which ignore multiple scattering start out similarly at low frequency, but gradually diverge as frequency increases and higher-order effects, which the telegrapher's equations do not include, come into play. The curve which does not omit multiple scattering predicts a much higher current until $\lambda_0/4$ starts to drop to the wire elevation. For $\lambda_0/4 \gg h$, the current is effectively induction-limited, and the multiple scattering represents the ground-plane proximity, which tends to reduce the series inductance of the model. The current dropoff below 1 kHz on this curve represents ohmic impedance dominating induction limiting at very low frequencies. In between the two frequency extremes, current is nearly frequency independent because the emf driving the wire increases linearly with ω , but the inductive impedance also increases linearly with ω , and the two effects cancel.

In the approximation that the wire sees the incident field plus that reflected by the ground plane, the power per unit length captured by the wire may be written, with $S_{gp}^{(p)} = 1 + RD_g^{(p)}$

$$P_{in} = \frac{1}{2} \operatorname{Re} \left[E^i S_{gp}^{(p)} \cdot \overline{I(\omega, \alpha) \cdot S_{gp}^{(p)}} \right] \quad (8-61)$$

At equilibrium, neglecting ohmic losses, this must also be the power radiated per unit length by the wire, which we can write as

$$P_{out} = \frac{1}{2} \operatorname{Re} \left[R_{rad} \left(I(\omega, \alpha) \cdot S_{gp}^{(p)} \right) \cdot \overline{\left(I(\omega, \alpha) \cdot S_{gp}^{(p)} \right)} \right] \quad (8-62)$$

where R_{rad} is identifiable as the radiation resistance. A similar pair of equations can be written with the infinite series of reflections included. This is obtained merely by substituting $S_{tot}^{(p)}$ for $S_{gp}^{(p)}$ where $S_{tot}^{(p)}$ is the fraction in (8-59)

$$S_{tot}^{(p)} = \frac{(1 + RD_g^{(p)})}{(1 - RS_c^{(p)})} \quad (8-63)$$

Figure 8.7 illustrates the radiation resistance for a copper wire of 1 mm radius under these two approximations.

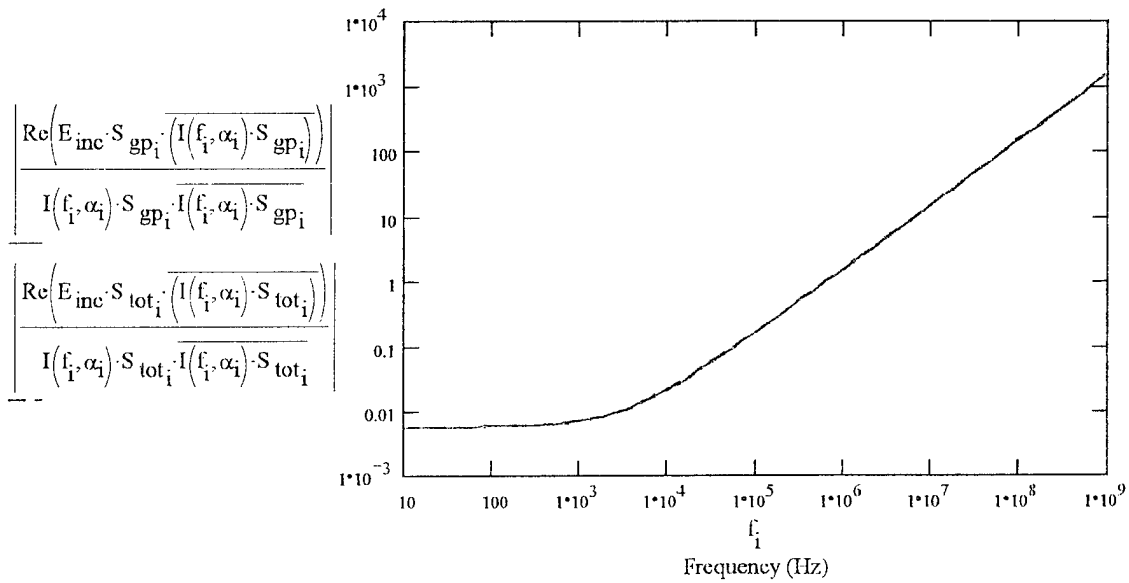


Figure 8.7. The radiation plus ohmic resistance for a 1 mm radius Cu wire 10 cm over a ground plane. It appears that, with our definition of radiation resistance, its value is invariant to the inclusion of zero (see Figure 8.4), one, or an infinity of reflections. One might interpret this to mean the radiation resistance does not depend on wire height over the ground plane. In a sense this is not surprising, since a wire close to a ground plane, which a field cannot couple effectively to, also cannot radiate effectively. However, this conclusion certainly is at variance with (3-19).

For wires close to a ground plane, the more accurate, Maxwell-like statistical cable model we use for each segment is based on (8-60). There can be, however, a physical problem with (8-60). In particular, as the separation h between the cable and the ground plane increases, it is necessary for the field to return to the free-space result. To enable this, a coefficient [see (3-16)]

$$\xi = \left(\frac{4\pi h}{\lambda} \right)^2 \quad (8-64)$$

is defined to enable taking a linear combination of the reflective and free-space solutions

$$T = \frac{\frac{1 + RD_d^{(p)}}{1 - RS_c^{(p)}} + \xi}{1 + \xi} \quad (8-65)$$

Then, the net effect on the particular current solution $I^{(p)}$ of adding a ground plane is to replace (8-27) by

$$I^{(p)} = E_0^i \sin \theta_z \cdot \frac{2\pi a}{s} \left(\frac{\mu_0 \kappa_2^{(p)} H_0^{(1)}(\kappa_2^{(p)} a)}{k_2^2 H_1^{(1)}(\kappa_2^{(p)} a)} - \frac{\mu_1 \kappa_1^{(p)} J_0(\kappa_1^{(p)} a)}{k_1^2 J_1(\kappa_1^{(p)} a)} \right)^{-1} \cdot T \quad (8-66)$$

instead of (8-60).

HOMOGENEOUS WAVENUMBER $\gamma(\omega)$ FOR A WIRE OVER A GROUND PLANE

At the time this work was performed, we had not investigated the exact solution of $\gamma(\omega)$ for the homogeneous current on a wire above a ground plane. Where $\gamma(\omega)$ was required, we approximated it with the ground-plane-absent result [(8-14) or Figure 8.1)]. Subsequently to the actual performance of this work, we deduced a technique which should lead to the exact $\gamma(\omega)$, although numerical implementation of this technique has not been performed.

In particular, this problem has a solution which is obtainable in analogy with the inhomogeneous, multiple-scattering approach. The wire will initially radiate (reactively in the near-field) in accordance with (8-13), thus giving a first-reflection coefficient of

$$S_g^{(h)} = RD_g^{(h)} = - \frac{H_0^{(1)}(2h\kappa_2^{(h)})}{H_0^{(1)}(\kappa_2^{(h)}a)} \quad (8-67)$$

instead of (8-56). Consequently, the non-scattered field at the surface of the wire, in the presence of a ground plane, will be

$$E_{z2}^{(h)'} = E_{z2}^{(h)}(a)(1 + RD_g^{(h)}) \quad (8-68)$$

This field will then lead to an infinite series of scattering terms, each term constituting a member of a power series in $RS_c^{(h)}$, where $S_c^{(h)}$ is given by (8-55) with $\gamma(\omega)$ replacing α ; i.e., $\kappa_{1,2}^{(h)}$ replacing $\kappa_{1,2}^{(p)}$. In other words, after the first scattering, we have

$$E_{z2}^{(h)''} = E_{z2}^{(h)}(a)(1 + RD_g^{(h)})(1 + RS_c^{(h)}) \quad (8-69)$$

where

$$S_c^{(h)} = \left[\frac{\mu_1 \kappa_1^{(h)} k_2^2 J_0(\kappa_1^{(h)}a) H_1^{(1)}(\kappa_2^{(h)}a)}{\mu_0 \kappa_2^{(h)} k_1^2 J_0(\kappa_1^{(h)}a) H_0^{(1)}(2h\kappa_2^{(h)})} - \frac{H_0^{(1)}(\kappa_2^{(h)}a)}{H_0^{(1)}(2h\kappa_2^{(h)})} \right]^{-1} \quad (8-70)$$

After all the infinite series of scattering has occurred, we shall have

$$E_{z2}^{(h) tot} = E_{z2}^{(h)}(a) \frac{(1 + RD_g^{(h)})}{(1 - RS_c^{(h)})} = E_{z2}^{(h)}(a) S_{tot}^{(h)} \quad (8-71)$$

Consequently, the free-space equation for $\gamma(\omega)$ (8-14) is replaced in the presence of a ground plane by

$$\frac{\mu_1 \kappa_1^{(h)}}{k_1^2} \frac{J_0(\kappa_1^{(h)}a)}{J_1(\kappa_1^{(h)}a)} = \frac{\mu_0 \kappa_2^{(h)}}{k_2^2} \frac{H_0^{(1)}(\kappa_2^{(h)}a)}{H_1^{(1)}(\kappa_2^{(h)}a)} \cdot \frac{(1 + RD_g^{(h)})}{(1 - RS_c^{(h)})} \quad (8-72)$$

where $S_g^{(h)}$ is given by (8-67) and $S_c^{(h)}$ is given by (8-70). At present, resources have not been allocated to solve (8-6) and (8-72) for $\gamma(\omega)$ in the presence of a ground plane.

SUMMARY OF DRIVER OPTIONS

The simplest expression for the driven current response is obtained from the frequency-invariant transmission-line model/solution of (8-51) - (8-54),

$$I^{(p)} = \frac{YE_z^i e^{\alpha z}}{\gamma^2 - \alpha^2} \quad (8-73)$$

This expression is normally adequate for cables close to a ground plane. The next level of cable-driver sophistication, which should be used when a cable is not close to other conductors, comes from modeling the fields around the cable as cylindrical harmonics [(8-26) and (8-27)] and applying the driven-cable boundary condition

$$E_z^{\text{wire}} = E_z^{\text{air}} + E_z^{\text{inc}} \quad (8-74)$$

This boundary condition results in the driven-current formula

$$I^{(p)} = E_z^i \frac{2\pi\alpha}{s} \left(\frac{\mu_0 \kappa_2^{(p)} H_0^{(1)}(\kappa_2^{(p)} a)}{k_2^2 H_1^{(1)}(\kappa_2^{(p)} a)} - \frac{\mu_1 \kappa_1^{(p)} J_0(\kappa_1^{(p)} a)}{k_1^2 J_1(\kappa_1^{(p)} a)} \right)^{-1} \quad (8-75)$$

For a cable h above a ground plane, E_z^i is replaced by $(1 + S_g^{(h)})E_z^i$ (8-56), where

$$S_g^{(p)} = RD_g^{(p)} = -e^{j2h\kappa_2^{(p)}} \quad (8-76)$$

represents a delayed reflection off the plane. Thus, assuming normal incidence on the ground plane, the next level of sophistication for the driven current is (8-58)

$$I^{(p)} = E_z^i \frac{2\pi\alpha}{s} \left(\frac{\mu_0 \kappa_2^{(p)} H_0^{(1)}(\kappa_2^{(p)} a)}{k_2^2 H_1^{(1)}(\kappa_2^{(p)} a)} - \frac{\mu_1 \kappa_1^{(p)} J_0(\kappa_1^{(p)} a)}{k_1^2 J_1(\kappa_1^{(p)} a)} \right)^{-1} (1 + RD_g^{(p)}) \quad (8-77)$$

The fourth model of cable drive on a wire over a ground plane can be approximated as the response of a wire in free space driven by 1) an incident field plus, 2) a reflection of the incident field from the ground plane, and plus 3) an infinite sum of fields scattering between the cable and the ground plane (8-60)

$$I^{(p)} = E_z^i \frac{2\pi\alpha}{s} \left(\frac{\mu_0 \kappa_2^{(p)} H_0^{(1)}(\kappa_2^{(p)} a)}{k_2^2 H_1^{(1)}(\kappa_2^{(p)} a)} - \frac{\mu_1 \kappa_1^{(p)} J_0(\kappa_1^{(p)} a)}{k_1^2 J_1(\kappa_1^{(p)} a)} \right)^{-1} \left(\frac{1 + RD_g^{(p)}}{1 - RS_c^{(p)}} \right) \quad (8-78)$$

where h is the distance of the cable above the ground plane. The fifth, and most sophisticated, model of cable drive on a wire over a ground plane includes the transition parameter ξ of (8-61), which permits construction of a “unified field theory” asymptoting to the fourth model if the wire elevation is not great compared to a wavelength, but alternatively asymptoting smoothly to the free-space model (8-27) if the wire elevation is great

$$I^{(p)} = E_0^i \sin \theta_z \cdot \frac{2\pi a}{s} \left(\frac{\mu_0 \kappa_2^{(p)} H_0^{(1)}(\kappa_2^{(p)} a)}{k_2^2 H_1^{(1)}(\kappa_2^{(p)} a)} - \frac{\mu_1 \kappa_1^{(p)} J_0(\kappa_1^{(p)} a)}{k_1^2 J_1(\kappa_1^{(p)} a)} \right)^{-1} \cdot T \quad (8-79)$$

In most problems, it is unnecessary to use the three most sophisticated models, although their application will only endanger one's computer budget.

SECTION SUMMARY

We have demonstrated that a wire illuminated in free space by a plane wave supports a current which separates into a driven and a homogeneous mode. The homogeneous mode does not have a radiation resistance, at least where the wire is uniform, and is excited only at wire bends, terminations, other wire inhomogeneities, or field nonuniformities. We have worked out the dispersion relation for the homogeneous solution and the coupling relation for the driven solution in the free field case. The driven solution involves so much radiation resistance that it only propagates termination effects two or three wavelengths. The homogeneous solution for an infinite wire in free space can only exist if the wire is not perfectly conducting. Our analysis has also been extended to a wire over a ground plane, except that we have not actually evaluated the transcendental equation numerically for the homogeneous dispersion relationship. Several approximations, including the telegrapher's equations, are numerically compared with the exact solution of Maxwell's equations. For wires close to a ground plane, telegrapher's equations solutions prove to be a reasonable model. For wires well removed from a ground plane, it is better to employ the solution derived more directly from Maxwell's equations. We also demonstrate (in Appendix 8A) that certain definitions of the quality factor Q , based on rate of energy dissipation of a resonator or resonant system, can lead to incorrect interpretations for the manner in which system energy transiently builds up during turn-on.

APPENDIX 8A. ENERGY BUILDUP AND THE MEANING OF Q

One definition of the quality factor in a resonant system is

$$Q = \omega_0 \cdot \frac{\text{(time-average energy stored inside a system)}}{\text{(energy loss rate of system)}} \quad (8A-1)$$

This statement can be expressed as the differential rate equation

$$\frac{dE_{av}}{dt} = - \frac{\omega_0}{Q} E_{av} \quad (8A-2)$$

Thus, if a system has been driven to the point where it contains energy $E_{av,0}$, and the drive is suddenly switched off, energy content will decay as

$$E_{av} = E_{av,0} e^{-\omega_0 t/Q} \quad (8A-3)$$

where ω_0 is the system's natural frequency. This result is correct. However, there is a strong implication from (8A-2) that, if $E_{av,0}$ is the equilibrium sinusoidal steady-state average system energy, upon turning on the drive, energy will build up as

$$E_{av} = E_{av,0} (1 - e^{-\omega_0 t/Q}) \quad (8A-4)$$

This equation, or at least (8A-2), its rate-equation equivalent, often appears in literature.[4]

However, (8A-4) cannot be correct: it indicates that, just after turn-on of the drive, power input is nonzero. Actually, (8-36) indicates that the drive (E_z^i in this case) does not input energy until the response (I^p in this case) has started to build up.

In order to obtain a more correct interpretation of Q and power build-up, let us consider the telegrapher's equations on a transmission line consisting of a length of wire over a ground plane. In the time domain, we have, in analogy with (8-43) - (8-50),

$$\frac{\partial V}{\partial z} = -l \frac{\partial I}{\partial t} + E_z^i(z) \quad (8A-5)$$

$$\frac{\partial I}{\partial z} = -c \frac{\partial V}{\partial t} \quad (8A-6)$$

where l and c are the complex inductance and capacitance per unit length of the wire with respect to the ground plane,

$$l = l' + jl'' \quad c = c' + jc'' \quad (8A-7)$$

These relationships can be combined to give, in sinusoidal steady state,

$$\frac{d^2 I}{dz^2} + lc\omega^2 I = j\omega c E_z^i(z) \quad (8A-8)$$

If the line is shorted to the ground plane at both ends, $z = 0$ and d , the eigenmodes, defined in the absence of loss, obey

$$\frac{d^2 I_n}{dz^2} + l' c' \omega_n'^2 I_n = 0 \quad \frac{dI_n}{dz} = 0 \text{ at } z = 0, d \quad (8A-9)$$

and are given by

$$I_n = \sqrt{\frac{2}{dl'}} \cos \frac{n\pi z}{d} \quad (8A-10)$$

These eigenmodes are orthonormal within a factor of $1/l'$ (self- and cross-terms integrate to δ_{mn}/l') on the wire, and have pure real resonant frequencies

$$\omega_n' = \frac{n\pi v'}{d} = \omega_{nR} \quad (8A-11)$$

where v' is the propagation velocity of the line with loss omitted, $v' = 1/(l' c)^{1/2}$.

If one expands the solution of (8A-8) in terms of the eigenmode functions,

$$I(z) = \sum_{n=1}^{\infty} B_n I_n(z) \quad (8A-12)$$

one finds the eigenmode coefficients to be

$$B_n = \frac{j\omega}{\omega^2 - \omega_n'^2} \int_0^d E(z) I_n(z) dz = \frac{j\omega F_n}{\omega^2 - \omega_n'^2} \quad (8A-13)$$

with this equation also defining F_n .

The correct way of reintroducing loss into (8A-13), so B_n does not actually go to infinity at resonance, is to replace $\omega^2 - \omega_n'^2$ with

$$\omega^2 - \omega_n'^2 \rightarrow (\omega + j\omega_{nL}^2) - \omega_{nR}^2 \quad (8A-14)$$

where

$$\omega_n^2 = (\omega_{nR} - j\omega_{nL})^2 = \frac{n^2 \pi^2}{d^2 (l' + j l'') c'} \quad (8A-15)$$

and where, in the interest of simplicity, we have assumed all losses are associated with the line inductance. The exact rational for the form of (8A-14) is a bit arcane, and outside the scope of our present objective. It involves considerations like the symmetry of l and c' with respect to ω , the anti-symmetry of l'' and c'' (l and l'' are Hilbert transform pairs, as are c' and c''), and especially the requirement that B_n always have both poles in the lower half-plane of ω space.[12]

Equation (8A-15) can be manipulated to show

$$Q_n = \frac{\omega_{nR}}{2\omega_{nI}} = \frac{l'}{l''} \quad (8A-16)$$

(This equation uses the definition that Q_n is the center frequency of a resonance divided by the bandwidth between the two 45° points:

$$Q_n = \frac{\omega_{nR}}{\Delta\omega_{45^\circ}} \quad (8A-17)$$

Equation (8A-17) actually proves to be a much less confusing definition of Q than (8A-1).)

The average electrical energy on the wire can be partitioned between modes as

$$E_e = \frac{1}{4} \int_0^d c' |V|^2 dz = \frac{1}{4} \int_0^d c' \left| \frac{1}{\omega c} \frac{dI}{dz} \right|^2 dz = \frac{1}{4} \sum_n \frac{\omega_n'^2}{\omega^2} |B_n|^2 \quad (8A-18)$$

The average magnetic energy can be similarly partitioned as

$$E_m = \frac{1}{4} \int_0^d l' |I|^2 dz = \frac{1}{4} \sum_n |B_n|^2 \quad (8A-19)$$

At resonance ω_n' , these two average energies are equal.

The power dissipation (which must equal the input power) can also be partitioned between modes

$$\begin{aligned} P_d &= \frac{1}{2} \operatorname{Re} \left[\int_0^d E_z^i(z) I(z)^* dz \right] = \frac{1}{2} \operatorname{Re} \left[\int_0^d E_z^i(z) \sum_n B_n^* I_n(z) dz \right] \\ &= \frac{\omega_{nR}}{2} \frac{l''}{l'} \sum_n |B_n|^2 = \frac{\omega_{nR}}{2Q_n} \sum_n |B_n|^2 \end{aligned} \quad (8A-20)$$

Equations (8A-18) - (8A-20) are clearly equivalent to (8A-1) for each mode's Q .

If we recall F_n from (8A-13), a lengthy, but ordinary, transient analysis of the telegrapher's equations (8A-5)-(8A-6) shows,[12] for drive at resonance, $\omega = \omega_{nR}$, that current on the wire builds up as

$$I(t, z) = \sum_{n=1}^{\infty} F_n I_n(z) \frac{Q_n}{\omega_{nR}} \cos \omega_{nR} t (1 - e^{-\omega_{nR} t}) \quad (8A-21)$$

Thus, magnetic (and total) energy on the wire builds up as $|I(t, z)|^2$. From (8A-21) we see this form has a

$$(1 - e^{-\omega_{nR} t})^2 = (1 - e^{-\omega_{nR} t/(2Q_n)})^2 = 1 - 2e^{-\omega_{nR} t/(2Q_n)} + e^{-\omega_{nR} t/Q_n} \quad (8A-22)$$

temporal dependence, as opposed to $(1 - e^{-\omega_{nR} t/Q_n})$. While this factor starts at 0 and ends at 1, like the factor in (8A-4), it initially has the correct zero energy derivative (zero power input) which (8A-4) does not. Perhaps as it must, however, (8A-2) does lead to the correct description of energy decay as previously indicated; transient analysis of the telegrapher's equations does indicate power decay characterized by $e^{-\omega_{nR} t/Q_n}$, as expressed in (8A-3).

REFERENCES

- [1]. R. Holland and R. St. John, "Statistical Description of Cable Current Response Inside a Leaky Enclosure," *Conference Proceedings*, Vol. II, pp. 1077-1085, 13th Annual Review of Progress in Applied Computational Electromagnetics, Monterey, CA, 17-21 March 1997.
- [2]. R. Holland and R St. John, "Statistical Coupling of EM Fields to Cables in an Overmoded Cavity," *Conference Proceedings*, Vol. II, pp. 877-887, 12th Annual Review of Progress in Applied Computational Electromagnetics, Monterey, CA, 18-22 March 1996.
- [3]. S. A. Schelkunoff, *Antenna Theory and Practice*, New York: John Wiley, pp.218-253, 1952.
- [4]. R. H. Price, H. T. Davis, and E. P. Wenaas, "Determination of the statistical distribution of electromagnetic-field amplitudes in complex cavities," *Phys. Rev. E*, vol. 48(8), pp. 4716-4729, December 1993.
- [5]. J. A. Stratton, *Electromagnetic Theory*, New York: McGraw-Hill, pp. 524-528, 1941.
- [6]. A. Sommerfeld, in *Differentialgleichungen der Physik*, vol. II, 7th ed., B. Riemann and H. Weber, editors, Verveg, pp. 461 and 507-511, 1927.

- [7]. G. Goubau, "Single conductor surface wave transmission lines," *Proc IRE*, vol. 39, pp. 619-624, June 1951.
- [8]. A. Sommerfeld, "Partial Differential Equations in Physics," *Lectures on Theoretical Physics*, vol. 6, New York: Academic Press, pp.246-257, 1964.
- [9]. J. Zenneck, *Ann. Physik*, vol. 23, p. 846; also *Lehrbuch der Drahtlosen Telegraphie*, 4th ed., Stuttgart: Ferdinand Enke, 1916.
- [10]. E. F. Vance, "Electromagnetic-pulse handbook for electric power systems," Defense Nuclear Agency, DNA-3466F Washington, DC., p. 187, 4 February 1975.
- [11]. W. J. Karzas, "Back door coupling of RF (microwave) energy to spacecraft interior cabling," Phillips Laboratory Technical Report, PL-TR-95-0475, Kirtland AFB, NM, June 1995.
- [12]. R. Holland, "RF cavity response: data acquisition and circuit analysis," Shield Rite Report 0045-14, Albuquerque, NM, 25 August 1996.

Chapter 9. STATISTICAL DISTRIBUTION OF FIELDS IN COMPLEX CAVITIES: THE JAYCOR MYSTIQUE

In 1988, Price *et al* from JAYCOR released a corporate report on the statistical distribution of electromagnetic fields within a complex cavity.[1] In 1993, a somewhat revised version of this work appeared in the open literature.[2]

We have found the style and form of this work, in both versions, to be extremely difficult to follow. Also, both versions of this work contain some peculiar definitions, notational and units conventions, assumptions of dubious validity, and outright errors. It is the intent of this section to provide a more readable presentation of the earlier work with the above difficulties pointed out and, where possible, mitigated.

The present document is not prepared as an indictment of the earlier study, which we believe is actually the first really fresh look at EM hazards in a generation. (We would not trouble ourselves criticizing and revising someone else's work unless we found it intrinsically outstanding.) Rather, it is our hope in this section to clarify the earlier document, so that, in the future, neither we nor others have so much trouble comprehending its message. This seems important to us, as the concepts developed by Price, *et al.*, are as fundamental to SEM as the classic Yee article is to FDTD.[3]

SPECIFIC MODE DENSITY

The Price, *et al.*, report (Eq. 1) begins with a formula for EM mode density associated with blackbody (Bosé-Einstein) statistics. In particular, let us assume we have a cubic cavity l on a side. At frequency v , there can be $2vl/c$ standing half-waves along each edge. If the structure were one-dimensional, this is the number of modes which could exist at frequencies of v and below.

In 3D, there can be up to $(2vl/c)$ standing half-waves along each edge. Thus, the number of modes here permitted with frequency below v corresponds to the volume of a sphere with radius $(2vl/c)$, except that only the eighth of the sphere where v is positive along all axes pertains:

$$N(v) = \frac{1}{8} \left(\frac{2vl}{c} \right)^3 \cdot \frac{4\pi}{3} \cdot 2 \quad (9-1)$$

where the factor of 2 is added to account for the two possible polarizations. The mode density is

$$\frac{dN(v)}{dv} = \frac{8\pi}{c^3} v^2 V \quad (9-2)$$

where we have replaced l^3 by the cavity volume V so the result is not restricted to cubic cavities.

A general conventional definition for Q of a resonant system is

$$Q = \omega \cdot \frac{\text{(time-average energy stored in system)}}{\text{energy loss rate in system}} \quad (9-3)$$

The Price, *et al.*, definition of Q appears, in a few instances to be half this conventional definition.

If a series RLC circuit is driven by a voltage source V , the current will be

$$I = V/Z_{in} \quad (9-4)$$

where

$$Z_{in} = R + j\omega L + \frac{1}{j\omega C} \quad (9-5)$$

For such a circuit we have, at resonance, the time-average stored energy as

$$U_m = \frac{1}{4}II^*L = U_e = \frac{1}{4}CV_C V_C^* = U/2 \quad (9-6)$$

and the power dissipation as

$$P_d = \frac{1}{2}II^*R \quad (9-7)$$

Thus, we find at resonance, ω_0

$$Q = \frac{\omega_0 L}{R} = \frac{1}{R\omega_0 C} \quad (9-8)$$

Also, the maximum current will flow at resonance,

$$I_{\max} = V/R \quad (9-9)$$

and the maximum power will dissipate at resonance

$$P_{\max} = \frac{1}{2}VV^*/R \quad (9-10)$$

At some frequency $\Delta\omega$ removed from resonance, the current will be

$$I = \frac{V/R}{1 + j2Q(\Delta\omega/\omega_0)} \quad (9-11)$$

The $\Delta\omega$ at which I and V are separated by 45° is the same $\Delta\omega$ at which the power dissipation drops by $\frac{1}{2}$:

$$\frac{\Delta\omega}{\omega_0} = \frac{1}{2Q} \quad (9-12)$$

This is the normal definition of the bandwidth of a resonant system.

Price, *et al.*, use a definition of bandwidth which appears different:

$$\frac{\Delta v_J}{v_0} = \frac{1}{Q_J} \quad (9-13)$$

Thus, their resonance bandwidth seemingly differs from the conventional usage by a factor of 2. Actually, their Δv_J is the full bandwidth between 45° points, while $\Delta\omega$ of (9-12) is a single sideband. Thus, there is actually no physical inconsistency, and we shall hereafter drop the J subscript on Δv .

The number of modes excited inside a cavity by a monochromatic excitation is

$$\frac{dN(v)}{dv} \cdot \Delta v = N_s = \frac{8\pi v^2 V}{c^3} \Delta V = \frac{8\pi V}{\lambda^3 Q} \quad (9-14)$$

according to the Price, *et al.*, convention. This number is dubbed the specific mode density. We realize this is a sort of qualitative factor, and wish to point out more than criticize the fact that it may have a factor of two vagueness.

MEASURED POWER IN AN OVERMODED CAVITY

We assume the fields in the cavity can be represented as a summation over the eigenmodes (no static fields)

$$\begin{aligned} \mathbf{B}(\mathbf{r},t) &= \sum_i \mathbf{B}_i(\mathbf{r},t) \\ \mathbf{E}(\mathbf{r},t) &= \sum_i \mathbf{E}_i(\mathbf{r},t) \end{aligned} \quad (9-15)$$

This is fine, but the Price, *et al.*, presentation next expands \mathbf{B}_i and \mathbf{E}_i into five factors

$$\begin{aligned} \mathbf{B}_i(\mathbf{r},t) &= B_{0i} \hat{\mathbf{b}}_i(\mathbf{r}) g_i(\mathbf{r}) f_i(\mathbf{r}) \sin(\omega t + \phi_i) \\ \mathbf{E}_i(\mathbf{r},t) &= E_{0i} \hat{\mathbf{e}}_i(\mathbf{r}) g_i(\mathbf{r}) h_i(\mathbf{r}) \cos(\omega t + \phi_i) \end{aligned} \quad (9-16)$$

Price, *et al.*, work with the \mathbf{B} - field expansion exclusively. The coefficient B_{0i} is the amplitude of mode I when this mode is normalized so that the total energy in mode I in the cavity is

$$U_i = \frac{B_{0i}^2 V}{8\pi} \quad (9-17)$$

using JAYCOR units (watts per square cm, etc.). We personally choose to use MKS units, in which case the analog of (9-17) is

$$U_i = \frac{B_{0i}^2 V}{2\mu_0} \quad (9-18)$$

where μ_0 is $4\pi \times 10^{-7}$ H/m. This means that, when ever we pop up a μ_0 , the JAYCOR notation would imply a 4π .

While correct, there is a subtlety in (9-17) or (9-18) which may not be deliberate. The actual magnetic energy associated with mode I is

$$U_m = \frac{B_{0i}^2 V}{4\mu_0} \quad (9-19)$$

but this quantity gets doubled upon addition of the electric energy. Some of the Price, *et al.*, phraseology implies that they may have missed this point. For instance, they refer to B_{0i} as the scalar amplitude of the magnetic field of mode i averaged over the cavity. We think that associating B_{0i} with the magnetic field, not the total electromagnetic time-average energy density is, at best, misleading. Note again that equations containing B_{0i} will differ from MKS to JAYCOR units. We shall try to mitigate this confusion by showing both forms of such equations.

The second factor, $\hat{\mathbf{b}}_i(\mathbf{r})$ is a unit vector pointing everywhere along $\mathbf{B}(\mathbf{r})$ of mode i . Price, *et al.*, next attempt to partition the expansion into a slowly varying spatial distribution $g_i(\mathbf{r})$ and a rapidly varying part of the spatial distribution $f_i(\mathbf{r})$. They eventually set $g_i(\mathbf{r})$ to 1, claiming physical grounds. The product $f_i(\mathbf{r}) g_i(\mathbf{r})$ has meaning in the work of Price, *et al.*, but the factoring is not of apparent purpose.

To elaborate, Price, *et al.*, defines $g_i(\mathbf{r})$ to be the amplitude of $B_i(\mathbf{r}, t)$ averaged over time and the "phase volume"

$$g_i(\mathbf{r}) = \left[\frac{2}{B_{0i}^2 V_{ph}(\mathbf{r})} \int_{V_{ph}(\mathbf{r})} \overline{B_i(\mathbf{r}', t)^2} d\mathbf{r}' \right]^{\frac{1}{2}} \quad (9-20)$$

where $V_{ph}(\mathbf{r})$ is defined to be a sphere of radius of $\lambda/2$ centered at \mathbf{r}' . We cannot imagine where this definition came from or why: It is never explicitly used. The Price, *et al.*, papers also systematically omit the $V_{ph}(\mathbf{r})$ term in the denominator of (9-20) and all following equations in their development. Unless detected, this omission causes the reader all sorts of dimensionality disagreements.

The remaining rapid variation $f_i(\mathbf{r})$ can be evaluated from other quantities as

$$B_i(\mathbf{r}, t) = \mathbf{b}_i(\mathbf{r}) \cdot \overline{[B_{0i} \mathbf{b}_i(\mathbf{r}) g_i(\mathbf{r}) f_i(\mathbf{r}) \sin(\omega t + \Phi_i)]} = B_{0i} g_i(\mathbf{r}) f_i \quad (9-21)$$

or

$$f_i(\mathbf{r}) = \frac{2 \mathbf{b}_i(\mathbf{r}) \cdot \overline{B_i(\mathbf{r}, t)}}{B_{0i} g_i(\mathbf{r})} \quad (9-22)$$

where a bar over a quantity here actually implies taking a mean square over the temporal dependence ($\overline{\sin(\omega t + \Phi_i)} \rightarrow \frac{1}{2}$), not taking a true average as stated repeatedly) in the Price, *et al.*, work.

PROPERTIES OF THE EIGENFUNCTION COMPONENTS

This section of the Price, *et al.*, work is especially sloppy, largely because the error in (9-20) is allowed to propagate. It will be true that the eigenmodes are orthogonal,

$$\int_V (\mathbf{b}_i g_i f_i) \cdot (\mathbf{b}_k g_k f_k) B_{0i} B_{0k} d\mathbf{r} = 2 U_i \mu_0 \delta_{ik} = B_{0i}^2 V \delta_{ik} \quad (9-23)$$

as Price, *et al.*, claim. However, their other integral in this section have problems. For instance, we find from our corrected version of (9-20) that

$$\int_V g_i^2(\mathbf{r}) d\mathbf{r}' = \frac{2}{B_{0i}^2} \int_V \frac{d\mathbf{r}}{V_{ph}(\mathbf{r})} \int_{V_{ph}(\mathbf{r})} \overline{B_i(\mathbf{r}', t)^2} d\mathbf{r}' =$$

$$2 \int_V \frac{d\mathbf{r}}{V_{ph}(\mathbf{r})} \int_{V_{ph}(\mathbf{r})} g_i(\mathbf{r}')^2 f_i(\mathbf{r}')^2 \overline{\sin(\omega t + \phi_i)^2} d\mathbf{r}' = \int_V \frac{d\mathbf{r}}{V_{ph}(\mathbf{r})} \int_{V_{ph}(\mathbf{r})} g_i(\mathbf{r}')^2 f_i(\mathbf{r}')^2 d\mathbf{r}' \quad (9-24)$$

(Note that here the bar genuinely implies taking an average over time.)

It is conceivably possible to take the slowly varying $g_i(\mathbf{r})^2$ factor across the integral over the phase volume, resulting in

$$\int_V g_i^2(\mathbf{r}) d\mathbf{r} = \int_V \frac{g_i^2(\mathbf{r})}{V_{ph}(\mathbf{r})} d\mathbf{r} \int_{V_{ph}(\mathbf{r})} f_i^2(\mathbf{r}') d\mathbf{r}' \quad (9-25)$$

or

$$\frac{1}{V_{ph}(\mathbf{r})} \int_{V_{ph}(\mathbf{r})} f_i^2(\mathbf{r}') d\mathbf{r}' = 1 \quad (9-26)$$

Price, *et al.*, again omit the $V_{ph}(\mathbf{r})$ term in their denominator of (9-26), thus causing the reader even more confusion. If (9-25) and (9-26) are valid, use of (9-23) forces the other result of this section in the Price, *et al.*, papers to be

$$\int_V g_i^2(\mathbf{r}) d\mathbf{r} = V \quad (9-27)$$

In the JAYCOR work, (9-26) and (9-27) are pretty much pontificated, with no mention that they cannot be true without basing them on (9-23)-(9-25) [although (9-23)-(9-25) do not guarantee the validity of (9-26) and (9-27)].

Let us now assume we have a \vec{B} sensor with physical area a_j at point \mathbf{r}_j . Let \mathbf{a}_j point along the direction of the sensor's greatest sensitivity. We can thus express \mathbf{a}_j as

$$\mathbf{a}_j = \hat{\mathbf{a}}_j a_j \delta(\mathbf{r} - \mathbf{r}_j) \quad (9-28)$$

where, $\hat{\mathbf{a}}_j$ is a unit vector aligned with \mathbf{a}_j . The voltage picked up is thus

$$V_j = \omega \mathbf{a}_j \cdot \mathbf{B}(\mathbf{r}_j, t) \quad (9-29)$$

and the power picked up by a square law detector of load impedance R is

$$P_j = \omega^2 \overline{(\mathbf{a}_j \cdot \mathbf{B}(\mathbf{r}_j, t))^2} / R \quad (9-30)$$

In the future, we shall denote $\mathbf{B}(\mathbf{r}_j, t)$ as \mathbf{B}_j . A similar convention shall be applied to other quantities evaluated at \mathbf{r}_j .

Let S be the power flux in the cavity as projected on \mathbf{a}_j . Then the sensor's free-field cross-section is σ_j , where

$$S_j \sigma_j = \overline{(\mathbf{a}_j \cdot \mathbf{B}_j)^2} \omega^2 / R = P_j \quad (9-31)$$

Moreover, S must obey, from conservation of power,

$$S_j = \frac{1}{2} B_j^2 c / \mu_0 \quad (9-32)$$

[The fraction in (9-32) could arguably claimed to be 1/3 or 1/6, as all the energy is not propagating along $\pm \mathbf{a}_j$.] We thus obtain

$$\sigma_j = \frac{\overline{(\mathbf{a}_j \cdot \mathbf{B}_j)^2} \omega^2}{R} \cdot \frac{2\mu_0}{B_j^2 c} \approx \frac{a_j^2 \omega^2 \mu_0}{Rc} \quad (9-33)$$

or

$$P_j = \frac{\overline{(\mathbf{a}_j \cdot \mathbf{B}_j)^2} \omega^2}{R} \cdot \frac{Rc \sigma_j}{a_j^2 \omega^2 \mu_0} = \frac{\overline{(\hat{\mathbf{a}}_j \cdot \mathbf{B}_j)^2}}{\mu_0} \frac{\sigma_j c}{\mu_0} \quad (9-34)$$

The JAYCOR units equivalent of (9-34) is

$$P_{jJ} = \frac{\sigma_j c}{4\pi} \overline{(\hat{\mathbf{a}}_j \cdot \mathbf{B}_j)^2} \quad (9-35)$$

At this point, we identify a basic contradiction which Price, *et al.*, have (or will) introduce. The power carried by the magnetic field is the sum of two squared quantities (the phase quadrature components of the magnetic field). As such, this power should have a chi square distribution with two degrees of freedom, provided each of the quadrature components is normally distributed (which they should be). Thus, if the sensor responded to B^2 , P_j could reasonably be expected to have a chi square distribution.

If frequency is varied, the phase quadrature components of \vec{B} will have a linear dependence on ω , and will not be normally distributed however. Thus, there is no reason to expect P_j as predicted by (9-30), (9-34) or (9-35) to fit a chi square distribution with two degrees of freedom. As best we can determine, Price, *et al.*, seem unaware of this issue, and subsequently forces P_j to be chi square by running the P_j ensemble (vs frequency) through a filter which removes long-term trends (such as an ω^2 dependence). This mandatory trend removal is not mentioned in the JAYCOR work, although we know it has been done.

If (9-34) for the power detected at r_j is expanded in the magnetic eigenmodes of (9-16), we obtain

$$P_j = \frac{\sigma_j c}{\mu_0} \left(\sum_i B_{0i} (\hat{a}_j \cdot \hat{b}_i) g_{ij} f_{ij} \sin(\omega t + \phi_i) \right)^2 =$$

$$\frac{\sigma_j c}{2\mu_0} \left[\sum_i B_{0i}^2 (\hat{a}_j \cdot \hat{b}_i)^2 g_{ij}^2 f_{ij}^2 + \sum_{\substack{i,k \\ i \neq k}} B_{0i} B_{0k} (\hat{a}_j \cdot \hat{b}_i) (\hat{a}_j \cdot \hat{b}_k) g_{ij} g_{kj} f_{ij} f_{kj} \cos(\phi_i - \phi_k) \right] \quad (9-36)$$

The trigonometric result occurs because

$$\overline{\sin(\omega t + \phi_i) \sin(\omega t + \phi_k)} = \frac{1}{2}(\cos(\phi_i - \phi_k) - \cos(2\omega t + \phi_i + \phi_k)) \quad (9-37)$$

In evaluating (9-36), we shall use the facts that eigenmodes integrated over V are orthogonal (9-23), while cross-mode terms evaluated locally do not vanish.

CAVITY RATE EQUATION AND RESONANCE FUNCTION

The Price, *et al.*, here put down some formulas for the energy balance in a general cavity. There formulas are not easy to understand or develop, and consequently we shall provide an alternate explication. We shall work in 1D, as this gives the same conclusions exactly as 3D, but makes the derivation easier to visualize physically.

Let us consider a lossy transmission line, short circuited at both ends, and with a localized delta-function drive. The transmission in equations are

$$\frac{\partial V}{\partial x} = -L \frac{\partial I}{\partial t} + E$$

$$\frac{\partial I}{\partial x} = -C \frac{\partial V}{\partial t} \quad (9-38)$$

where L can be non-ideal. These equations can be manipulated to give, in the $e^{i\omega t}$ domain,

$$\frac{\partial^2 I}{\partial x^2} + k^2 I = -j\omega CE \quad (9-39)$$

Now assume the line is driven by a point voltage source at x_0 ,

$$E = E_0 \delta(x - x_0) e^{j\omega t} \quad (9-40)$$

and that the line extends from 0 to ℓ :

$$\frac{\partial^2 I}{\partial x^2} + k^2 I = -j\omega CE_0 \delta(x - x_0) \quad (9-41)$$

We can expand I in the current eigenmodes (in this case, a Fourier series)

$$I = \sum_n A_n \cos \frac{n\pi x}{\ell} \quad (9-42)$$

Some easy manipulations lead to A_n being evaluated as

$$A_n = \frac{-j\omega CE_0 \cos(n\pi x_0/\ell)}{\frac{\ell}{2} \left(\frac{\omega^2}{c^2} - \frac{n^2\pi^2}{\ell^2} \right)} \quad (9-43)$$

Note that mode n is only strongly driven if x_0 falls at a point where mode n has a high current response. The mode n current is

$$I_n = -\frac{j\omega CE_0 \cos(n\pi x_0/\ell) \cos(n\pi x/\ell)}{\frac{\ell}{2c^2} \left(\omega^2 - \frac{n^2\pi^2 c^2}{\ell^2} \right)} \quad (9-44)$$

We also have

$$c^2 = \frac{1}{LC} = \frac{1}{(L' - jL'')C} \approx \frac{1}{L'C} (1 + jL''/L') \quad (9-45)$$

where L'' represents inductive losses and L''/L' is the inductive loss tangent of the line.

If A_n is unity, the electric plus magnetic energy stored on the line in mode n is

$$U_n = \ell L' / 4 \quad (9-46)$$

The power dissipated along the line is

$$P_{nd} = \frac{1}{2} \operatorname{Re} (Z_s I_n I_n^*) = \frac{1}{2} \omega L'' \cos^2(n\pi x/\ell) \quad (9-47)$$

which integrates over the line to

$$P_n = \omega \ell L'' / 4 \quad (9-48)$$

Thus, according to (9-3),

$$Q_n = \frac{\omega_n U_n}{P_n} = \frac{L'}{L''} \quad (9-49)$$

We can thus expand the term appearing in the denominator of (9-44) as

$$\frac{n^2 \pi^2 c^2}{\ell^2} = \frac{n^2 \pi^2 c_0^2}{\ell^2} (1 + j/Q_n) = \omega_n^2 (1 + j/Q_n) \quad (9-50)$$

This makes it possible to expand the current in mode n as

$$I_n = \frac{-jE_0 \cos(n\pi x_0/\ell) \cos(n\pi x/\ell)}{\ell L \left((\omega - \omega_n) - \frac{j\omega_n}{2Q_n} \right)} \quad (9-51)$$

Thus, the electrical energy contained in this mode is

$$U_{ne} = \int_0^\ell \frac{1}{2} L I_n I_n^* dx = \frac{\frac{1}{4} |E_0|^2 \cos^2 n\pi x_0}{\ell L \left[(\omega - \omega_n)^2 + \left(\frac{\omega_n}{2Q_n} \right)^2 \right]} = \frac{1}{2} U_n \quad (9-52)$$

The power input into mode n by the voltage discontinuity is

$$P_n = \frac{1}{2} \operatorname{Re} [E_o I_n(x_o)^*] = \frac{\frac{\omega_n}{4Q_n} \cdot (|E_o|^2/L) \cos^2(n\pi x_o/\ell)}{(\omega - \omega_n)^2 + \left(\frac{\omega_n}{2Q_n}\right)^2} = \frac{U_n \omega_n}{Q_n} \quad (9-53)$$

The total power input on the line is

$$P_c = \frac{1}{2} \operatorname{Re} [E_0 J(x_0)^*] = (|E_0|^2/L) \sum_m \frac{\frac{\omega_m}{4Q_m} \cos^2(m\pi x_0/\ell)}{(\omega - \omega_m)^2 + \left(\frac{\omega_m}{2Q_m}\right)^2} \quad (9-54)$$

For modes near resonance, ω is nearly ω_m , and P_c can be re-evaluated as

$$P_c = (|E_0|^2/L) \sum_m \frac{\frac{\omega_m}{4Q_m} \cos^2(m\pi x_0/\ell)}{(\alpha + 1) \left(\frac{\omega_m}{2Q_m}\right)^2} \quad (9-55)$$

where α is some averaging parameter to be fitted for accounting that all the modes are not driven right at resonance.

The Price, *et al.*, articles make the rather extreme assumption that $\alpha = 0$, thus leading to the result

$$P_c = (|E_0|^2/L) \frac{Q}{\omega} \sum_m \cos^2(m\pi x_0/\ell) \quad (9-56)$$

Here, the debatable assumption is also made that Q does not depend much on m . Substitution of $(|E_0|^2/L)$ back into (9-53) re-express the power input to mode n as

$$P_n = \frac{\left(\frac{\omega_n}{2Q_n}\right)^2 P_c \sum_m \cos^2(m\pi x_0/\ell)}{(\omega - \omega_n)^2 + \left(\frac{\omega_n}{2Q_n}\right)^2} = \frac{\left(\frac{\omega_n}{2Q_n}\right)^2 P_c \epsilon_n}{(\omega - \omega_n)^2 + \left(\frac{\omega_n}{2Q_n}\right)^2} \quad (9-57)$$

In (9-57), ϵ_n is the coupling coefficient for mode n ,

$$\epsilon_n = \frac{\cos^2(n\pi x_0/\ell)}{\sum_m \cos^2(m\pi x_0/\ell)} \quad (9-58)$$

Although not pointed out in the first JAYCOR release, by the second release they had isolated two attributes of ϵ_n which (9-58) makes fairly apparent: For large n , ϵ_n will be a very rapidly changing function of n , and in general it will be true that

$$\sum_n \epsilon_n = 1 \quad (9-59)$$

From (9-3) and (9-57), we thus see that, at steady state, the total energy in mode n on the cable is

$$U_n = \frac{Q_n P_n}{\omega} = \frac{\frac{\omega_n}{4Q_n} P_c \epsilon_n}{(\omega - \omega_n)^2 + \left(\frac{\omega_n}{2Q_n}\right)^2} \quad (9-60)$$

It is important to point out that, in our simplified 1D model, all losses are internal, and no energy leaks back out through the port at which it was injected.

If steady state conditions do not prevail, the energy balance for mode n will be a first-order differential equation of the form

$$\frac{dU_n}{dt} = -\beta U_n + P_n = -\beta U_n + \frac{\left(\frac{\omega_n}{2Q_n}\right)^2 P_c \epsilon_n}{(\omega - \omega_n)^2 + \left(\frac{\omega_n}{2Q_n}\right)^2} \quad (9-61)$$

where β is some constant to be determined. It is easy to evaluate β at steady state from (9-60):

$$\beta = \frac{\omega_n}{Q_n} \quad (9-62)$$

so that

$$\frac{dU_n}{dt} + \frac{\omega_n U_n}{Q_n} = \frac{\left(\frac{\omega_n}{2Q_n}\right) P_c \epsilon_n}{(\omega - \omega_n)^2 + \left(\frac{\omega_n}{2Q_n}\right)^2} \quad (9-63)$$

We also recall from (9-20) that U_n is related to B_{0n} by

$$U_n = \frac{B_0 n^2 V}{2\mu_0} \quad (9-64)$$

STATISTICAL PROPERTIES OF THE MEASURED POWER

We now begin a section which is marked by exceedingly lengthy formulas, which probably appear more intimidating than they actually are. The mean of the measured power data is denoted

$$\mu = E(P_j) \quad (9-65)$$

and the variance is

$$\sigma^2 = E(P_j^2) - (E(P_j))^2 \quad (9-66)$$

where $E()$ denotes the expectation.

In view of (9-36), $E(P_j)$ can be written

$$\begin{aligned} E(P_j) &= \frac{\sigma_f^2}{2\mu_o} \sum_i E(B_{oi}^2) E((\hat{a}_j \cdot \hat{b}_j)^2) E(g_{ij}^2) E(f_{ij}^2) \\ &+ \sum_{i,k} \sum_{i \neq k} E(B_{oi} B_{ok} \cos(\phi_i - \phi_k)) E(\hat{a}_j \cdot \hat{b}_i) E(\hat{a}_j \cdot \hat{b}_k) E(g_{ij}) E(g_{kj}) E(f_{ij}) E(f_{kj}) \end{aligned} \quad (9-67)$$

The expectation $E(P_j^2)$ is even more cumbersome. Taking care not to express separately the expectation of terms which are not independent, we find

$$E(P_j^2) = \left(\frac{\sigma_f^2}{2\mu_o}\right)^2 [E(T_1) + E(T_2) + E(T_3)] \quad (9-68)$$

where

$$\begin{aligned}
E(T_1) &= E\left[\left(\sum_i B_{0i}^2 (\hat{a}_j \cdot \hat{b}_i)^2 g_{ij}^2 f_{ij}^2\right)^2\right] = \sum_k E(B_{0k}^4) E((\hat{a}_j \cdot \hat{b}_k)^4) E(g_{kj}^4) E(f_{kj}^4) \\
&+ \sum_{\substack{k, l \\ k \neq l}} E(B_{0k}^2) E(B_{0l}^2) E((\hat{a}_j \cdot \hat{b}_k)^2) E((\hat{a}_j \cdot \hat{b}_l)^2) E(g_{kj}^2 g_{lj}^2) E(f_{kj}^2) E(f_{lj}^2)
\end{aligned} \tag{9-69}$$

$$\begin{aligned}
E(T_2) &= 2 \sum_{\substack{i \\ k \neq l}} E\left(B_{0i}^2 B_{0k} B_{0l} \cos(\phi_k - \phi_l)\right) E((\hat{a}_j \cdot \hat{b}_i)^2) E(\hat{a}_j \cdot \hat{b}_k) \\
&\cdot E(\hat{a}_j \cdot \hat{b}_l) E(g_{ij}^2 g_{ki} g_{lj}) E(f_{ij}^2) E(f_{kj}) E(f_{lj})
\end{aligned} \tag{9-70}$$

$$\begin{aligned}
E(T_3) &= \sum_{\substack{k \neq l \\ m \neq n}} E(B_{0k} B_{0l} B_{0m} B_{0n} \cos(\phi_k - \phi_l) \cos(\phi_m - \phi_n)) \\
&\cdot E(\hat{a}_j \cdot \hat{b}_k) (\hat{a}_j \cdot \hat{b}_l) (\hat{a}_j \cdot \hat{b}_m) (\hat{a}_j \cdot \hat{b}_n) E(g_{kj} g_{lj} g_{mj} g_{nj}) E(f_{kj} f_{lj} f_{mj} f_{nj})
\end{aligned} \tag{9-71}$$

Some factors in this very intimidating-looking set of equations are actually easy to evaluate. For example, the probability density function of θ is

$$P(\theta) = \frac{1}{2} \sin \theta \tag{9-72}$$

Thus, the expectation of $\hat{a}_j \cdot \hat{b}_i$ is

$$E(\hat{a}_j \cdot \hat{b}_i) = \frac{1}{2} \int_0^\pi \cos \theta \sin \theta d\theta = 0 \tag{9-73}$$

Similarly, we can find

$$E((\hat{a}_j \cdot \hat{b}_i)^2) = 1/3 \quad E((\hat{a}_j \cdot \hat{b}_i)^4) = 1/5 \tag{9-74}$$

JAYCOR workers state that the spatially rapid function f_{ij} , almost by definition, averages to zero

$$E(f_{ij}) \stackrel{?}{=} 0 \tag{9-75}$$

We think, however, that either $\hat{a}_j \cdot \hat{b}_i$ or f_{ij} can be bipolar, but both cannot be. It seems more logical to let \hat{b}_i reverse direction where necessary, as it is already permitted to change orientation. This convention invalidates the JAYCOR claim of (9-75), and we will not invoke it in our review.

By definition, we have

$$V_{ph} = \frac{\pi \lambda^3}{6} \quad (9-76)$$

Thus, it must be true that

$$E(f_{ij}^2) = \frac{\int f_i^2 d\mathbf{r}}{V} \approx \frac{\frac{V}{V_{ph}} \int f_i^2 d\mathbf{r}}{V} \quad (9-77)$$

Because of (9-26), we are forced to conclude that we thus have

$$E(f_{ij}^2) = 1 \quad (9-78)$$

At this point, the JAYCOR people assume that, for a rectilinear cavity, we can express $f_i(\mathbf{r})$ as

$$f_i(\mathbf{r}) = 2\sqrt{2} \sin \frac{\ell\pi x}{A} \sin \frac{m\pi y}{B} \sin \frac{n\pi z}{C} \quad (9-79)$$

[We note that this expression may be incompatible with (9-75). The right side should have absolute value signs.] Equation (9-79) leads to the results

$$\begin{aligned} E(f_{ij}^2) &= 1 \\ E(f_{ij}^4) &= 27/8 \end{aligned} \quad (9-80)$$

These expectations are, at least, independent of (ℓ, m, n) and (A, B, C) , and do not depend on the right side of (9-79) being modified by an absolute value operator.

At this point, it is apparent from (9-73) that the second term in (9-67) is zero. This result is valid even if (9-75) is not. The expectation for B_{oi}^{-2} can be evaluated from (9-18)

$$E(B_{0i}^2) = \frac{2\mu_0}{V} E(U_i) \quad (9-81)$$

using MKS units. We thus find from (9-67)

$$\mu = E(P_j) = \frac{\sigma_j c}{2\mu_0} \cdot \frac{1}{3} \cdot \frac{2\mu_0}{V} \sum_i E(U_i) E(g_{ij}^2) E(f_{ij}^2) \quad (9-82)$$

In spite of the shortcomings of the derivation of (9-27), it implies that

$$E(g_{ij}^2) = g_j^2 \approx 1 \quad (9-83)$$

Also, we have

$$\sum_i E_i(U_i) = U \quad (9-84)$$

the total energy rattling around in the cavity. Thus, we obtain the mean power sensed as

$$E(P_j) = \frac{\sigma_j c U g_j^2}{3V} \quad (9-85)$$

where appeal is made to (9-80) and (9-82).

We can determine at once from (9-73) that

$$E(T_2) = 0 \quad (9-86)$$

This conclusion does not depend on the dubiously valid (9-75).

In (9-71) for $E(T_3)$, only terms with even powers of the dot products can be nonzero. Thus, only terms with $(k, l) = (m, n)$ or (n, m) are nonzero, and $E(T_3)$ becomes

$$\begin{aligned} E(T_3) &= 2 \sum_{\substack{k \neq l \\ k, l}} E\left(B_{0k}^2 B_{0l}^2 \cos^2(\phi_k - \phi_l)\right) E\left(\hat{a}_j \cdot \hat{b}_k\right)^2 E\left(\hat{a}_j \cdot \hat{b}_l\right)^2 E(g_{kj}^2) E(g_{lj}^2) \\ &= \frac{2}{9} \sum_{\substack{k \neq l \\ k, l}} E\left(B_{0k}^2 B_{0l}^2 \cos^2(\phi_k - \phi_l)\right) g_j^4 \end{aligned} \quad (9-87)$$

We can also express $E(T_1)$ as

$$E(T_1) = \sum_k E(B_{0k}^4) \cdot 1/5 E(g_{kj}^2) E(g_{lj}^2) E(f_{kj}^2) E(f_{lj}^2) + \sum_{\substack{k \neq l \\ k, l}} E(B_{0k}^2) E(B_{0l}^2) \cdot 1/9 \quad (9-88)$$

by applying (9-74), (9-80) and (9-82). Finally, assuming

$$E(g_{kj}^4) = g_j^4 \approx 1 \quad (9-89)$$

and applying the second part of (9-80) leaves the formula for $E(T_1)$

$$E(T_1) = \frac{27}{40} \sum_k E(B_{0k}^4) g_j^4 + \frac{1}{9} \sum_{\substack{k \neq l \\ k, l}} E(B_{0k}^2) E(B_{0l}^2) g_j^4 \quad (9-90)$$

We now combine (9-68), (9-86), (9-87) and (9-88) to obtain

$$E(P_j^2) = \left(\frac{\sigma_j c g_j^2}{2 \mu_0} \right)^2 \left[\frac{27}{40} \sum_k E(B_{0k}^2) + \frac{1}{9} \sum_{\substack{k \neq l \\ k, l}} E(B_{0k}^2) E(B_{0l}^2) + \sum_{\substack{k \neq l \\ k, l}} E(B_{0k}^2 B_{0l}^2 \cos^2(\phi_k - \phi_l)) \right] \quad (9-91)$$

Thus the variance of the sensed power becomes

$$\begin{aligned} \sigma^2 &= E(P_j^2) - (E(p_j))^2 = \\ &\left(\frac{\sigma_j c g_j^2}{2 \mu_0} \right)^2 \left[\left(\frac{27}{40} - \frac{1}{9} \right) \sum_k E(B_{0k}^4) + \frac{2}{9} \sum_{\substack{k \neq l \\ k, l}} E(B_{0k}^2 B_{0l}^2 \cos^2(\phi_k - \phi_l)) \right] = \\ &\left(\frac{\sigma_j c}{2 \mu_0} \right)^2 \left[\frac{123}{360} \sum_k E(B_{0k}^4) + \frac{2}{9} \sum_{\substack{k \neq l \\ k, l}} E(B_{0k}^2 B_{0l}^2 \cos^2(\phi_k - \phi_l)) \right] \end{aligned} \quad (9-92)$$

where the last sum no longer excludes $k = l$ terms.

The remaining expectations are more of a mess to evaluate. For instance, we have

$$E\left(\sum B_{0k}^4\right) = E\left(\sum_k \frac{U_k^2 \cdot 4\mu_0^2}{V^2}\right) = \frac{4\mu_0^2}{V^2} \sum_k E\left[\frac{\left(\frac{\omega_k}{4Q_k}\right)^2 \epsilon_k^2 p_c^2}{\left((\omega - \omega_k)^2 + \left(\frac{\omega_k}{2Q_k}\right)^2\right)^2}\right] \quad (9-93)$$

This summation may be approximated in integral form if it is multiplied first by the mode density of (9-2).

$$E\left(\sum B_{0k}^4\right) \approx \int_{\omega - \Omega}^{\omega + \Omega} \frac{\left[\frac{\omega_k \mu_0 P_c \epsilon}{2QV}\right]^2}{\left[(\omega - \omega_k)^2 + \left(\frac{\omega_k}{2Q_k}\right)^2\right]^2} \cdot \frac{8\pi V \omega_k^2}{(2\pi c)^3} d\omega_k \quad (9-94)$$

If we make the approximation that the denominator of the integral acts like a δ function at $\omega_k = \omega$, we obtain

$$E\left(\sum B_{0k}^4\right) = \frac{8\pi V \omega^4}{(2\pi c)^3} \cdot \left[\frac{\mu_0 P_c}{2QV}\right] \epsilon^{(2)} I \quad (9-95)$$

where

$$\epsilon^{(2)} = E(\epsilon_k^2) \quad (9-96)$$

is not simply ϵ^2 due to the rapid and random fluctuation of ϵ_k vs k and where I is the integral

$$I = \int_{-\infty}^{\infty} \frac{d\omega_k}{\left[(\omega - \omega_k)^2 + \left(\frac{\omega_k}{2Q_k}\right)^2\right]^2} = \frac{4\pi Q^3}{\omega^3} \quad (9-97)$$

Equation (9-97) is evaluated through the following sequence of variable changes

$$\begin{aligned} u &= \omega_k - \omega \\ \theta &= \tan^{-1} u / (\omega / 2Q) \end{aligned} \quad (9-98)$$

We can evaluate $E(\sum B_{0k}^4)$ from (9-95) and (9-97) as

$$E\left(\sum B_{0k}^4\right) = \frac{8\pi V}{(2\pi c)^3} \left[\frac{\mu_0 P_c \omega^2}{2QV} \right]^2 \cdot \frac{4\pi Q^3}{\omega^3} \epsilon^{(2)} \quad (9-99)$$

If we recognize that [see (9-14)]

$$\frac{Q}{V} = \frac{8\pi \omega^3}{(2\pi c)^3 N_s} \quad (9-100)$$

we can express $E(B_{0k}^4)$ as

$$E\left(\sum_k B_{0k}^4\right) = \left[\frac{\mu_0 P_c \omega^2}{\pi c^3} \right]^2 \frac{\epsilon^{(2)}}{\pi N_s} \quad (9-101)$$

or, in JAYCOR units

$$E\left(\sum_k B_{0k}^4\right) = \left[\frac{4P_c \omega^2}{c^3} \right] \frac{\epsilon^{(2)}}{\pi N_s} \quad (9-102)$$

Further application of (9-100) causes (9-101) to become

$$E\left(\sum_k B_{0k}^4\right) = \left[\frac{8\pi}{V} \frac{Q}{\omega} (N_s \mu_0 / 8) P_c \right]^2 \frac{\epsilon^{(2)}}{\pi N_s} \quad (9-103)$$

with the JAYCOR - equivalent being obtained simply from the transformation $\mu_0 \rightarrow 4\pi$.

Price, *et al.*, originally did not attempt to treat the coupling coefficient with extra special care. Thus, their original formula for $\epsilon^{(2)}$ was

$$\epsilon^{(2)} = \bar{\epsilon}(\omega)^2 \quad (9-104)$$

where

$$\bar{\epsilon}(\omega) = \frac{N}{D} \quad (9-105)$$

with

$$N = \int_{\omega-\Omega}^{\omega+\Omega} \frac{\left[\frac{\omega_n}{2Q_n} \right]^2 \epsilon_n \cdot \frac{8\pi V \omega_n^2}{(8\pi c)^3} d\omega_n}{\left[(\omega - \omega_n)^2 + \left(\frac{\omega_n}{2Q_n} \right)^2 \right]} \quad (9-106)$$

In view of (9-57) for P_n , the power going into mode n , N can also be interpreted as

$$N = \eta(\omega) = \sum_n P_n \epsilon_n / P_c \quad (9-107)$$

i.e., as the total coupling efficiency for all the energy going into the cavity. If the energy is directly injected into the cavity, N and $\eta(\omega)$ will be unity, as summing the P_n 's of (9-57) and evaluating ω at ω_n illustrate.

The denominator of (9-105) is the same as (9-106) for the numerator, but with the ϵ_n factor omitted:

$$D = \int_{\omega-\Omega}^{\omega+\Omega} \frac{\left[\frac{\omega_n}{2Q_n} \right]^2 \cdot \frac{8\pi V \omega_n^2 d\omega_n}{(2\pi c)^3}}{\left[(\omega - \omega_n)^2 + \left(\frac{\omega_n}{2Q_n} \right)^2 \right]} \quad (9-108)$$

Upon evaluating D in (9-108) using the same techniques as applied to (9-100), including application of the transformations of (9-98), we find

$$D = \frac{\pi N_s}{2} \quad (9-109)$$

where we have again used (9-100).

Thus, we see that

$$\eta(\omega) = \bar{\epsilon}(\omega) N_s \cdot \frac{\pi}{2} \quad (9-110)$$

This equation states that, within an approximate factor of $(\pi/2)$, the total coupling coefficient to the cavity is the sum of the coupling coefficients to the individual modes.

The total energy in the cavity is obtained from (9-60) and (9-81).

$$U = \frac{V}{2\mu_0} E \left(\sum_k B_{0k}^2 \right) = E \left(\sum_i U_i \right) = \int_{\omega-\Omega}^{\omega+\Omega} \frac{\frac{\omega_k}{4Q_k} P_c \epsilon_k}{(\omega - \omega_n)^2 + \left(\frac{\omega_n}{2Q_n} \right)^2} \cdot \frac{8\pi V \omega_k^2}{(2\pi c)^3} d\omega^k \quad (9-111)$$

where the mode density, (9-2), is again applied to convert the summation to an integral. This integral is very similar to (9-106) for N . An identical evaluation process yields

$$U = \frac{V}{8\pi} \left[\frac{4\bar{\epsilon}(\omega) P_c \omega^2}{c^3} \right] = \frac{P_c \eta(\omega) Q}{\omega} \quad (9-112)$$

and

$$E \left(\sum_k B_{0k}^2 \right) = \frac{\mu_0}{4\pi} \left[\frac{4\bar{\epsilon}(\omega) P_c \omega^2}{c^3} \right] \quad (9-113)$$

where the term outside the brackets of (9-113) disappears for JAYCOR units.

Equations (9-101) and (9-112) can be combined to show

$$\sum_k E(B_{0k}^4) = \left(\frac{\mu_0}{4\pi} \right)^2 \left[\frac{8\pi U}{V} \right]^2 \frac{\epsilon^{(2)}}{\bar{\epsilon}(\omega)^2} \cdot \frac{1}{\pi N_s} \quad (9-114)$$

where the $\mu_0/4\pi$ term is gone in JAYCOR units.

Lastly, let us consider the expectation term with the cosine factor in (9-92). For an RLC series circuit, the impedance is

$$Z = j\omega L + \frac{1}{j\omega C} = \frac{V}{I} \quad (9-115)$$

where L may be complex. Then we have

$$I = \frac{V}{j\omega L' + \frac{1}{j\omega C} + \frac{\omega L'}{Q}} \quad (9-116)$$

The current may be seen to lead the voltage by $\phi + \pi/2$, where

$$\tan(\phi + \pi/2) = -\frac{\text{Re}(Z)}{\text{Im}(Z)} = \frac{\omega L/Q}{\omega L - \frac{1}{\omega C}} \approx \frac{\omega}{2Q_k(\omega - \omega_k)} \quad (9-117)$$

(The Price, *et al.*, papers omit the $\pi/2$ term, which subsequently cancels out anyway.) From (9-111), we have

$$\begin{aligned} \sum_{k,l} E(B_{0k}^2 B_{0l}^2 \cos^2(\phi_k - \phi_l)) &= \int_{\omega_k - \Omega}^{\omega_k + \Omega} \int_{\omega_l - \Omega}^{\omega_l + \Omega} \left(\frac{2\mu_0}{V} \right) \frac{\omega_k \epsilon_k P_c / 4Q_k}{\left((\omega - \omega_k)^2 + \left(\frac{\omega_k}{2Q_k} \right)^2 \right)} \cdot \frac{8\pi V \omega_k^2}{(2\pi c)^3} \\ &\cdot \left(\frac{2\mu_l}{V} \right) \frac{\omega_l \epsilon_l P_c / 4Q_l}{\left((\omega - \omega_l)^2 + \left(\frac{\omega_l}{2Q_l} \right)^2 \right)} \cdot \frac{8\pi V \omega_l^2}{(2\pi c)^3} \cos^2(\phi_k - \phi_l) d\omega_k d\omega_l \end{aligned} \quad (9-118)$$

A considerable amount of algebra converts (9-118) to

$$\begin{aligned} \sum_{k,l} E(B_{0k}^2 B_{0l}^2 \cos^2(\phi_k - \phi_l)) &= \\ \left(\frac{\mu_0 \bar{\epsilon}(\omega) P_c}{2\pi^2 c^3 Q} \right)^2 \int_{-\infty}^{\infty} \int_{-\infty}^{\infty} &\frac{\omega_k^3 \omega_l^3 \cos^2(\phi_k - \phi_l) d\omega_k d\omega_l}{\left[(\omega - \omega_k)^2 + \left(\frac{\omega_k}{2Q_k} \right)^2 \right] \left[(\omega - \omega_l)^2 + \left(\frac{\omega_l}{2Q_l} \right)^2 \right]} \end{aligned} \quad (9-119)$$

From (9-117), we find

$$\sec^2(\phi_k + \pi/2) d\phi_k = \frac{\omega_k d\omega_k}{2Q_k(\omega - \omega_k)^2} = \frac{2Q_k}{\omega_k} \tan^2(\phi_k + \pi/2) d\omega_k \quad (9-120)$$

Equation (9-120) gives

$$d\omega_k = \frac{\omega_k}{2Q_k} \frac{d\phi_k}{\sin^2(\phi_k + \pi/2)} \quad (9-121)$$

so that we have

$$\frac{\omega_k}{2\phi_k} d\phi_k = \sin^2(\phi_k + \pi/2) d\omega_k = \frac{d\omega_k}{\frac{1}{\tan^2(\phi_k + \pi/2)} + 1} =$$

(9-122)

$$\frac{d\omega_k}{\frac{(\omega - \omega_k)^2}{(\omega_k/2Q_k)^2} + 1} = \frac{(\omega_k/2Q_k)^2 d\omega_k}{(\omega - \omega_k)^2 + (\omega_k/2Q_k)^2}$$

or

$$\frac{\omega_k d\omega_k}{(\omega - \omega_k)^2 + (\omega_k/2Q_k)^2} = \frac{2Q_k}{\omega_k} d\phi_k$$

(9-123)

Substitution of (9-123) into (9-119) gives

$$\sum_{k,l} E\left(B_{0k}^2 B_{0l}^2 \cos^2(\phi_k - \phi_l)\right) =$$

$$\left(\frac{\mu_0 \bar{\epsilon}(\omega) P_c \omega^2}{\pi^2 c^3}\right)^2 \int_{-\pi/2}^{\pi/2} \int_{-\pi/2}^{\pi/2} \cos^2(\phi_k - \phi_l) d\phi_k d\phi_l = \frac{1}{2} \left(\frac{\mu_0 \bar{\epsilon}(\omega) P_c \omega^2}{\pi^2 c^3}\right)^2$$

(9-124)

Applying (9-112) to (9-124) finally yields

$$\sum_{k,l} E\left(B_{0k}^2 B_{0l}^2 \cos^2(\phi_k - \phi_l)\right) = \left(\frac{\mu_0}{4\pi}\right) \cdot \frac{1}{2} \cdot \left(\frac{8\pi U}{V}\right)^2$$

(9-125)

Thus, from (9-92), (9-114) and (9-125), we obtain

$$E(P_j^2) - (E(P_j))^2 = \left(\frac{\sigma_j c U g_j^2}{3V}\right)^2 \left[1 + \frac{123 \epsilon^{(2)}}{40\pi N_s \bar{\epsilon}(\omega)^2}\right]$$

(9-126)

The final result applies in MKS or JAYCOR units. As a rule, expectations of the B_{0k} 's are unit dependent, while expectations of powers and energies are not. Equations (9-125) and (9-126) contrast this situation nicely. Note that the second term in the brackets of (9-126) goes away for a well overmoded cavity.

Comparison of (9-85) and (9-126) indicate that the mean and standard deviation of P_j for well overmoded cavities should both be

$$\mu = \sigma = \frac{\sigma_j c U g_j^2}{3V} \quad (9-127)$$

This attribute is well known for chi square distributions with two degrees of freedom.

From (9-3) and (9-85), it is possible to derive a formula relating the Q of a complex cavity to readily measurable quantities:

$$Q = \frac{3\omega V}{\sigma_j c g_j^2} \frac{E(P_j)}{P_c} \quad (9-128)$$

In many cases, it may be true that the deviation of Q from infinity is due to several separable factors. For instance, there may be internal loss and P apertures through which energy can escape. In this case, the overall system Q is representable by the relationship

$$Q^{-1} = Q_\Omega^{-1} + \sum_{p=1}^P Q_p^{-1} \quad (9-129)$$

where Q_Ω is associated with internal ohmic dissipation.

For the simplest case, where $P = 1$, Q_Ω and Q_1 may be determined by first foiling over the aperture. Then (9-128) will give Q_Ω . The aperture then unfoiled, which causes (9-129) to give Q . From Q_Ω and Q , Q_1 , may be readily extracted. This scheme is easily extended to P apertures by foiling and unfoiling apertures one at a time.

COMPARISON OF THEORY WITH EXPERIMENT: THE K-S TEST

Let us have a measurement ensemble with N measurements. These measurements can be taken as functions of any variable. In our work, frequency, sensor orientation, or sensor portions within the cavity would be permissible variables. Let $F(x)$ be the hypothesized cumulative probability distribution, where x represents the observed dependent variable (in our case P_j). Let $F^*(x)$ be the actually measured cumulative probability distribution. Then for each of the n points in the measurement ensemble, we can define

$$d_n = |F(P_{jn}) - F^*(P_{jn})| \quad (9-130)$$

where P_{jn} is the n th largest value of P_j . We can also define

$$D_N = \max_n \{d_n\} \quad (9-131)$$

Let us now introduce the Kolmogorov - Smirnov distribution

$$Q(\lambda) = \sum_{k=-\infty}^{\infty} (-1)^k e^{-2k^2\lambda^2} \quad (9-132)$$

This is a cumulative probability distribution which is 0 at $\lambda = 0$ and 1 at $\lambda = \infty$.

If $F^*(P_j)$ is represented by $F(P_j)$ with 90% confidence, then 90% of the time D_N will be less than λ/\sqrt{N} . More generally, if $F^*(P_j)$ is represented by $F(P_j)$ with $1 - Q(\lambda)$ confidence, we have

$$P\left(D_N > \frac{\lambda}{\sqrt{N}}\right) = Q(\lambda) \quad (9-133)$$

or D_N will exceed λ/\sqrt{N} only $Q(\lambda)$ of the time. Alternatively, we can express (9-133) as

$$P\left(D_N < \frac{\lambda}{\sqrt{N}}\right) = 1 - Q(\lambda) \quad (9-134)$$

If one knows the desired confidence limit $1 - Q(\lambda)$, one can find λ from inverting (9-132) or using a look-up table.[4] For example, if $1 - Q(\lambda)$ is .9, λ is .57; if $1 - Q(\lambda)$ is .99, λ is .44. Thus, the permitted deviation $|F(P_j) - F^*(P_j)|$ is $.57/\sqrt{N}$ for 90% confidence and $.44/\sqrt{N}$ for 99% confidence. Note that the higher the desired confidence, the tighter the restriction placed on $|F(P_j) - F^*(P_j)|$.

An alternative way of expressing (9-133) involves reversing the inequality sign. Then we can say that the probability that D_N will be bounded by λ/\sqrt{N} is only $Q(\lambda)$. Should this bounding condition turn out to be met, there is a $1 - Q(\lambda)$ confidence that $F(P_j)$ is the correct cumulative probability distribution.

We note in conclusion that any monotonic transformation may be applied to P_j without affecting the validity of the Kolmogorov - Smirnov test: It constitutes a bound on what is permitted on the vertical axis only, and cannot be altered in result by any distortion imposed on the horizontal axis.

REFERENCES

[1] Price, R. H., *et al*, "Determination of the Statistical Distribution of Electromagnetic Field Amplitudes in Complex Cavities," 88JAL129, JAYCOR, 1 June 1988.

- [2] Price, R. H., H. T. Davis, and E. P Wenaas, "Determination of the Statistical Distribution of Electromagnetic-Field Amplitudes in Complex Cavities," *Phys. Rev. E*. Vol. 48, pp. 4716-4729, December 1993.
- [3]. K. S. Yee, "Numerical Solution of Initial Boundary Value Problems in Isotropic Media," *IEEE Trans. Antennas Propagat.*, Vol. AP-14, pp. 302-307, May 1966.
- [4] Roe, P. R., *Probability and Statistics in Experimental Physics*, pp. 189-203, Springer-Verlag, Inc., New York, New York, 1992.

Chapter 10. CONCLUSIONS

This document describes the electromagnetic fields (or power flux densities) inside an enclosure either internally driven or excited by an externally incident field which can leak through apertures or other points of entry. It also treats the coupling of these fields to the cabling or wiring harness inside the enclosure. This study is performed from a statistical, not deterministic, perspective.

The fields inside such an enclosure must be described not only in terms of their statistical distribution, but also in terms of their autocorrelation; the fields at observation points separated by less than a wavelength are not totally independent variables. The same is true of field responses from drives differing by only a very small frequency shift (so the entire enclosure as measured in dimensions of wavelength changes by less than unity). In Section 2, we illustrate how to create electromagnetic field drivers to couple to the wiring harness, where these fields have any desired statistical distribution, and also possess local autocorrelation with respect to small shifts in position or frequency. Special emphasis is placed on field distributions which have normally distributed phase-quadrature components. Such fields have power-flux distributions which are chi square with two degrees of freedom. Consideration is also made of the situations where the power-flux distributions are log normal or log log normal. Additionally, we discuss compound distributions, such as those whose cumulative distribution functions are made up of a power series of normal cumulative distribution functions, where the coefficients of the power series sum to unity.

Actual field data do not often look chi square in power or normal in phase-quadrature field. There is usually a slow drift or trend superimposed on the response. This trend is due to factors such as a frequency-dependent Q or aperture cross-section (assuming frequency is the variable undergoing change to generate a data ensemble). In some respects, sweep-frequency measured power-flux data often looks like an amplitude-modulated signal. The curiosity of this case is that it is the carrier which is desired and the modulation or trend which is unwanted, at least for the first-order statistical studies. Separating the carrier from the modulation and then discarding the modulation is referred to as "detrending". The method we use for detrending is also discussed in Section 2.

Section 3 continues the discussion of how to generate fields which have simultaneously the desired distribution and autocorrelation. (Introduction of autocorrelation distorts the distribution. In Section 3, we show how to restore the distribution without, in turn, compromising the autocorrelation.) We then illustrate how to apply these simulated fields to cable models and how to obtain the simulated cable currents. This is first done using the telegrapher's equations for a cable close to a ground plane, where the four telegrapher's-equation circuit parameters are well defined (and nearly frequency independent). Subsequently, this simulation is generalized to eliminate the need for a proximate ground and frequency independence in the series and shunt parameters.

One of the beauties of statistical cavity response modeling is that we do not simultaneously have to solve the fields everywhere, use the fields to drive the cables, and then couple the cable currents back into the fields. This does not mean we can relax the requirement that the cable currents be in some sort of thermodynamic equilibrium with the fields. The physics for ensuring this equilibrium is incorporated by damping the cable currents with a radiation resistance. A convenient formula is presented indicating how much radiation resistance per unit length is physical. For a cable 5 cm off a ground plane, this radiation resistance is $120 \Omega/m$ at 317 GHz, and increases cubically with frequency and quadratically with elevation off the ground plane.

After much care has been taken to generate drive fields with the proper trendless distribution and autocorrelation, and after frequency-dependent radiation resistance has been added to the cable model, our procedure gives cable currents with normally distributed phase-quadrature components. This result passes a 90% confidence Kolmogorov-Smirnov statistical test when the drive fields are also set up to be of normally distributed phase quadrature.

In Section 4, we concentrate on log normal distributions. Log normal distributions tend to occur whenever some ensemble of results depends on a large number of variable factors. Taking the log of such a result converts the product of the factors into a summation, which the Central Limit Theorem then indicates will be normally distributed. It develops that, if the power-flux density is log normally distributed, the squares of the phase-quadrature field components will be also very nearly log normal. From this conclusion, it is easy to obtain the distribution of the phase-quadrature components themselves. The main result of this section is a set of formulas relating the power-flux log normal distribution parameters to those of the phase-quadrature-squared log normal parameters.

There is one problem with log normal models: they tend to give exaggerated population densities at the upper and lower tails. The first of these situations leads to unreasonably pessimistic likelihoods of system upset or failure. Consequently, we construct an alternative hybrid distribution where power flux is log normal over the central 80% of its range and chi square (two degrees of freedom) at the upper and lower 10% tails. This hybrid model corresponds to phase-quadrature field components being log normal over the central 90% of their range, and normal at the upper and lower 5% tails. The hybrid distribution model eliminates the exaggerated upper distribution tail problems of the pure log normal model; comparison with experimental data taken on the EMPTAC facility and on the Celestron 8 satellite telescope confirms this success, although better comparison with experiment on the Celestron 8 occurs if the cross-over to chi square occurs at $p = 0.875$ instead of $p = 0.9$.

Much of our understanding of such enclosures is owed to Lehman, who, like everyone else, observed that the interior of a cavity indeed has physical properties which make the electromagnetic power-flux density sampled by an interior dipole antenna look chi square with two degrees of freedom. However, he also observed that a leaky enclosure can be illuminated from three different directions, with two possible polarizations accompanying each choice of illumination direction. Thus, he concluded that power flux inside an externally illuminated leaky

chamber, as projected on a dipole antenna, should also have attributes of a chi square distribution with six degrees of freedom. The curious mixture of these two distributions which Lehman deduced is explained in Section 5. Its probability density function (pdf) is actually a logarithmic convolution of the chi square probability density functions with two and six degrees of freedom, which turns out to be a modified Bessel function of the second kind, and of order two. This pdf may be completely characterized by a single parameter, which, for instance, can be very simply related to the mean power flux or to the standard deviation of the power flux inside the enclosure. It proves to be fairly difficult and complex, however, to back the pdf of the phase-quadrature field components out of the Bessel function distribution for the power-flux pdf. A major portion of Section 5 is devoted to this manipulation.

The Lehman distribution has truly surprising fidelity in the replication of experimentally observed power-flux cumulative probability distributions. Its success in replicating the all-important upper tail of the distributions is especially remarkable. Moreover, this replication may be achieved without first applying trend-removal manipulations, which is an operation some would regard as dubious, especially if not later recompensed. A number of illustrations are presented which show just how well the Lehman distribution matches EMPTAC and Celestron 8 power-flux measurements. Perhaps even more significantly, cable current distributions deduced from Lehman-modeled field drivers are remarkably accurate, even at the all-critical upper tail. The Lehman distribution is the only tool, of our knowledge, which seems able to anticipate the upper-tail behavior with good fidelity, especially given that, by definition, the majority of the data to which the Lehman-model fit is matched, is midrange. It is very unusual to see a current cumulative distribution function based on Lehman-modeled field drivers differ by more than a factor of two from subsequently observed cable current cumulative distribution functions.

The Lehman technique for using logarithmic convolution to mix the internal and external attributes of a leaky enclosure can be generalized to other topologies, some quite complex. For example, the fields inside a leaky enclosure in a stirred-mode chamber become a triple logarithmic convolution with two of the variates being chi square with two degrees of freedom, and the third variate having six degrees of freedom. This process can also be used to deduce the response of a leaky enclosure to plane-wave illumination, given its response to mode-stirred excitation. As a final example, the response inside the inner region of a doubly shielded enclosure is shown to be the result of a quadruple logarithmic convolution, with two of the variates having two degrees of freedom, and two having six degrees of freedom.

Section 6 is, in some respects, a continuation of Section 5. For example, the Lehman and chi square models are compared head to head versus experimental results: the superiority of the Lehman model is always very obvious. Additionally, in this section we introduce the beta probability distribution for power-flux density. We have not yet deduced formulas for relating the phase-quadrature field components to power-flux density in this case, so its applicability is somewhat limited just now. We do, however, present some ideas on how to simplify the extraction of this relationship.

In Section 6, we also present the results of a thorough check-out of our modeling techniques on a computerized, automated experimental setup and data-recording system using the G.P.S. bus as the enclosure vehicle (see Volumes II and III of this document).

Here, we additionally introduce the concept of Acceptance Limits, which, unlike Confidence Limits, actually bound the reliability of a model. (This is quite different from obtaining a measure of how confident we are the model is correct. It is sometimes difficult to translate Confidence Limits into practical results. Acceptance Limits, on the other hand, provide obviously useful information, such as, "The model response never deviates on a cumulative distribution plot by more than 50% from the measured response, even at the upper extremity, $p = 1$.") These, and all our other probabilistic concepts, as well as the different pdf's we have introduced, are thoroughly exercised, compared, and critiqued in this section.

The basic element or building block of statistical electromagnetics, be it Bosé-Einstein statistics of coupling to cables in an enclosure, are the eigenmodes of the enclosure. Consequently, Section 7 is devoted to the studying of these eigenmodes. We first consider the eigenmodes of a lossless, leakless volume--it is much easier to do this, and then to add loss and leaks as perturbations.

The ideal enclosure eigenmodes obey Maxwell's equations and, on the internal surface of the enclosure, homogeneous boundary conditions. They may be expressed in either electric-field or magnetic-field form with complete equivalence. The total electric or magnetic energy inside the enclosure is expressed as a summation of the eigenmode coefficients squared times a scaling factor--the eigenmodes are orthogonal, and either the electric-field form or the magnetic-field form (but not both simultaneously) can be made orthonormal with respect to energy content. That is, it is possible to scale the eigenmodes so a mode containing one joule of energy has a coefficient of one in either the electric-field or the magnetic-field expression. If the cavity is driven by electric and magnetic current densities, the excitation strength of each mode is readily expressed as integrals over the enclosure volume of these densities weighted by the modal field distributions.

Upon addition of the loss perturbation to the enclosure description, it is possible to approximate the total power dissipation of the enclosure as a similar series involving the squares of the eigenmode coefficients. This is particularly easy to implement if dissipation can be expressed as loss tangents of the permittivity and permeability. If this is the case, and if the loss tangents are uniform throughout the cavity, the Q of each mode is just the reciprocal of the sum of the reciprocal loss tangents. Otherwise, the terms in the eigenmode sum of power dissipation involve integrals over the enclosure of the eigenmodes squared times the local dissipation parameters (that is, the imaginary parts of ϵ and μ).

Section 7 also includes a detailed discussion of start-up transients as they pertain to eigenmode expansions, and describes a particular caution which must be exercised if this process is formulated in such a way as to involve the Q 's of the modes.

If the enclosure is driven through apertures, an additional aperture surface integral must be added to the formula relating modal amplitudes to the drive. This aperture term is found in accordance with Babinet's Principle, Schelkunoff's Equivalence Principle (some cases only) or, for electrically small apertures, by Bethe hole theory.

Eigenmode evaluation and analysis go very naturally with Lagrangian techniques. Consequently, Section 7 also includes a discussion of evaluation the electric and/or magnetic eigenmodes by this approach, as well as an alternative derivation for relating eigenmode excitation amplitudes to volume electric and magnetic current densities and to illumination through apertures. As a part of this discussion, we illustrate how to partition the drive coming through apertures as excitors of the various eigenmodes, and how to partition (approximately) energy leaking back out as dampers of the eigenmodes. Lastly, Section 7 describes how to expand the enclosure Green's functions in various combinations and permutations of the electric-field and/or magnetic-field eigenmodes: these different combinations relate electric sources to electric fields, electric sources to magnetic fields, etc.

In Section 8, we discuss pickup and scattering by a wire with much more detail than that used in Section 2. In this section, we do retain the assumption that the wire is very small compared to a wavelength, so the current on the wire and the fields they scatter remain completely azimuthally independent. We first obtain the exact, Bessel function homogeneous solution for a signal propagating on an infinite wire in free space. This solution moves at very nearly the speed of light, and can only exist on an infinite wire if some small loss is present in the wire. This solution is primarily characterized by its dispersion relation, which is the complex-plane solution of a quite complicated transcendental equation including the wire loss. Real and imaginary parts of the wavenumber versus frequency are plotted for a Cu wire of 1 mm radius. At 1 Ghz, this solution will *e*-fold in 770 m.

A similar exact Bessel-function inhomogeneous solution is then deduced for a wire driven by an obliquely incident plane wave. Here, the critical plot is the induced or driven wire current as a function of frequency for angle of illumination held constant. If there are no discontinuities on the wire, it develops that the homogeneous solution cannot radiate. In view of reciprocity, this statement is merely a tautology, since a mode which cannot be field driven (is inhomogeneous) cannot drive fields. Energy can couple between the two modes at bends, shadow lines, wire ends, and other nonuniformities, especially including discontinuities, however.

The inhomogeneous solution, unlike the homogeneous solution, does have a radiation resistance to maintain equilibrium between fields and wire currents. This radiation resistance, $\omega\mu_0/8 \Omega/m$, agrees with other results obtained with quite different assumptions. This relatively high value of radiation resistance implies that a wire cannot see how it is terminated if the termination is more than two or three wavelengths removed--a result which is quite familiar to experimentalist, but unexpected by theoreticians. An interesting plot is presented comparing ohmic losses with radiation losses, both as functions of frequency, also for a 1 mm radius Cu wire. The losses cross over around 10 kHz.

At this point, we present a summary of transmission line theory, including again the telegrapher's equation, and illustrate how the single wire is a special case of this model. We also relate the telegrapher's parameters (r , l , g , c) to the characteristic impedance Z_c , and demonstrate the rather surprising result that a single wire transmission line has an r which goes negative above 10 kHz (although the total losses, of course, stay positive). We then compare the telegrapher's equation solution with the exact solution, and illustrate how the telegrapher's equation is not well suited to modeling single isolated wires.

Next, we reintroduce a ground plane, and solve for the inhomogeneous case by letting the wire reflect itself as an infinite series of reflections in the ground plane. We set up the same problem for the homogeneous case, but cannot present results, as we have not yet had support or occasion to solve the resulting transcendental ground-plane-present dispersion relation. As one would expect, the telegrapher's solution and the exact, ground-plane-present solution (with only the first reflection tracked) start out in good agreement, but, for a 1 mm Cu wire 10 cm over a ground plane, begin to diverge around 100 MHz.

The discussion concerning perils of modal startup descriptions involving Q , which we began in Section 7, are summarized and concluded here.

The original statistical electromagnetic modal expansion work of Price and Davis is notoriously tedious, and, in some places, hard to follow. Additionally, it contains some peculiar unit definitions, and at least one outright systematic error. Section 9 is written to provide a more readable presentation of this work, and to correct the outright error(s).

The present document is not prepared as an indictment of the earlier study, which we believe is actually the first really fresh look at EM hazards in a generation. (We would not trouble ourselves criticizing and revising someone else's work unless we found it intrinsically outstanding.) Rather, it is our hope in this section to clarify the earlier document, so that, in the future, neither we nor others have so much trouble comprehending its message. This seems important to us, as the concepts developed by Price, *et al.*, are fundamental to statistical electromagnetics.

The main issues addressed in Section 9 are the topics of eigenmode density and the number of modes in an enclosure excited between the half-power points by monochromatic illumination. Secondary issues include the electric and magnetic energy pumped into each mode, the distinction between slow (modulation) and rapid (carrier) fluctuation in the power-flux density at any given dipole-antenna observer, and partitioning of the power stored and dissipated in each mode. Additional secondary issues treated in Section 9 include the effective coupling coefficients of each of the modes, analogies between an actual 3D enclosure versus simplified results obtained with a 1D violin-string-type resonator, and the relationship between the variance of power seen at a dipole antenna and the total energy in the cavity.

Section 9 concludes with a tutorial review of the Kolmogorov-Smirnov test for statistical significance and fidelity of a distribution model.

DISTRIBUTION LIST

DTIC/OCP
8725 John J. Kingman Rd, Suite 0944
Ft Belvoir, VA 22060-6218 1 cy

AFSAA/SAMI
1570 Air Force Pentagon
Washington, DC 20330-1570 1 cy

AFRL/VSIL
Kirtland AFB, NM 87117-5776 2 cys

AFRL/VSIH
Kirtland AFB, NM 87117-5776 1 cy

Dr. R. Earl Good
Director
AFRL/DE
3550 Aberdeen Ave SE
Kirtland AFB, NM 87117-5776 1 cy

Shield Rite
P. O. Box 8250
Albuquerque NM 87198 2 cys

Official Record Copy
Dr Patrick J. McDaniel
AFRL/DEBE
3550 Aberdeen Ave SE
Kirtland AFB, NM 87117-5776 5 cys